

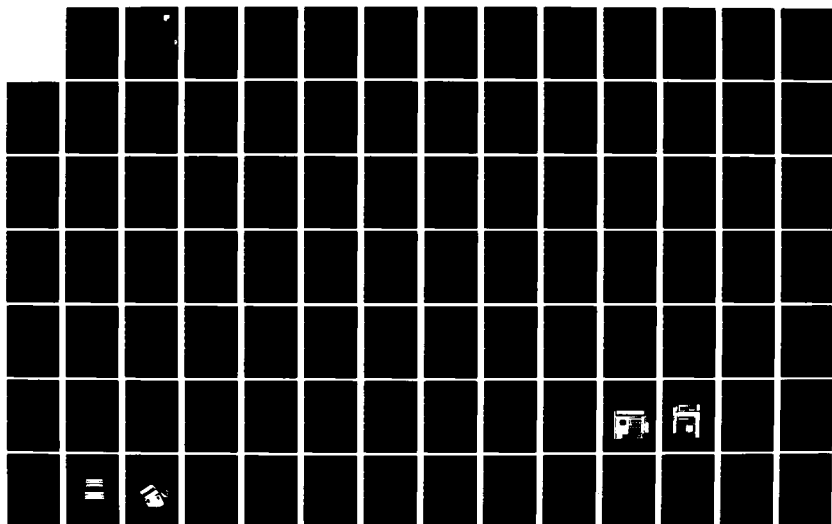
AD-A127 578

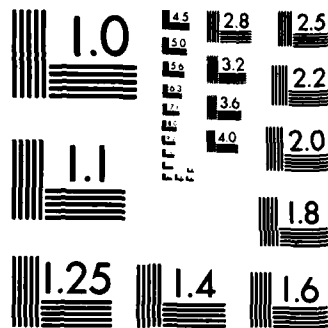
SURFACE ACOUSTIC WAVE NON-LINEAR INTERACTIONS IN
LITHIUM NIOBATE(U) ROME AIR DEVELOPMENT CENTER GRIFFISS
AFB NY R D COLVIN JAN 83 RADC-TR-83-9

1/4

UNCLASSIFIED

F/G 20/5 NL





MICROCOPY RESOLUTION TEST CHART
NATIONAL BUREAU OF STANDARDS-1963-A

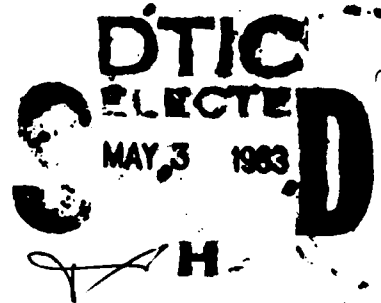
12

RADC-TR-83-9
In-House Report
January 1983



***SURFACE ACOUSTIC WAVE NON LINEAR
INTERACTIONS IN LITHIUM NIOBATE***

Roger D. Colvin, Captain, USAF



APPROVED FOR PUBLIC RELEASE; DISTRIBUTION UNLIMITED

DTIC FILE COPY

ROME AIR DEVELOPMENT CENTER
Air Force Systems Command
Griffiss Air Force Base, NY 13441

83 05 02 01 2

This report has been reviewed by the RADC Public Affairs Office (PA) and is releasable to the National Technical Information Service (NTIS). At NTIS it will be releasable to the general public, including foreign nations.

RADC-TR-83-9 has been reviewed and is approved for publication.

APPROVED:



JOHN K. SCHINDLER
Chief, Antennas & RF Components Branch
Electromagnetic Sciences Division

APPROVED:



ALLAN C. SCHELL
Chief, Electromagnetic Sciences Division

FOR THE COMMANDER:



JOHN P. HUSS
Acting Chief, Plans Office

If your address has changed or if you wish to be removed from the RADC mailing list, or if the addressee is no longer employed by your organization, please notify RADC (EEA) Hanscom AFB MA 01731. This will assist us in maintaining a current mailing list.

Do not return copies of this report unless contractual obligations or notices on a specific document requires that it be returned.

Unclassified

SECURITY CLASSIFICATION OF THIS PAGE (When Data Entered)

REPORT DOCUMENTATION PAGE		READ INSTRUCTIONS BEFORE COMPLETING FORM
1. REPORT NUMBER RADC-TR-83-9	2. GOVT ACCESSION NO.	3. RECIPIENT'S CATALOG NUMBER
4. TITLE (and Subtitle) SURFACE ACOUSTIC WAVE NON-LINEAR INTERACTIONS IN LITHIUM NIOBATE		5. TYPE OF REPORT & PERIOD COVERED In-House Report
		6. PERFORMING ORG. REPORT NUMBER
7. AUTHOR(s) Roger D. Colvin, Capt, USAF		8. CONTRACT OR GRANT NUMBER(s)
9. PERFORMING ORGANIZATION NAME AND ADDRESS Rome Air Development Center (EEA) Hanscom AFB, MA 01731		10. PROGRAM ELEMENT, PROJECT, TASK AREA & WORK UNIT NUMBERS 62702F 46001404
11. CONTROLLING OFFICE NAME AND ADDRESS Rome Air Development Center (EEA) Hanscom AFB, MA 01731		12. REPORT DATE January 1983
		13. NUMBER OF PAGES 347
14. MONITORING AGENCY NAME & ADDRESS (if different from Controlling Office) Same		15. SECURITY CLASS. (of this report) Unclassified
		15a. DECLASSIFICATION DOWNGRADING SCHEDULE
16. DISTRIBUTION STATEMENT (of this Report) Approved for public release; distribution unlimited.		
17. DISTRIBUTION STATEMENT (of the abstract entered in Block 20, if different from Report) Same		
18. SUPPLEMENTARY NOTES Submitted in August 1982 to the Faculty of the Graduate School, University of Missouri-Columbia, in partial fulfillment of the requirements for the degree of Doctor of Philosophy.		
19. KEY WORDS (Continue on reverse side if necessary and identify by block number) Surface acoustic wave Mixing Nonlinear interactions Laser probe Lithium niobate Waveguide Convolution Multimoding		
20. ABSTRACT (Continue on reverse side if necessary and identify by block number) This report presents investigations of three types on non-linear surface acoustic wave (SAW) interactions in lithium niobate (LiNbO ₃). In all cases there are two waves interacting. In the first case, convolution, the waves are collinear and counter propagating. In the second case, collinear mixing, the waves are collinear and co-propagating. In the third case, non-collinear mixing, the waves are non-collinear and co-propagating. The theory for these interactions is presented first and is followed by experiments for each of the interactions. The convolver investigations are		

Unclassified

SECURITY CLASSIFICATION OF THIS PAGE (When Data Entered)

Unclassified

SECURITY CLASSIFICATION OF THIS PAGE(When Data Entered)

directed at understanding and quantifying the various losses and improving the efficiency for high frequency (800 MHz) operation. Convolvers were tested as high as 1 GHz which is the highest frequency of operation ever reported for a SAW convolver. This establishes the potential for greater than 300 MHz instantaneous bandwidth. As a result the size, weight, and power savings are ten thousand times better than present digital technology. Investigations include propagation loss, diffraction, beam steering, attenuation, multimoding, output plate resistivity, and output matching. An upper practical limit seems to be 800 MHz. Efficiencies obtained at this frequency were within a few dB of those at 150 MHz. *

The collinear mixing experiments emphasized improving efficiency, making the interaction broadband, and suppressing unwanted frequencies. Investigation included profiles of fundamental signals and mixing products obtained with a laser probe, broadband and narrow-band transducers for the output (depending on application), and a measure of the bilinearity of the mixer. A dynamic range of 60 dB was typical, and bandwidths greater than 30 percent were demonstrated. Since the conversion loss is worse than a diode mixer, its applications will probably be limited to those requiring bilinearity or to cases where it can be integrated with other SAW devices on the same substrate. Such planar monolithic RF circuits would be much smaller and lower cost than mixers presently used in command, control, communication and intelligence (C³I) systems.

Non-collinear mixing was investigated with a goal of achieving additional suppression of unwanted frequencies over the collinear case. This should be possible because the waves are spatially separated in aximuth. 38, X and Y, Z lithium niobate were investigated for two different angles of interaction. The mixed frequency was at least 8.5 dB weaker than the collinear mixer, and there was no improvement in the suppression of unwanted frequencies. Therefore, non-collinear mixing is not recommended for use as a mixer, but it may be useful for other applications. Appendices give details on the operation of the laser probe, computer programs used to analyze SAW transducers, and broadband and narrow-band output transducers.

Unclassified

SECURITY CLASSIFICATION OF THIS PAGE(When Data Entered)

ACKNOWLEDGEMENTS

The work reported here was performed at the Rome Air Development Center, Electromagnetic Sciences Division, Hanscom AFB, MA. and submitted in August 1982 to the Faculty of the Graduate School, University of Missouri-Columbia, in partial fulfillment of the requirements for the degree of Doctor of Philosophy. Dr. P.H.Carr and A.J.Slobodnik, Jr. of RADC are acknowledged for their countless hours of discussions, criticisms, and encouragement. G.A. Roberts and J.H. Silva of RADC provided expert fabrication and bonding of the SAW transducers. Without their contribution many of the tests would not have been possible.

The author is thankful to Dr. E.J. Charlson for his patience and support.

Finally, the author wishes to thank his wife, Frances, for her patience and understanding.



Accession For	
DTIC GRAHI	<input checked="checked" type="checkbox"/>
DTIC TAB	<input type="checkbox"/>
Unannounced	<input type="checkbox"/>
Justification	
By _____	
Distribution/	
Availability Codes	
Dist	Avail and/or Special
A	

TABLE OF CONTENTS

Chapter	Page
I. SURVEY AND HISTORICAL BACKGROUND.....	1
II. THEORY.....	7
2.1 General Piezoelectric Theory.....	7
A. Derivation of Linear Equations.....	7
B. Solutions to Linear Equations.....	10
C. Derivation of Nonlinear Equations...	12
2.2 Convolution.....	13
A. Derivation of an Alternate Form for Nonlinear Equations (2.19) and (2.20).....	13
B. Solutions to Nonlinear Equations....	18
C. Definition of Convolver Output Quantities.....	22
2.3 Collinear Mixing: a Two-Parameter Phe- nomenological Model.....	27
A. Derivation of Equations.....	27
B. Addition of Dispersion Parameters to the Equations.....	34
C. Discussion of Dispersion and Dif- fraction.....	36
2.4 Non-Collinear Mixing.....	39
A. Introduction.....	39
B. Derivation of Phase Matching Equations.....	42
C. Equations for Approximate Phase Matching.....	49
D. Designing Non-Collinear Mixers.....	51

Chapter		Page
III.	CONVOLUTION.....	58
	3.1 Introduction.....	58
	3.2 Acoustic Losses.....	61
	A. Crystal Propagation Loss.....	61
	B. Diffraction & Beam Steering.....	63
	C. Waveguide Attenuation.....	65
	D. Multimoding.....	68
	3.3 Electrical Losses.....	90
	A. Theoretical Bilinear Conversion Factor.....	90
	B. Experimental Bilinear Conversion Factor.....	93
	C. Output Plate Resistivity.....	99
	D. Transmission Line Effects and Out- put Matching.....	102
	3.4 Performance.....	109
	A. Dynamic Range.....	109
	B. Spurious Levels.....	117
	3.5 Conclusion.....	124
IV.	COLLINEAR MIXING.....	126
	4.1 Introduction.....	126
	4.2 Laser Probing.....	127
	4.3 Broadband Mixing.....	136
	4.4 Narrowband Mixing and Bilinearity.....	153
V.	NON-COLLINEAR MIXING.....	165
	5.1 Introduction.....	165
	5.2 Results for Y,Z LiNbO ₃ with $\omega_1/\omega_2 =$ 2.60.....	166
	5.3 Results for 38,X LiNbO ₃ with $\omega_1/\omega_2 =$ 0.41.....	173
	5.4 Results for 38,X LiNbO ₃ with $\omega_1/\omega_2 =$ 2.44.....	179

5.5 Conclusion.....	184
VI. SUMMARY AND CONCLUSIONS.....	188
REFERENCES.....	193
Appendices	Page
A. A LASER PROBE FOR MICROWAVE ACOUSTIC SURFACE WAVE INVESTIGATIONS.....	209
A.1 Spot Size Much Larger than Acoustic Wavelength.....	209
A.2 Spot Size Much Smaller than Acoustic Wavelength.....	220
A.3 Applications.....	223
A.4 Determining Spot Size.....	227
A.5 Reflectivity of Lithium Niobate.....	230
B. COMPUTER PROGRAMS FOR SAW TRANSDUCER ANALYSIS.	235
B.1 Analysis of Single Channel SAW Filters..	235
B.2 Analysis of SAW Filters with Two or More Channels.....	240
C. STAGGER TUNING OF SAW FILTERS FOR BROAD BANDWIDTH AND GOOD SHAPE FACTOR.....	262
C.1 Introduction.....	262
C.2 Other Approaches.....	265
C.3 Stagger Tuning.....	284
C.4 Experiment.....	289
C.5 Phase Differences - Experiment.....	311
C.6 Phase Differences - Theory.....	320
C.7 Conclusion.....	324
D. NARROWBAND MATCHING OF SAW FILTERS.....	325
VITA.....	335

LIST OF ILLUSTRATIONS

<u>Figure</u>		<u>Page</u>
2.1	Schematic of convolution.....	14
2.2	Schematic of collinear mixing.....	28
2.3	Distance at which non-linear products peak on Y,Z LiNbO ₃	38
2.4	Profiles of two fundamental signals at various distances from the input.....	40
2.5	Schematic of non-collinear mixing.....	41
2.6	Definition of regions for non-collinear mixing.....	53
2.7	Frequency ratio required to steer mixed frequencies on Y,Z LiNbO ₃	55
2.8	Frequency ratios required to steer mixed frequencies on Y,Z LiNbO ₃	56
3.1	Schematic of SAW convolver.....	59
3.2	Spectrum analyzer test setup.....	66
3.3	Network analyzer test setup.....	67
3.4	Peak acoustic energy in SAW waveguide.....	69
3.5	Schematic of dual channel SAW convolver.....	71
3.6	Picture of dual channel SAW convolver.....	72
3.7	Profiles of SAW in 5 λ waveguide.....	74
3.8	Schematic of modes present in 5 λ waveguide..	76
3.9	Profiles of SAW in 15 λ waveguide.....	80
3.10	Profiles of SAW in 37 λ waveguide.....	81
3.11	Profiles of SAW in 37 λ waveguide.....	82
3.12	Profiles of SAW in 45 λ waveguide.....	83
3.13	Profiles of oppositely propagating acoustic waves near center of waveguide.....	86
3.14	Profiles of SAW outside a 5 λ waveguide.....	91
3.15	Picture of 800 MHz SAW convolver.....	96
3.16	F factor (efficiency) test setup.....	97
3.17	Al film resistance.....	101
3.18	Plate uniformity (800 MHz).....	103
3.19	Plate uniformity test setup.....	105
3.20	Plate output impedance (1600 MHz).....	106
3.21	Output impedance of resistor.....	108
3.22	Plate uniformity (1980 MHz).....	110
3.23	Plate uniformity (1832 MHz).....	111
3.24	Plate uniformity and spurious signals (160 MHz).....	112
3.25	Dynamic range and spurious level test setup.....	113

<u>Figure</u>		<u>Page</u>
3.26	Dynamic range of convolved 1600 MHz output.....	115
3.27	Dynamic range of convolved 2 GHz output.....	116
3.28	Bandwidth of 330 MHz convolver.....	118
3.29	Bandwidth test setup.....	119
3.30	Bandwidth of 800 MHz convolver.....	120
3.31	Spurious signals of 160 MHz and 800 MHz convolvers.....	122
4.1	Build up and decay of SAW mixing signals....	128
4.2	Spatial dependence of sum frequencies.....	131
4.3	Spatial dependence of difference frequencies.....	134
4.4	Spatial dependence of sum and difference frequencies.....	135
4.5	Frequency spectrum of filter.....	137
4.6	Picture of SAW and diode mixers.....	138
4.7	Closeup picture of SAW mixer.....	139
4.8	Schematic of single channel SAW mixer.....	141
4.9	Output spectrum of SAW single channel mixer.....	142
4.10	Output spectrum of SAW single channel mixer with grating filter.....	143
4.11	Schematic of dual channel SAW mixer.....	146
4.12	Output spectrum of dual channel SAW mixer.....	148
4.13	Schematic of dual channel SAW mixer with added filter.....	149
4.14	Output spectrum of dual channel SAW mixer with added filter.....	150
4.15	Schematic of single channel SAW mixer with narrowband output transducer and matching...	154
4.16	Linearity of SAW and diode mixers.....	156
4.17	Bilinearity of SAW and diode mixers.....	157
4.18	Output spectrum of SAW mixer with narrowband output transducer.....	160
4.19	Output spectrum of SAW mixer with narrowband output transducer and narrowband matching....	162
5.1	Frequency ratio required to steer mixed frequencies on Y,Z LiNbO ₃	168
5.2	Schematic of non-collinear mixing on Y,Z LiNbO ₃	169
5.3	Definition of angles and terms used in non-collinear mixing.....	170
5.4	Profiles of acoustic waves on Y,Z LiNbO ₃	171
5.5	Output spectrum for non-collinear mixing on Y,Z LiNbO ₃	174

<u>Figure</u>		<u>Page</u>
5.6	Frequency ratios required to steer mixed frequencies on 37, X LiNbO ₃	176
5.7	Schematic of non-collinear mixing on 37,X LiNbO ₃	177
5.8	Profiles of acoustic waves on 38,X LiNbO ₃	178
5.9	Output spectrum for non-collinear mixing on 37,X LiNbO ₃	180
5.10	Schematic of non-collinear mixing on 37,X LiNbO ₃	181
5.11	Profiles of acoustic waves on 38,X LiNbO ₃	183
5.12	Growth and decay of difference signal in region IV.....	185
A.1	Schematic of laser/SAW interaction.....	210
A.2	Schematic of laser scattering directions....	212
A.3	Schematic of scattered laser waves adding coherently at a distant point.....	214
A.4	Schematic of laser probe test setup.....	218
A.5	Schematic of laser probe test setup.....	219
A.6	Picture of laser probe.....	221
A.7	Closeup picture of jig holding SAW to be laser probed.....	222
A.8	Plot of scattering angles for laser probe...	224
A.9	Schematic defining terms and angles for SAW propagation in anisotropic crystal.....	226
A.10	Determining laser spot size.....	228
A.11	Sensitivity of laser probe to polarization..	233
B.1	Flow chart for "Raytheon" computer program.....	236
B.2	Definition of flow chart symbols.....	237
B.3	Flow chart for multi-channel SAW computer program-part A.....	242
B.4	Flow chart for multi-channel SAW computer program-part B.....	243
B.5	Circuit diagram for dual channel SAW filter.....	246
B.6	Simplified circuit diagram for dual channel SAW filter.....	247
C.1	Frequency spectrum of filter.....	263
C.2	Schematic diagram of dual channel filter....	264
C.3	Insertion losses and input impedances for single channel - theory.....	266
C.4	Insertion losses for various Reeder matching network values - theory.....	268

<u>Figure</u>		<u>Page</u>
C.5	Input impedances for C.4.....	269
C.6	Input impedances for C.4.....	270
C.7	Insertion losses for various Reeder matching network values - theory.....	271
C.8	Input impedance for C.7.....	272
C.9	Input impedance for C.7.....	273
C.10	Input impedance for various Reeder matching network values - theory.....	275
C.11	Insertion losses for C.10.....	276
C.12	Insertion losses and input impedances for chirp filters - theory.....	277
C.13	Insertion losses for modified chirp filters - theory.....	279
C.14	Schematic for phase reversal transducer (PRT).....	280
C.15	Insertion losses for apodized dual channel filters - theory.....	282
C.16	Transducer photolithographic masters.....	283
C.17	Circuit diagram for dual channel filter.....	286
C.18	Insertion loss and photolithographic master for dual channel filter - theory.....	288
C.19	Input impedances and insertion losses for dual channel filters - experimental.....	290
C.20	Inductor evaluation.....	292
C.21	Inductance versus frequency for M35T47 inductor.....	293
C.22	Improved circuit diagram for dual channel filter.....	295
C.23	Input impedances and insertion losses for each channel - theory.....	296
C.24	Experiment corresponding to C.23.....	297
C.25	Input impedances and insertion losses for dual channel - theory - corresponding to C.19.....	299
C.26	Input impedances and insertion losses for each channel - theory.....	301
C.27	Experiment corresponding to C.26.....	302
C.28	Input impedance and insertion losses for each channel - theory.....	303
C.29	Experiment corresponding to C.28.....	304
C.30	Input impedances and insertion losses for dual channel - theory.....	305
C.31	Experiment corresponding to C.30.....	306
C.32	Input impedances and insertion losses for each channel - theory.....	308
C.33	Experiment corresponding to C.32.....	309
C.34	Input impedances and insertion losses for each channel - theory.....	310
C.35	Experiment corresponding to C.34.....	312
C.36	Input impedance and insertion loss for dual channel - theory.....	313

<u>Figure</u>		<u>Page</u>
C.37	Experiment corresponding to C.36.....	314
C.38	Experimental insertion loss for dual channel with no matching.....	315
C.39	Experimental insertion loss and phase of dual channel with matching.....	316
C.40	Experimental insertion loss of dual channel with and without matching. Also circuit diagram.....	319
D.1	Schematic of single channel SAW mixer with narrowband output transducer and matching...	326
D.2	Output transducer insertion loss (theory) and photolithographic master.....	328
D.3	Insertion loss of output transducer with matching - experiment.....	329
D.4	Input impedances corresponding to D.3.....	330
D.5	Input impedances of various combinations of L and C.....	333

<u>Table</u>		<u>Page</u>
2.1	Convolver Losses.....	26
2.2	Definition of subscripts for mixing.....	35
2.3	Angles of phase velocities and interaction lengths for non-collinear mixing.....	52
3.1	Experimental convolver losses.....	62
3.2	Convolver efficiencies (F factor).....	94
4.1	SAW mixer insertion losses.....	152
4.2	Conversion loss for SAW and diode broad- band mixers.....	152
4.3	Bilinearity data for SAW and diode mixers.....	159
4.4	Conversion loss for SAW bilinear mixers.....	163

CHAPTER I

SURVEY AND HISTORICAL BACKGROUND

This thesis presents the results of investigations of three types of non-linear surface acoustic wave (SAW) interactions in lithium niobate (LiNbO_3). In all cases there are two waves interacting. In the first case, convolution, the waves are collinear and counter-propagating. In the second case, collinear mixing, the waves are collinear and co-propagating. In the third case, non-collinear mixing, the waves are non-collinear and co-propagating. These interactions can be visualized with the aid of Figures 2.1, 2.2, and 2.5.

The non-linearities investigated in this thesis are due solely to non-linearities in the crystal itself. Another area of investigation, currently enjoying much activity, is the enhancement of non-linearities due to the addition of a semiconductor above the substrate^{1.1-1.12}. In that case, the electric field of the acoustic wave is coupled into the semiconductor, in which the non-linearities are much stronger than those of the piezoelectric crystal alone. In principle, therefore, semiconductor enhancement should be superior. In practice, however, all of the various semiconductor implementations turn out to be vastly inferior in terms of manufacturability, complexity, repeatability, and cost. Therefore, if adequate performance

can be obtained from the piezoelectric crystal alone, it is clearly preferred. Thus, the investigations discussed in this thesis did not utilize semiconductor enhancement.

Wang^{1.13} first demonstrated the convolution concept using bulk waves in 1966. The convolution process was independently rediscovered later by Quate and Thompson^{1.14} who passed longitudinal bulk waves in LiNbO_3 . Svaasand^{1.15} was the first to exhibit convolution with surface waves. Kino et. al. worked extensively with all the possible permutations on this mixing process and contributed significantly to a comprehensive understanding of the process.^{1.1, 1.16, 1.17} While references 1.13-1.17 document the earliest work, they were only demonstrations of the concept. Those early devices were plagued with inadequate dynamic range, narrow bandwidth, and spurious signals of several types. Significant advancements were subsequently made with the addition of beamwidth-compressing multistrip couplers (BWC-MS),^{1.18-1.20} and a broadband matching network.^{1.21} The BWC-MS increased dynamic range by a factor of 10, eliminated some of the spurious signals, and did not limit the bandwidth. The broadband matching network made 40 percent bandwidth easily achievable.

This author noted that by raising the operating frequency to 800 MHz, it should be possible to attain a 320 MHz instantaneous bandwidth. This would be a significant improvement in the capabilities of spread spectrum

communication and radar systems. Thus, the purposes of the convolver work in this thesis were to demonstrate operation at 800 MHz, to quantify the various losses, and to understand the interactions well enough to optimize convolution at this frequency.

Concerning collinear mixing, all of the earliest work was on the generation of harmonics. Since bulk waves have been utilized for many years, it is not surprising that the first harmonics were observed as a bulk wave interaction.^{1.22} However, as surface waves became commonly used, the study of surface non-linearities soon followed. Most workers chose a crystal and orientation known to have strong non-linearities and then sought equations to describe the observed build-up of non-linear products. In most cases the interaction was modeled with a single phenomenological parameter.^{1.23-1.26}

In several notable exceptions, the build-up was related to material constants.^{1.27-1.29} However, those models predicted only the initial slope of the amplitude versus distance curve for the non-linear product. A more complete study should include a prediction of where the build-up will peak and then start to decay. Another deficiency of the early studies is that they used only the elastic constants, and ignored the other material constants. Since much of the early experimental work was at low frequencies (10-200 MHz) where the effects of attenuation and dispersion are not significant within the length of

available substrates, the agreement with these equations was very good. However, at higher frequencies (greater than 400 MHz) attenuation and dispersion are much more important and have to be considered ^{1.30-1.33}. Equations were found that adequately describe these effects.^{1.34} Fortunately, the mixing of two non-harmonically related waves is very similar to the generation of harmonics, and the same equations can be used for both. Also, it is now possible to relate the strength of the non-linearity to all the crystal constants and to predict those orientations of each material that are best.^{1.35} The purpose of the collinear mixing work in this thesis was to consider ways of optimizing the efficiency and bandwidth of the non-linear interaction and suppressing unwanted non-linear products for commonly used orientations of lithium niobate.

Non-linear interactions between non-collinear surface waves have been studied by several investigators. Carr obtained indirect evidence of sum frequency generation on LiNbO_3 by observing an increase in the attenuation of one of two intersecting non-collinear surface waves when the amplitude of the other wave was increased from zero.^{1.36} Tanski and Mayer detected a sum frequency beam generated on single crystal copper,^{1.37,1.38} and Feldmann and Henaff detected a sum frequency signal on LiNbO_3 under conditions of exact phase matching.^{1.39} In the last two cases, phase matching was achieved by choosing propagation directions where pseudo or "leaky" surface waves exist. The pseudo

surface waves travel at faster velocities than ordinary surface waves, and by choosing a suitable combination of the two types of waves, phase matching was accomplished.

Davis and Newhouse detected a phase-mismatched difference frequency surface wave^{1.40} and perfectly phase-matched sum and difference frequency surface waves.^{1.10,1.41,1.42} Phase matching was achieved by using an anisotropic crystal whose surface wave phase velocities vary suitably with direction. Thus, ordinary surface waves could be used, and the inherent attenuation of leaky waves could be avoided. The angles between beams are in most cases smaller than if leaky waves are used, but with a smaller angle configuration, longer interaction regions are possible. Thus better conversion efficiency for perfectly phase matched mixed frequency waves is possible. The purpose of the non-collinear investigations in this thesis was to improve the performance of the collinear mixer by seeking better rejection of the input signals while maintaining or improving the dynamic range (efficiency) of the difference frequency at the output.

Chapter 2 gives a general piezoelectric theory and then the applicable theory for each of the three types of non-linear interactions discussed here. Chapter 3 contains results of experiments on high frequency convolvers. Emphasis is on understanding the various losses and improving the efficiency for high frequency (≈ 800 MHz)

operation. Chapter 4 presents the results of experimental investigations of collinear mixing. Emphasis is on improving efficiency, making the interaction broadband, and suppressing unwanted frequencies. Chapter 5 details experiments of non-collinear mixing. The goal was to gain additional suppression of unwanted frequencies over that obtained in the previous chapter using collinear mixing. Chapter 6 contains a summary and conclusions. Appendix A gives details on a laser probe which was used to obtain acoustic wave profiles and explains how other information can be obtained from these profiles. Appendix B describes two sets of computer programs that were used to analyze the SAW transducers in the various experimental devices. Appendix C gives the theoretical and experimental details concerning one of the broadband transducers used in Chapter 4. Appendix D describes a narrowband matching network used to improve the out-of-band rejection of a SAW mixer discussed in Chapter 4. Finally, the author's VITA is included.

CHAPTER II

THEORY

2.1 General Piezoelectric Theory

A. Derivation of Linear Equations

In any piezoelectric problem there are essentially six quantities that must be considered: stress (T_{ij}), strain (S_{kl}), electric field (E_n), electric displacement (D_m), entropy (S), and temperature (T). The first two quantities are second-order tensors, the next two are vectors, and the latter two are scalars.

By choosing T_{ij} , D_m , and S as the dependent variables and expanding in a power series, the following equations can be obtained.^{2.1} Note that standard summation notation for tensors has been used.^{2.2} Note further that a development very similar to the one given below can be found in Reference 2.3.

$$\begin{aligned}
 T_{ij} = & \frac{\partial T_{ij}}{\partial S_{kl}} S_{kl} + \frac{\partial T_{ij}}{\partial E_n} E_n + \frac{\partial T_{ij}}{\partial T} (T - T_0) + 1/2 \left[\frac{\partial^2 T_{ij}}{\partial S_{kl} \partial S_{qr}} S_{kl} S_{qr} + \right. \\
 & \frac{\partial^2 T_{ij}}{\partial S_{kl} \partial E_n} S_{kl} E_n + \frac{\partial^2 T_{ij}}{\partial S_{kl} \partial T} S_{kl} (T - T_0) + \frac{\partial^2 T_{ij}}{\partial E_n \partial E_p} E_n E_p + \\
 & \left. \frac{\partial^2 T_{ij}}{\partial E_n \partial T} E_n (T - T_0) + \frac{\partial^2 T_{ij}}{\partial T \partial T} (T - T_0)^2 \right] + \dots, \quad (2.1)
 \end{aligned}$$

$$\begin{aligned}
D_m = & \frac{\partial D_m}{\partial S_{kl}} S_{kl} + \frac{\partial D_m}{\partial E_n} E_n + \frac{\partial D_m}{\partial T} (T-T_0) + 1/2 \left[\frac{\partial^2 D_m}{\partial S_{kl} \partial S_{qr}} S_{kl} S_{qr} + \right. \\
& \frac{\partial^2 D_m}{\partial S_{kl} \partial E_n} S_{kl} E_n + \frac{\partial^2 D_m}{\partial S_{kl} \partial T} S_{kl} (T-T_0) + \frac{\partial^2 D_m}{\partial E_n \partial E_p} E_n E_p + \\
& \left. \frac{\partial^2 D_m}{\partial E_n \partial T} E_n (T-T_0) + \frac{\partial^2 D_m}{\partial T \partial T} (T-T_0)^2 \right] + \dots, \quad (2.2)
\end{aligned}$$

$$\begin{aligned}
S-S_0 = & \frac{\partial S}{\partial S_{kl}} S_{kl} + \frac{\partial S}{\partial E_n} E_n + \frac{\partial S}{\partial T} (T-T_0) + 1/2 \left[\frac{\partial^2 S}{\partial S_{kl} \partial S_{qr}} S_{kl} S_{qr} + \right. \\
& \frac{\partial^2 S}{\partial S_{kl} \partial E_n} S_{kl} E_n + \frac{\partial^2 S}{\partial S_{kl} \partial T} S_{kl} (T-T_0) + \frac{\partial^2 S}{\partial E_n \partial E_p} E_n E_p + \\
& \left. \frac{\partial^2 S}{\partial E_n \partial T} E_n (T-T_0) + \frac{\partial^2 S}{\partial T \partial T} (T-T_0)^2 \right] + \dots, \quad (2.3)
\end{aligned}$$

$$\frac{\partial D_m}{\partial E_n} = \epsilon_{mn} \quad \text{gives the linear dielectric permeability,}$$

$$\frac{\partial T_{ij}}{\partial S_{kl}} = c_{ijkl} \quad \text{yields the linear elastic coefficients,}$$

$$\frac{\partial S}{\partial T} = \frac{\rho C}{T} \quad \text{is the density times specific heat divided by the absolute temperature.}$$

By introducing the appropriate thermodynamic function, which in this case is the Electric Gibbs Function G_2 , several important symmetry properties can be shown.

$$dG_2 = T_{ij} dS_{ij} - D_m dE_m - SdT \quad (2.4)$$

Thus, since the above is a perfect differential,

$$T_{ij} = \frac{\partial G_2}{\partial S_{ij}}, \quad D_m = - \frac{\partial G_2}{\partial E_m}, \quad S = - \frac{\partial G_2}{\partial T} \quad (2.5)$$

It then follows that

$$\frac{\partial T_{ij}}{\partial E_n} = \frac{\partial^2 G_2}{\partial S_{ij} \partial E_n} = \frac{\partial^2 G_2}{\partial E_n \partial S_{ij}} = - \frac{\partial D_n}{\partial S_{ij}} = - e_{nij}, \quad (2.6)$$

$$\frac{\partial T_{ij}}{\partial T} = \frac{\partial^2 G_2}{\partial S_{ij} \partial T} = \frac{\partial^2 G_2}{\partial T \partial S_{ij}} = - \frac{\partial S}{\partial S_{ij}} = - \lambda_{ij}, \quad (2.7)$$

$$\frac{\partial D_m}{\partial T} = - \frac{\partial^2 G_2}{\partial E_m \partial T} = - \frac{\partial^2 G_2}{\partial T \partial E_m} = \frac{\partial S}{\partial E_m} = p_m, \quad (2.8)$$

If all higher-order terms are omitted from Equations (2.1), (2.2), and (2.3), the linear piezoelectric constitutive relations result.

$$T_{ij} = c_{ijkl} S_{kl} - e_{nij} E_n - \lambda_{ij} (T - T_0), \quad (2.9a)$$

$$D_m = e_{mkl} S_{kl} + \epsilon_{mn} E_n + p_m (T - T_0), \quad (2.9b)$$

$$(S - S_0) = \lambda_{kl} S_{kl} + p_n E_n + \frac{\rho C}{T} (T - T_0) \quad (2.9c)$$

If temperature changes are now neglected, Equations (2.9) become

$$T_{ij} = c_{ijkl} S_{kl} - e_{nij} E_n, \quad \text{linear piezoelectric} \quad (2.10)$$

$$D_m = \epsilon_{mn} E_n + e_{mkl} S_{kl}, \quad \text{constitutive relations}$$

The other linear equations describing acoustic wave propagation in an arbitrary, anisotropic piezoelectric medium are as follows:^{2.4}

$$\frac{\partial T_{ij}}{\partial x_i} = \rho \frac{\partial^2 u_j}{\partial t^2}, \quad \text{equations of motion,} \quad (2.11)$$

$$\frac{\partial D_i}{\partial x_i} = 0, \quad \text{derived from Maxwell's} \quad (2.12)$$

$$E_i = - \frac{\partial \phi}{\partial x_i}, \quad \text{equations under the} \\ \text{quasi-static assumption,}$$

$$S_{kl} = 1/2 \left[\frac{\partial u_k}{\partial x_l} + \frac{\partial u_l}{\partial x_k} \right], \quad \text{linear, strain-mechanical} \quad (2.13) \\ \text{displacement relations,}$$

where ρ is the mass density, ϕ the electromagnetic potential, and u the mechanical displacement.

B. Solutions to Linear Equations

By substitution, Equations (2.10) through (2.13) can be reduced to

$$c_{ijkl} \frac{\partial u_k}{\partial x_{li}} + e_{kij} \frac{\partial \phi}{\partial x_{ki}} = \rho \frac{\partial^2 u_j}{\partial t^2} \quad (2.14) \\ j = 1, 2, 3$$

$$e_{ikl} \frac{\partial u_k}{\partial x_{li}} - \epsilon_{ik} \frac{\partial \phi}{\partial x_{ki}} = 0 \quad (2.15)$$

Surface wave solutions of Equations (2.14) and (2.15) are assumed to be of the standard, complex travelling-wave form in which V_s is the wave velocity, α the exponential decay into the crystal, and ω the steady-state angular frequency, namely,

$$u_i = \beta_i \exp \left[-\frac{\alpha \omega x_3}{V_s} \right] \exp \left[j\omega \left(t - \frac{x_1}{V_s} \right) \right] \quad (2.16)$$

$i = 1, 2, 3$

$$\phi = \beta_4 \exp \left[-\frac{\alpha \omega x_3}{V_s} \right] \exp \left[j\omega \left(t - \frac{x_1}{V_s} \right) \right] \quad (2.17)$$

The surface waves under consideration are assumed to be traveling in the x_1 direction along a surface whose normal is in the x_3 direction. The displacements and potentials are considered to be independent of the x_2 coordinate.

Substituting Equations (2.16) and (2.17) into Equations (2.14) and (2.15) yields a linear, homogeneous system of four equations in the unknowns, $\beta_1, \beta_2, \beta_3$, and β_4 . The determinant of the coefficients of the unknowns in these equations must be zero in order that a non-trivial solution exist. Since the fields must be bounded, or go to zero as $x_3 \rightarrow \infty$, only the roots with non-negative real parts are allowed. The roots are either pure imaginary or occur in pairs with positive and negative real parts. In general for piezoelectric crystals, roots occur such that four with positive real parts can be selected. Upon obtaining the admissible roots, they can be substituted back

into the linear, homogenous system of four equations, and the unknowns, β_i , can be found to within a constant factor.

C. Derivation of Nonlinear Equations

Since this thesis deals with non-linear, or higher-order terms, some of the symmetry properties associated with the coefficients of Equations (2.1) and (2.2) are also listed.

They are

$$\frac{\partial^2 T_{ij}}{\partial E_n \partial S_{kl}} = - \frac{\partial^2 D_n}{\partial S_{ij} \partial S_{kl}} = - \frac{\partial e_{nij}}{\partial S_{kl}} = \frac{\partial c_{ijkl}}{\partial E_n}, \quad (2.18a)$$

$$\frac{\partial^2 T_{ij}}{\partial E_n \partial E_p} = - \frac{\partial^2 D_n}{\partial S_{ij} \partial E_p} = - \frac{\partial e_{nij}}{\partial E_p} = \frac{\partial \epsilon_{np}}{\partial S_{ij}}. \quad (2.18b)$$

The following definitions can also be made:

$$\frac{\partial^2 T_{ij}}{\partial S_{kl} \partial S_{qr}} = \frac{\partial c_{ijkl}}{\partial S_{qr}}, \quad \frac{\partial^2 D_m}{\partial E_n \partial E_p} = \frac{\partial \epsilon_{mn}}{\partial E_p}. \quad (2.18c)$$

If terms higher than second-order and temperature changes are now neglected, and the coefficients of Equations (2.18) are substituted, Equations (2.1) and (2.2) become

$$T_{ij} = c_{ijkl} S_{kl} - e_{nij} E_n + 1/2 \left[\frac{\partial c_{ijkl}}{\partial S_{qr}} S_{kl} S_{qr} - 2 \frac{\partial e_{nij}}{\partial S_{kl}} S_{kl} E_n - \frac{\partial e_{nij}}{\partial E_p} E_p E_n \right], \quad (2.19)$$

$$D_m = e_{mkl} S_{kl} + \epsilon_{mn} E_n + 1/2 \left[\frac{\partial e_{mkl}}{\partial S_{qr}} S_{kl} S_{qr} + 2 \frac{\partial e_{mkl}}{\partial E_n} S_{kl} E_n + \frac{\partial \epsilon_{mn}}{\partial E_p} E_n E_p \right]. \quad (2.20)$$

2.2 Convolution

A. Derivation of an Alternate Form of Non-linear Equations (2.19) and (2.20)

The alternate form of non-linear equations (2.19) and (2.20) above is based on the work of Ganguly and Davis.^{2,5} The solution of their non-linear equations leads to a figure of merit, M , that is related to the material constants of the piezoelectric crystal. For completeness, it is shown in part A of this section that Ganguly and Davis' non-linear equations are equivalent to the non-linear equations above, (2.19) and (2.20). This is significant because (2.19) and (2.20) were derived from the six fundamental quantities: stress, strain, electric field, electric displacement, entropy, and temperature. Part B of this section gives the development of solutions to Ganguly and Davis' equations. Part C explains other parameters needed to describe the performance of a SAW convolver.

In the degenerate surface acoustic wave (SAW) convolver, two oppositely directed waves with equal frequencies are mixed due to the non-linearities of the elastic, piezoelectric, electrostrictive, and dielectric properties of the medium. A sum frequency with no spatial phase variation is generated. This signal is detected by a plate electrode along the delay line. This can be visualized with the aid of Figure 2.1. Specifically, the two SAWS have wave vectors \vec{k}_1 and $\vec{k}_2 = -\vec{k}_1$ and frequencies ω_1 and $\omega_2 = \omega_1$. These waves travel in opposite directions on

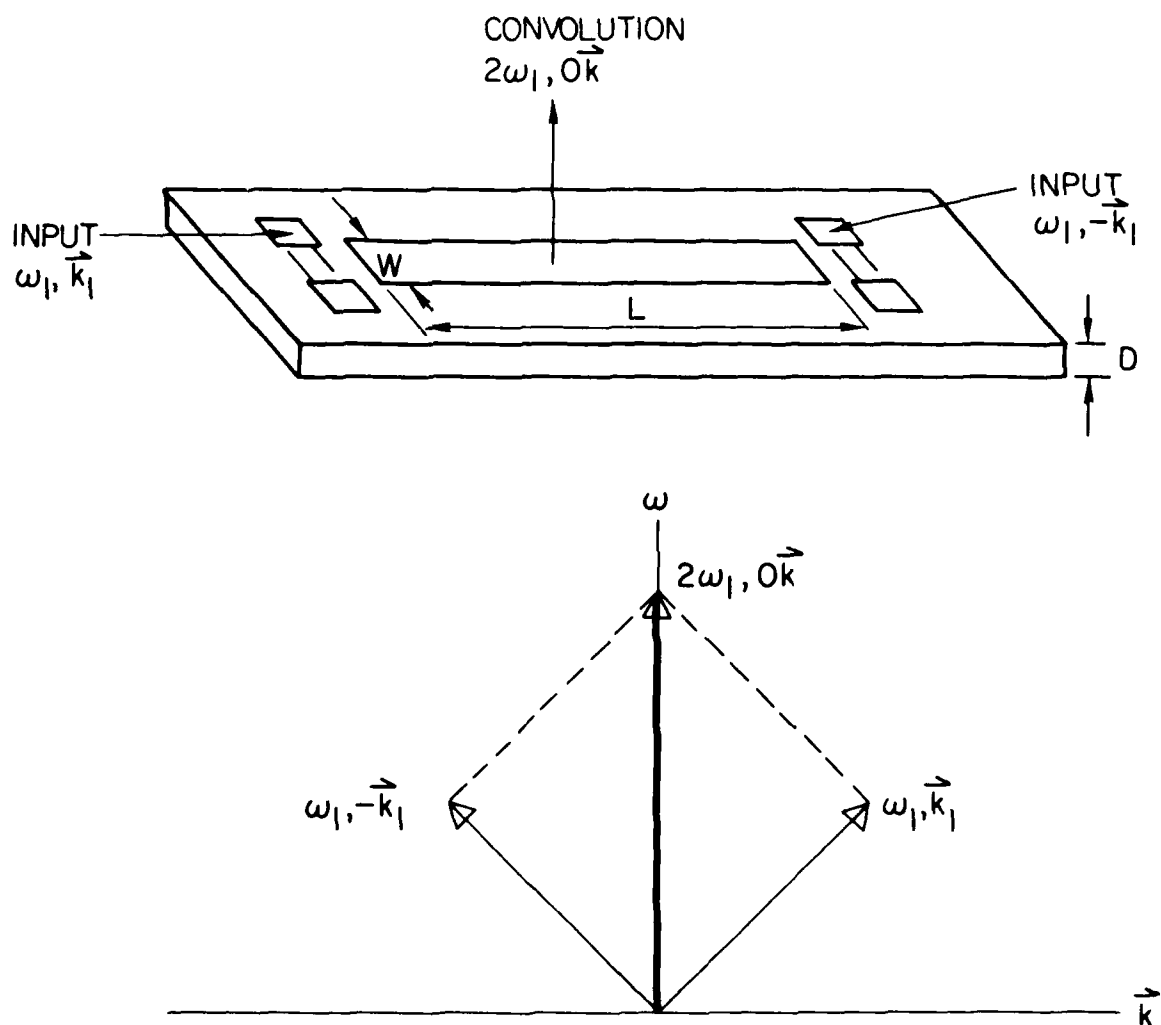


Figure 2.1 (Top) Schematic diagram of SAW convolver. (Bottom) ω, k diagram for SAW convolver. (The term $(\omega_1 - \omega_1), (k_1 + k_1)$ does exist, but is not utilized and therefore not shown).

solid substrate of thickness D with an infinitesimally thin metallic electrode on top of the surface. D is much greater than the acoustic wavelength (λ) so the substrate is assumed to be semi-infinite for surface wave propagation. The only assumption is that a signal at frequency $\omega_3 = \omega_1 + \omega_2$ and wave vector (parallel to the surface) $\vec{k}_3 = \vec{k}_1 + \vec{k}_2 = 0$ is generated due to the non-linear interaction. $\vec{k}_3 = 0$ defines a standing wave. A coordinate system is chosen in which the Z axis is perpendicular to the surface, and the X axis is parallel to the direction of propagation of the incident waves. The solid occupies the space $Z < 0$, and there is no variation along the Y axis.

The stress equation of motion and the charge equation of electrostatics in the stationary material coordinate system are given by

$$\rho' \frac{\partial^2 u_j}{\partial t^2} - \frac{\partial T_{ij}}{\partial x_i} = F_K^{NL} \quad (2.21)$$

$$\frac{\partial D_i}{\partial x_i} = Q_i^{NL} \quad (2.22)$$

where ρ' is the density of the material, and u_j the particle displacement vector. Equation (2.21) has units of force and in the linear case is equal to zero. In the non-linear case it will be non-zero, hence the symbol F_K^{NL} . Likewise, Equation (2.22) has units of charge and in the linear case is equal to zero. In the non-linear case it will be non-

zero, hence the symbol Q_i^{NL} .

The constitutive relations for the linear stress tensor, T_{ij} , and the linear electric displacement vector, D_i , are

$$T_{ij} = c_{ijkl} \frac{\partial u_k}{\partial x_l} + e_{kij} \frac{\partial \phi}{\partial x_k} \quad (2.23)$$

$$D_i = e_{ikl} \frac{\partial u_k}{\partial x_l} - \epsilon_{ik} \frac{\partial \phi}{\partial x_k} \quad (2.24)$$

Here c_{ijkl} , e_{ikl} , and ϵ_{ik} are the elements of the second order elastic, piezoelectric, and dielectric tensors, respectively. ϕ is the electrostatic potential. Equations (2.21) and (2.22) are the non-linear version of the linear equations (2.11) and (2.12). Equations (2.23) and (2.24) are equivalent to Equation (2.10), but have been written in a slightly different form for convenience.

Up to terms quadratic in small field variables, the non-linear quantities, F_K^{NL} and Q_i^{NL} , are given by

$$F_K^{NL} = - \frac{\partial T_{ij}^{NL}}{\partial x_i} \quad (2.25)$$

$$Q_i^{NL} = + \frac{\partial D_i^{NL}}{\partial x_i} \quad (2.26)$$

where T_{ij}^{NL} and D_i^{NL} have the following forms:

$$\begin{aligned}
 T_{ij}^{NL} = & e_{kijlm} \frac{\partial \phi}{\partial x_k} \frac{\partial u_l}{\partial x_m} + 1/2 C_{ijklmn} \frac{\partial u_k}{\partial x_l} \frac{\partial u_m}{\partial x_n} \\
 & - 1/2 d_{klij} \frac{\partial \phi}{\partial x_k} \frac{\partial \phi}{\partial x_l} + 1/2 C_{ijkl} \frac{\partial u_m}{\partial x_k} \frac{\partial u_m}{\partial x_l} \\
 & + C_{kjml} \frac{\partial u_i}{\partial x_k} \frac{\partial u_m}{\partial x_l} + e_{kmj} \frac{\partial u_i}{\partial x_m} \frac{\partial \phi}{\partial x_k}
 \end{aligned} \tag{2.27}$$

$$\begin{aligned}
 D_i^{NL} = & - d_{ijkl} \frac{\partial \phi}{\partial x_j} \frac{\partial u_k}{\partial x_l} + 1/2 e_{ijklm} \frac{\partial u_j}{\partial x_k} \frac{\partial u_l}{\partial x_m} \\
 & + 1/2 \epsilon_{ijk} \frac{\partial \phi}{\partial x_j} \frac{\partial \phi}{\partial x_k} + 1/2 e_{ikm} \frac{\partial u_l}{\partial x_k} \frac{\partial u_l}{\partial x_m}
 \end{aligned} \tag{2.28}$$

The parameters e_{kijlm} , c_{ijklmn} , d_{klij} , and ϵ_{ijk} are, respectively, the third order piezoelectric, elastic, electrostrictive, and dielectric tensors. T_{ij}^{NL} and D_i^{NL} are considered to be weak perturbations on linear quantities T_{ij} and D_i . T_{ij}^{NL} and D_i^{NL} are responsible for coupling the two incident waves.

The linear combination of Equations (2.23) and (2.27) can be derived from Equation (2.19). The linear combination of Equations (2.24) and (2.28) can be derived from Equation (2.20). This can be done with the following substitutions:^{2.6,2.7}

$$S_{ij} = 1/2 \left[\frac{\partial u_i}{\partial x_j} + \frac{\partial u_j}{\partial x_i} + \frac{\partial u_k}{\partial x_i} \frac{\partial u_k}{\partial x_j} \right] \quad (2.29)$$

$$E_i = - \frac{\partial \phi}{\partial x_i} - \frac{\partial \phi}{\partial x_i} \frac{\partial u_k}{\partial x_j} \quad (2.30)$$

$$\frac{\partial e_{nij}}{\partial E_p} = d_{nijp} \quad (2.31)$$

Terms of third and higher order have been neglected.

B. Solutions to Nonlinear Equations

The boundary conditions used in solving Equations (2.21) and (2.22) are:^{2.5}

$$T_{13} + T_{13}^{NL} = T_{23} + T_{23}^{NL} = T_{33} + T_{33}^{NL} = 0 \quad (2.32a)$$

$$\phi = 0 \text{ (short circuit)} \quad (2.32b)$$

$$\frac{d}{dt} (D_3 + D_3^{NL}) = 0 \text{ (open circuit)} \quad (2.32c)$$

$$\frac{\partial \phi}{\partial x} = 0 \quad (2.32d)$$

at $z = 0$.

At $z = D$, the boundary conditions are

$$u_i = 0 \quad (2.33a)$$

$$\phi = 0 \quad (2.33b)$$

when $D/\lambda \rightarrow \infty$.

One can visualize these boundary conditions by referring again to Figure 2.1. The subscripts 1,2,3 refer to directions X,Y,Z. The acoustic wave propagates in the X direction along a surface whose normal is in the Z direction. $Z = 0$ is the top surface, and $Z = D$ is the bottom surface. Equation (2.32a) means the surfaces are not bound, but rather are free to move. Both top and bottom surfaces are at zero potential, and the mechanical displacement has decayed to zero at the bottom surface.

For brevity, the following notation is used:

$$\tau_j = u_j, \quad j = 1, 2, 3 \quad (2.34a)$$

$$\tau_4 = \phi \quad (2.34b)$$

A perturbation method^{2.5} is used to solve the system of Equations (2.21) - (2.28), and the solution is written in the form

$$\tau_\beta = 0^\tau_\beta + 1^\tau_\beta, \quad \beta = 1, 2, 3, 4 \quad (2.35)$$

0^τ_β is the solution to the linear problem obtained by setting $F_K^{NL} = Q_i^{NL} = 0$. 1^τ_β is the solution of Equations (2.21) and (2.22) when F_K^{NL} and Q_i^{NL} are derived from Equations (2.25) - (2.28) by substituting 0^τ_β for u_i and ϕ . 0^τ_β may be written in the form

$$\begin{aligned} 0^\tau_\beta = & \frac{g_1}{2k_1} \sum_{\rho=1}^4 A_{\beta\rho} \exp \left[-\alpha_\rho k_1 z \right] \exp \left[i(\omega_1 t - k_1 x) \right] \\ & + \frac{g_2}{2k_1} \sum_{\rho=1}^4 A_{\beta\rho}^* \exp \left[-\alpha_\rho^* k_1 z \right] \exp \left[i(\omega_1 t + k_1 x) \right] \end{aligned} \quad (2.36)$$

representing the two incident waves (ω_1, \vec{k}_1) and $(\omega_1, -\vec{k}_1)$ of amplitudes g_1 and g_2 respectively.

The calculation of the decay constants α_ρ , the coefficients $A_{\beta\rho}$, and the surface wave velocity $V_S = \omega_1/k_1$

to satisfy the boundary conditions is standard.^{2.8} The equations of motion for l^T_β can now be obtained by calculating the driving terms F_K^{NL} and Q_i^{NL} from Equations (2.25) - (2.28) and (2.36).

Coefficients from the series solution of l^T_β can be used to define a quantity called M. This M factor is the strength of acoustic non-linearity for any specified direction of propagation and is used as a figure of merit. For the Y cut, Z propagating orientation, Ganguly^{2.5} calculated $M = 2.63 \times 10^{-4}$ Vm/W (units are volt-meter/watt). This can be compared with the measured values of 0.79×10^{-4} Vm/W (Ref 2.9), and 0.9 to 1.2×10^{-4} Vm/W (Ref 2.5). The agreement between theory and experiment is actually considered quite good for this orientation, especially considering the inaccuracy of the higher order constants used in the theory. The non-linearity is dominated by third order piezoelectric constants.^{2.5} As the propagation direction is rotated away from Z, the piezoelectric interaction decreases, and the electrostrictive interaction increases until both make about the same level contribution. The dielectric and elastic interactions are small for all propagation directions^{2.5} on Y cut crystals.

For the crystal-cut 128° from Y and X propagating, M is calculated^{2.5} to be 1.02×10^{-4} Vm/W. This orientation is also referred to in the literature as 38,X meaning the surface perpendicular is rotated 38° from +Z which, of

course, is equivalent to a 128° rotation from +Y. The piezoelectric interaction dominates for angles of propagation in the vicinity of 55° away from +X, where M is largest. Unfortunately, the linear piezoelectric coupling is very small for this orientation. For other angles, the magnitude of the piezoelectric interaction drops to levels comparable to that of the other constants, particularly the electrostrictive and dielectric.^{2,5}

For X cut LiNbO_3 , numerical calculations show that $M=0$ for any propagation direction. In this cut the crystal surface is a plane of mirror symmetry, and the non-linear interaction does not produce any electric potential. In general, the piezoelectric interaction tends to dominate in orientations where M is large, and the Y, Z orientation is evidently one of the best for convolution.

C. Definition of Convolver Output Quantities

It is now well-established^{2,10,2.11} that the RMS open-circuit output voltage, V_o , of a degenerate acoustic convolver is proportional to the product of the two acoustic input power densities (P_{1a}/W , P_{2a}/W), and it can be expressed by the general relation:

$$V_o(2\omega) = \frac{M}{W} (P_{1a} P_{2a})^{1/2}, \quad (2.37)$$

where W is the beam width of the two incident waves. From Equation (2.37) it is seen that the narrower the beamwidth, the larger the output voltage. To determine the best

performance of the device, it is necessary to consider the maximum power available at the output port. To do so, the internal impedance of the system must be known. It is defined as the ratio of V_o to the short circuit output current. This impedance can be expressed as a function of the medium parameters by solving the linear problem, and by viewing the non-linear effect as an extra electric charge generator.^{2,9} The solution is rather simple if the system is reduced to one dimension normal to the surface of the substrate. The real part of the internal impedance, R_a , is then found to be proportional to the ratio of the bulk-wave piezoelectric coupling coefficient, r_a , to the area of the interaction region, WL (See Figure 2.1). The imaginary part, C_a , is proportional to WL . The capacity due to the substrate thickness, C_o , must also be included and is usually smaller than C_a . Using these terms and relations the internal impedance can be written as:

$$Z_i = \frac{r_a}{WL} + \frac{1}{jc_a 2\omega WL} + \frac{1}{jc_o 2\omega} \quad (2.38)$$

where $r_a = WL R_a$ and $c_a = C_a/WL$. The maximum available power follows:

$$P_{\max} = \frac{V_o^2}{4R_a} = \frac{V_o^2 WL}{4r_a} \quad (2.39)$$

By using Equation (2.37), P_{\max} can be expressed as follows:

$$P_{\max} = F_{\text{int}} P_{1a} P_{2a} \quad (2.40)$$

$$\text{where } F_{\text{int}} = \frac{M^2 L}{4r_a W} = \frac{M^2}{4R_a W^2}, \text{ and} \quad (2.41)$$

$$P_{ia} = P_i - IL_i, \quad i = 1, 2. \quad (2.42)$$

F_{int} is the bilinear factor of the device, and IL is the insertion loss of the SAW transducer. From Equation (2.41) one may compute the internal resistance, R_a . In a typical example^{2.9} $R_a = 3$ ohms. A measure of V_o across a 50 ohm load, therefore, is a valid measurement of the open circuit output voltage because $R_a \ll 50$ ohms. One obvious conclusion is that the narrower the beamwidth, W , the larger F_{int} is. Since measurements are made in electromagnetic power rather than acoustic power, one more parameter is needed:

$$F_{\text{ext}} = \frac{P_{\text{out}}}{P_1 P_2} \quad (2.43)$$

where all powers are now electromagnetic.

Typically P_{out} falls considerably short of P_{max} minus the two transducer insertion losses. The other losses can be accounted for with the following equation.^{2.12}

$$F_{\text{ext}} = \frac{1}{W^2} + T^4 + M^2 + H^2 + \frac{1}{2R_L} + \text{transformer loss} \\ + \text{BWC loss} + \text{acoustic loss} + \frac{W}{\text{mw}}, \quad (2.44)$$

where each term is expressed in dB. In this last equation

$\frac{1}{W^2}$ = sheet current in the output electrode which
is proportional to the reciprocal of the
acoustic beamwidth squared, the beamwidth
being expressed in meters,

T = transducer insertion losses (two),

M = figure of merit as discussed in section 2.2B,

$$H^2 = \frac{V_L^2}{V_{OC}} ,$$

$\frac{1}{2R_L}$ = correction for voltage-to-power conversion,

transformer = a transformer may be used to impedance
loss match the output,

BWC loss = a beamwidth compressing multistrip coupler
may be used to decrease W,

acoustic loss = losses due to propagation, diffraction,
beam steering, multimoding, etc., and

$\frac{W}{mw}$ = 30 dB: converts watts to dBm.

Two typical examples are presented in Table 2.1. The first is from a convolver made by Thomson CSF (T-CSF) which operated at 156 MHz; the second is from an 800 MHz RADC device, discussed length in Chapter 3 of this thesis.

	(T-CSF)	(RADC)	
$\frac{1}{W^2}$	+78	+76	dB
T^4	-16	-15	dB
M^2	-81	-87	dB
$\frac{H^2}{2R_L}$	-21	-20	dB
transformer loss	-0.5	0	dB
BWC loss	-1.5	0	dB
Acoustic loss	-1.0	-16	dB
$\frac{W}{mw}$	-30	-30	dBm
F_{ext}	-73	-92	dBm

Table 2.1 - Convolver Losses

The investigations in Chapter 3 of this thesis focus on the acoustic loss term in the above example. The larger operating frequency (800 MHz versus 156 MHz) was chosen because it offers the possibility of much larger instantaneous bandwidth. As will be seen in Chapter 3, there are many contributions to the acoustic loss term. Measuring, understanding, and minimizing these losses were the primary goals of Chapter 3.

2.3 Collinear Mixing: A Two-Parameter Phenomenological Model

A. Derivation of Equations

Collinear mixing is represented schematically in Figure 2.2. A physical transducer layout is shown in the upper portion, while the ω, \vec{k} diagram is given below. In the previous section it was shown that some orientations of certain piezoelectric crystals have relatively strong non-linearities. Mixing takes place when two signals are multiplied via the non-linearities of the crystal. This can be seen from the identity

$$2 \cos A \cos B = \cos (A-B) + \cos (A+B), \quad (2.45)$$

where $A = (k_1 z - \omega_1 t)$ and $B = (k_2 z - \omega_2 t)$. Equation (2.45) applies only to the sum and difference, while in actuality the fundamental signals, first order mixing products, and harmonics (a signal mixing with itself) also mix with each other to produce higher order products. The process continues, producing an infinite series of products.

Most researchers have chosen a crystal and an orientation known to have strong non-linearities and then sought equations to describe the build up of observed non-linear products. Much of the early work was for second harmonics and at low frequencies (10-200 MHz).^{2.13-2.15} These equations predict that harmonics continue to build up until attenuation loss starts to dominate. This has been verified experimentally within the limits of available substrate length. However, at higher frequencies (greater

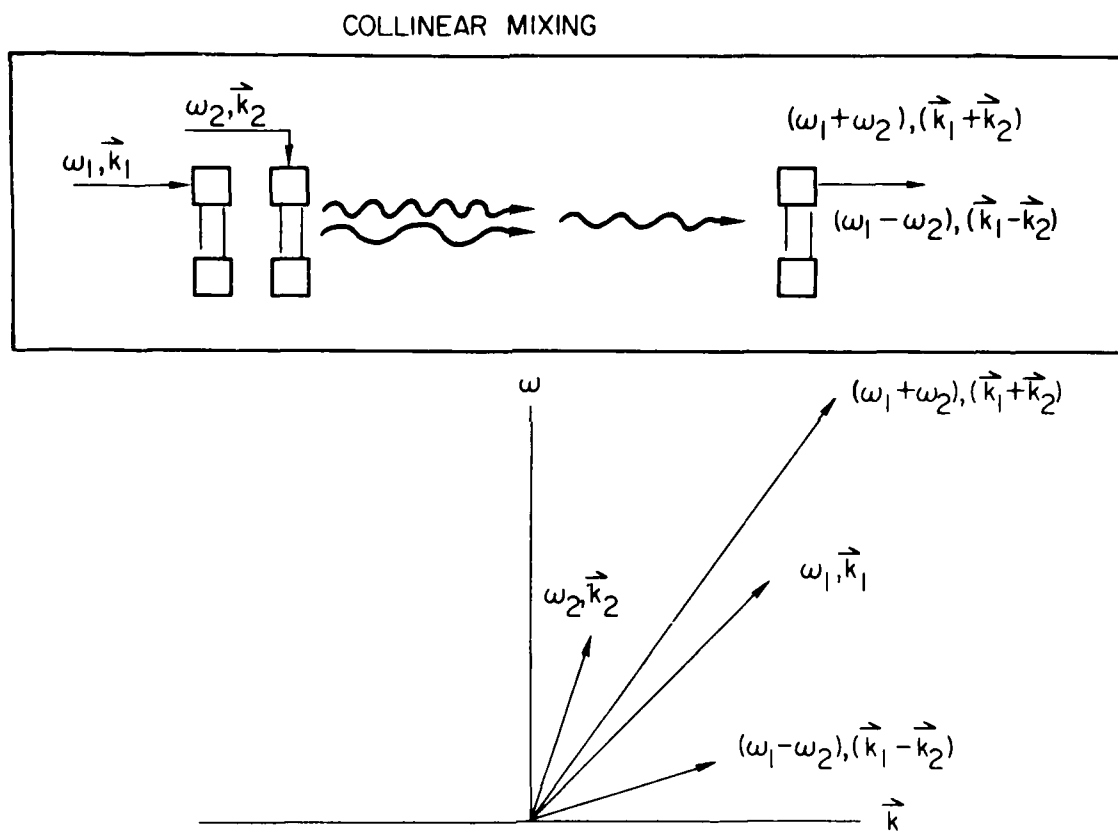


Figure 2.2 (Top) Schematic diagram of SAW collinear mixer.
(Bottom) ω, k diagram for SAW collinear mixer.

than 400 MHz) attenuation and dispersion become much more important and cannot be neglected.^{2.16-2.19}

Since attenuation and dispersion are so important at higher frequencies, it is the purpose of this section to describe a theory that includes these effects. In the previous section it was stated that quadratic terms were adequate to describe the non-linear interactions and that these non-linearities depend on both second order and third order material constants. One of these constants may dominate for a particular crystallographic orientation, but its relative contribution will change when the orientation, i.e. the direction of propagation, is changed. The approach taken in this section is to combine all the non-linear contributions into a single parameter, β , for each orientation. β may either be related to M which is calculated from the material constants as described in the previous section, or determined indirectly by curve fitting to experimental data as described below.^{2.13,2.20} On the free surface of a crystal (and on any plane parallel to the free surface) the one dimensional wave equation applies:

$$\frac{\partial^2 S}{\partial t^2} = v_s^2 \frac{\partial^2 S}{\partial z^2} \quad (2.46)$$

where S could be any displacement, strain, or combination of surface wave variables, and Z is the direction of propagation. The fact that S decays with depth from the

surface is implicitly contained in the value of V_s used. The simplest model which can be proposed for describing the mixing of acoustic surface waves is one dimensional and contains a single parameter characterizing the non-linearity.

A phenomenological model is followed which was postulated by Adler, et al,^{2.13,2.20} and introduces a quadratic non-linearity by means of a single non-linear parameter. Associating S with a strain and replacing S by $S + \beta S^2$ on the right hand side of Equation (2.46) gives

$$\frac{\partial^2 S}{\partial t^2} = v_s^2 \frac{\partial^2}{\partial z^2} \left[S + \beta S^2 \right] \quad (2.47)$$

or

$$\frac{\partial^2 S}{\partial t^2} - v_s^2 \frac{\partial^2 S}{\partial z^2} = \beta v_s^2 \frac{\partial^2 S^2}{\partial z^2} \quad (2.48)$$

Equation (2.48) is then the one-dimensional, single-parameter, mathematic model postulated, β being the phenomenological non-linear parameter. In Equation (2.48) the left hand side is the linear wave equation; the right hand side is the non-linear term representing the source of the parametric interaction.

Consider a group of surface waves propagating in the Z direction consisting of many different frequencies. A strain associated with this disturbance can be written as a sum of strains over all the frequencies.

$$\begin{aligned}
S = \sum_i S_i = \sum_i X_i(z) \cos [k_i z - \omega_i t] \\
+ Y_i(z) \sin [k_i z - \omega_i t]
\end{aligned} \tag{2.49}$$

where X_i and Y_i are the strain amplitudes in the X and Y directions respectively. They are assumed to be slowly varying in the sense that they satisfy the following conditions

$$X_i \gg \frac{1}{k_i} \frac{\partial X_i}{\partial z} \gg \frac{1}{k_i^2} \frac{\partial^2 X_i}{\partial z^2} \gg \dots \tag{2.50}$$

This implies that the amplitude changes are small within an acoustic wavelength. For compactness it is convenient to define

$$Co(i) = \cos [k_i z - \omega_i t], \tag{2.51a}$$

$$Si(i) = \sin [k_i z - \omega_i t], \tag{2.51b}$$

and rewrite the strain equation (2.49) as

$$S = \sum_i S_i = \sum_i X_i Co(i) + Y_i Si(i) \tag{2.52}$$

which is just an "in phase" and "quadrature" decomposition.

Then

$$\frac{\partial^2 S}{\partial t^2} = \Sigma_i - \omega_i^2 S_i \quad (2.53)$$

$$\begin{aligned} \frac{\partial^2 S}{\partial z^2} = & \Sigma_i \left[-k_i^2 X_i + 2k_i \frac{\partial Y_i}{\partial z} \right] \text{Co}(i) \\ & + \left[-k_i^2 Y_i - 2k_i \frac{\partial X_i}{\partial z} \right] \text{Si}(i) \\ & + \text{terms containing second derivations of} \\ & X_i \text{ and } Y_i \end{aligned} \quad (2.54)$$

which we omit because of condition (2.50).

$$\begin{aligned} S^2 = & \Sigma_p \Sigma_q \left[X_p \text{Co}(p) X_q \text{Co}(q) \right. \\ & + X_p \text{Co}(p) Y_q \text{Si}(q) + Y_p \text{Si}(p) X_q \text{Co}(q) \\ & \left. + Y_p \text{Si}(p) Y_q \text{Si}(q) \right] \end{aligned} \quad (2.55)$$

$$\begin{aligned} \frac{\partial S^2}{\partial z} = & \Sigma_p \Sigma_q \left[X_p X_q \text{Co}(p) \frac{\partial \text{Co}(q)}{\partial z} + X_p X_q \text{Co}(q) \frac{\partial \text{Co}(p)}{\partial z} \right. \\ & + X_p \text{Co}(p) Y_q \frac{\partial \text{Si}(q)}{\partial z} + X_p Y_q \text{Si}(q) \frac{\partial \text{Co}(p)}{\partial z} \\ & + Y_p \text{Si}(p) X_q \frac{\partial \text{Co}(q)}{\partial z} + Y_p X_q \text{Co}(q) \frac{\partial \text{Si}(p)}{\partial z} \\ & + Y_p \text{Si}(p) Y_q \frac{\partial \text{Si}(q)}{\partial z} + Y_p Y_q \text{Si}(q) \frac{\partial \text{Si}(p)}{\partial z} \\ & \left. + \text{derivative terms of } Y_p, Y_q, X_p, \text{ and } X_q \right] \end{aligned} \quad (2.56)$$

$$\frac{\partial^2 S^2}{\partial z^2} = \Sigma_p \Sigma_q \left[X_p X_q \text{Co}(p) \frac{\partial^2 \text{Co}(q)}{\partial z^2} + X_p X_q \frac{\partial \text{Co}(q)}{\partial z} \frac{\partial \text{Co}(p)}{\partial z} \right.$$

$$\begin{aligned}
& + x_p x_q \text{Co}(q) \frac{\partial^2 \text{Co}(p)}{\partial z^2} + x_p x_q \frac{\partial \text{Co}(p)}{\partial z} \frac{\partial \text{Co}(q)}{\partial z} \\
& + x_p \text{Co}(p) y_q \frac{\partial^2 \text{Si}(q)}{\partial z^2} + x_p y_q \frac{\partial \text{Si}(q)}{\partial z} \frac{\partial \text{Co}(p)}{\partial z} \\
& + x_p y_q \text{Si}(q) \frac{\partial^2 \text{Co}(p)}{\partial z^2} + x_p y_q \frac{\partial \text{Co}(p)}{\partial z} \frac{\partial \text{Si}(q)}{\partial z} \\
& + y_p \text{Si}(p) x_q \frac{\partial^2 \text{Co}(q)}{\partial z^2} + y_p x_q \frac{\partial \text{Co}(q)}{\partial z} \frac{\partial \text{Si}(p)}{\partial z} \\
& + y_p x_q \text{Co}(q) \frac{\partial^2 \text{Si}(p)}{\partial z^2} + y_p x_q \frac{\partial \text{Si}(p)}{\partial z} \frac{\partial \text{Co}(q)}{\partial z} \\
& + y_p \text{Si}(p) y_q \frac{\partial^2 \text{Si}(q)}{\partial z^2} + y_p y_q \frac{\partial \text{Si}(q)}{\partial z} \frac{\partial \text{Si}(p)}{\partial z} \\
& + y_p y_q \text{Si}(q) \frac{\partial^2 \text{Si}(p)}{\partial z^2} + y_p y_q \frac{\partial \text{Si}(p)}{\partial z} \frac{\partial \text{Si}(q)}{\partial z} \\
& + \text{first and second derivative terms of } y_p, y_q, x_p, \\
& \text{and } x_q \quad \quad \quad (2.57)
\end{aligned}$$

Next, derivatives are taken, like terms are combined, the identities

$$2 \sin A \sin B = \cos (A-B) - \cos (A+B), \quad (2.58a)$$

$$2 \cos A \cos B = \cos (A-B) + \cos (A+B), \quad (2.58b)$$

$$\text{and } 2 \sin A \cos B = \sin (A-B) + \sin (A+B), \quad (2.58c)$$

are used, related terms are reduced to perfect squares, like terms are again combined, and derivatives of $y_p, y_q, x_p,$ and x_q are dropped because of condition (2.50). Finally,

$$\frac{\partial^2 S^2}{\partial z^2} = \sum_p \sum_q \left[1/2 (k_q + k_p)^2 (x_p x_q - y_p y_q) \text{Co}(p+q) \right]$$

$$\begin{aligned}
& + 1/2 (k_q - k_p)^2 (X_p X_q + Y_p Y_q) \text{Co}(p-q) \\
& + 1/2 (k_q + k_p)^2 (X_p Y_q + Y_p X_q) \text{Si}(p+q) \\
& + 1/2 (k_q - k_p)^2 (X_p Y_q - Y_p X_q) \text{Si}(p-q) \Big] \quad (2.59)
\end{aligned}$$

B. Addition of Dispersion Parameters to the Equations

Now we introduce the dispersion parameters, Δ_s and Δ_d as shown in Equations (2.60), where s means sum and d means difference. Then

$$\text{Co}(p+q) = \sin(\Delta_s z) \text{Si}(p+q) + \cos(\Delta_s z) \text{Co}(p+q) \quad (2.60a)$$

$$\text{Co}(p-q) = \sin(\Delta_d z) \text{Si}(p-q) + \cos(\Delta_d z) \text{Co}(p-q) \quad (2.60b)$$

$$\text{Si}(p+q) = \cos(\Delta_s z) \text{Si}(p+q) + \sin(\Delta_s z) \text{Co}(p+q) \quad (2.60c)$$

$$\text{Si}(p-q) = \cos(\Delta_d z) \text{Si}(p-q) + \sin(\Delta_d z) \text{Co}(p-q) \quad (2.60d)$$

Equations (2.60) are then substituted into (2.59). Then the new version of Equations (2.59) plus (2.54) and (2.53) are substituted into (2.48). After equating sine and cosine coefficients in this equation one obtains

$$\frac{\partial X_i}{\partial z} = \frac{\beta}{2k_i} \left[\text{Si}(i) \cdot \text{coefficients of } \frac{\partial^2 S^2}{\partial z^2} \right] \quad (2.61a)$$

$$\frac{\partial Y_i}{\partial z} = \frac{-\beta}{2k_i} \left[\text{Co}(i) \cdot \text{coefficients of } \frac{\partial^2 S^2}{\partial z^2} \right] \quad (2.61b)$$

Finally, we account for the heretofore neglected attenuation by adding terms $-\alpha_i X_i$ and $-\alpha_i Y_i$ to Equations (2.61a) and (2.61b). Thus, we have

$$\frac{\partial X_i}{\partial z} = -\alpha_i X_i + \frac{\beta}{2k_i} \left[S_i(i) \cdot \text{coefficients of } \frac{\partial^2 S^2}{\partial z^2} \right] \quad (2.61c)$$

$$\frac{\partial Y_i}{\partial z} = -\alpha_i Y_i - \frac{\beta}{2k_i} \left[C_o(i) \cdot \text{coefficients of } \frac{\partial^2 S^2}{\partial z^2} \right] \quad (2.61d)$$

The following table is an aid in understanding the meaning of the subscripts.

i	p + q	p - q
1	1 + 1	1 - 1
2	1 + 2	1 - 2
	1 + 1	1 - 1
	2 + 2	2 - 2
3	1 + 1	1 - 1
	1 + 2	1 - 2
	1 + 3	1 - 3
	2 + 2	2 - 2
	2 + 3	2 - 3
	3 + 3	3 - 3

Table 2.2 Definition of subscripts for mixing

Subscript i is the number of input frequencies. Subscripts p and q represent the first order mixing products produced from i inputs.

Equations (2.61c) and (2.61d) are a system of coupled ordinary differential equations describing the amplitude variations of each frequency component (X_i, Y_i) . They are an initial value problem with β and the Δ 's as free parameters. Such a system is easily solved by standard numerical integration routines. Initial values, frequencies, and attenuation constants, α_i , must be known a priori. If one can then find a β and a Δ by iteration such that measured and calculated values agree, then the model is good. If velocity changes linearly with frequency, then $\Delta_s = \Delta_d$ making the equations simpler.

C. Discussion of Dispersion and Diffraction

The above equations have been solved by Adler, et al.^{2.13,2.20} They then compared the solutions to experiments using X cut, Y propagating α - quartz, (1 $\bar{1}$ 0) cut, (001) propagating BGO, and Y cut, Z propagating LiNbO₃ at various frequencies. Agreement between theory and experiments was excellent. Of particular interest was the agreement with the experimental results of Slobodnik^{2.16} using Y,Z LiNbO₃ at a fundamental frequency of 900 MHz. Agreement was excellent for all four harmonics with $\beta = 0.57$ and $\Delta = 6.2 \text{ cm}^{-1}$. One conclusion drawn from this is that even a well polished bare substrate has significant dispersion that cannot be neglected. This is because there is always some degree of roughness left no matter how good the polish. This of course becomes more important at higher frequencies because a given roughness becomes a larger

fraction of one acoustic wavelength. The significance of dispersion is further supported by the experimental data in Figure 2.3. Here we see that the distance from the input transducer at which the non-linear product peaks is not predictable regardless of whether it is a harmonic, sum, or difference. The conclusion is that the dispersion varies between the experimental samples due to differences in sample preparation. The only other variable that affects the spatial dependance of the non-linear products is attenuation, and it is well known and predictable.^{2.21} (Note: all the data in Figure 2.3 is for Y,Z LiNbO₃, and all samples were well-polished by SAW standards). Several figures in Chapter IV give additional data showing the build up and decay of non-linear products for various conditions and frequencies. From those figures, various references^{2.13,2.16,2.20} and the equations in this section, one can conclude that the growth and decay of non-linear products has the following functional dependance: $I(x) = e^{\beta x} + e^{-\alpha x} \cos(\Delta)$. I is the intensity of the SAW; x is the propagation direction; β is the strength of the non-linearity; α is the attenuation constant; and Δ is the dispersion parameter. α is well-known and has the form $\alpha = af + bf^2$ where f is the frequency of the SAW. Thus, the non-linear product has an exponential growth, and the decay is an exponential multiplied by a cosine. The dispersion parameter, Δ , is the one that varies from crystal to crystal; α and β can be predicted with reasonable

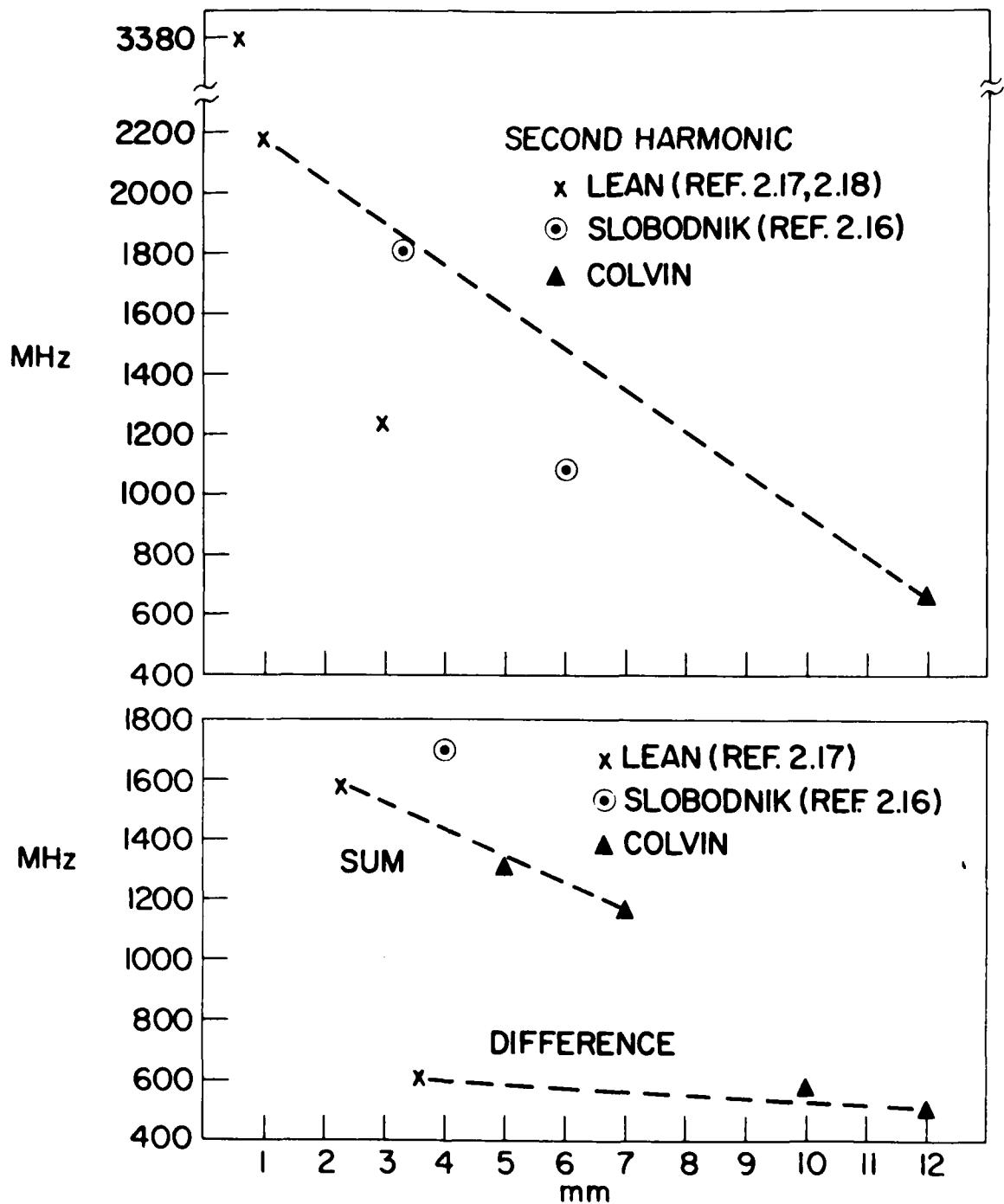


Figure 2.3 (Top) Distance from input transducer at which second harmonic peaks on Y,Z LiNbO₃. (Bottom) Distance from input transducer at which sum or difference frequencies peak on Y,Z LiNbO₃. The dashed lines are placed arbitrarily. The Figure demonstrates that the distances are not predictable as explained in the text.

confidence.

A further consideration is the diffraction of the fundamental signals. Figure 2.4 shows a set of profiles of two fundamental signals as a function of distance from the input. Here we see that one fundamental is diffracting much more than the other. These plots were taken from an actual device described in Chapter IV. To date, all theoretical predictions of build-up and decay of non-linear products have assumed no diffraction. Thus this is another source of error in trying to predict the build-up and decay of non-linear products.

For the above stated reasons of diffraction and non-predictability of dispersion, there was no attempt at predicting the spatial dependence of build up and decay for the harmonics or sum and difference frequencies in Chapter IV. Rather, they were experimentally determined with a laser probe (see Appendix A and Chapter IV). And it has already been shown that by curve fitting with the two parameter model discussed in this section, agreement with theory can be obtained after the fact.

2.4 Non-Collinear Mixing

A. Introduction

The idea of non-collinear mixing is best introduced by considering the schematic at the top of Figure 2.5. Here there are two fundamental inputs, one of which makes a small angle (5° - 15°) relative to the other. The dashed lines show that a sum frequency can propagate in the

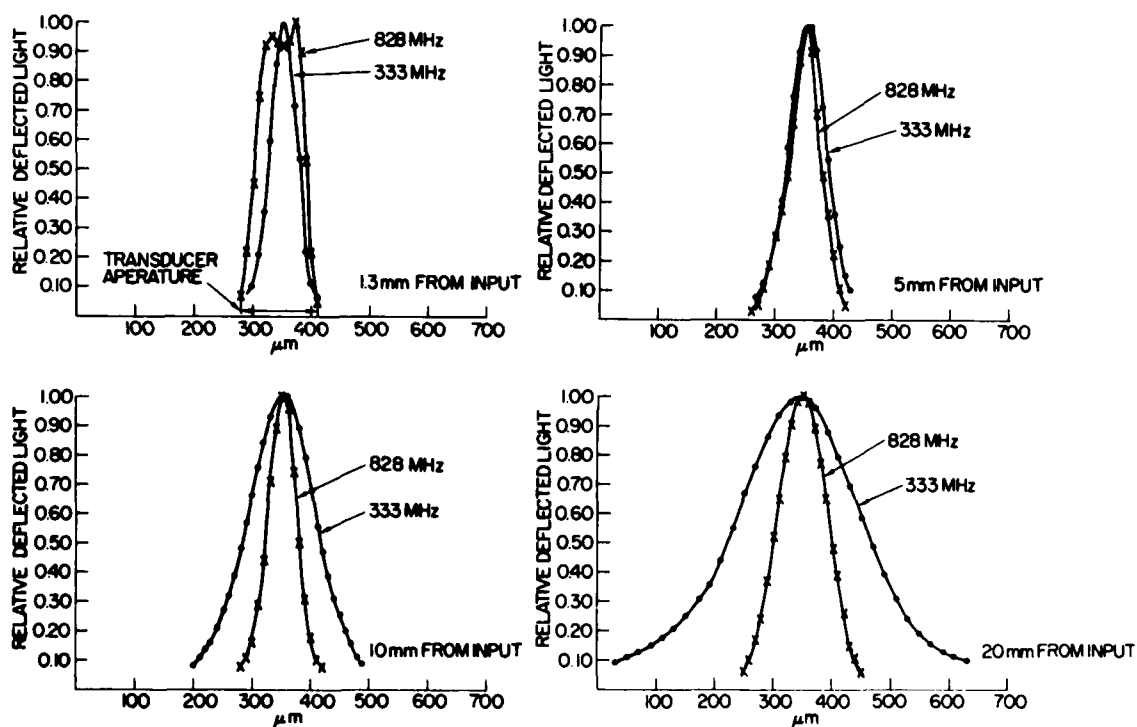


Figure 2.4 Profiles of two fundamental signals used for collinear mixing as they propagate down the crystal.

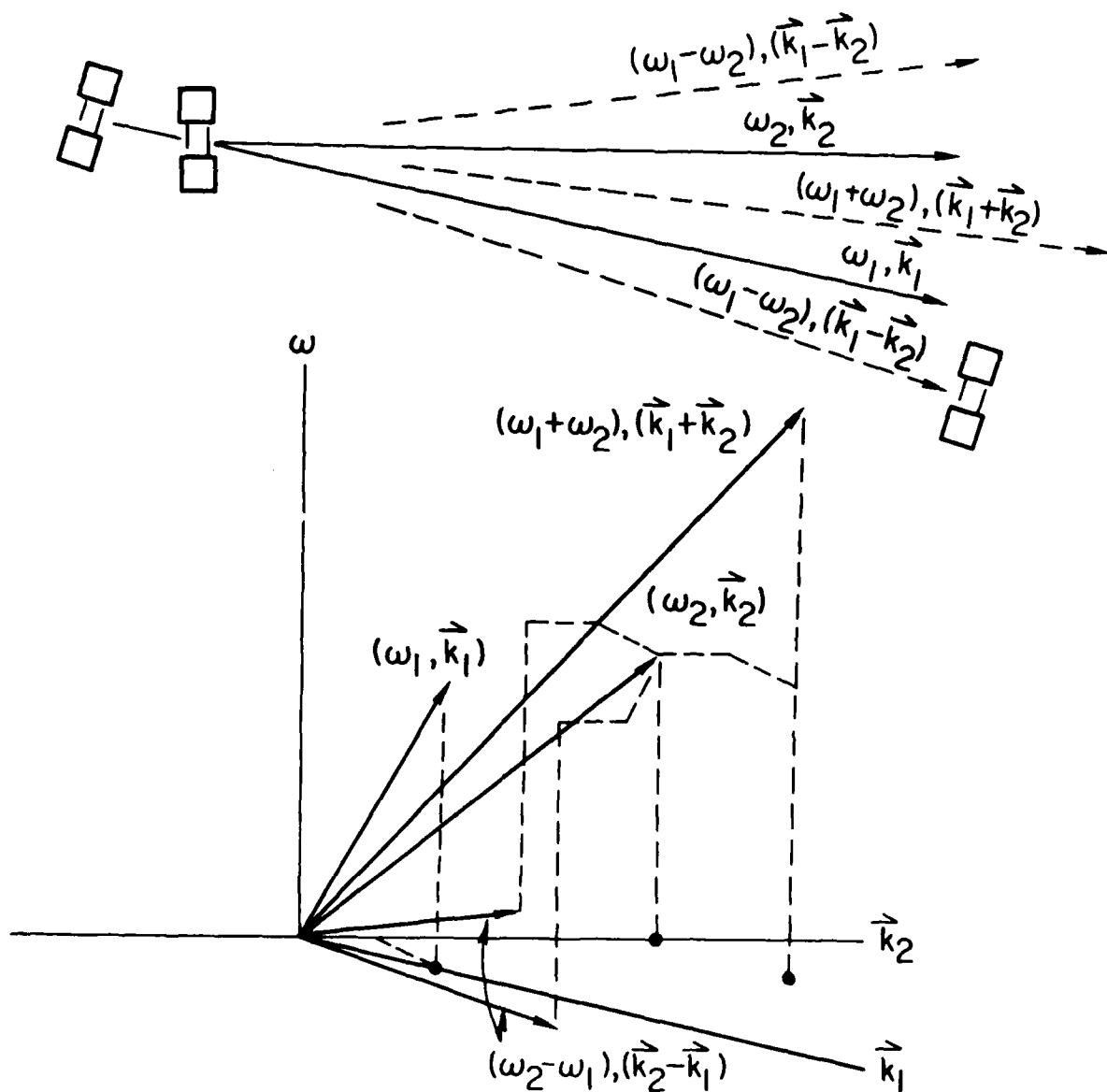


Figure 2.5 (Top) Schematic diagram of non-collinear mixing including three possible types of interaction. Each of the signals makes an angle, θ_n , with the $+x$ crystalline axis, e.g. $\theta_2 = 90^\circ$ for Y,Z and $\theta_2 = 0^\circ$ for 38,X LiNbO₃. (Bottom) ω, k diagram for the signals above. Dashed lines give the projection of each signal into the k plane.

region between the fundamental inputs, and that the difference frequency can propagate in either of the regions outside the boundary of the fundamental inputs. The angle of propagation is determined by the ratio of input frequencies, ω_1/ω_2 . In general, there will be a sum and either difference frequency simultaneously present. As the ratio ω_1/ω_2 is varied, the two signals are steered within their allowed regions. The bottom of Figure 2.5 gives the ω, \vec{k} diagram for each of the possible signals. The dashed lines give the projection of the various vectors onto the \vec{k} plane.

There are several necessary conditions for non-collinear mixing to occur. One is a sufficient power density to adequately couple to the crystal non-linearities. Another is that the phase velocities of the non-linear

products $\left| \frac{\omega_1 \pm \omega_2}{\vec{k}_1 \pm \vec{k}_2} \right|$, must approximately match the acoustic velocity of the crystal for the intended direction of propagation. One consequence of this is that non-collinear mixing is not possible on isotropic crystals, whereas collinear mixing is. Further, the generation efficiency of the mixed signal depends on how closely the phase velocities, $\left| \frac{\omega_1 \pm \omega_2}{\vec{k}_1 \pm \vec{k}_2} \right|$, match the velocity of the crystal for that direction of propagation.

B. Derivation of Phase Matching Equations

The necessary conditions and equations for phase

matching will now be formally developed. Assume that an input surface wave beam has frequency ω_1 and wave vector \vec{k}_1 , where \vec{k}_1 makes an angle θ_1 with the reference direction. Let this intercept the other input beam of frequency ω_2 and wave number \vec{k}_2 making an angle θ_2 with the reference direction. Each of the signals makes an angle, θ_n , with the +X crystalline axis. For example, θ_2 equals 90° for Y,Z and θ_2 equals 0° for 38,X LiNbO₃. A third beam with frequency ω_3^\pm and wave number \vec{k}_3^\pm will be produced if the amplitudes of beams 1 and 2 are sufficient for non-linear mixing and if the following conditions representing conversion of energy and momentum are met:

$$\omega_3^\pm = \omega_1 \pm \omega_2 \quad (2.62)$$

$$\vec{k}_3^\pm = \vec{k}_1 \pm \vec{k}_2 \quad (2.63)$$

The angle between \vec{k}_3^\pm and the reference direction is designated θ_3^\pm . Under conditions where the difference frequency surface wave is perfectly phase matched, the sum frequency beam will in general be mismatched. A quantitative measure of this mismatch is

$$\Delta k = k_3^+ - (k_1 + k_2) \quad (2.64)$$

where $|\vec{k}_3^+| = \frac{\omega_3^+}{v(\theta_3^+)}$ and $|\vec{k}_1 + \vec{k}_2| = \frac{\omega_3^+}{v_3^+}$. Beams 1 and 2 are

the inputs, and beam 3⁺ is the generated sum frequency. V_3^+ is the phase velocity of the surface wave 3⁺ at angle θ_3^+ from the reference direction. $V(\theta_3^+)$ is the surface wave phase velocity of the substrate material at angle θ_3^+ from the reference direction. Equation (2.64) can be separated into components as follows:

$$\begin{aligned} \Delta \vec{k} = & \left[k_3^+ \cos \theta_3^+ - k_1 \cos \theta_1 - k_2 \cos \theta_2 \right] \hat{x} \\ & + \left[k_3^+ \sin \theta_3^+ - k_1 \sin \theta_1 - k_2 \cos \theta_2 \right] \hat{y} \end{aligned} \quad (2.65)$$

or

$$\Delta \vec{k} = |\Delta \vec{k}| \left[\hat{x} \cos \theta_+ + \hat{y} \sin \theta_+ \right] \quad (2.66)$$

where θ_+ is the direction $\Delta \vec{k}$ makes with the reference direction.

$$|\vec{k}_3^+ - \Delta \vec{k}| \sin \theta_3 = k_1 \sin \theta_1 + k_2 \sin \theta_2 \quad (2.67a)$$

$$|\vec{k}_3^+ - \Delta \vec{k}| \cos \theta_3 = k_1 \cos \theta_1 + k_2 \cos \theta_2 \quad (2.67b)$$

$$\text{Thus, } \tan \theta_3 = \frac{\frac{k_1}{k_2} \sin \theta_1 + \sin \theta_2}{\frac{k_1}{k_2} \cos \theta_1 + \cos \theta_2} \quad (2.68)$$

Substituting $\frac{k_1}{k_2} = \frac{v_2}{v_1} \frac{\omega_1}{\omega_2}$ into Equation (2.68),

rearranging terms, and using a trigonometric identity gives

$$\frac{\omega_1}{\omega_2} = \frac{v_1 \sin(\theta_2 - \theta_3)}{v_2 \sin(\theta_3 - \theta_1)} \quad (2.69)$$

Equations (2.68) and (2.69) may be thought of as the phase information in (2.64). The magnitude information in Equation (2.64) can be obtained by squaring each of Equations (2.67), adding them together, and using trigonometric identities. The result is the following relation:

$$|\vec{k}_3^+ - \Delta \vec{k}|^2 = k_1^2 + k_2^2 + 2k_1 k_2 \cos(\theta_1 - \theta_2). \quad (2.70)$$

The left hand side of Equation (2.70) is equal to

$$|\vec{k}_1 + \vec{k}_2|^2 \text{ and } \left[\frac{\omega_1 + \omega_2}{v_3^+} \right]^2. \text{ Equation (2.70) can then be}$$

divided by $k_2^2 = \left[\frac{\omega_2}{v_2} \right]^2$ to give

$$\left[1 + \frac{\omega_1}{\omega_2} \right]^2 \left[\frac{\omega_2}{v_3^+} \right]^2 \left[\frac{v_2}{\omega_2} \right]^2 = \left[\frac{\omega_1}{\omega_2} \right]^2 \left[\frac{v_2}{v_1} \right]^2 + 1$$

$$+ 2 \frac{\omega_1}{\omega_2} \frac{v_2}{v_1} \cos(\theta_1 - \theta_2) \quad (2.71)$$

Next, Equation (2.69) can be used to replace $\frac{\omega_1}{\omega_2}$ in the right hand side of Equation (2.71) giving

$$\left(1 + \frac{\omega_1}{\omega_2}\right)^2 = \left[\frac{V_3^+}{V_2}\right]^2 \left[1 + \frac{\sin^2(\theta_2 - \theta_3)}{\sin^2(\theta_3 - \theta_1)} + 2 \frac{\sin(\theta_2 - \theta_3) \cos(\theta_1 - \theta_2)}{\sin(\theta_3 - \theta_1)}\right]. \quad (2.72)$$

Rewriting Equation (2.72) gives

$$\frac{1}{\left(1 + \frac{\omega_1}{\omega_2}\right)} = \left[\frac{V_2}{V_3^+}\right] \frac{\sin(\theta_3 - \theta_1)}{\left[\sin^2(\theta_2 - \theta_3) + \sin^2(\theta_3 - \theta_1) + \frac{1}{2 \sin(\theta_2 - \theta_3) \sin(\theta_3 - \theta_1) \cos(\theta_2 - \theta_1)}\right]^{1/2}}. \quad (2.73)$$

In shortened notation this becomes

$$\frac{1}{1 + \frac{\omega_1}{\omega_2}} = \left[\frac{V_2}{V_3^+}\right] \frac{\sin(\theta_3 - \theta_1)}{\text{Denom}^{1/2}}, \quad (2.74)$$

$$\text{where Denom} = \left[\sin^2(\theta_2 - \theta_3) + \sin^2(\theta_3 - \theta_1) + 2 \sin(\theta_2 - \theta_3) \cdot \sin(\theta_3 - \theta_1) \cos(\theta_2 - \theta_1)\right].$$

Squaring Equation (2.74) and rearranging yields

$$\left[\frac{V_3}{(\omega_2 + \omega_1)}\right]^2 = \frac{V_2^2}{\omega_2^2} \frac{\sin^2(\theta_3 - \theta_1)}{\text{Denom}} = \frac{1}{|\vec{k}_1 + \vec{k}_2|^2} \quad (2.75)$$

Finally, an equation for the phase velocity of the mixed frequency beam is obtained by multiplying Equation (2.69), the phase information, with Equation (2.75), the magnitude information. First, however, Equation (2.69) is put into a more convenient form. This is done by adding 1 to both sides, squaring, and putting terms over a common denominator. This gives

$$\frac{(\omega_2 + \omega_1)^2}{\omega_2^2} = \left[\frac{v_2^2 \sin^2 (\theta_3 - \theta_1) + 2v_1 v_2 \sin (\theta_2 - \theta_3) \sin (\theta_3 - \theta_1) + v_1^2 \sin^2 (\theta_2 - \theta_3)}{v_2^2 \sin^2 (\theta_3 - \theta_1)} \right] \quad (2.76)$$

This can be reduced to

$$\frac{(\omega_2 + \omega_1)^2}{1} = \frac{\omega_2^2 [v_2 \sin (\theta_3 - \theta_1) + v_1 \sin (\theta_2 - \theta_3)]^2}{v_2^2 \sin^2 (\theta_3 - \theta_1)} \quad (2.77)$$

Now, multiplying Equation (2.77) by (2.75) gives

$$\frac{(\omega_2 + \omega_1)^2}{|\vec{k}_1 + \vec{k}_2|^2} = \frac{[v_1 \sin (\theta_2 - \theta_3) + v_2 \sin (\theta_3 - \theta_1)]^2}{\text{Denom}} \quad (2.78)$$

The following trigonometric identity, valid for any θ_3 , has been found.^{2.22}

$$\text{Denom} = \sin^2 (\theta_2 - \theta_1) \quad (2.79)$$

This can be proven by expanding all the terms, then combining and cancelling carefully. With this substitution, Equation (2.78) reduces to

$$\frac{(\omega_2 + \omega_1)^2}{|\vec{k}_1 + \vec{k}_2|^2} = \left[\frac{V_1 \sin(\theta_2 - \theta_3) + V_2 \sin(\theta_3 - \theta_1)}{\sin(\theta_2 - \theta_1)} \right]^2 \quad (2.80)$$

In full generality Equation (2.80) can be written in the form

$$\left[\frac{(\omega_1 \pm \omega_2)^2}{|\vec{k}_1 \pm \vec{k}_2|^2} \right] = \left[\frac{V(\theta_1) \sin(\theta_2 - \theta_3^\pm) + V(\theta_2) \sin(\theta_3^\pm - \theta_1)}{\sin(\theta_2 - \theta_1)} \right]^2 \quad (2.81)$$

where $V(\theta_1)$ is the phase velocity of the medium at the angle θ_1 from the reference direction. When $\frac{\omega_1 \pm \omega_2}{|\vec{k}_1 \pm \vec{k}_2|} = V(\theta_3^\pm)$ which is the surface wave phase velocity of the material under consideration at direction θ_3^\pm , a perfectly matched mixed frequency beam is generated. This condition, referred to as the phase matching condition, must be met at least approximately if the sum or difference frequency beam is to propagate in the medium. For Y cut LiNbO_3 and one input on the Z axis, an exact phase match can only be obtained for an input beam separation of 3° or less.^{2.22} The same is true of 41.5° rotated Y-cut LiNbO_3 with one input on the X axis.^{2.22}

C. Equations for Approximate Phase Matching

An exact velocity match is not required for mixed frequency beam generation if the beam interaction is short enough. In this case, the difference frequency beam amplitude, A_3 , varies in the interaction region as^{2.22}

$$A_3 \approx \frac{1}{b} \sinh \frac{bX_3}{2} \quad (2.82)$$

where X_3 is the interaction length (Regions I and II of Figure 2.6), and b depends on the input beam amplitudes, phenomenological coupling constants, and the wave vector mismatch $\Delta \vec{k} = \vec{k}_3 - (\vec{k}_1 - \vec{k}_2)$. For experimentally obtainable beam amplitudes, $b = i|\Delta \vec{k}|$ unless $\Delta \vec{k}$ is nearly equal to zero. Thus the hyperbolic sine in Equation (2.82) becomes $\sin(1/2 \cdot \Delta \vec{k} \cdot X_3)$. The right hand side of Equation (2.82) can then be written as

$$A_3 \approx 1/2 \cdot X_3 \left[\frac{\sin (1/2 \cdot \Delta \vec{k} \cdot X_3)}{(1/2 \cdot \Delta \vec{k} \cdot X_3)} \right]. \quad (2.83)$$

(This variation in amplitude is due to dispersion and does not occur for the case of perfect phase matching). When X_3 is held fixed, A_3 decreases by a factor of $\pi/2$ as $\Delta \vec{k}$ increases from zero to π/X_3 . Thus if the condition

$$\Delta \vec{k} \cdot X_3 < \pi \quad (2.84)$$

is met, it should be possible to steer the wave vector of the difference frequency beam over a continuous range of angles, (θ_3^-), simply by varying the ratio of input frequencies given by Equation (2.69). Thus, if $\Delta \vec{k}$ varies from 0 to π/X_3 , the power in the difference frequency beam would decrease by $20 \text{ Log } (\pi/2)$ or 3.9 dB.

The value of $\Delta \vec{k}$ for difference frequency generation is given by the following expression:

$$\Delta \vec{k} = \vec{k}_3 - \vec{k}_3 \left[\frac{V(\theta_3^-)}{V_3} \right] \quad (2.85a)$$

or

$$\Delta \vec{k} = \left[\frac{V_3 - V(\theta_3^-)}{V_3} \right] \vec{k}_3 \quad (2.85b)$$

Combining (2.85b) and (2.84), we obtain

$$\frac{\Delta \vec{k}}{\vec{k}_3} = \frac{V_3 - V(\theta_3^-)}{V_3} \leq \frac{\pi \lambda_3}{X_3 2\pi} = \frac{1}{2p} \quad (2.86)$$

where $p = \frac{X_3}{\lambda_3}$ is the length of the interaction region in difference frequency wavelengths. For example, a phase mismatch of 1/100, or 1 percent, requires that p be less than 50 wavelengths.

D. Designing Non-Collinear Mixers

To design a non-collinear mixer, the various equations must be used in the following manner. Equation (2.86) is used to compute the required interaction length, p , for a given $\frac{\Delta \vec{k}}{\vec{k}_3}$. A value of $\frac{\Delta \vec{k}}{\vec{k}_3}$ must be chosen with the knowledge that a larger $\frac{\Delta \vec{k}}{\vec{k}_3}$ requires a smaller p . As p gets smaller, the mixing efficiency decreases because there simply is not enough interaction time to produce sufficient difference frequency signals. Conversely, a longer interaction region limits the range of θ_3 for which the additional loss penalty is bounded by the 3.9 dB mentioned above.

Equation (2.81) is used to find a phase matched or near phase matched condition. θ_1 , θ_2 and their corresponding phase velocities are chosen. Then Equation (2.81) is iterated until a θ_3 is found for a phase match or near phase match. If no match is found, a new value of θ_1 is chosen, and the iteration continues. This process is best done by computer, and has been tabulated in graphical form by Davis^{2.22} for several common materials. A phase mismatch is related to the interaction length, p , by Equation (2.86) and to a loss in mixed frequency amplitude by Equation (2.82). Finally, Equation (2.69) is used to compute ω_1 after ω_2 is chosen by the designer. Transducer aperture is independent of the equations presented here. In general a small aperture will give

greater acoustic power density and is limited by diffraction and increasing radiation resistance which may be difficult to match to the rest of a system.

Equations (2.69) and (2.81) have been solved by Davis^{2.22} for Y cut LiNbO₃ and 41.5° rotated Y-cut LiNbO₃ with $\frac{|\Delta \vec{k}|}{k_3} \leq \frac{1}{100}$. The results of those calculations are listed in Table 2.3 along with three measured examples from Chapter V.

	Material Cut	p (λ)	θ ₂ (Deg)	θ ₁ (Deg)	θ ₃ (Deg)
Theory	Y	50	90	100	103
Exp.	Y	180	90	100	106
Theory	41.5	50	0	10	-4
Exp.	38	150	0	10	-6.8
Theory	41.5	50	0	10	15.5
Exp.	38	152	0	10	16.8

Table 2.3 Angles of phase velocities and interaction lengths for non-collinear mixing difference frequencies on LiNbO₃. Theory data are from Reference 2.22 Experimental data are from Chapter V of this dissertation.

θ_i are the angles of the phase velocities, and p, the interaction length, is computed using the group velocities associated with θ₂ and θ₁. Note also that the interaction region is triangular in shape (see Figure 2.6), and that Davis' calculations are based on a rectangular interaction region. Therefore, the effective length for the

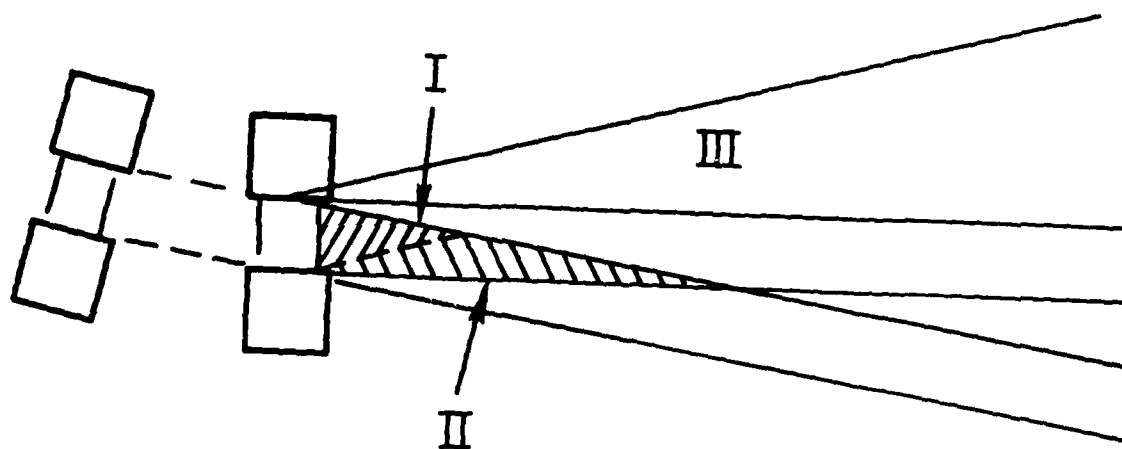


Figure 2.6 The difference frequency amplitude is non-zero in three regions labeled I, II, and III. I and II are in the interaction region. Depending on the ratio of input frequencies, Region III may instead exist below the lowest region shown. (See Figure 2.5)

experimental values in Table 2.3 is somewhat shorter than indicated.

Since in each example, p is longer than the theoretical value, the maximum value of θ_3 should be reduced to compensate. Instead, the θ_3 values used in the experiments were slightly larger. This analysis identifies one area where the efficiency of the devices in Chapter V could have been improved. The larger values of θ_3 were chosen because it was desired to achieve as much spatial separation as possible between ω_1 and ω_2 at angles θ_1 and θ_2 . Smaller values of θ_3 were not chosen for this reason.

A few comments should be made concerning Equation (2.69). Velocities V_1 and V_2 refer to angles θ_1 and θ_2 , respectively. In general, the equation represents a family of curves, one for each combination of θ_1 and θ_2 .

θ_3 is the independent variable, and the velocities are found from Slobodnik's handbook.^{2.23} Equation (2.69), or one of its curves, is used to obtain ω_1/ω_2 after θ_1 , θ_2 , and θ_3 are known. Recall that this value of θ_3 is an upper limit and smaller values may be freely chosen. Figure 2.7 demonstrates how the shape of the curve changes as the angle between θ_1 and θ_2 is changed. Figure 2.8 shows that the curve is symmetric about θ_2 when θ_1 is changed from an angle less than θ_2 to an angle greater than θ_2 . Two aspects of these curves are consequences of Equation (2.81). The first is that the sum frequency is generated for θ_3 between θ_1 and θ_2 , and the difference frequency is

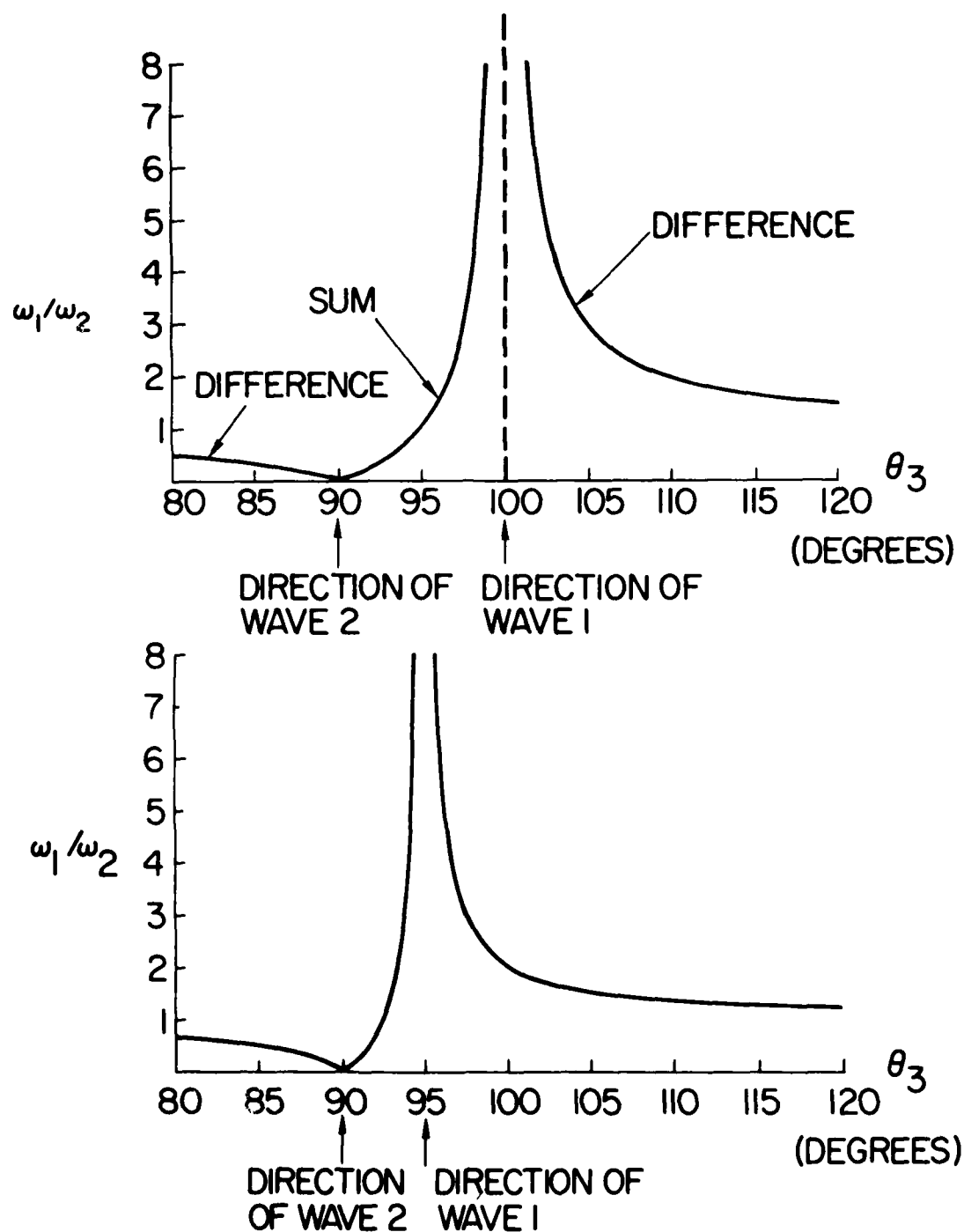


Figure 2.7 Frequency ratio required to steer a mixed frequency product on Y cut LiNbO_3 , (90° is Z axis). The mixed frequency propagates at θ_3 .

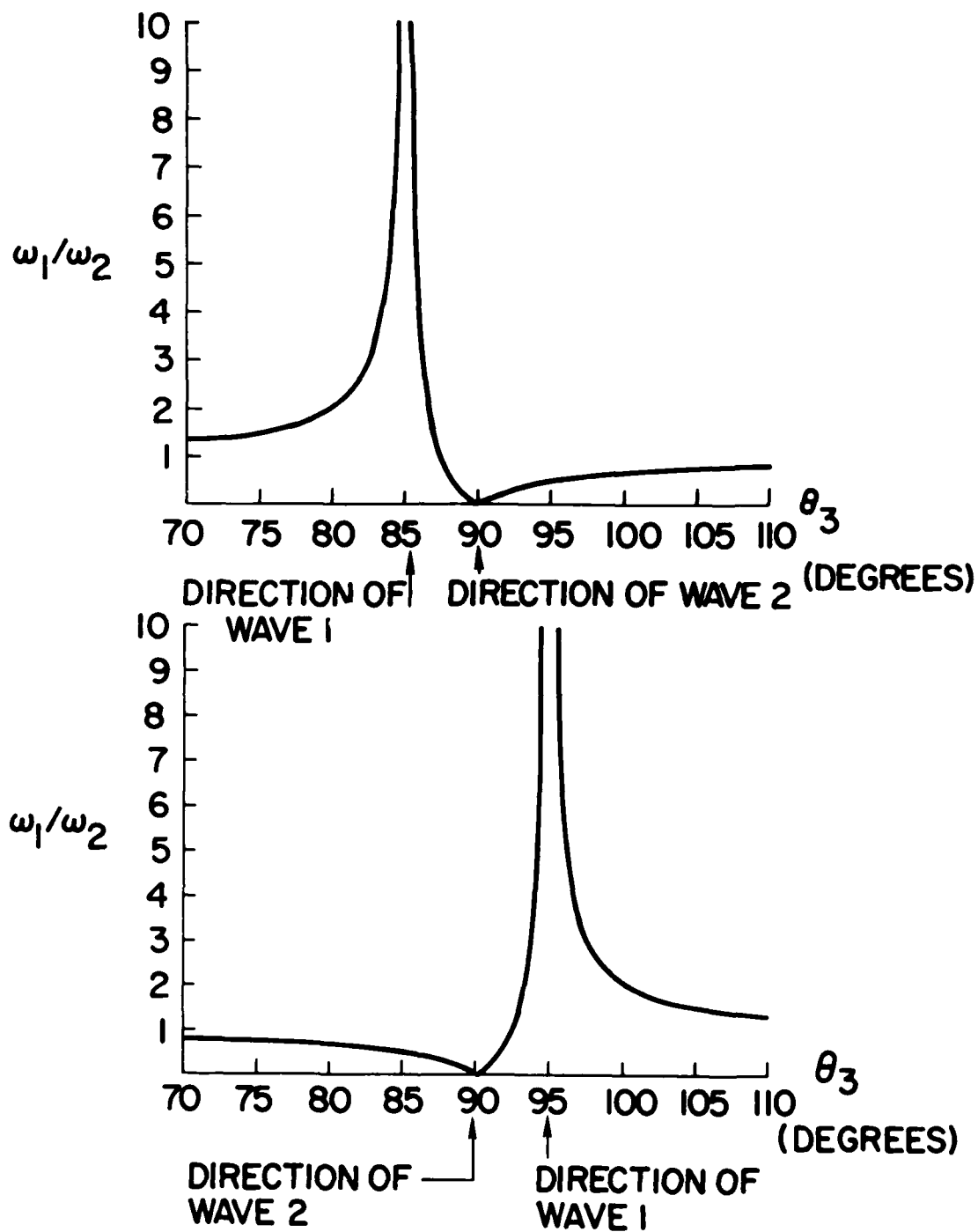


Figure 2.8 Frequency ratio required to steer a mixed frequency product on Y cut LiNbO_3 . (90° is Z axis). The mixed frequency propagates at θ_3 .

generated for all other values of θ_3 . The second is that if a perfect phase match is obtained for the difference frequency, then the sum frequency cannot simultaneously have a perfect phase match, and vice versa.

There are several possible applications for this device. A directional coupler could use the property that no mixed frequency is generated in the reverse directions. Also it could be used as a switch with ω_1 steering to one output port or another. As a mixer, however, this steering property tends to limit bandwidth since it will steer past the output transducer. Therefore, for mixing, it is necessary to use a portion of the curve (Figure 2.7) that minimizes this effect. For example in the top of Figure 2.8 as ω_1/ω_2 varies from 3 to 6, θ_3 changes 1.5° , while in contrast varying ω_1/ω_2 from 1.5 to 3 causes θ_3 to change by 6.5° .

CHAPTER III

CONVOLUTION

3.1 Introduction

The degenerate elastic surface acoustic wave (SAW) convolver is a monolithic device.^{3.1} This makes it inherently low cost, light weight, and rugged. It is used to perform the matched filter function.^{3.1} The coded reference may be any arbitrary waveform since it is generated externally and then input to the device. Further, the code rate and waveform type may be changed at any time making this an even more attractive device. There are several schemes involving external electronics to make the convolver into an asynchronous correlator.^{3.2}

The emphasis of this chapter is to determine whether it is practical to work at 800 to 1000 MHz input frequency where there is potential for extremely large instantaneous bandwidth. The result is that practical convolvers with input frequencies in the 300 to 800 MHz range can be achieved provided the special problems associated with high frequencies are dealt with properly.

An elastic convolver is shown schematically in Figure 3.1. Multiplication of the reference and signal inputs takes place as the acoustic signals pass each other due to elastic non-linearities in the crystal. Integration is

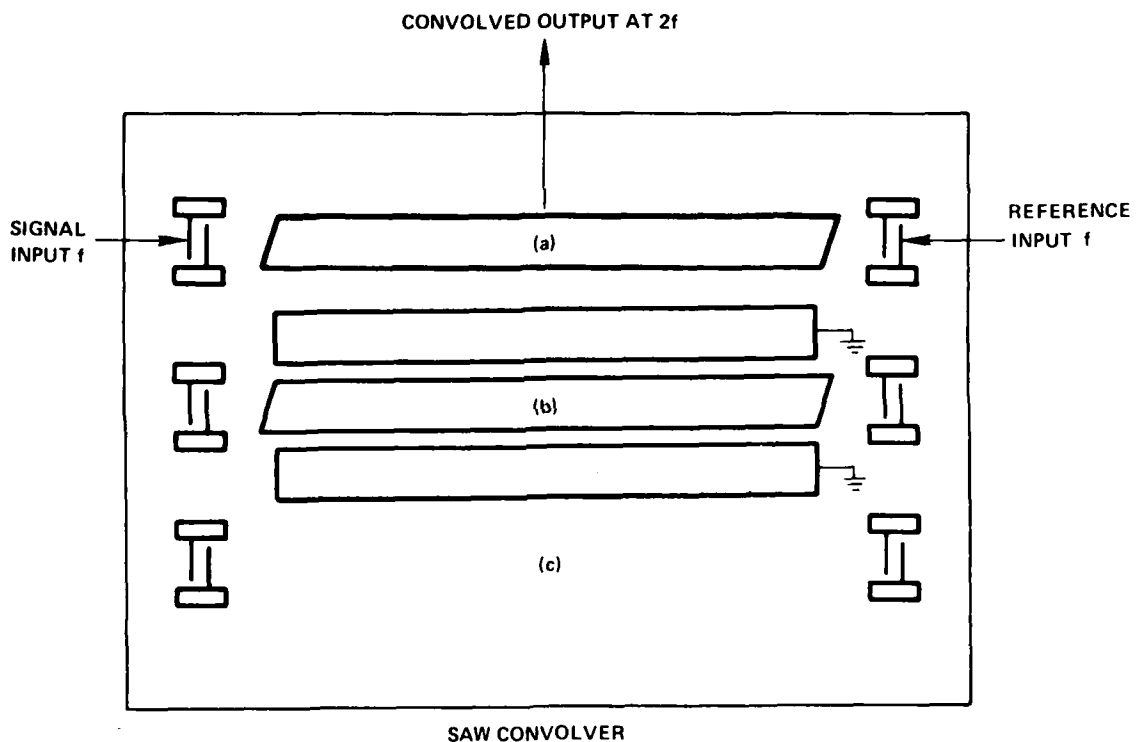


Figure 3.1 (a) Al film forms the 8.6 mm long output plate. The ground plane is a metal slab underneath the LiNbO_3 crystal. The signal and reference inputs are launched by interdigital transducers. (b) Ground planes are Al films on both sides of the output plane. (c) Reference channel for measuring insertion loss.

performed by an output electrode or plate which is fabricated by evaporating a thin aluminum film onto the lithium niobate (LiNbO_3) crystal. The two interdigital input transducers are deposited at the same time. Several output plate configurations are possible; two of them are shown in Figure 3.1. In Figure 3.1a the ground plane is formed by the metal slab underneath the LiNbO_3 crystal. In Figure 3.1b the ground planes are formed by the metal plates on both sides of the output plate. Continuous plates such as these can only be used with a degenerate convolver, wherein both inputs have the same frequency, $\omega = 2\pi f$, and equal but oppositely directed propagation constants, $\vec{k} = 2\pi/\lambda$. Since

$$\omega_1 \pm \omega_2 = \omega_3 \quad (3.1)$$

$$\vec{k}_1 \mp \vec{k}_2 = \vec{k}_3 \quad (3.2)$$

for the degenerate case, the output sum frequency is 2ω and $\vec{k} = 0$. The non-degenerate case occurs when the input frequencies are not the same. Then, an interdigital output transducer must be used and designed according to Equation 3.2.

Section 3.2 explores the various acoustic losses. These include input matching, propagation on a bare crystal, diffraction, beam steering, and attenuation due to the waveguide. Laser-probe studies of 5, 15, 37, and 45 λ

waveguides show the beating of modes characteristic of overmoded waveguides. Section 3.3 investigates the electrical losses associated with coupling to the convolved signal. These include the configuration of the output plate geometry, output electrode resistivity, transmission line effects, and output matching. Section 3.4 gives the dynamic range, harmonic suppression, spurious levels, and bandwidth of a nearly optimized 800 MHz device.

3.2 Acoustic Losses

The first step is to measure the insertion loss of a clear path, i.e. with no output plate between the transducers, as shown in Figure 3.1c. This parameter is listed in column three of Table 3.1 for several devices. In all cases matching was limited to a single series inductor. A very flat 40 percent bandwidth is possible using the Reeder type matching network.^{3.3} This network is also practical at UHF frequencies when a microstrip transmission line is used instead of its lumped element equivalent.^{3.4} The emphasis of this effort however, was on the other convolver parameters which are a more necessary first step. The first of these, insertion loss (IL) of the two transducers, is determined by taking the measured delayline loss with no plate between and subtracting propagation loss, and diffraction and beam steering loss.^{3.5}

A. Crystal Propagation Loss

An empirical expression for propagation loss is

DEVICE NO.	FREQ. (MHz)	DELAY LINE IL (dB)	PROPAGATION LOSS (dB)	BEAM STEERING ANGLE (DEGREES)	DIFFRACTION & BEAM STEERING (dB)	TWO TRANSDUCERS IL (dB)	DELAY LINE LENGTH (mm)	AI ATTN. (dB/cm)	PLATE ATTN. (dB)	PLATE LENGTH IN EM WAVELENGTHS
13	916	28.0	5.05	0.32 ± 0.10	6.49 ± 0.06	16.46	22.35 ⁽¹⁾	5.1 ± 0.5	4.4	0.32
20	990	25.0	3.00	0.49 ± 0.03	5.82 ± 0.76	16.18	10.00	8.6 ± 0.5	7.4	0.37
21	800	20.5	2.05	0.40 ± 0.02	3.78 ± 0.27	14.67	10.00	5.8 ± 0.6	5.0	0.31
19	800	23.0	2.05	0.42 ± 0.04	4.10 ± 0.58	16.85	10.00	—	—	0.31
18	800	—	2.05	—	—	16.75	10.00	5.8 ± 0.6	5.0	0.31
17	800	22.0	4.58	0.07	2.62	14.80	22.35	4.4 ± 0.4 ⁽²⁾	3.8	0.31
15	800	25.5	4.58	—	—	16.30	22.35	—	—	0.31
20	330	17.5	0.45	0.49 ± 0.03	5.50 ± 0.35	11.55	10.00	—	≈ 0.0	0.12
T-CSF	167									0.30

DELAY LINE IL (INSERTION LOSS) WITH NO PLATE BETWEEN EQUALS PROPAGATION LOSS PLUS DIFFRACTION AND BEAM STEERING PLUS IL OF TWO TRANSDUCERS.

- (1) ALL OUTPUT PLATE LENGTHS WERE 8.6 mm EXCEPT T-CSF WHICH WAS 41.2 mm
- (2) FILM THICKNESS 300 Å. ALL OTHER FILMS WERE 500 Å. (T-CSF IS UNKNOWN)
- (3) ALL CRYSTALS WERE 450 μm THICK EXCEPT NO. 18 AND 19 WHICH WERE 35 μm THICK. (T-CSF IS UNKNOWN) T-CSF REFERS TO A CONVOLVER MADE BY A FRENCH COMPANY: THOMSON CSF.

Table 3.1 Experimental Convolver Losses

given by

$$\text{Propagation Loss (dB/}\mu\text{sec)} = (\text{VAC}) F^2 + (\text{AIR}) F, \quad (3.3)$$

where F is the frequency in GHz and VAC and AIR are defined constants depending on the crystal.^{3.5} For 38,X and Y,Z lithium niobate, VAC is 0.75 and 0.88, and AIR is 0.30 and 0.19 respectively.^{3.5} The computed values are listed in column four of Table 3.1.

B. Diffraction and Beam Steering

Diffraction losses may be read from a universal diffraction-loss curve.^{3.5} The only information needed is propagation path length, transducer aperture normalized to an acoustic wavelength, and γ , the slope of the power flow angle. In anisotropic crystals such as lithium niobate the phase velocity and group velocity will not have the same direction. The power will flow at the angle of the group velocity. These crystals are characterized by computing phase velocity versus propagation direction. A plot of magnitude versus angle for the phase velocity is called the velocity surface. For the 38,X orientation, $\gamma = -.244$. For the Y,Z orientation, γ is only approximately known since the velocity surface is not parabolic there. For this work, a value of $\gamma = -.75$ was used because experimentally it appears to be the best approximation. The aperture for all devices was $130 \mu\text{m}$, except T-CSF which was $110 \mu\text{m}$. T-CSF was a device manufactured by Thomson-CSF, a French company. Beam steering is usually assumed negligible. However, for the

devices in Table 3.1 it was not. The beam steering was measured with the aid of a laser probe^{3.6} and is included as part of the acoustic waveguide profiles given later in this section (Figures 3.9 - 3.12). The beam steering angle is defined as $\phi = \gamma(\theta - \theta_0)$ where γ is the slope of the power flow angle, $(\theta - \theta_0)$ is the difference between the phase velocity and pure mode axis directions. If the pure mode axis corresponds to one of the principal axis of the crystal, then θ_0 will equal zero. The beam steering shown in Figures 3.9-3.12 is ϕ . (For a geometric interpretation see Figure A.9 of Appendix A). The loss due to this effect can be computed separately. For the special case of the acoustic beam intercepting one half the output transducer, the loss is 6 dB.^{3.7}

However, it is incorrect to simply add the contributions of diffraction and beam steering. Examples of this are given in References 3.5 and 3.8. Instead, the combined contributions must be computed numerically since the complex integral cannot be solved in closed form. This was done, and the results are given in column six of Table 3.1. The error due to considering only diffraction ranged from nearly zero to 4.4 dB. The average error was 2.2 dB per device. The insertion loss (IL) for two transducers was then determined by subtracting propagation loss and diffraction plus beam steering loss from the delay line insertion loss.

The delay line insertion loss was measured with a

spectrum analyzer using the set up shown in Figure 3.2(a) and photographed in Figure 3.2(b). Input impedances (and output impedances of the convolver plate), S_{11} , were measured with the network analyzer shown in Figures 3.3(a) and (b).

C. Waveguide Attenuation

Attenuation due to the presence of the aluminum (Al) film was measured using the laser probe. An earlier attempt at measuring the film attenuation by comparing the insertion losses of a clear path with that of a path containing an aluminum film was not very successful.^{3.9} That method is complicated by diffraction and beam steering since the waveguiding aluminum film prevents both. The method is further complicated by the fact that the film covered only a fraction (0.39 or 0.86) of the total path. The results using a laser probe are given in columns nine and ten of Table 3.1. The films were all 40 Å of Cr plus 460 Å of Al except for device 17 which had 40 Å Cr and 260 Å Al. The results agree well with those of Davis^{3.10} who did a much more extensive set of measurements. The 38,X device at 916 MHz has the same value of kh as a Y,Z device at 800 MHz ($k = 2\pi/\lambda$ and h is the Al film thickness). For the devices listed in Table 3.1 the acoustic beam was confined by the narrow waveguiding film, and multiple modes were present. In view of these conditions Davis' measurements would be considered more accurate.

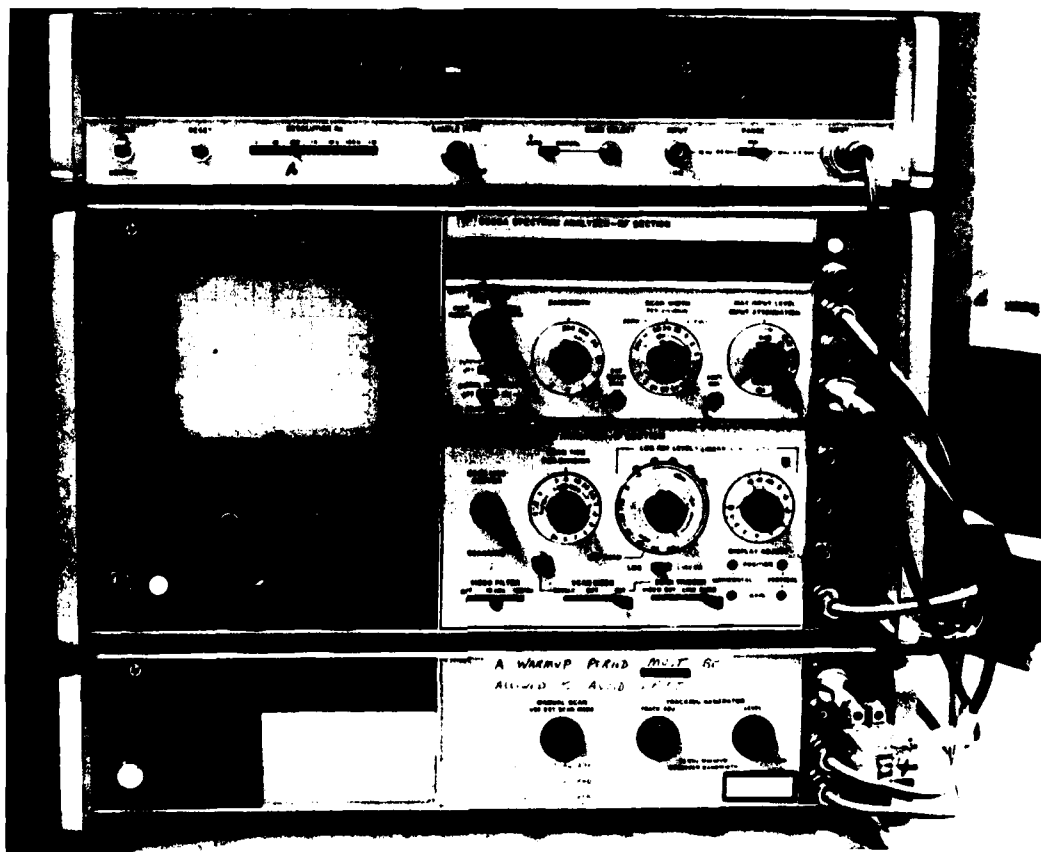
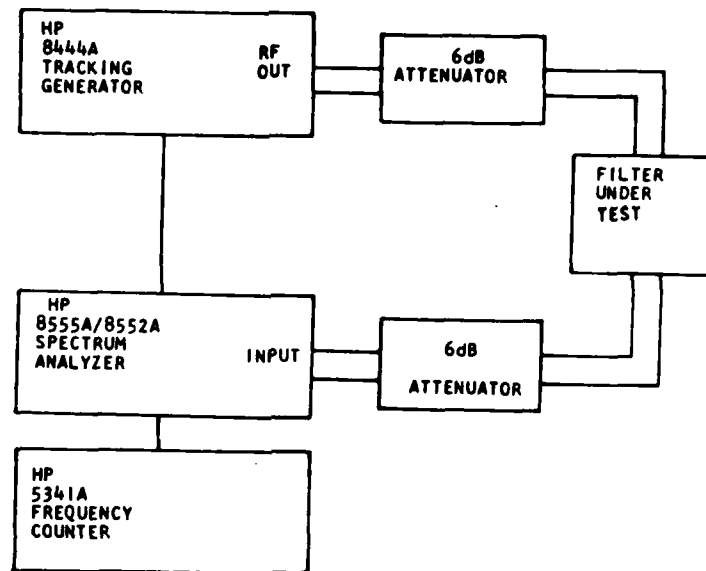


Figure 3.2 (Top) Block diagram of Spectrum Analyzer test setup. The 6 dB pads (attenuators) are necessary to prevent reflections from distorting frequency data.
(Bottom) Photograph of Spectrum Analyzer test setup used to obtain frequency response data.

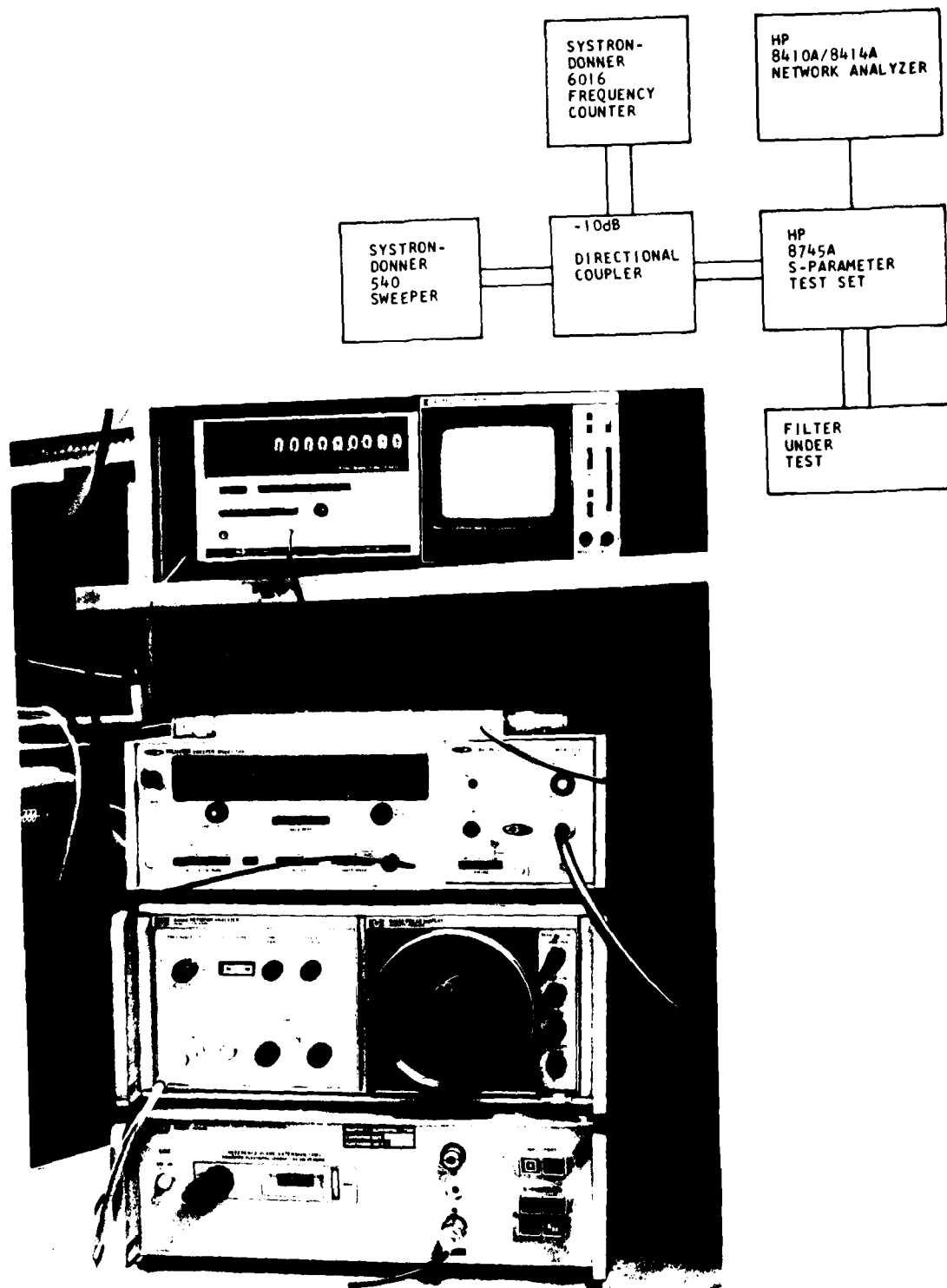


Figure 3.3 (Top) Block diagram of Network Analyzer test setup. (Bottom) Photograph of Network Analyzer test setup used to obtain input and output impedance data.

D. Multimoding

The degenerate elastic SAW convolver consists of a $\Delta V/V$ waveguide formed by a thin film of aluminum, evaporated onto a piezoelectric substrate and has a SAW transducer on each end. When multimoding is present, the fundamental and first symmetric modes have group velocity differences of about 0.5 percent in a 5λ waveguide.^{3.11,3.12} When the waveguide is used as a convolver, unwanted modes will cause distortions which may degrade the maximum power output or efficiency and minimum achievable time sidelobes for a coded signal. For a five wavelength (5λ) wide waveguide, the multimoding can cause a variation in the detected SAW profile intensity, as shown in Figure 3.4, of more than 3 dB along the length of the waveguide with only one input active. This is the first published data on multimoding in an elastic SAW convolver; however, multimoding effects in the separated medium or air-gap convolver have been reported.^{3.13} In theory these waveguides are similar, but in practice they are quite different. It will be shown that the principle variation in the detected SAW profile intensity is due to the beating of the fundamental mode with the next higher symmetric mode. The first antisymmetric mode is also present with significant intensity and is due to beam steering (misalignment) or asymmetric excitation.^{3.14,3.15}

A laser probe^{3.6} was used to look at the acoustic wave propagating in one of the waveguides fed by a beamwidth

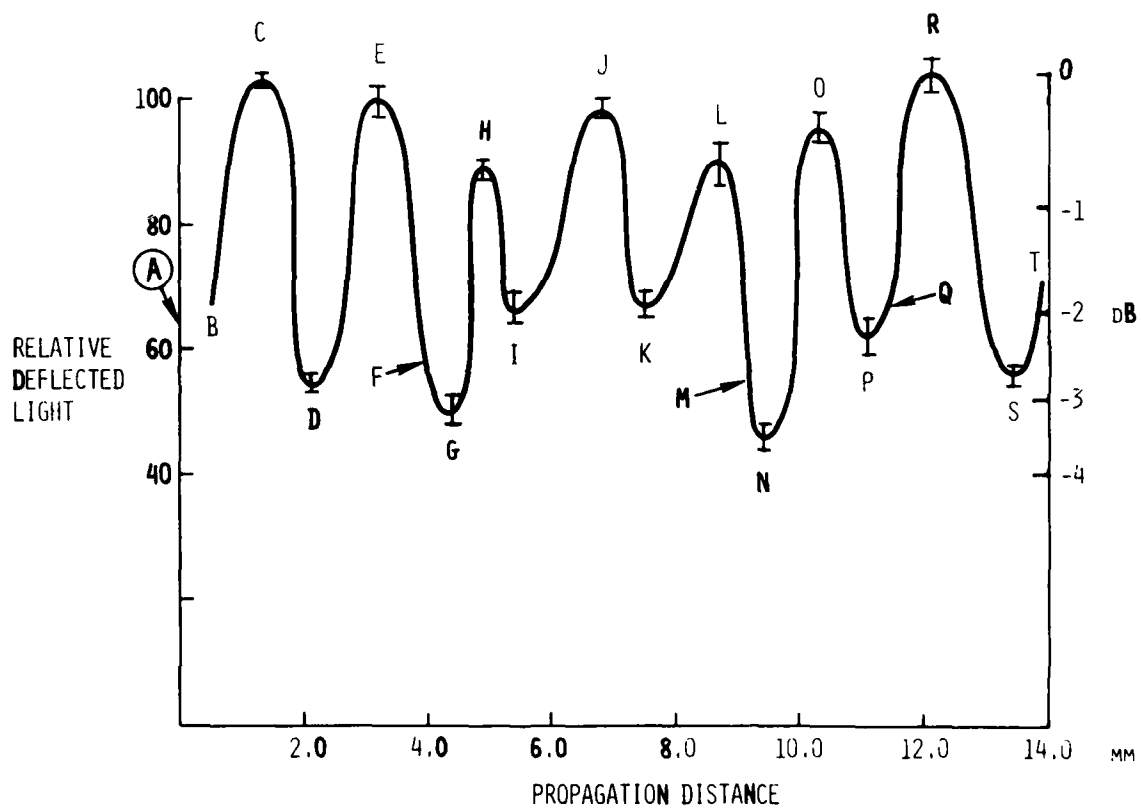


Figure 3.4 Maximum detected acoustic intensity (for each profile using a laser probe having a spot size of about 1.8λ) as the laser probe moves down the 14.0 mm length of a 5λ waveguide. The letters A thru T are the positions of profiles given in Figure 3.7.

compression multistrip coupler (BWC-MS-C)-Figures 3.5 and 3.6. The BWC-MS-C is an array of metal stripes that act much as a transducer would. The acoustic wave is incident on one side of the coupler, is converted into an electromagnetic wave, and is then launched again as an acoustic wave from the opposite side and opposite end of the coupler. In the BWC case the launching end is much shorter than the receiving end, hence the beam width is compressed. The aluminum waveguide measured $145\text{ }\mu\text{m}$ wide by 14 mm long (5λ by 480λ) and had $2500\text{ }\text{\AA}$ of aluminum and no chromium.^{3.16} The YZ cut of lithium niobate was operated at 120 MHz ($1\lambda = 29.07\text{ }\mu\text{m}$). However, the profiles will be the same for any 5λ waveguide with a length of 480λ . First, the laser was scanned down the length of the plate. Large variations in detected peak acoustic power (on the order of 3 dB) were found and are shown in Figure 3.4. The laser spot was round, gaussian and about $50\text{ }\mu\text{m}$ in diameter. Features of less than $50\text{ }\mu\text{m}$ could be distinguished, but obviously there was some averaging of the peaks and valleys in the profiles. In addition, the desired spot size/acoustic wavelength ratio of more than ten to one was not met since the spot size was about $50\text{ }\mu\text{m}$ and the diffraction grating (acoustic wavelength) was $29\text{ }\mu\text{m}$.

The equations concerning the laser probe are those of P. Beckmann and A. Spizzichino (see Appendix A.1 and A.4). Since their assumption that the laser spot size is much larger (>10) than the grating is not satisfied, an

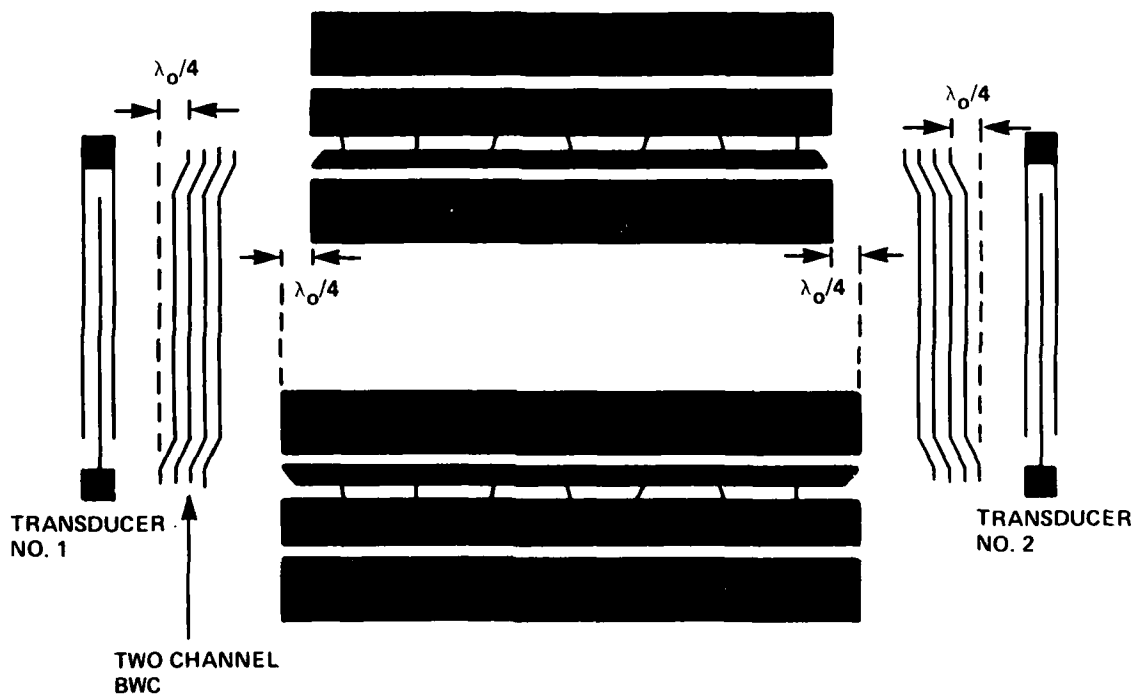


Figure 3.5 Schematic representation of the 5λ waveguide. The beam width compressors (BWC) are 15:1 and launch two SAW waves rather than the more typical one wave design. The convolver plate is interconnected with a larger busbar to alleviate the resistivity problem. The outer most plates are electrical ground planes. Ref 3.16



Figure 3.6 Photograph of the convolver shown schematically in Figure 3.5. The interaction length is 4 μ sec (14 mm). Ref 3.16

examination is in order. The reflected power is inversely proportional to the number of diffractions. Thus in this intermediate case (spot size $\approx 2\lambda$) the diffraction is present but weak. Also the grating sidelobes broaden as spot size decreases. The good reflectivity of aluminum helped offset this, and the response from bare lithium niobate was indeed weak. Also there is a significant correction term in this regime due to edge effects. Another experiment was conducted reducing the RF input power and hence the acoustic amplitude by 10 dB. The detected light output fell by 10 ± 0.02 dB indicating the measured intensity profiles are correct. This experiment used the sidelobe $m=1$. Other probe techniques used when spot size is less than the acoustic wave use the specular reflection $m=0$. (see Appendix A.2) Thus there was no contribution from that source in this case.

The intensities in Figure 3.4 are the peak value of the profile at the indicated distance from the input transducer. Error bars are the result of three sets of data. The letters A thru T denote the location at which the profiles shown in Figures 3.7 were taken. Each profile of Figure 3.7 is a plot of acoustical intensity versus distance perpendicular to the axis of propagation. Location A corresponds to the acoustic wave launched by the BWC-MSD and is the profile just prior to entering the waveguide. The acoustic intensity profiles in B through T of Figure 3.7 are scaled to each other with one half intensity

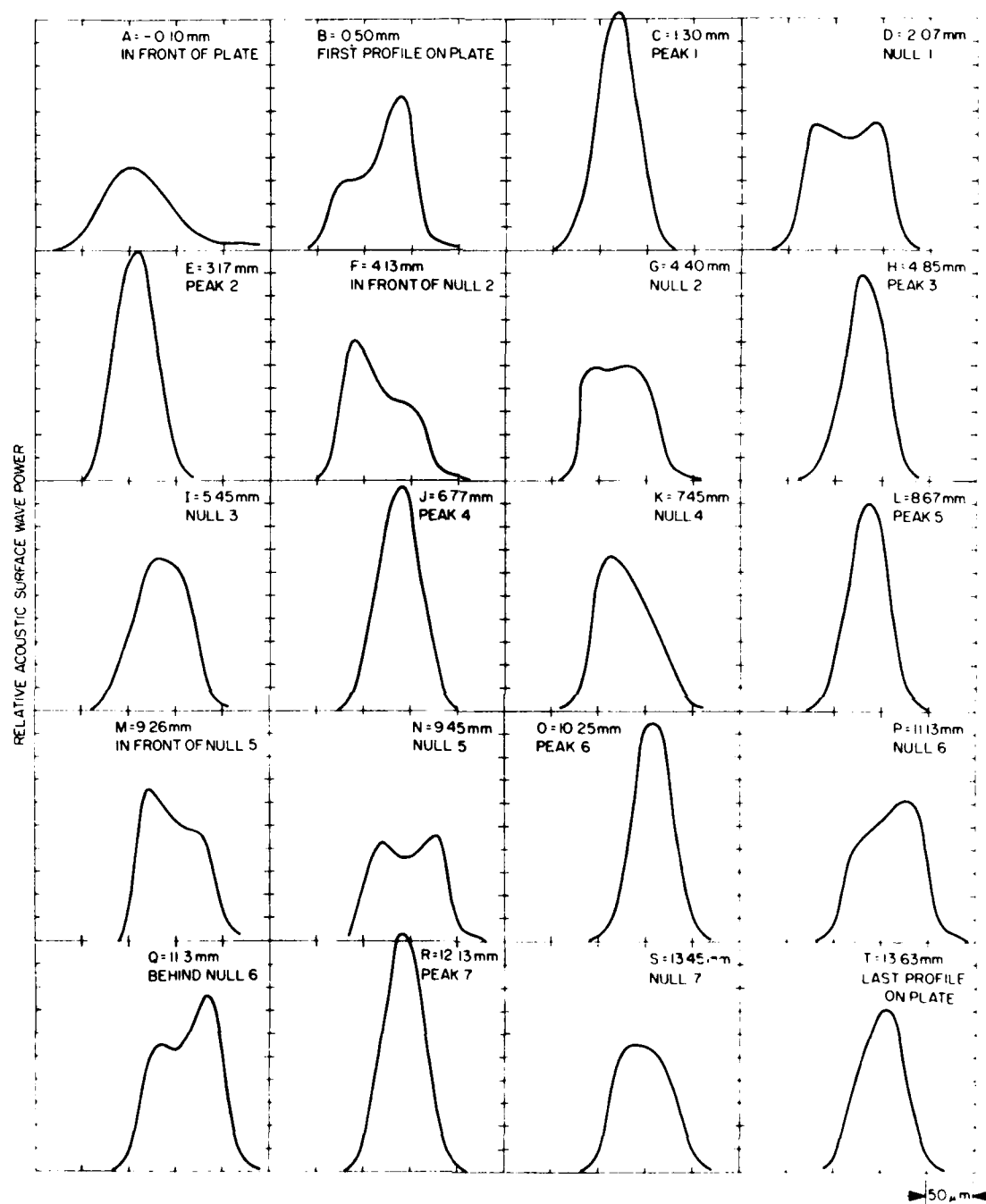


Figure 3.7 Profiles of the acoustic wave as it propagates down the 14.0 mm waveguide. The letters A thru T are the positions on the waveguide where the profiles were taken and correspond to A thru T in Figure 3.4. Profile A is immediately in front of the waveguide.

corresponding to 3 dB. The intensity of profile A is not scaled to the others since the aluminum film increases the sensitivity of the laser probe by a factor of about four, and the meter was set to a different scale. Surface wave reflections were suppressed with an acoustic absorber behind the waveguides and the input transducer.

The bottom of the crystal was scored with a diamond pattern to diffuse potential plate modes (volume waves) which are a possible source of ambiguity. Using a convolver identical to the one that was laser probed, two coded signals were convolved and observed with an oscilloscope. The plate modes were well suppressed.^{3.16}

Since convolver efficiency (F factor) is inversely proportional to width^{3.12}, there is a desire to make the aluminum plate as narrow as possible. Five wavelengths (5λ) were chosen as a compromise value. The lower limit is set due to aluminum film resistivity and dispersion, and by practical limits on beamwidth compression. A beamwidth compression multistrip coupler (BWC-MS) is limited to a compressed beam of about 5λ .^{3.17} The convolver will operate on a coded waveform, typically bi-phase modulated "chips". These chips will be distorted due to dispersion. Thicker aluminum and more narrow waveguides make dispersion worse.^{3.11,3.18,3.19} A 5λ waveguide has four modes ($n = 0,1,2,3$) below cutoff.^{3.12} The first three modes are shown schematically in Figure 3.8(a). Modes 0 and 2 are even or symmetric while modes 1 and 3 are odd or antisymmetric. The

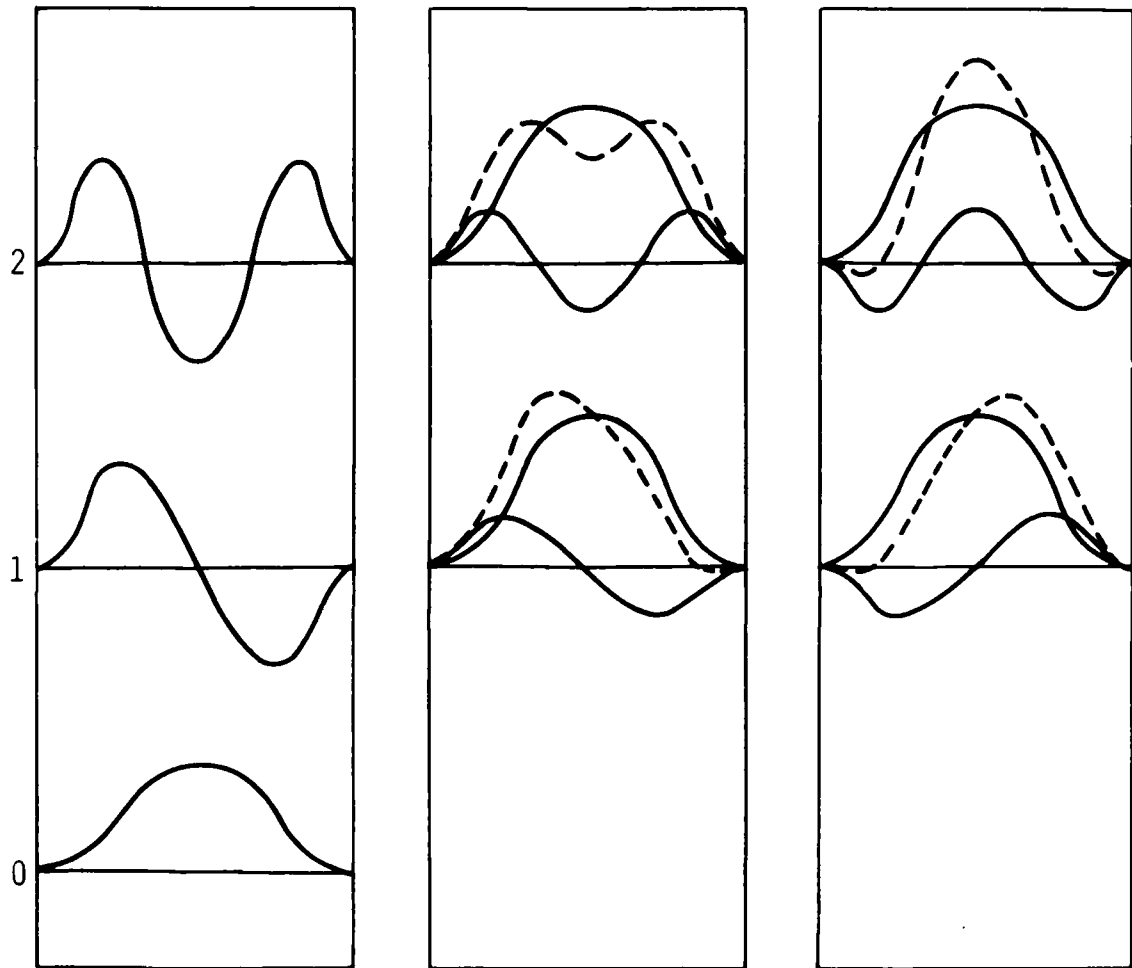


Figure 3.8 (a) Schematic representation of first three waveguide modes: first symmetric (fundamental), first antisymmetric and second symmetric. (b) (Top) - in-phase addition of modes 0 and 2, (Bottom) in-phase addition of modes 0 and 1, (c) (Top) out-of-phase addition of modes 0 and 2, (Bottom) out-of-phase addition of modes 0 and 1.

dashed lines in Figure 3.8(b) and (c) show schematically the worst-case in-phase and out-of-phase addition of modes 0 and 1 and modes 0 and 2. Note that modes 1 and 2 have one third the amplitude of the fundamental mode 0 in this schematic representation.

Y-cut, Z propagating lithium niobate was chosen because this orientation has the largest nonlinearities.^{3.9,3.20,3.21} The Z axis of propagation is a pure mode with crystalline anisotropy symmetric about it. Thus if the transducer or beamwidth compressor launches a symmetric wave with no beam steering, no odd modes will be excited in the ideal waveguide, even though they are below cut-off, because of orthogonality. If in addition, the acoustic wave is weighted to have a profile corresponding exactly to the fundamental mode, only the fundamental mode will be excited - regardless of how many modes are below cut-off in the ideal waveguide. Another possibility is a symmetric excitation with beam steering. In this case only symmetrical modes are excited, but there soon is a conversion to mode 1.^{3.14,3.5} Of course in real life, a perfectly symmetric wave cannot be created and some beam steering, although unintentional, is always there. The degree to which these small errors affect waveguide modes can best be determined experimentally.

The peaks of Figure 3.4 (C,E,H,J,L,O,R) correspond to mode 2 adding out-of-phase with mode 0 (top of Figure 3.8c). The nulls (D,G,I,K,N,P,S) correspond to mode 2 adding to

mode 0 (top of Figure 3.8b). The nulls of I,K,P, and S do not have the characteristic dip shown in Figure 3.8b and nulls D,G and N. I,K,P and S do have mode 2 adding; the difference is that in these cases it has less intensity than for D,G, and N. This can be proven by overlaying one of these profiles with an adjacent peak (e.g. H and I). The fact that the bottom half of the null profile is wider than the bottom half of the peak profile can only happen if mode 2 adds in-phase with mode 0 in one case and adds out-of-phase with mode 0 in the other case. The periodicity of the peaks is a direct measure of the difference in velocities of the two modes - average periodicity is 1.81 mm. Using the theoretical dispersion curves of phase velocity in reference 3.12 the predicted periodicity due to the beating of modes 0 and 2 is 1.85 mm, in excellent agreement with experiment. The predicted periodicity of modes 0 and 1 is 4.18 mm. It was measured to be 4.08 mm (using M and Q of Figure 3.7) - also in excellent agreement. The theoretical curves did not include mass loading; we must conclude that it shifts the two curves equally.

The skewing to the right or left (profiles B, F, M, and Q) is due to the presence of mode 1 shown in the bottom of Figure 3.8(b) and 3.8(c) or possibly due to mode 3. The beating of the various modes is a continuous process as they propagate down the waveguide together. There are no spontaneous changes in amplitude. Due to differences in their velocities, they gradually build up or decay as they

add in-phase or out-of-phase with each other. There are probably more antisymmetric profiles present than shown in Figure 3.7. Modes 0,1,2 and 3 being present simultaneously with varying intensities and phases make it difficult to pick out all the antisymmetric modes.

The intended Z axis of propagation is an axis of symmetry in lithium niobate. Any odd modes then must be due to asymmetric excitation or due to beam steering caused by misalignment. The excitation in this case, A of Figure 3.7, was only approximately symmetric and is a possible source of the odd modes. The other possible source of odd modes is a mode conversion caused by the acoustic beam hitting the waveguide wall due to unintentional misalignment of transducers or waveguide on the Z axis.^{3.14} Further, odd modes may be generated simply by containing the diffraction of the acoustic beam if the waveguide walls have a relatively rough edge.^{3.15} If the mode is below cut off, there will be a mode conversion, or, if the mode is above cut off, the result will be an internal reflection.^{3.14}

Waveguides of 5, 15, 37 and 45 wavelengths width have been laser probed and are shown in Figures 3.7, 3.9, 3.10, 3.11 and 3.12 respectively. All exhibited a strong mode 1. In Figure 3.10 a beam steering angle of only 0.07 degrees (4.6λ offset) was enough to cause a very large mode 1. Mode 2 was detected in all but the 45λ waveguide, Figure 3.12. If the 45λ waveguide had been longer, mode 2 would probably have been found there also. Referring again to Reference

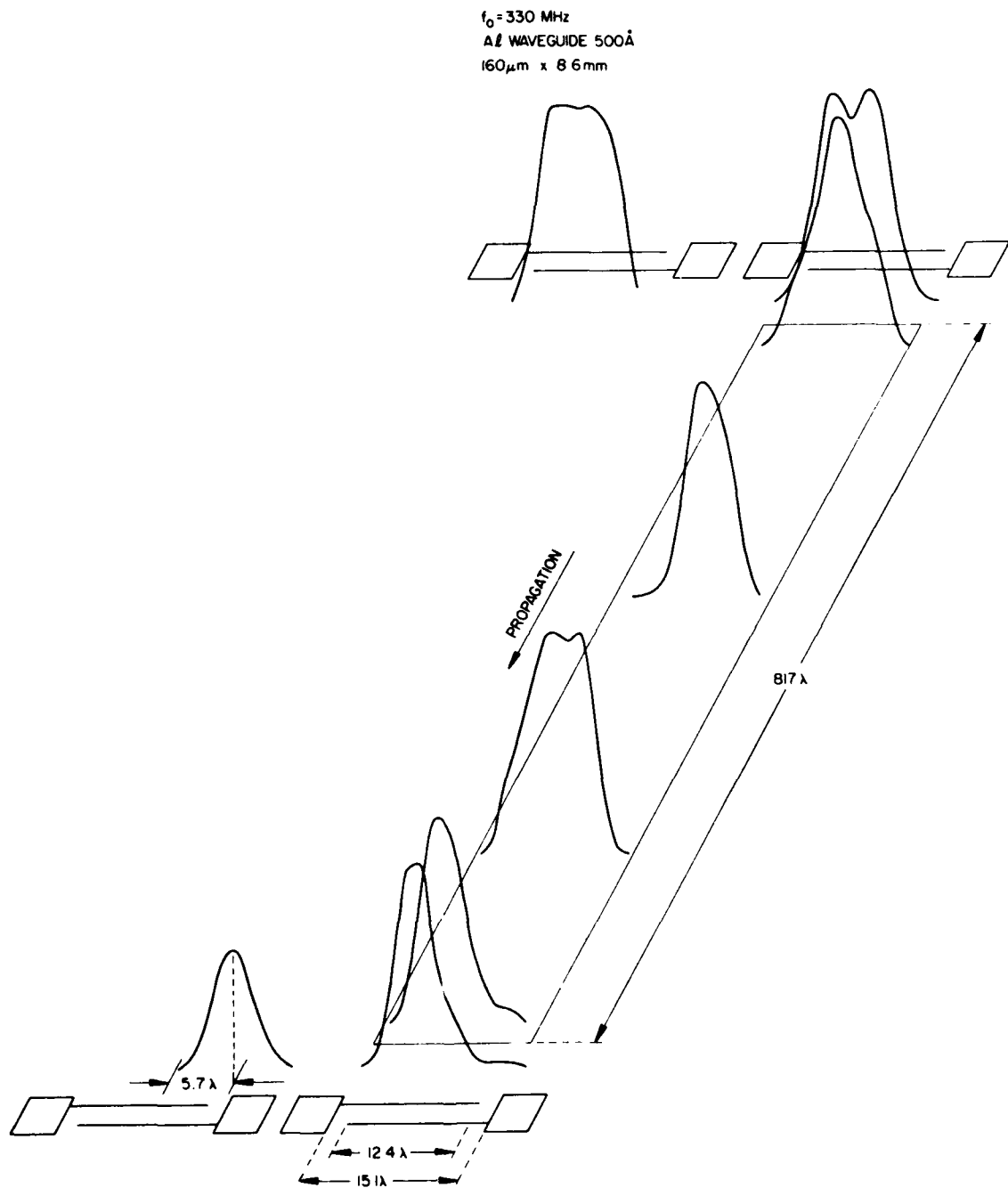
YZ LiNbO_3 ACOUSTIC WAVEGUIDE EFFECTS

Figure 3.9 Acoustic wave profiles at 330 MHz for a clear path showing 5.7λ of beam steering and for a waveguide of 15λ by 817λ with a 500 \AA Al film. Modes 0, 1 and 2 are present.

YZ LiNbO_3 ACOUSTIC WAVEGUIDE EFFECTS

$f_0 = 800 \text{ MHz}$
 $\lambda_L \text{ WAVEGUIDE } 300 \text{ \AA}$
 $160 \mu\text{m} \times 17.3 \text{ mm}$

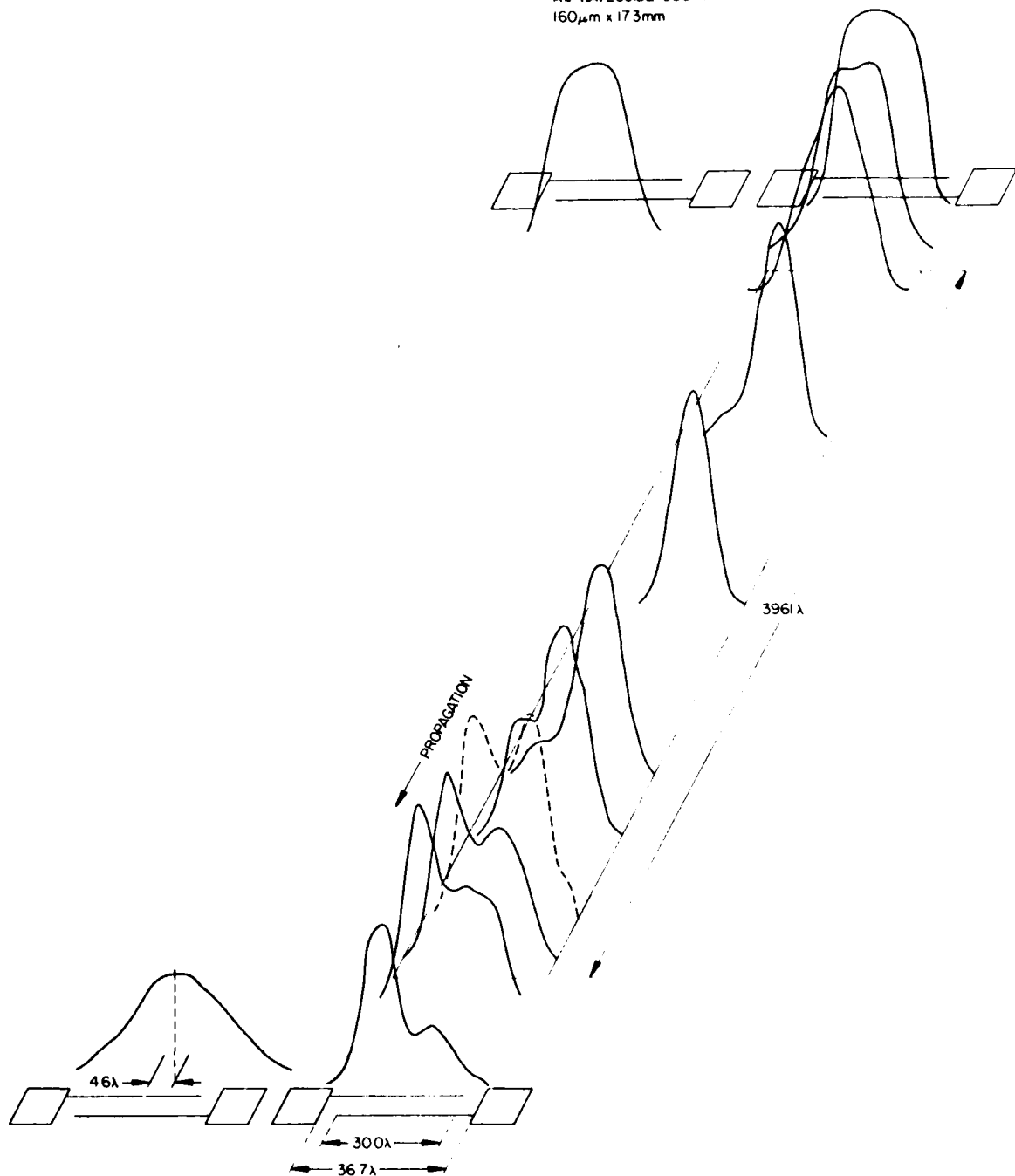


Figure 3.10 Acoustic wave profiles at 800 MHz for a clear path showing 4.6λ of beam steering and for a waveguide of 37λ b. 3961λ with a 300 \AA Al film. Modes 0, 1 and 2 are present.

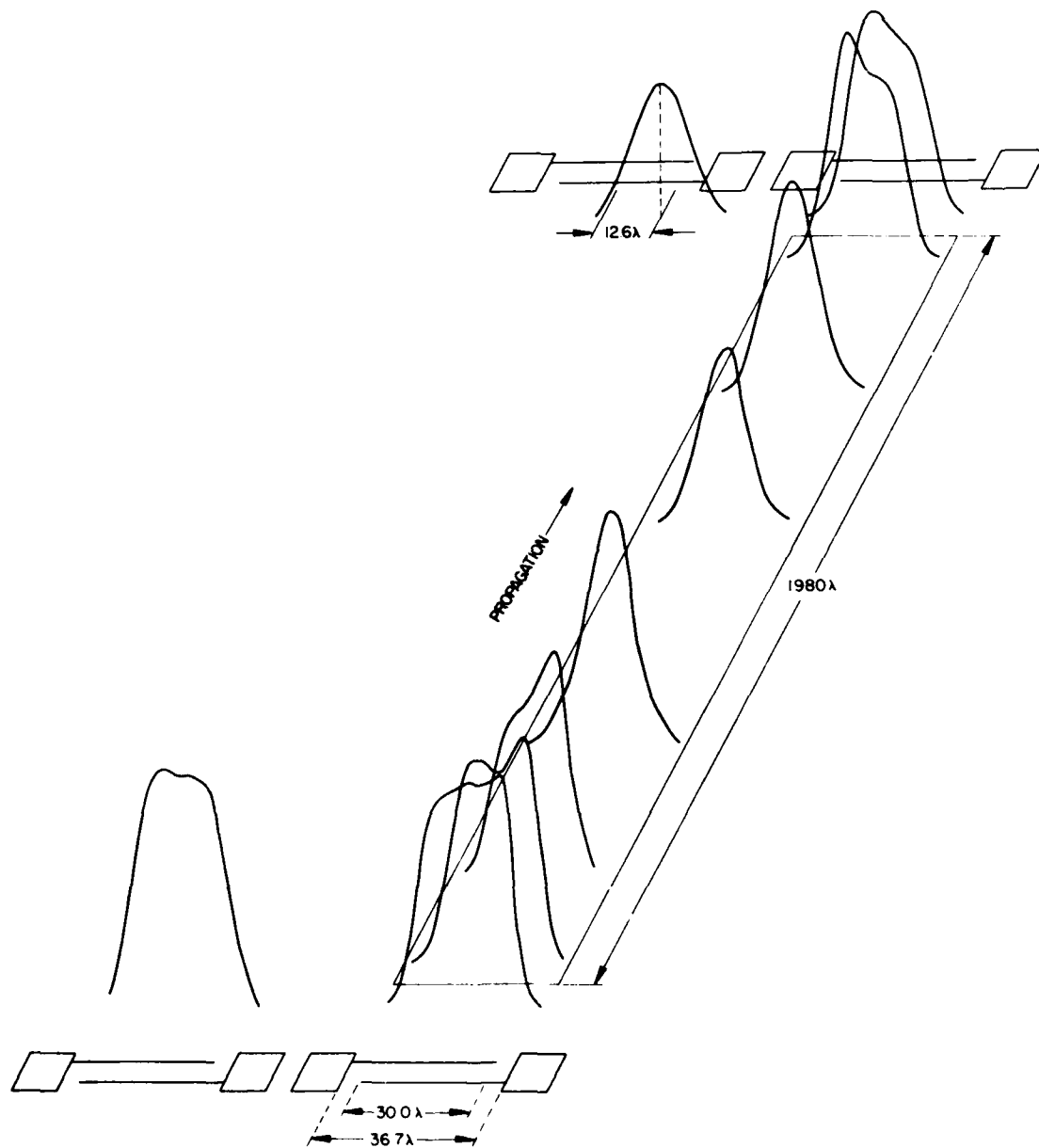
YZ LiNbO_3 ACOUSTIC WAVEGUIDE EFFECTS $f_0 = 800 \text{ MHz}$ $\Lambda = \text{WAVEGUIDE } 500 \text{ \AA}$ $160 \mu\text{m} \times 8.6 \text{ mm}$ 

Figure 3.11 Acoustic wave profiles at 800 MHz for a clear path showing 12.7λ of beam steering and for a waveguide of 37λ by 1980λ with a 500 \AA Al film. Modes 0 and 1 are present.

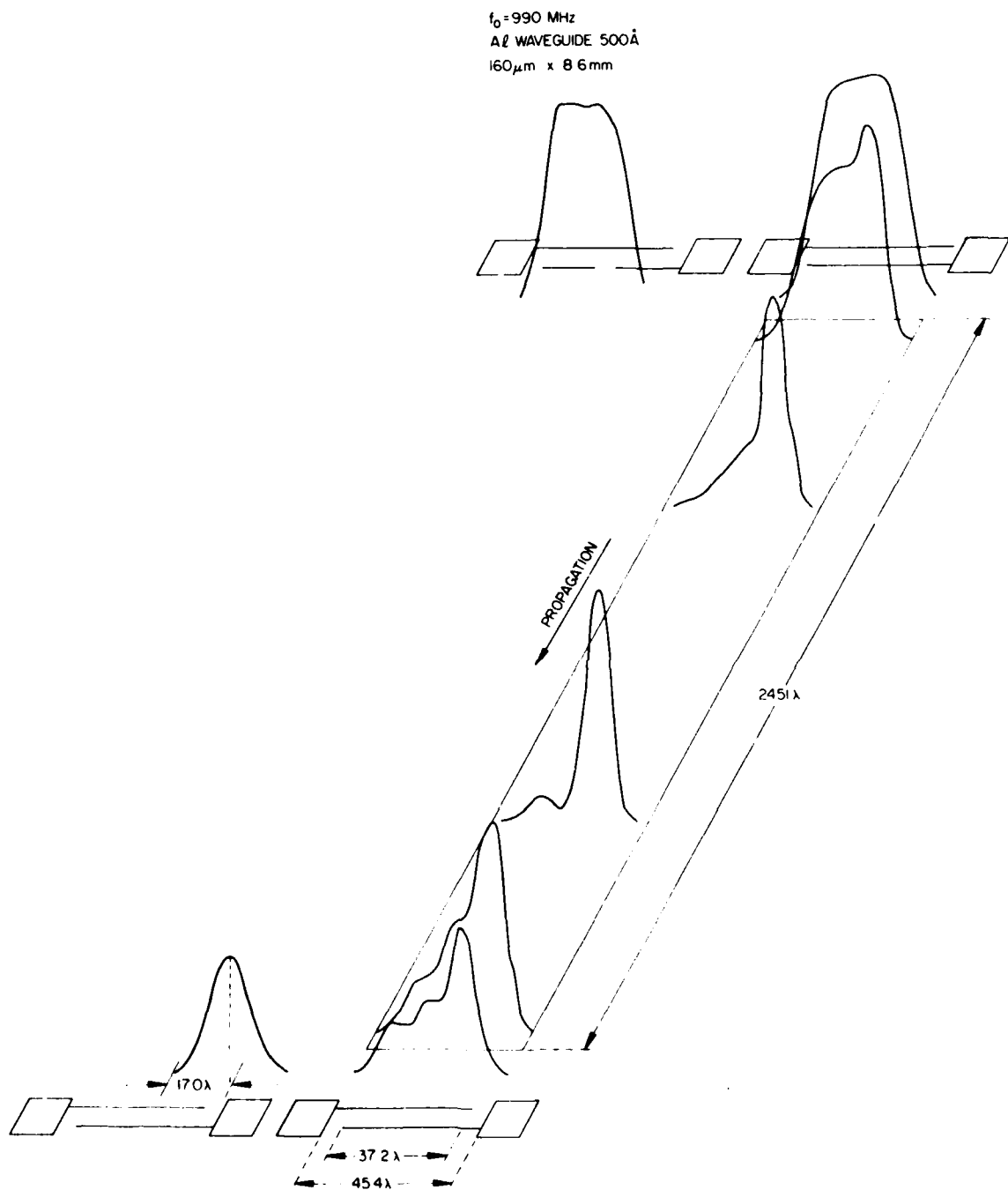
YZ LiNbO_3 ACOUSTIC WAVEGUIDE EFFECTS

Figure 3.12 Acoustic wave profiles at 990 MHz for a clear path showing 17λ of beam steering and for a waveguide of 45λ by 245λ with a 500 \AA Al film. Modes 0 and 1 are present. This is third overtone operation of device in Figure 3.9.

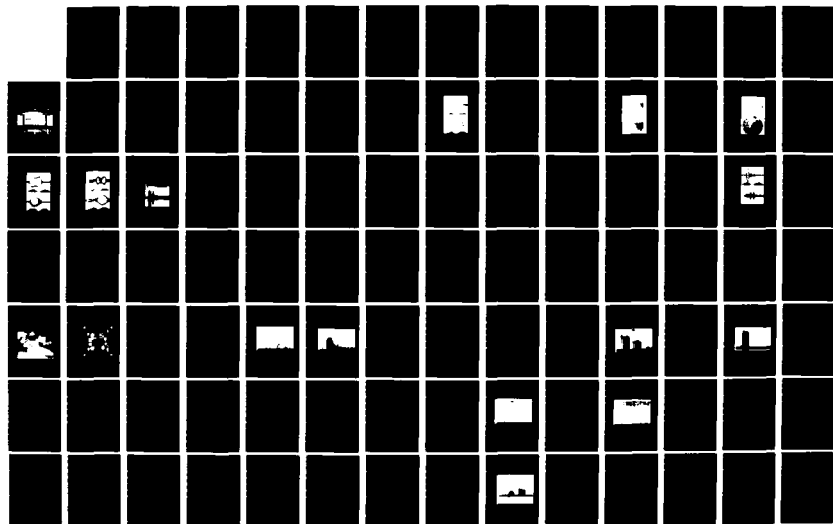
AD-A127 578

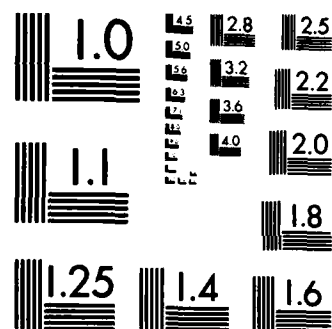
SURFACE ACOUSTIC WAVE NON-LINEAR INTERACTIONS IN
LITHIUM NIOBATE(U) ROME AIR DEVELOPMENT CENTER GRIFFISS
AFB NY R D COLVIN JAN 83 RADC-TR-83-9

2/4

UNCLASSIFIED

F/G 28/5 NL





MICROCOPY RESOLUTION TEST CHART
NATIONAL BUREAU OF STANDARDS-1963-A

3.12, we see that the phase velocity, V_p , differences get smaller as the waveguide width gets larger. This means that the beating of modes will occur more slowly in the larger waveguides.

$$\frac{V_{go}}{1} \cdot \frac{V_{go}}{f_0} \cdot \frac{1}{(V_{p0}-V_{p1})} = \text{beat length for modes 0 and 1,} \quad (3.4)$$

where V_{go} is the group velocity of the fundamental mode.

The beat lengths for modes 0 and 1 and modes 0 and 2 are:

$5\lambda \rightarrow 4.8 \text{ mm and } 1.85 \text{ mm}; 12\lambda \rightarrow 8.8 \text{ mm and } 2.7 \text{ mm}$ respectively, and $37\lambda \rightarrow 7.2 \text{ mm}$ for modes 0 and 1 (estimated).

In Figures 3.9 - 3.11 there are no whole periods for the beating of modes 0 and 1 or modes 0 and 2. However, there are half periods for modes 0 and 1 which are in reasonable agreement with the theory. In addition to longer beat lengths for modes 1 and 2, mode 2 has less intensity in the larger waveguide widths. A possible explanation is that at wider waveguide widths many modes can exist. Apparently the energy going into higher order modes is distributed among the many modes rather than going preferentially into mode 2. Thus, no one mode has a strong enough intensity to be significant. However, asymmetries still cause a significant conversion to mode 1.

The presence of asymmetric modes is most pronounced in Figure 3.12. The position occupied by the third profile

was scanned again with the acoustic wave propagating from the other direction. The result is shown in Figure 3.13. The two counter propagating waves nearly miss each other! The resulting interaction cannot be efficient. This is a good argument for avoiding very wide waveguides.

The following are some possible solutions to multimoding: one, use a 15λ waveguide since experimentally it appears to be the width that is least sensitive to the excitation of unwanted modes as in Figure 3.9. The main objection to this approach is the loss in efficiency due to a wide waveguide. It should, however, be mentioned that the efficiency is directly related to the absolute width and not effective width in wavelengths.^{3.12} This means that an efficient convolver can be designed by using a narrow waveguide and a high frequency of operation. For frequencies above 300 MHz, a beamwidth compressing multistrip coupler (BWC-MS) is not needed provided moderate (12 percent) bandwidths are acceptable. And up to 350 MHz the attenuation is not significant.^{3.10}

Two, use a 5λ waveguide with properly weighted input. As mentioned in the theory, if the exciting wave profile has the same shape as the fundamental mode (mode 0), only the fundamental will be excited. Apodizing the transducer will not work because for large bandwidth, the transducer does not have enough fingers. A BWC-MS can be apodized but has a severe diffraction problem as can be seen in Figure 3.7 where ideally A should have a square profile. A promising

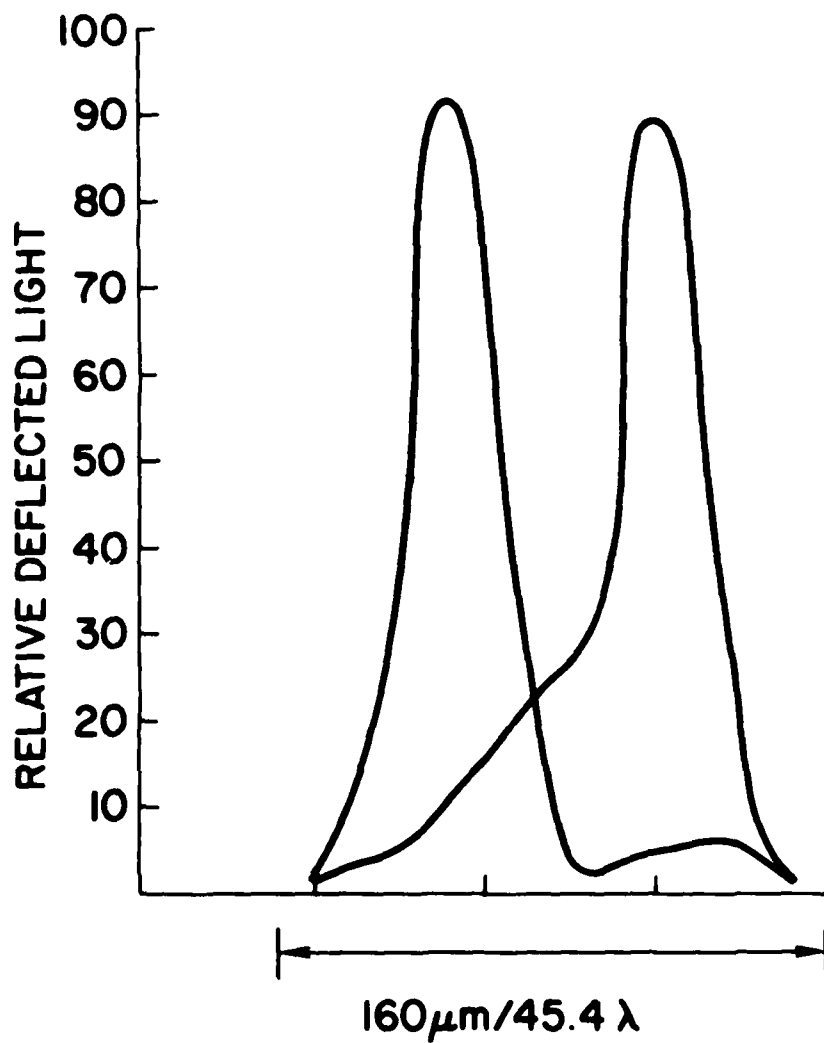


Figure 3.13 The acoustic wave profile on the right is the same as the third profile in the direction of propagation shown in Figure 3.12. The profile on the left was taken at the same position but with the wave being launched from the transducer on the opposing end.

approach is to use a resistive film to preferentially attenuate the edges.^{3.22} The shape of this resistive film for the fundamental mode is a cosine and can be obtained experimentally by taking the average of a peak and adjacent null in Figure 3.7.

Three, use a 2.5λ waveguide. Here only modes 0 and 1 can exist, and it is predicted that mode 1 even if present would not be a significant problem. This width does, however, present two problems: high plate resistivity and dispersion of the fundamental mode. The resistivity can be addressed with multiple bonds^{3.23} or aluminum interconnects to a large bus bar running the length of the plate.^{3.16} The dispersion may or may not be prohibitive depending on the application. A possible solution to the dispersion is to use dispersive transducers - also called chirp transducers. Typically, they have a linear dispersion, but an arbitrary dispersion is achievable and could be designed with a computer. Another possible solution for dispersion is to use an external predistortion filter.^{3.24}

Presently only the laser probe can give the profiles shown in Figures 3.7 and 3.9 - 3.12. However, information similar to Figure 3.4 can in principle be obtained from a plate uniformity response. A cw signal would be convolved with a pulse which must be much shorter (0.1) than the smallest beat length and observed on an oscilloscope. The convolved signal gives the average of the cross sections rather than the peak of the cross sections as in Figure 3.4.

Also two acoustic signals have been dispersed rather than one, and the output is an amplitude rather than an intensity (amplitude squared) which is obtained from a laser probe. In the case of Figure 3.4 the required pulse length, p , would be $p < (1.81 \text{ mm}) (0.1) (0.287 \text{ } \mu\text{sec/mm}) = 0.026 \text{ } \mu\text{sec}$. In many cases this short pulse will give a weak response buried in the noise - depending on F factor and dynamic range. Hence a longer pulse is used resulting in averaging of the features. Other complications may include long line effects and number and placement of bonds to the waveguide. Therefore, this method is seldom successful.

Also, multimoding will be evident as ripples in the frequency response of the device operated as a delay line if there are two dominant modes of similar intensity and appropriate beat length.^{3.13} While the ripples were not observed in these examples, they have been seen in other cases.^{3.13} Yet another method of analysis is the observation of the impulse response of the delay line. If there is only one other dominant mode, it will show up as a delayed pulse provided the delay line is long enough. Its amplitude can readily be measured by comparing to the fundamental. In this case the fundamental will have a rounded peak and additional small sidelobes compared to the response of an undistorted delay line.

The preceding paragraphs describe detection of multimodes in devices operated as a delay line. The real question however is, "How do they affect the convolved

output?" Before answering this question some observations are in order. First, different modes will not convolve because they are all orthogonal. However, two odds or two evens will convolve, i.e., $M_0 * M_0$, $M_1 * M_1$, and $M_2 * M_2$ are valid while $M_0 * M_1$, $M_1 * M_2$, and $M_0 * M_2$ are not valid. Second, the process is bilinear. If $M_0 * M_0$ is taken as a reference and M_1 and M_2 are 20 dB less than M_0 , then $M_1 * M_1 = -40$ dB and $M_2 * M_2 = -40$ dB. Third, each mode will have its own dispersion curve. This means the fundamental will be dispersed whether other modes are present or not. Fourth, the convolved modes $M_1 * M_1$ or $M_2 * M_2$ may not show up in the convolved output. Since they have different velocity, they will appear later in time. If the device is short, they may be hidden under the base of the main lobe, $M_0 * M_0$. If the device is long and a code is convolved, they may appear as part of the sidelobe structure and not be discernable. All the devices reported in this paper were 2.5 μ sec long and tested with cw (uncoded) waveforms. Multimoding effects were not directly observed in the convolved output.

The next investigation regards "What happens to the acoustic energy outside the waveguide?" Theory predicts that the fundamental mode will decay exponentially moving away from the waveguide. This can be visualized with the aid of Figure 3.8a. The device of Figure 3.5 and 3.6 was again laser probed. In this case, however, there are several complications. One is the presence of multimodes.

Another is the differences in reflectivity between a bare crystal and aluminum. A second question was "How much acoustic power is in the other aluminum films and do we need to worry about it?" The results of the laser probing are given in Figure 3.14. There are three sets of curves. The location of the aluminum films are shown in the hatched areas at the bottom. The curves have been corrected for differences in reflectivity of Al and bare LiNbO_3 (see Appendix A.5). The first set of curves shown as solid lines result from two identical scans. The deviations between them are a continuous set of error bars. The solid curves are an extension of profile "E" in Figure 3.7. The dashed lines are an identical set of two scans except input power was reduced 10 dB. At the peak in the waveguide there was precisely 10 dB less intensity as expected. The relationship generally held true elsewhere. The "X" curve was a single scan at a different position - the adjacent null D in Figure 3.7. Two conclusions are drawn. First, multimoding effects are present outside the waveguide. Second, the acoustic wave intensities are small enough outside the waveguide to assume their effect is negligible.

3.3 Electrical Losses

A. Theoretical Bilinear Conversion Factor

It is convenient to define a parameter which gives a measure of the efficiency of the device. This bilinear conversion factor $F_{\text{external}}^{3.1}$ is

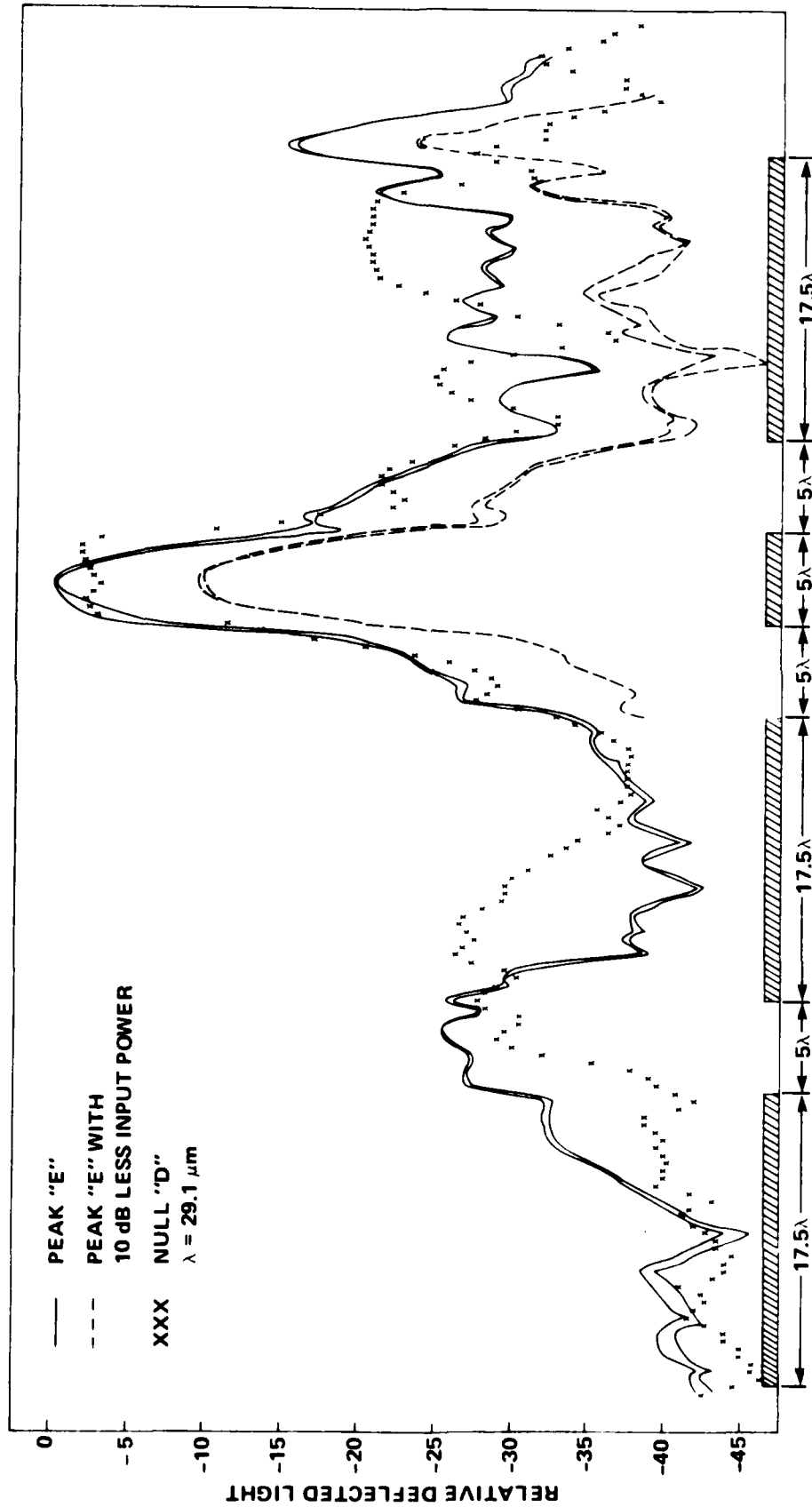


Figure 3.14 Acoustic wave profiles obtained by laser probe of 5λ waveguide in Figure 3.5 and 3.6. Profiles traverse one set of four Al plates. The positions of the traverses "E" and "D" refer to peak "E" and null "D" in Figures 3.4 and 3.7. Double lines result from two identical scans and are effectively continuous error bars.

$$F_{\text{ext}} \text{ (dBm)} = \frac{P_{\text{out}}}{P_1 P_2} \cdot \quad (3.5)$$

All powers are electromagnetic and are expressed in decibels referred to 1 mw. P_1 and P_2 are the input powers. F_{internal} is more useful for comparison purposes since the input transducer insertion losses (IL_1 and IL_2) are removed (however, propagation, diffraction, beam steering and plate attenuation losses are not removed).

$$F_{\text{int}} \text{ (dBm)} = F_{\text{ext}} - (IL_1 + IL_2) \quad (3.6)$$

or stated another way,

$$F_{\text{int}} \text{ (dBm)} = \frac{P_{\text{out}}}{P_{1a} P_{2a}}, \quad (3.7)$$

where P_{1a} and P_{2a} are now acoustic input power levels. Defranould and Maerfeld^{3.12} have related F_{int} to device parameters. With some manipulation, the maximum available power can be expressed as

$$F_{\text{int,max}} = \frac{M^2}{4W^2 R_a} = \frac{M^2 L}{4W r_a}, \quad (3.8)$$

where M is a figure of merit for the non-linear material, W is the beam width of the two incident acoustic waves, L is the length of the integrating electrode, R_a is the real part of the internal impedance of the interaction region, and $r_a = WL R_a$ with r_a equal to the bulk wave piezoelectric coupling coefficient. R_a can be found from the output impedance plot by removing the contributions of plate resistance, transmission line effects, and impedance

transformers (if any are used). From this one can see that the output power is proportional to length and inversely proportional to width-in meters. M is independent of frequency but depends on the material, crystal cut, and direction of propagation.^{3.20} For Y cut, Z propagating lithium niobate, M has been measured as 7.9×10^{-5} Vm/W.^{3.12} M has been related to the third order elastic, piezoelectric, dielectric, and electrostrictive constants. For Y, Z orientation the non-linearity is dominated by third order piezoelectric constants. However, for other propagation directions this domination is no longer true.^{3.20}

For device 20 at 330 MHz (Table 3.2), W equals $160 \mu\text{m}$ and R_a is about 10 ohms. This predicts $F_{\text{int,max}}$ of -52 dBm compared to a measured F_{int} of -59.5 dBm. For T-CSF^{3.25}, W equals $110 \mu\text{m}$, and R_a is about 6 ohms. This predicts $F_{\text{int,max}}$ of -47 dBm compared to a measured F_{int} of -58.5 dBm. The above theory assumes a lossless case. After including the accountable losses of propagation loss, plate attenuation, and output transmission loss, F_{int} becomes -55.0 dBm for device 20 and -54.5 dBm for T-CSF. This indicates that the devices are not optimized in their coupling to the available energy.

B. Experimental Bilinear Conversion Factor

The bilinear conversion factors for several devices are listed in Table 3.2. The written comments at the right of Table 3.2 refer to the bonding configuration at

DEVICE NO.	INPUT FREQ (MHz)	CRYSTAL CUT	F _{ext} ⁽¹⁾ (-dBm)	TRANS-DUCER IL (dB)	F _{int} (-dBm)	OUTPUT TRANS-MISSION LOSS (dB)	OUTPUT MATCH
13	916	38, X	102.0	15.5	86.5	7.2	
20	990	Y, Z	92.5 97.5	16.0 16.0	76.5 81.5	1.9 4.2	RESISTOR TERMINATIONS
21	800	Y, Z	78.0 86.5 83.0 83.5	14.5 14.5 14.0 14.0	63.5 72.0 69.0 69.5	0.2 7.0 5.5 5.5	RESISTOR TERMINATIONS GROUND PLANES BESIDE-END TAPS END TAPS
16	800	Y, Z	85.0 83.5	16.5 16.5	68.5 67.0	5.5 0.5	END TAPS OUTPUT CAPACITOR
18	800	Y, Z	86.0 90.5	16.5 16.5	69.5 74.0	5.0 8.7	END TAPS
17	800	Y, Z	88.0 89.5 91.5	14.5 15.0 15.0	73.5 74.5 76.5	1.1 1.8 3.0	GROUND PLANES BESIDE-END TAPS END TAPS
15	800	Y, Z	96.0 94.5	16.0 15.5	80.0 79.0	2.2 3.6	GROUND PLANES BESIDE-END TAPS END TAPS
20	330	Y, Z	71.5	12.0	59.5	3.7	
T-CSF(2)	167	Y, Z	73.0	14.5	58.5	2.4	END TAPS

(1) -1.5 dB ACCURACY

(2) MANUFACTURED BY THOMSON CSF - ON LOAN FROM MIT LINCOLN LABORATORY - REF 3.25

Table 3.2 Performance of nine degenerate elastic SAW convolvers. Headings are explained in the text. The Transducer IL (insertion loss) is computed as in Table 3.1 but differs due to differences in transducer matching.

the output of each convolver. Referring to Figure 3.1, it is helpful to know that the output plate in path (a) has three bonding pads - one at each end and one in the center. Path (b) has bonding pads only at each end. No comment implies the use of a center tap. Resistor terminations mean a center tap output plus each end terminated with a resistor. End taps means that the output is bonded to both ends, and the center tap is not connected.

In all the cases listed in Table 3.2, the plate was 8.6 mm by 160 μm giving a propagation time of 2.5 μsec on Y, Z LiNbO₃ and 2.2 μsec on 38, X LiNbO₃. The input pulse lengths were always as long as the plate length. For ground planes located beside the output plate, the spacing was 54 μm . For example, Device No. 15 is shown in Figure 3.15. All the devices have a 500 \AA film except No. 17 which has a 300 \AA film. The crystals were 450 μm thick, and the transducer apertures were all 130 μm . The only exception to the above description is the device at 167 MHz.^{3.25} It had an output plate of 41 mm by 110 μm with a ground plane on each side. It used a 15:1 beamwidth compressor, but the compressed acoustic power densities were very similar to the other devices.

A generalized schematic of the F factor (F_{ext}) test setup is given in Figure 3.16. The two steps in obtaining an F factor are (a) measure P_{out}/P_1 , and (b) measure P_2 . First a reference level is established on the scope. Then test point A (T.P.A) is connected to T.P.B. R_1 is

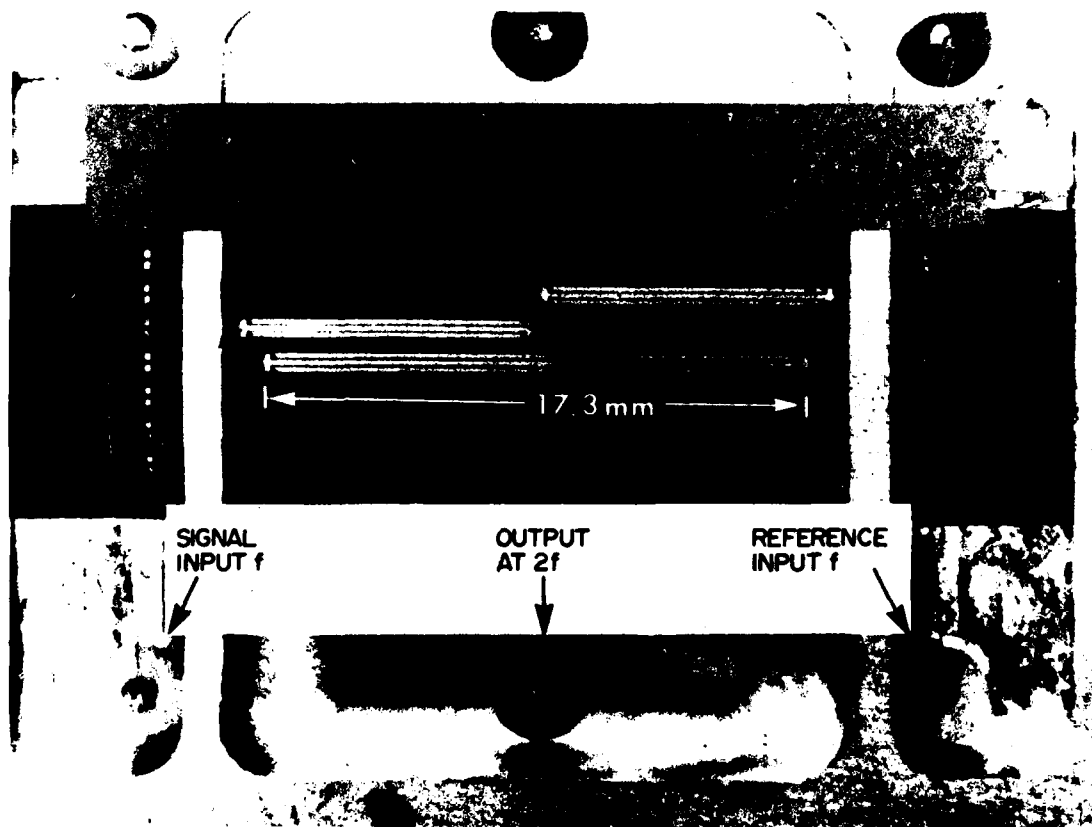


Figure 3.15 Picture of a convolver corresponding to schematic in Figure 1b. There are two channels with 8.6 mm plates and one channel with 17.3 mm plate. This is device 15 of Tables 3.1 and 3.2.

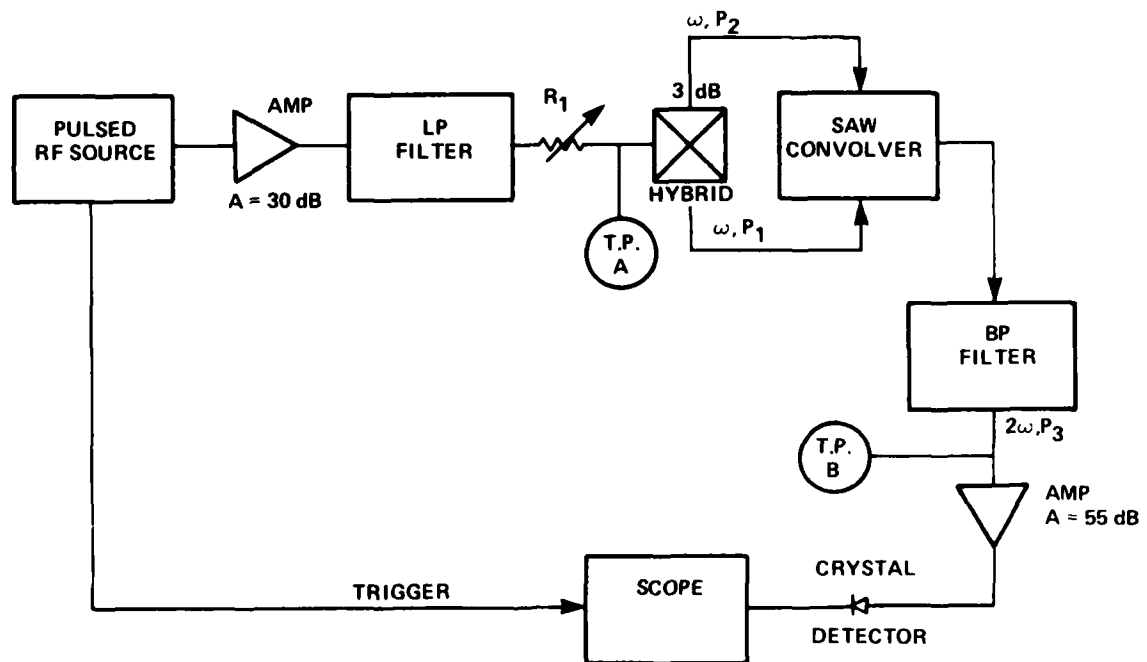


Figure 3.16 Block diagram of "F" factor (efficiency) test setup. T.P. A and B are connected for part (b) of the measurement procedure - see text.

incremented until the same level is established on the scope as before, and 3.5 dB is subtracted from the value of R_1 to account for the hybrid. Also there is a calibration curve to account for the frequency dependence of R_1 , the 55 dB amplifier, and the crystal detector because the output is at 2ω , but when T.P.A is connected to T.P.B the output is at ω . Thus R_1 minus 3.5 dB minus the calibration factor becomes P_{out}/P_1 . Correction factors ranged from 3 to 8 dB depending on frequency. Next, the pulsed source is switched to cw, and the power is measured at T.P.A. Again 3.5 dB is subtracted to account for the hybrid. This gives P_2 which must be expressed in dBm.

Starting in Table 3.2 with device 21 (samples 3 and 4), 15 and 17 (samples 1 and 2), and using F_{int} as a criteria, one can conclude there is little difference in F factor (within experimental error) between having the ground planes beside and having the ground planes below. Comparing device 21 (samples 2 and 4), and 18 and 17 (samples 2 and 3), we see that a center tap is worse than end taps by 2 to 4.5 dB; but most of this is due to differences in output impedances. Comparing 13 and 15 (sample 2) both of which have the same film thickness and 22.35 mm total path length, one can conclude that 38,X orientation is about 7.5 dB less efficient than Y,Z orientation. And after allowing for differences in output matching, it is about 4 dB less efficient. Comparing devices 17 (sample 2) and 15 (sample 2), one can conclude the thinner 300Å film yields about 2.5

dB less loss.

The use of plate termination improved the F factor substantially at 800 and 990 MHz. Comparing device 20, samples 1 and 2, there is a 5 dB improvement. Comparing device 21, samples 1 and 2, there is an 8.5 dB improvement. These are partly explained by the better output match. The rest of the explanation involves several complex interactions which are discussed more fully in section 3.3D.

The device labeled T-CSF was manufactured by Thomson CSF and was on loan from MIT Lincoln Laboratory for testing. It is used here as a baseline. Device 20 at 330 MHz is important because the F factor is within 1 dB of the baseline device and no beamwidth compressor was needed. Further, the absolute bandwidths are nearly identical. Comparing device 20 at 330 MHz with device 21 (sample 1) at 800 MHz, one can see a 7.5 dB difference in F_{ext} after including output losses. This is mostly accounted for by additional propagation loss and Al film attenuation at 800 MHz. However, when comparing device 20 at 990 MHz with device 21 at 800 MHz, after accounting for differences in propagation and Al film losses there is an additional loss of 8 dB that cannot be accounted for. It is likely this additional loss is due to the uneven energy distribution shown in Figures 3.12 and 3.13.

C. Output Plate Resistivity

As mentioned before, a narrow waveguide (Al film) will give best efficiency. Unfortunately, ohmic losses can

be very significant. The devices in Table 3.2 are relatively short, 8.635 mm by 160 μ m (or 54 squares). The output plate had a d.c. ohmic resistance of 1.08 ohm/square or 58 ohms for a total thickness of 500 \AA (40 \AA chromium and 460 \AA aluminum). For a thickness of 300 \AA (40 \AA chromium and 260 \AA aluminum) the resistance was 1.92 ohm/square and a total of 104 ohms. However, the plate was always connected electrically in parallel, so one half of these values should be used. The evaporation conditions were a room temperature substrate and 16 \AA /sec deposition rate.

Acoustic dispersion and attenuation are functionally directly dependent on kh . ($k = 2\pi/\lambda$ and h is Al film thickness). This means that at higher frequencies thinner films must be used. This requirement coupled with the desire for longer devices creates a need to optimize resistivity. Knowing that thin films are very sensitive to evaporation rate, experiments were conducted for which results are given in Figure 3.17. In all cases a predeposition of 40 \AA Cr was deposited at 10 \AA /sec and better than 10^{-7} Torr onto glass slides. The Al was then deposited at various rates and thicknesses with a vacuum in the range of 1 to 10×10^{-7} Torr. Measurements were made with a four point probe. The conclusion is that for films of less than 1000 \AA , and sheet resistances below 0.5 ohm per square the deposition rate should be at least 16 \AA /sec.

The predeposition of Cr is needed for adhesion of the Al to LiNbO_3 . Some workers prefer to omit the Cr. In this

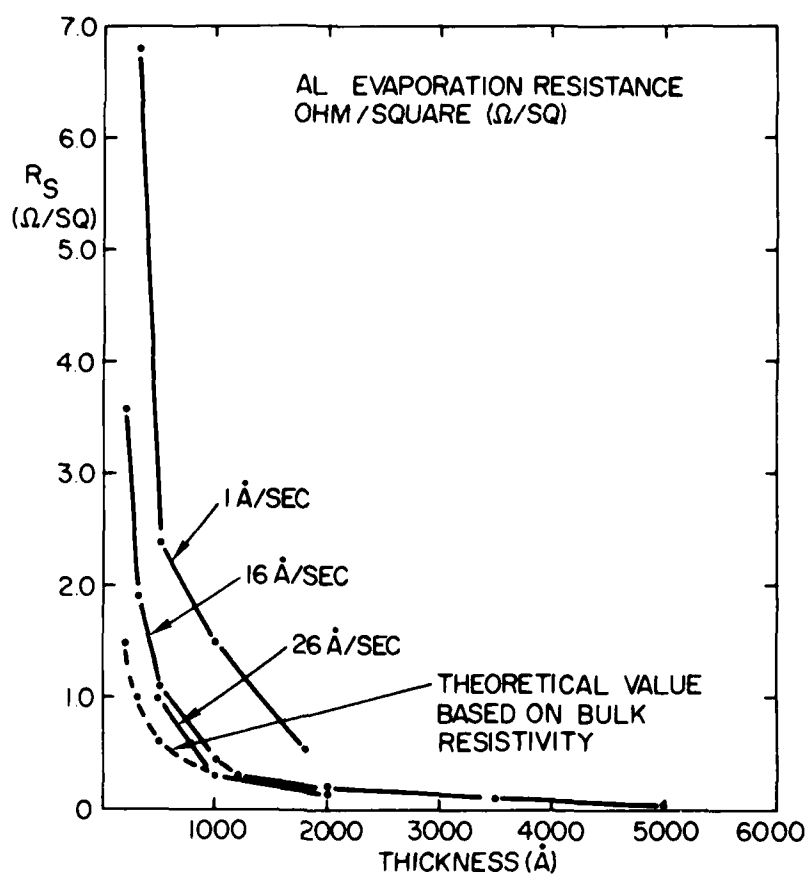


Figure 3.17 Resistivity (in ohms/square) of various Aluminum films showing the effects of thickness and evaporation rate. Each thickness includes 40 Å of chromium.

case adequate adhesion is obtained by evaporating the Al onto a heated substrate. Temmyo^{3.26} has experimentally generated a family of curves for resistivity versus film thickness for various substrate temperatures. The conclusion of his work is that for a substrate temperature of 130°C, the resistivity of Al films increases rapidly for thickness less than 400Å. His conditions were no Cr, 7×10^{-6} Torr, and 3-5Å/sec deposition rate onto a glass substrate.

D. Transmission Line Effects and Output Matching

For all the devices considered here, the output plate acts like a transmission line with reflections and standing waves. The problem is most severe for a center tapped plate that is one-half wavelength. Reflections received at the center-tapped output are 180 degrees out-of-phase with the signal. The standing wave ratio will be reduced somewhat by the resistivity of the plate attenuating the reflected signal. In some cases the resistivity will nearly eliminate the standing wave. Referring to Table 3.1, we see that none of the devices were a half wavelength long. The EM velocity is reduced by $\sqrt{\epsilon_r}$ or $\sqrt{44}$ for Y,Z LiNbO₃. Nonetheless, the effect of partial cancellation due to the reflected wave was significant. The top of Figure 3.18 is typical. It shows the plate uniformity response obtained by the convolution of CW in one port and a short pulse in the other port. It is from device 21 with output frequency (2ω) of 1600 MHz. The ripple is about 2 dB. The test setup is

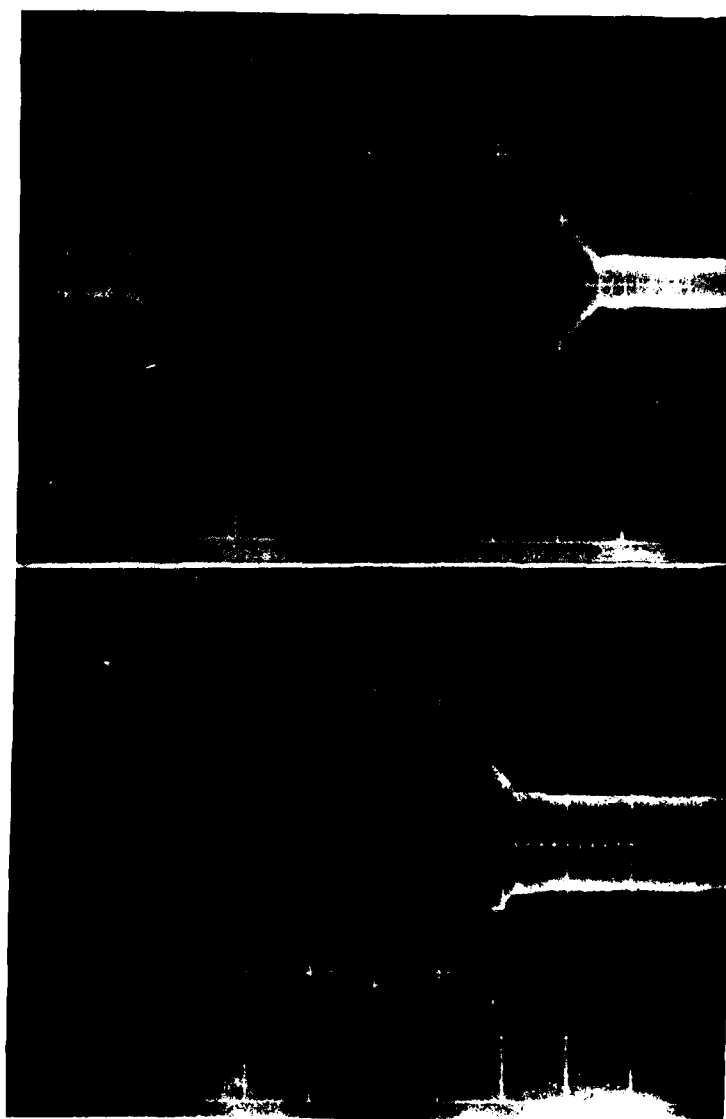


Figure 3.18 Plate uniformity response of device 21 at 1600 MHz output frequency. (Top) without plate terminations showing 2 dB of ripple. (Bottom) with plate terminations of $Z = 28$ ohms showing 1 dB of ripple. Vert. 100 mV/div., Horiz. 0.5 μ sec/div.

given in Figure 3.19. A short pulse is convolved with CW, i.e. it is an impulse response. The output is at 2ω . The output impedance is shown on a Smith chart at the top of Figure 3.20 as the frequency is swept from 1000 to 2200 MHz. There is an additional marker dot for 1600 MHz which occurs at 75 degrees. The result of this nonuniformity will be to degrade the minimum achievable time sidelobes when using coded signals.

The remedy is to terminate the transmission line in its characteristic impedance. It is a microstrip with relative dielectric of 44 (for Y,Z LiNbO_3) and characteristic impedance $Z_0 = 28\Omega$. The termination may be either a resistor or an inductance of value Z_0 . Goll and Bennett^{3.27} have done an analysis showing the effect of both. The resistor gives best uniformity but dissipates power. When using a resistor, there may still be a nonuniformity (a second order effect) since the phase associated with the distributed non-linear sources is a linear function of position. The inductance, on the other hand, causes a total reflection but adds a -90 degree phase shift. The result is that for lines of $\lambda/2$ or less, the reflected signals will be additive. There will be ripples in the uniformity, but they will have much less amplitude. (Note that use of a capacitor will cause the reflected signal to subtract and cause a loss of output.) Goll and Bennett report that inductor terminations gave a 7 dB increase in output power and added about 1 dB to the ripple

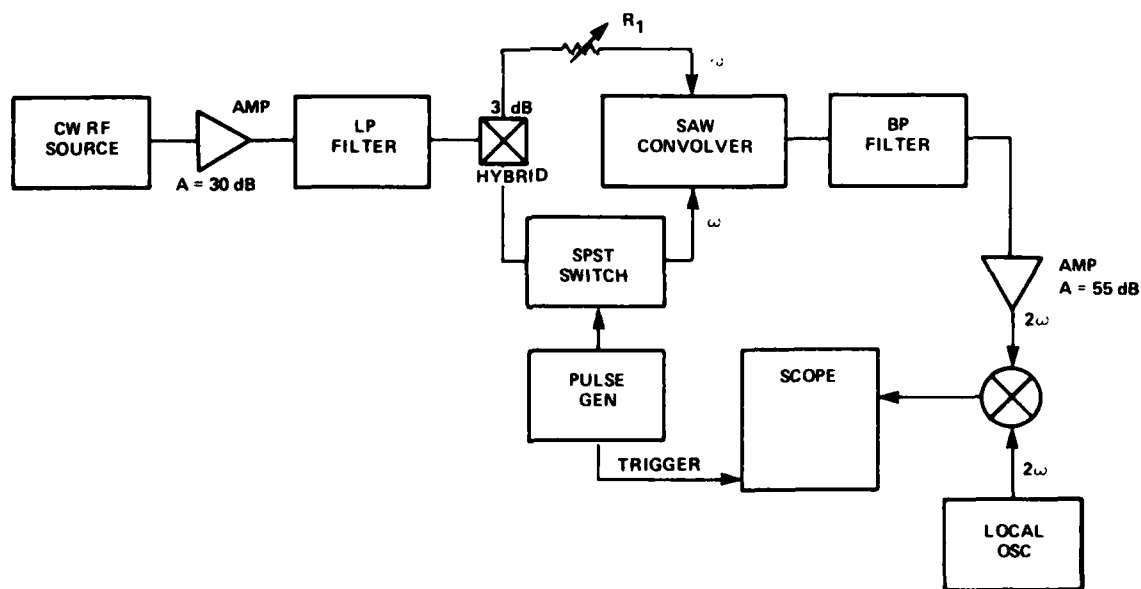


Figure 3.19 Block diagram of Plate Uniformity test setup. A short pulse is convolved with cw to give an approximate impulse response.

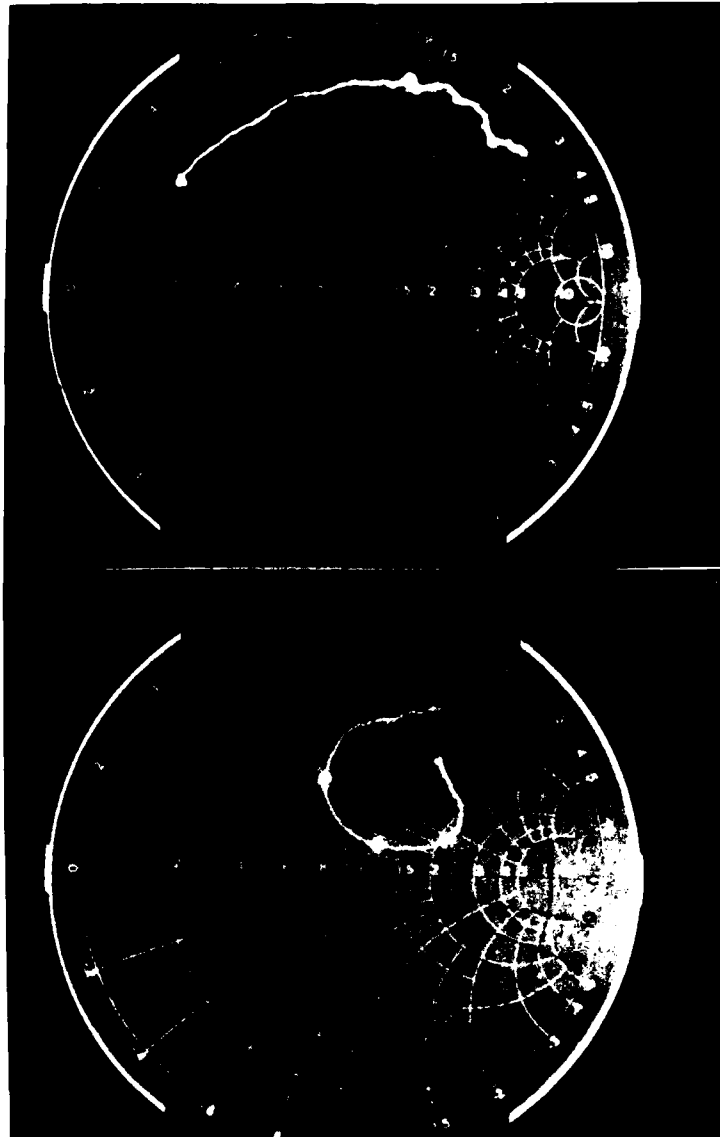


Figure 3.20 Output impedance (S_{11}) of device 21. (Top) without plate terminations. Frequency sweeps 1000 - 2200 MHz with marker dot at 1600 MHz (75°). (Bottom) with plate terminations of $Z = 28$ ohms. Frequency sweeps 1000 - 2200 MHz with marker dots at 1400, 1600 and 1800 MHz.

in the uniformity compared to a resistor termination. This degradation is less than theoretically expected and is probably due to resistivity in the plate. The increased output power is due to no power dissipation in the reactive elements and possibly due to a better match of the distributed non-linear sources to their load impedance.

Devices 20 and 21 were terminated with resistors. However, at the output frequencies of 1600 and 1980 MHz respectively, they were more inductive than resistive as shown in the top of Figure 3.21. Referring to the top of Figure 3.20, we see another example of this. The output plate is of course a capacitor. Yet at these frequencies it is strongly inductive due to the finite length of the bond wire. At frequencies below 900 MHz it is a well behaved capacitor with some resistance due to the resistivity of the film. The bottom of Figure 3.18 shows an improved uniformity for device 21 with the aid of inductive resistors for terminations. The bottom of Figure 3.20 shows the corresponding output impedance as frequency is swept from 1000 to 2200 MHz. Marker dots are at 1400, 1600 and 1800 MHz. Terminations have the added advantage of transforming the output impedance^{3.28} making a better match to the outside 50 ohm system. This is especially important since neither wire wound nor ferrite loaded transmission line impedance transformers are commercially available at these frequencies. Several other matching schemes for the output were tried with limited success. For example, consider

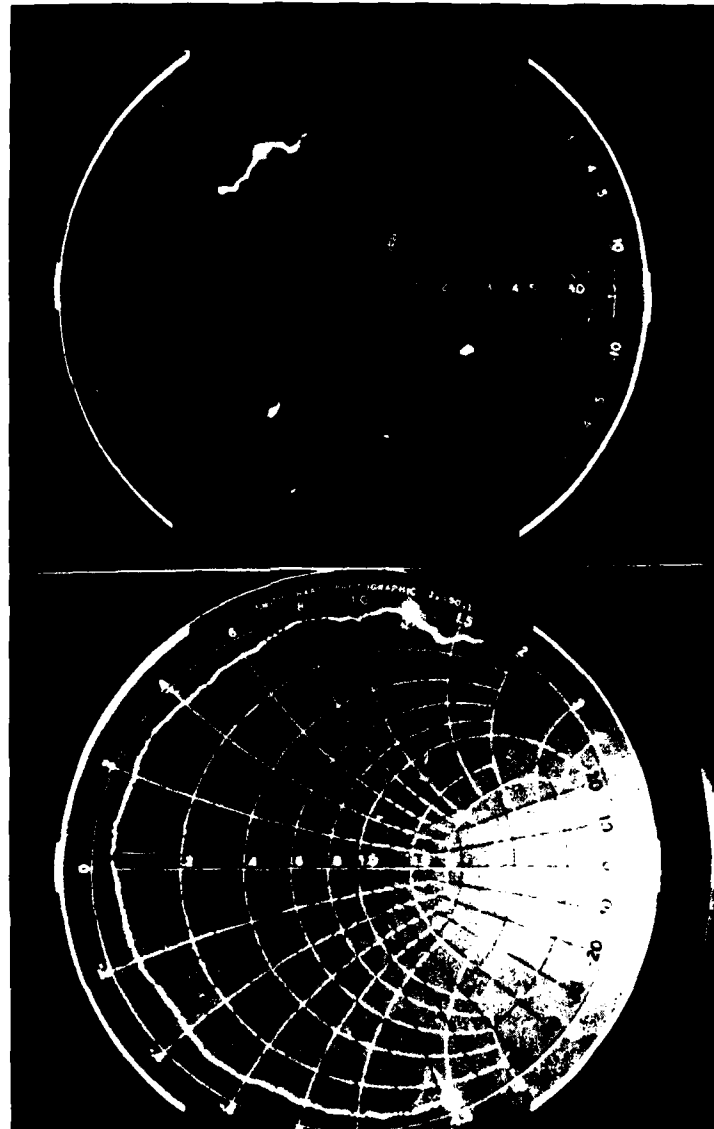


Figure 3.21 (Top) Impedance (S_{11}) of a 12 ohm resistor. Frequency sweeps 1000 - 2200 MHz with marker dot at 1600 MHz, $Z = 28$ ohms at 1600 MHz. (Bottom) Impedance (S_{11}) of a 1pf chip capacitor. Frequency sweeps 1000 - 2200 MHz with marker dot at 1984 MHz.

device 20 at 990 MHz (1980 MHz output) in Figure 3.22 and device 13 at 916 MHz (1832 MHz output) in Figure 3.23. The top traces are without matching. The bottom traces result from termination with carefully chosen inductive-looking capacitors, e.g. see the bottom of Figure 3.21. The uniformity responses should have a flat top. They do not because the reactance is not exactly Z_0 and because it is reactive rather than resistive.^{3.27} The conclusion is that parasitics from bond wires and various shunt capacitances are dominant over desired matching elements. Finally, the uniformity of a nearly optimum device is shown in the top of Figure 3.24. It is T-CSF operating at 167 MHz and is described in Table 3.2 and Reference 3.12. The large spike at the left is feedthrough of the short pulse which was convolved with CW from the other input port.

3.4 Performance

A. Dynamic Range

Convolution using device 21 was measured at 800 MHz with two rectangular pulses of 2.5 μ sec. This is schematically depicted in Figure 3.25. The power level of the reference (Figure 3.1a) was held at a constant level of 25 dBm. The signal (also 25 dBm) was attenuated with a precision step attenuator from 1 to 52 dB. The convolved output at 1600 MHz was bandpass filtered to reject the fundamental frequency, attenuated (with a precision step attenuator), amplified, envelope detected with a crystal,

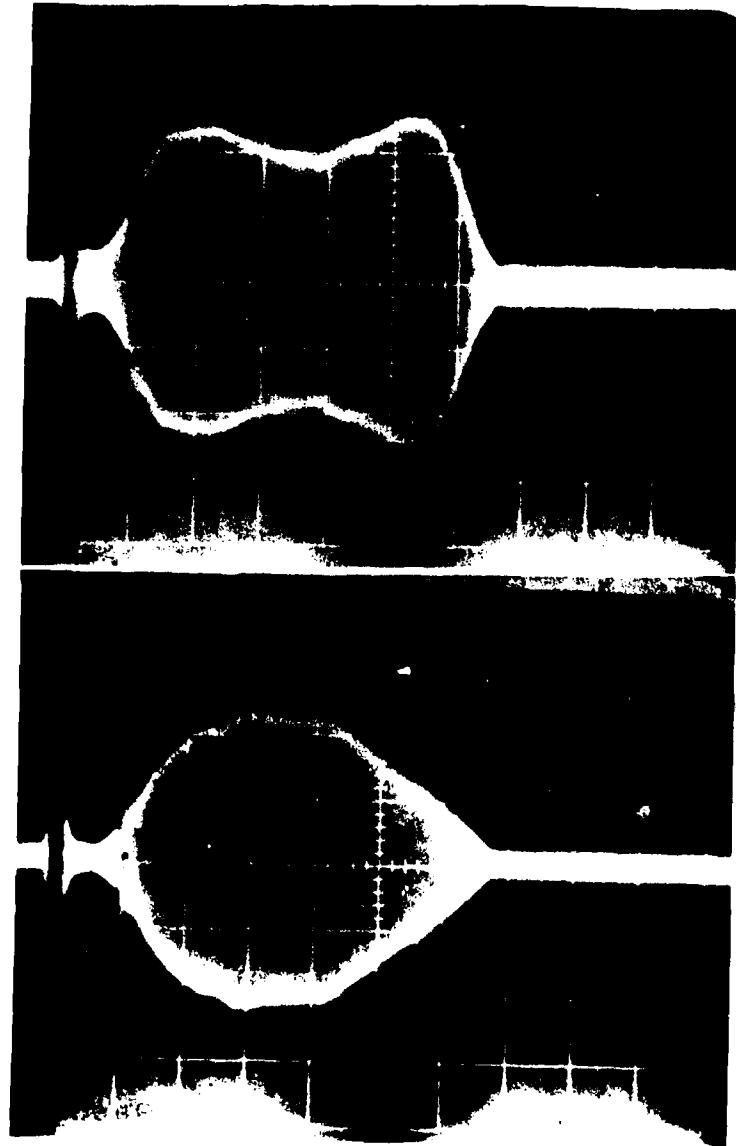


Figure 3.22 Plate uniformity response of device 20 at 1980 MHz output frequency. (Top) without plate terminations, showing 3 dB of ripple, (Bottom) with plate terminations. Vert. 20 mV/div., Horiz. 0.5 μ sec/div.

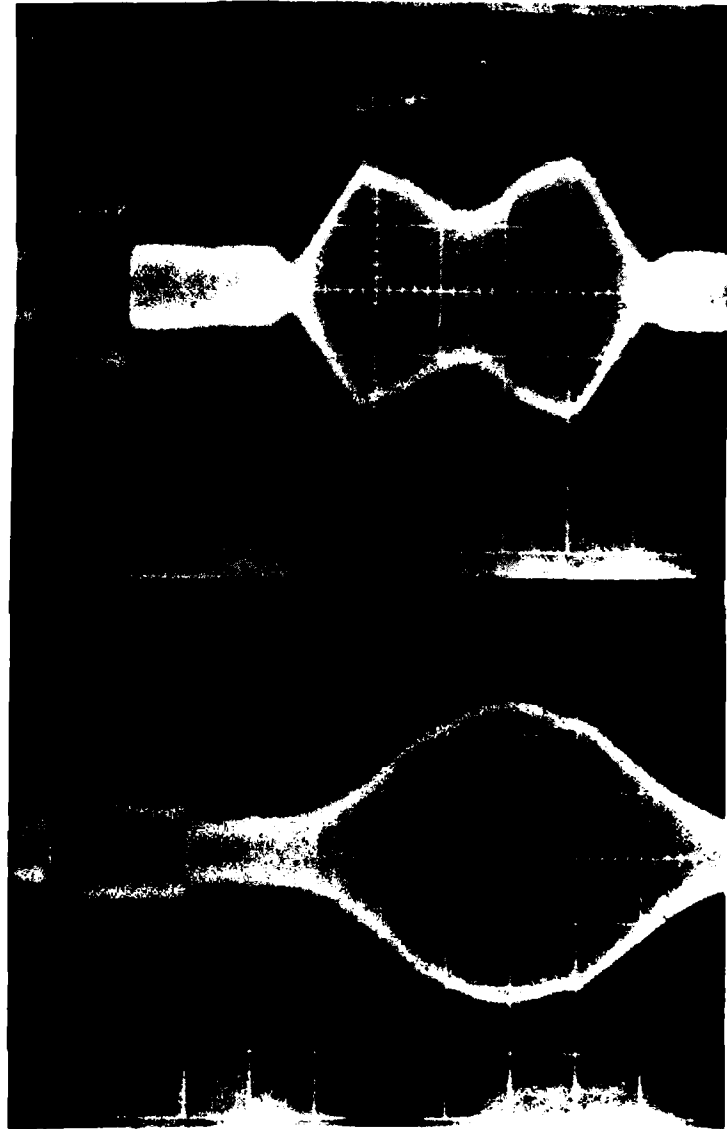


Figure 3.23 Plate uniformity response of device 13 at 1832 MHz output frequency. (Top) without plate terminations, showing 4 dB of ripple, (Bottom) with plate terminations. Vert 20 mV/div., Horiz. 0.5 μ sec/div.

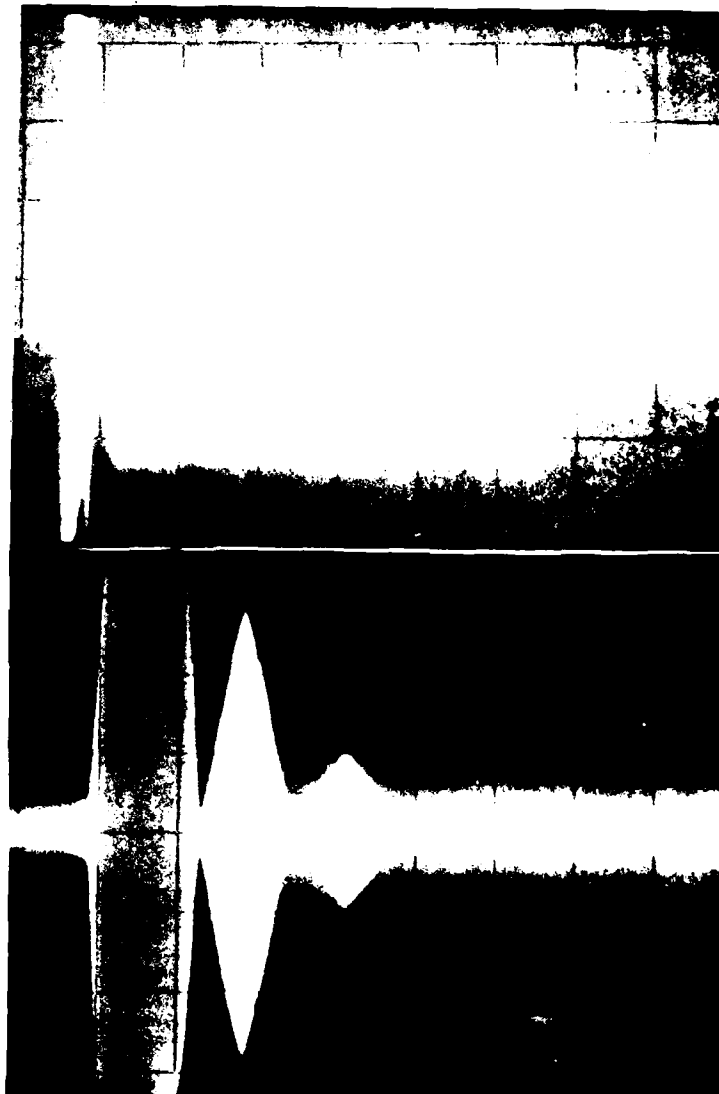


Figure 3.24 (Top) Plate uniformity response of device T-CSF (Ref. 3.25) showing about 0.5 dB of ripple. Horiz. 2 μ sec/div. (Bottom) Convolution of two cw RF pulses of 12 μ sec each. The desired convolution is off scale. Next are the undesired spurious signals: first - autoconvolution, then - double transit convolution. Horiz. 5 μ sec/div.

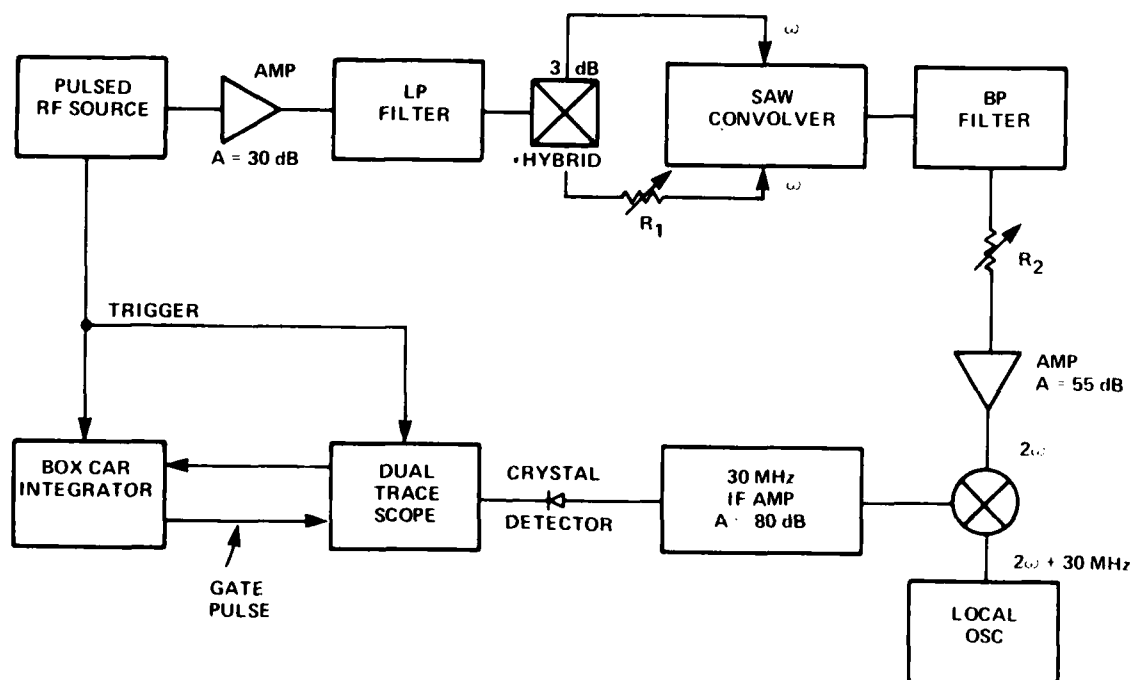


Figure 3.25 Block diagram of Dynamic Range and Spurious Level test setup. As R_1 increases R_2 decreases keeping external power levels constant.

and displayed on an oscilloscope. As the input attenuator was increased, the output attenuator was decreased so the power through the amplifiers and oscilloscope always remained constant. When power is varied in only one input as described above, the output should be linearly proportional to the input. This measure of dynamic range is shown in the top of Figure 3.26. The plate configuration was that of Figure 3.1a. The usable dynamic range was about 44 dB. The upper limit of about 1W for pulses is determined by burnout of the interdigital transducers. The device in Figure 3.26a was tested to 25 dBm; hence, the dynamic range is about 5 dB more than shown on the graph.

In order to investigate harmonic generation, we observed the linearity of the input. For this experiment, an 800 MHz pulse was sent from one interdigital transducer to the other interdigital transducer (Figure 3.1c), which now serves as an output for the 800 MHz pulse. For the case of no plate, the data of the bottom of Figure 3.26 shows a 4 dB deviation from the linear curve at maximum input power. This indicates that power is starting to enter higher harmonics. When an 8.6 mm plate was placed in the path (Figure 3.1a) the harmonics were suppressed by the dispersion of the thin-film plate.^{3.10,3.29,3.30}

These same two measurements are given for $38, X \text{ LiNbO}_3$ (device 13) in Figure 3.27. The lower F_{ext} of this device results in less dynamic range. The conclusions for second harmonics are the same.

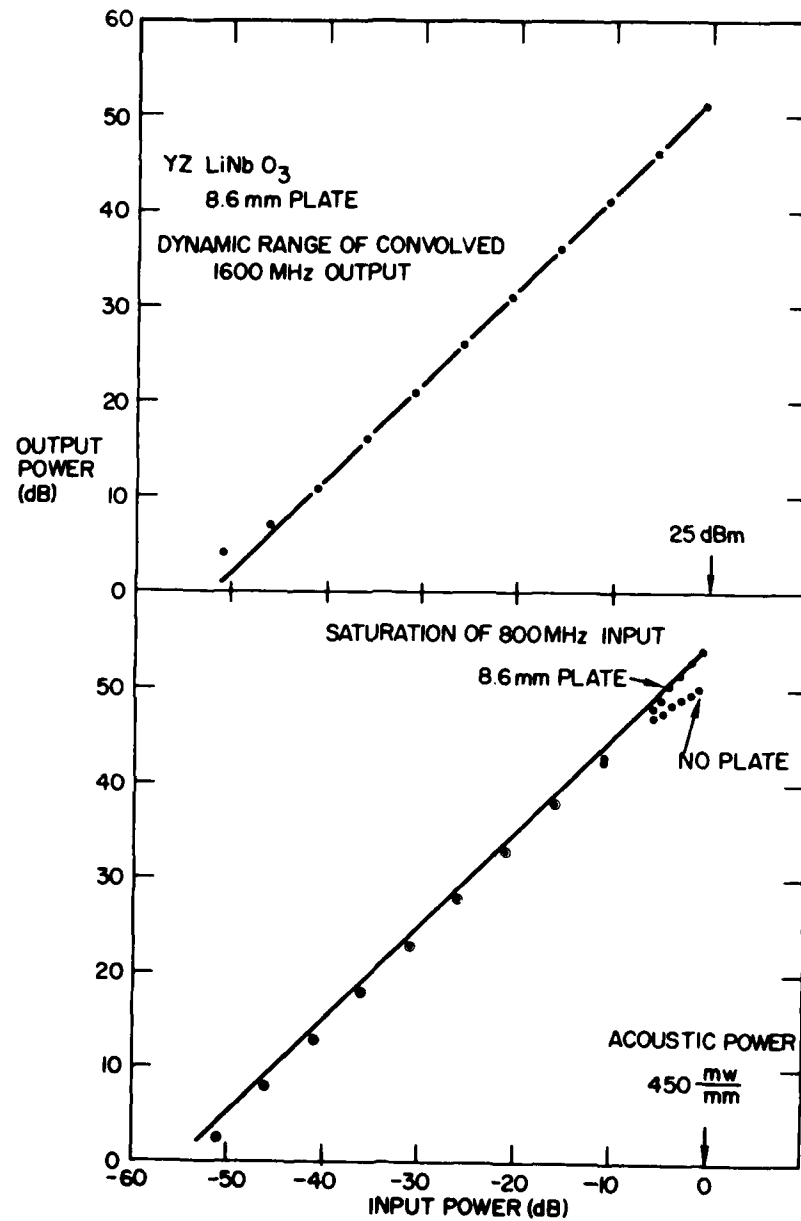


Figure 3.26 Convolved output power at 1600 MHz versus power into one input while other input is held constant at 25 dBm. (b) 800 MHz acoustic power transmitted from one interdigital transducer to the other. (See Figure 1c)

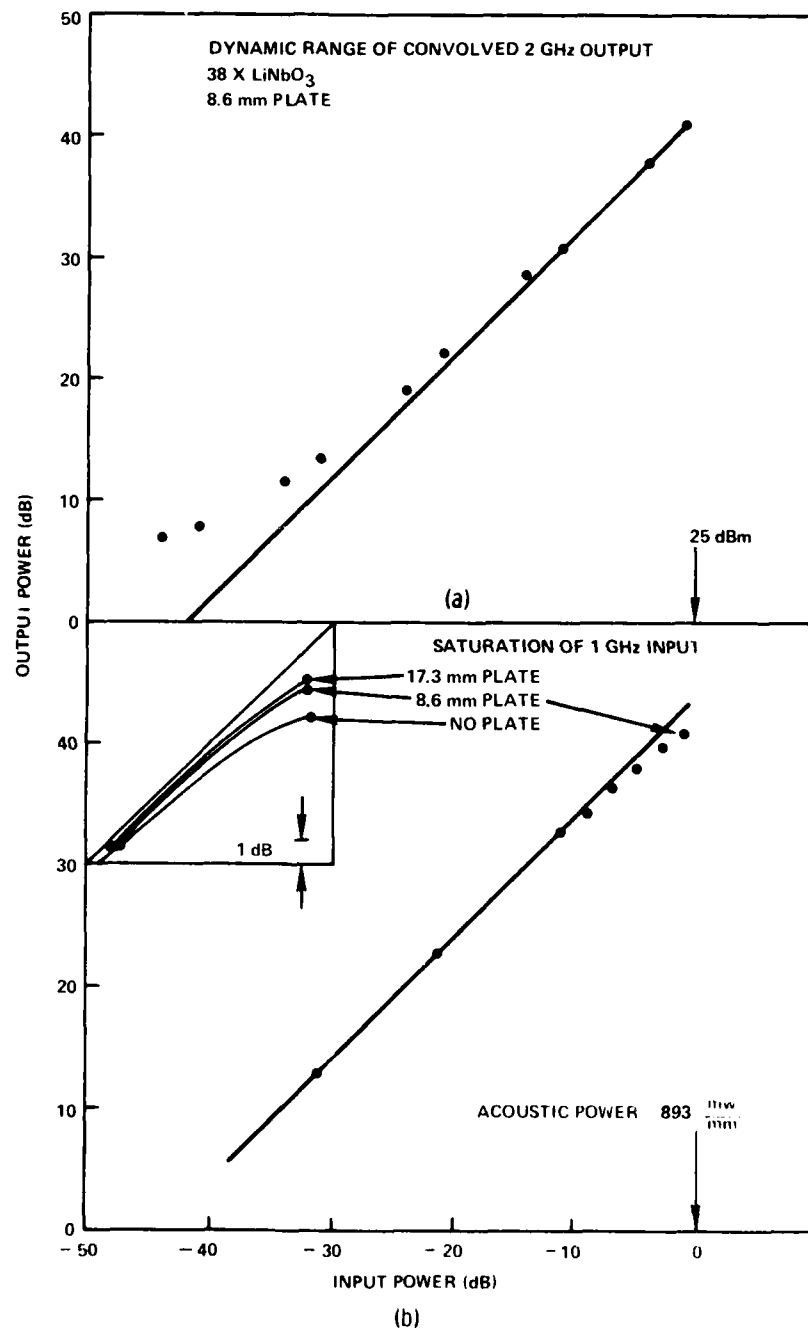


Figure 3.27 Convolved output power at 2000 MHz versus power into one input while the other input is held constant at 25 dBm. (b) 1000 MHz acoustic power transmitted from one interdigital transducer to the other.

The bandwidth of device 20 at 330 MHz was measured at the output to be 47 MHz as shown by Figures 3.28 and 3.29. This is the same absolute bandwidth at T-CSF, yet no beamwidth compressor was needed. The efficiencies are nearly identical because the transducer of device 20 had an aperture of nearly the same width as the compressed beam of T-CSF. When scaling to higher frequencies, the photolithography for the beamwidth compressing multistrip coupler becomes difficult, thus explaining the desire to not use one. However, the use of a smaller aperture does impose the limit of less attainable fractional bandwidth at these frequencies. This is less of an issue at higher frequencies where the same aperture would then have more wavelengths. An alternative is the use of parabolic horns to obtain the beamwidth compression.^{3.31}

The bandwidth of device 21 was also measured ($f_0 = 800$ MHz) and is recorded in Figure 3.30. The 76 MHz bandwidth agrees closely with the bandwidth of the device operated as a delay line.

B. Spurious Levels

Autoconvolution (or self convolution) occurs when one acoustic wave propagates past the plate, is reflected off the opposing transducer, and on the return trip convolves with itself. It is normally measured with one input terminated in 50 ohms. Double transit convolution occurs when both waves are reflected from the opposing ends and convolve with each other on the return trip.

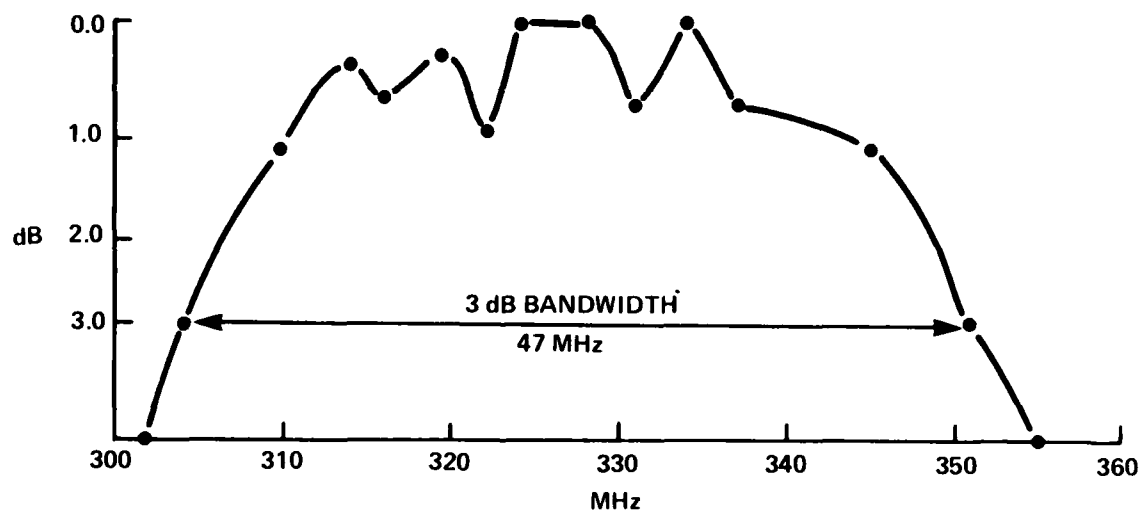


Figure 3.28 3 dB bandwidth of device 20 measured at the output.

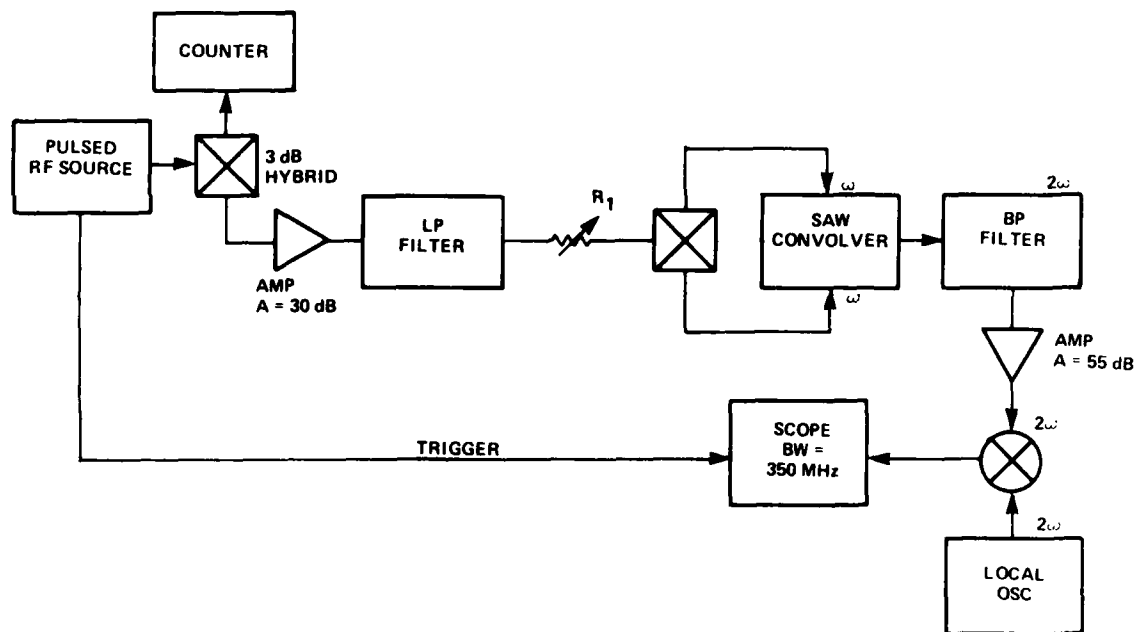


Figure 3.29 Block diagram of bandwidth test setup.

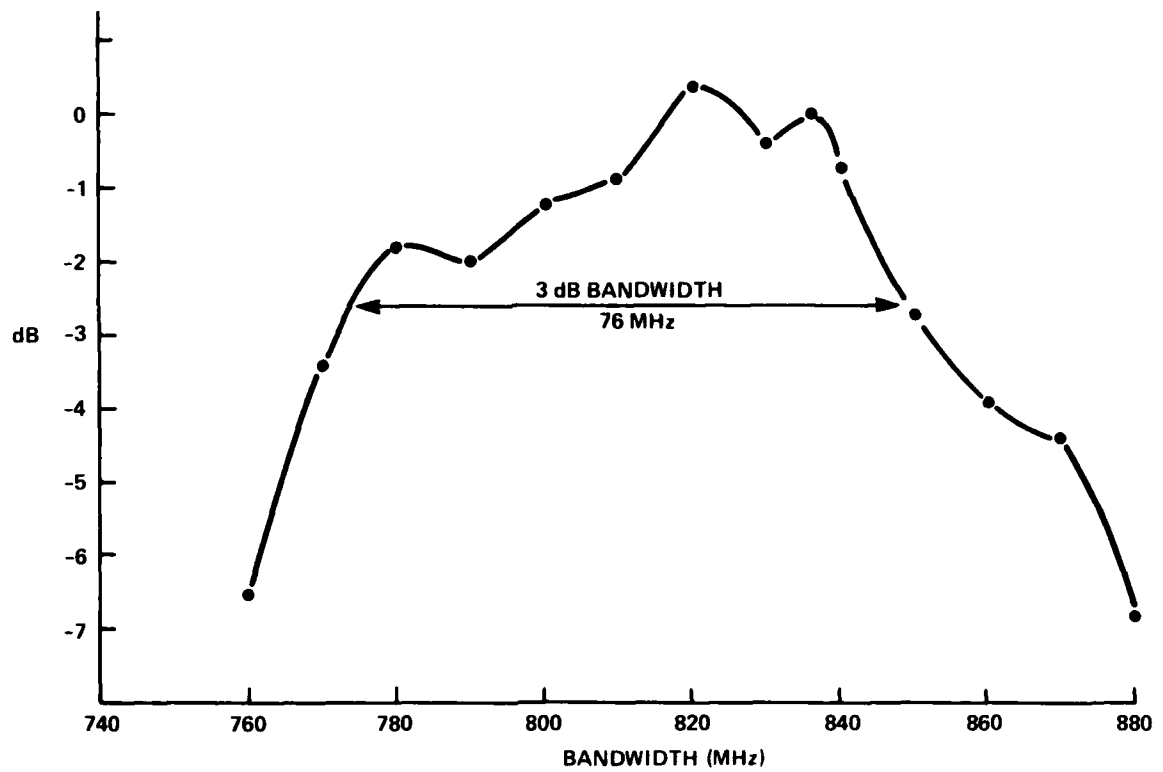


Figure 3.30 3 dB bandwidth of device 21 measured at the output.

Autoconvolution occurs first in time and is usually the stronger spurious. The bottom of Figure 3.24 shows the output of T-CSF when both inputs are uncoded rectangular RF pulses. The desired main peak is off the screen, with the autoconvolution next in time, and the double transit convolution last. Respectively they are -15 dB and -25 dB with respect to the main peak. With one input terminated in 50 ohms, the autoconvolution is -21 dB. For device 20 at 330 MHz, top of Figure 3.31, autoconvolution is -21 dB and double transit is -19 dB. For device 21 at 800 MHz, bottom of Figure 3.31, autoconvolution is -34 dB and double transit is -55 dB. The main peak has been attenuated 34 dB in this figure. There was no attempt to reduce these spurious levels for devices 20 and 21.

There are, however, several possible schemes to reduce these spurious signals. The first is simply for the opposing transducer to have a large insertion loss. A better scheme is to have that transducer fed from a very low impedance^{3.32} such as that of a common base transistor and for the transducer to have double electrode fingers. Autoconvolution can be eliminated by increasing the physical separation from the end of the plate to the transducer to equal one half the plate length. Another scheme is the use of unidirectional transducers (UDT) which provide simultaneously low insertion loss and higher reflection suppression, eliminating the tradeoff in conventional bidirectional transducers. The three principle types of UDT

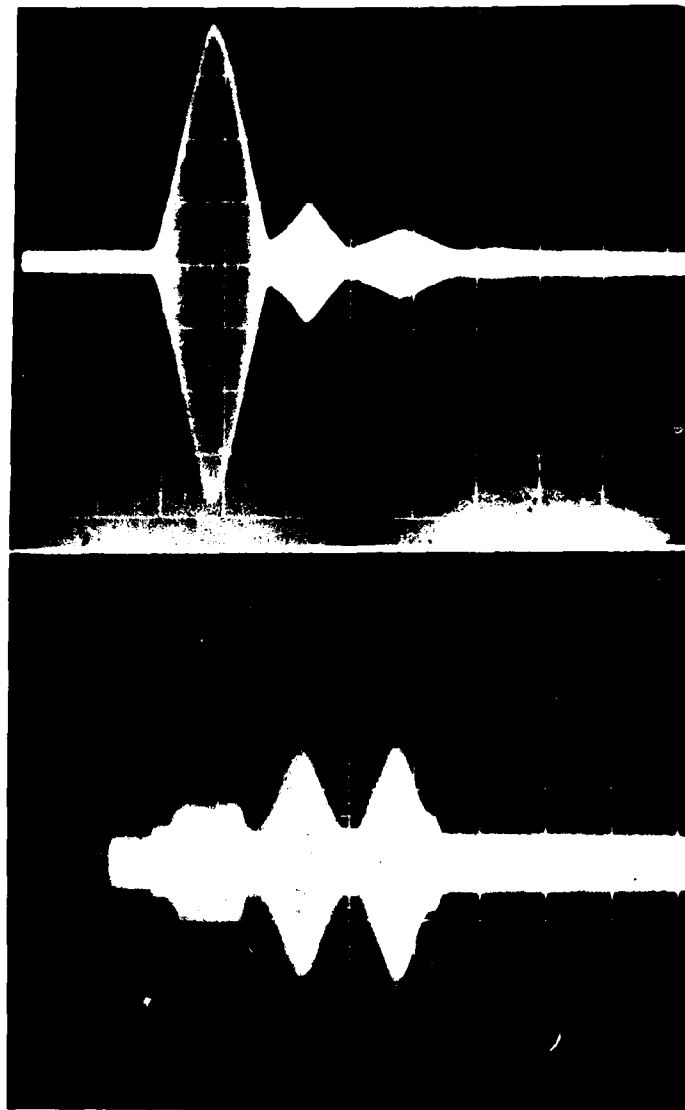


Figure 3.31 (Top) Convolution of two cw RF pulses of 2 μ sec each by device 20 at 330 MHz input frequency. The desired convolution is first, then comes the undesired spurious of autoconvolution and double transit convolution. Horiz. 1 μ sec/div. (Bottom) Convolution of two cw RF pulses of 1.5 μ sec each by device 21 at 800 MHz input frequency. The first (rectangular) pulse is direct RF feed-through. The next signal is the desired convolution but attenuated by 34 dB. Next is autoconvolution. Double transit is not visible.

are (1) a multiphase (usually three-phase) interdigital transducer 3.33 requiring insulated or air-gap crossovers, (2) a multiphase transducer utilizing a meander line running through an interdigital pattern, 3.34 or (3) a bidirectional transducer inside a folded, U-shaped 3 dB multistrip coupler. The transducer may or may not be offset from the center line of the U-shaped pattern. 3.35 The most serious limitation of the UDT is that the bandwidth of the high reflection suppression is much less than the bandwidth of the transducer insertion loss. Yet another scheme for reducing spurious signals involves the multistrip coupler echo trap. 3.36 This requires the addition of a 3 dB multistrip coupler, a transducer, and a variable load at each end of the convolver plate. By appropriate design it can reduce reflections over an octave of bandwidth but adds a 6 dB penalty in dynamic range. Finally, the use of two convolver channels are mentioned, e.g. Figure 3.5. The basic concept here is that one channel has 180 degrees more phase shift than the other. In this scheme the two outputs are fed to a sum/difference hybrid where the desired signals add together and the spurious reflections add 180 degrees out-of-phase. Alternatively this phase shift may be accomplished in the transducers 3.37 or in multistrip couplers if they are used, e.g. Figure 3.5.

3.5 Conclusion

The various loss mechanisms for degenerate elastic SAW convolvers have been investigated. The result has been the presentation of enough data for one to design optimum convolvers with input frequencies in the 300 to 800 MHz range. Convolvers were tested as high as 1 GHz, which is the highest frequency of operation ever reported for a SAW convolver. An upper practical limit seems to be 800 MHz input frequency. This provides the potential for 300 MHz instantaneous bandwidth. As a result the size, weight, and power savings are ten thousand times better than present digital technology. Autoconvolution and double transit convolution are the worst spurious effects. However, the higher attenuation at these frequencies has the benefit of reducing these spurious signals which are the result of reflections. Y,Z lithium niobate is the optimum material when all factors are considered. The aluminum film suppresses harmonics and allows a linear dynamic range up to 1 watt of input power. Beamwidth compressors may not be needed at high frequencies because transducers can be both broadband and have a small aperture. Multimoding effects were not evident in the convolved output. However, longer interaction times and successful achievement of low time sidelobes for coded signals may preclude working at these frequencies depending on the level of mode suppression required.

The convolvers were only 2.5 μ sec long, but using the data presented here, they can be successfully designed and fabricated for longer lengths. Dynamic range is adequate for many applications, and methods are available for reducing the undesired spurious signals.

CHAPTER IV

COLLINEAR MIXING

4.1 Introduction

Although collinear mixing had been demonstrated prior to the effort described in this Chapter,^{4.1-4.3} there were several important questions left unanswered. Could the mixing be made broadband? Was it possible to simultaneously reject all the unwanted non-linear products? How efficient would the mixing be? And finally, what would be the linear dynamic range? The purpose of this chapter was to address these questions in an experimental manner.

The theory describing collinear mixing has already been presented in Section 2.3. This chapter discusses experimental investigations in three parts. Before addressing the above questions, however, Section 4.2 gives laser probe results which allow spatial observation of the mixing products and choice of the optimum location of an output transducer. Section 4.3 then describes the achievement of a broad bandwidth for the difference frequencies and simultaneously the rejection of unwanted signals. Finally, Section 4.4 describes the achievement of a narrow bandwidth for a difference frequency and improved rejection of unwanted signals. Discovery that the mixing process is bilinear makes this device very attractive since

a double-balanced diode mixer is not bilinear.

4.2 Laser Probing of Collinear Mixing

Laser probing of the SAW crystal is schematically depicted in the upper right hand corner of Figure 4.1. The device depicted consisted of two broadband transducers placed very close to each other. Their apertures were each 130 μm . The crystal was Y-cut, Z-propagating lithium niobate (LiNbO_3) and was bare except for the two input transducers. The laser spot may be scanned along the length of the crystal as shown by the arrows, or it may be scanned transversely giving a profile or cross section of the acoustic wave. (Actually the spot is stationary and the crystal is translated). Details of laser probe operation are given in Appendix A, but the essential features are that the laser light is scattered in a unique direction by each acoustic frequency and with an intensity proportional to the intensity of the acoustic signal. This means that the photodetector for the scattered light must be moved to a different angle for each acoustic frequency. Each of the curves in Figure 4.1 gives a one dimensional plot of the signal being probed. This means that at each position on the abscissa, the laser has been scanned transversely to obtain the peak signal at that position. Note that the ordinate gives relative deflected light in dB. This axis could be converted to relative acoustic power by the use of equation (A.7) which scales the axis by a constant. Since

SAW MIXING

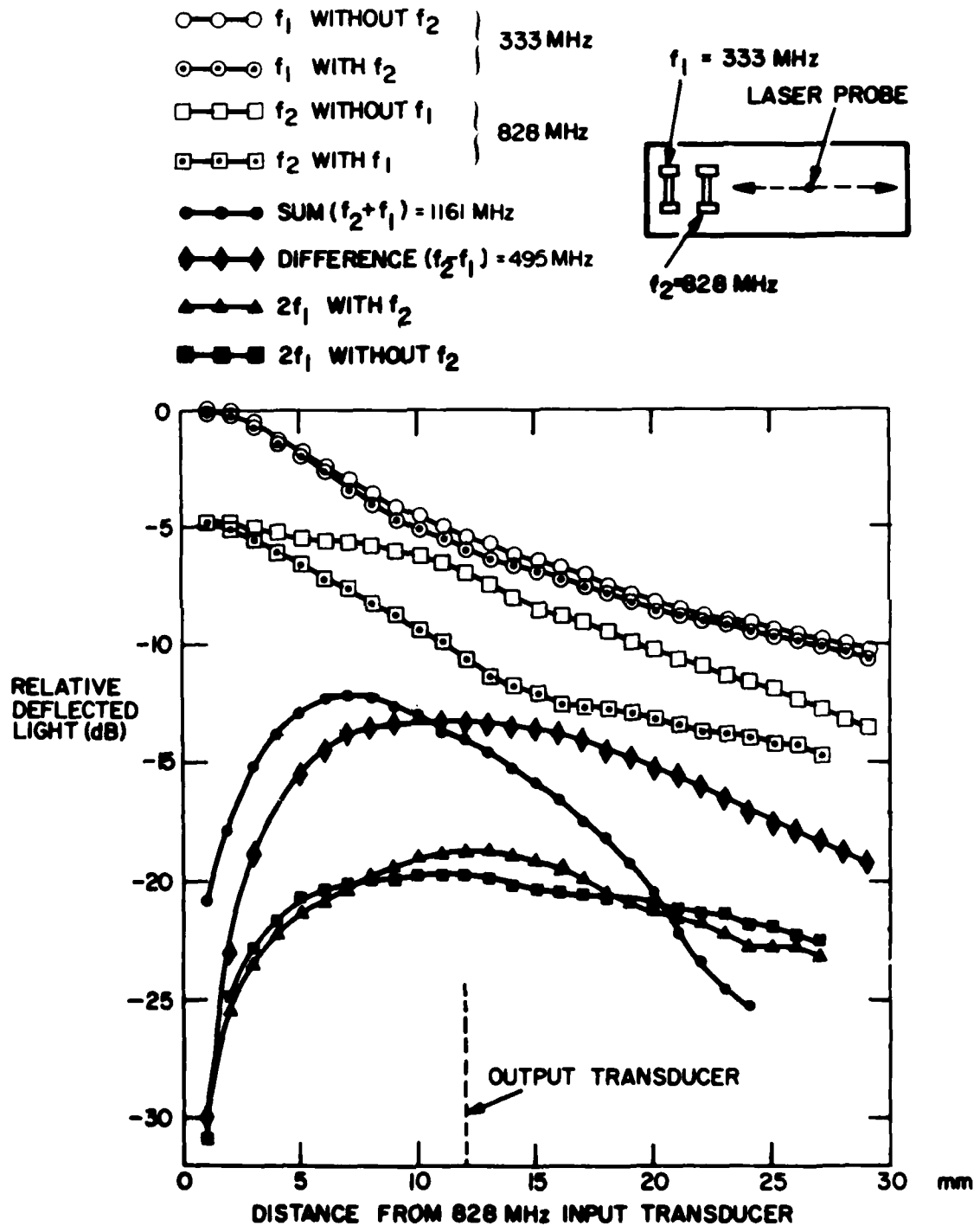


Figure 4.1 Laser probe measurements giving relative power levels versus distance for the two fundamental frequencies and their nonlinear products.

the position of the peaks, general shape of the curves, and other qualitative features are unchanged, this added step was not taken.

Data were taken on signals that consisted of various combinations of two frequencies: f_1 at 333 MHz and f_2 at 828 MHz. If only f_1 is present, then the only possible non-linearities are harmonics of f_1 . If both f_1 and f_2 are present, then additional power can leave f_1 and go into the sum, the difference, and their mixing products. This explains why the light scattered by f_1 has less intensity when f_2 is present. The same argument applies to f_2 . The sum builds up, peaks at 7 mm, and decays sooner than the difference which peaks at 12 mm. This is because the sum has shorter wavelengths and therefore more wavelengths of interaction per distance traveled. The more rapid decay is also due to the shorter wavelength; it has greater attenuation due to propagation loss and is more sensitive to dispersion. As discussed in Section 2.3, the mechanical polish of a bare crystal has enough dispersion to be significant at these frequencies. Also note that the decay slopes are different, the sum having a steeper rate of decay for the reasons mentioned above.

As discussed in Section 2.3, two factors make it difficult to theoretically predict the location of peaks and the slopes of build up and decay: dispersion due to mechanical polish and differences in diffraction of the propagating signals. Since dispersion is related to the

surface polish, it will vary from vendor to vendor, and possibly even from batch to batch. Processes differ markedly, and even the same process may not be repeatable due to size of grit used, amount of fluid used, rate of rotation, pressure applied, and amount of material removed by each successively finer grit. The importance of dispersion at 1800 MHz (second harmonic of a 900 MHz fundamental) has been established by Adler and Nassar^{4.4} and Slobodnik^{4.2}. In order to improve the efficiency of the non-linear processes, the transducer apertures of the device used in this study were made small to increase the acoustic power densities. However, since aperture size strongly affects diffraction, a trade-off is necessary. The diffraction is worse for the lower frequency transducer since they both have a 131 μ m aperture. For this particular device, the 333 MHz signal diffracted severely, and the 828 MHz signal diffracted very little. This is shown in Figure 4.2. The result is decreased interacting efficiency for propagation distances greater than 5 mm. If one wanted to measure the effect of dispersion, it would be necessary to use the second harmonic of one signal rather than a mixing product of two signals because the two signals would both be diffracting.

Returning to Figure 4.1, the second harmonic of f_1 has two curves for the same reason the fundamental of f_1 has two curves. When f_2 is present, some of the f_1 power goes into sums and differences and less is available to generate

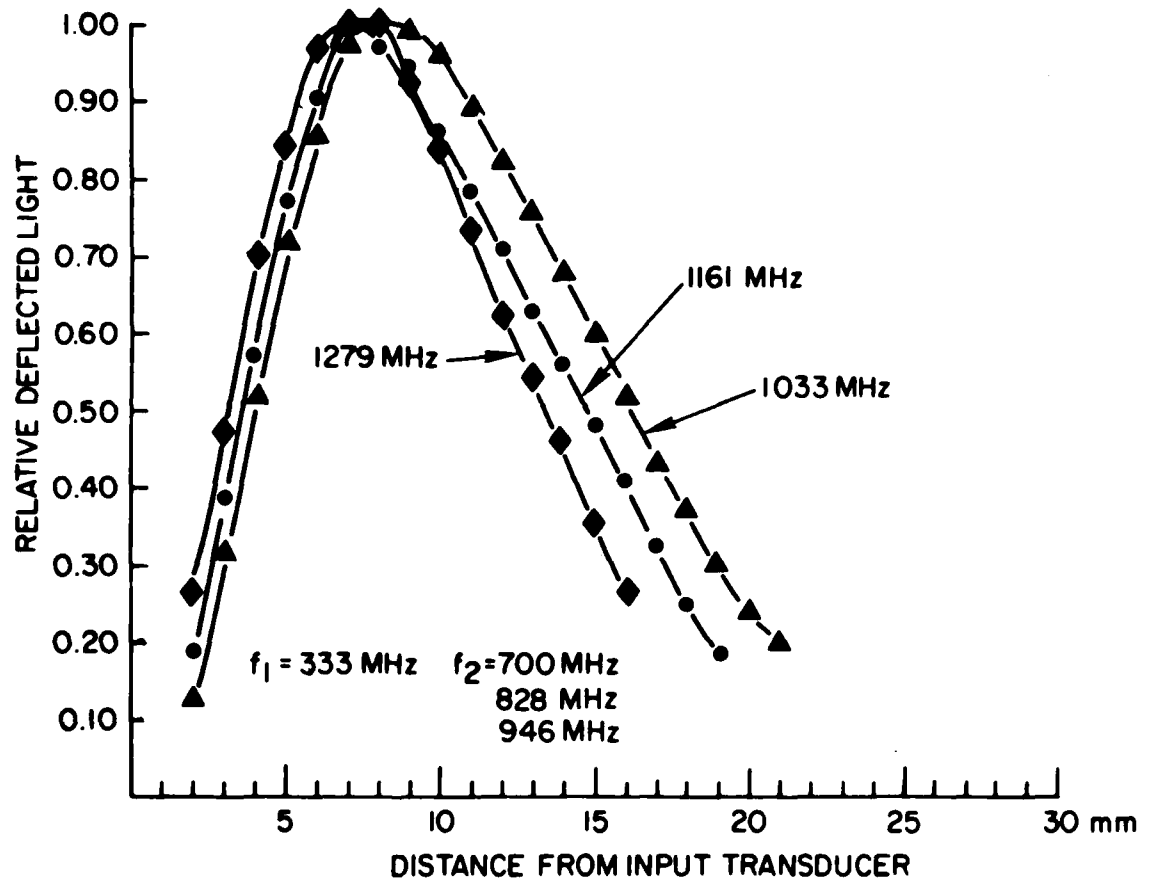


Figure 4.2 Laser probe measurements giving relative power levels versus distance for three different sum frequencies on the same crystal.

a second harmonic. The sum signal is stronger and occurs sooner than the difference signal. Thus, it is primarily the sum signal that prevents the peak of the second harmonic of f_1 from occurring as soon as when f_2 is absent.

The relative amplitudes of the various products are power dependent. A square law dependence is assumed and is shown in Section 4.4 to be an excellent approximation. Square law dependence means that if the power, P_1 , of f_1 were doubled, its second harmonic would be quadrupled (6 dB), the sum of f_1+f_2 would double (3 dB), and the difference would double (3 dB). This happens because the harmonic is proportional to P_1^2 and the sum and difference are proportional to $P_1 P_2$. This result implies that eventually the non-linear product could be higher than the signal generating it. Of course that cannot happen because saturation of the crystal, a physical limit on the elastic constants, occurs first. In the SAW device of this study, the 828 MHz transducer burned out before the crystal saturated. Burnout is catastrophic failure due to arcing between interdigital fingers and occurred at about 400 mw. The 333 MHz transducer withstood 1 watt because it had more interdigital fingers and hence less current density per finger.

The next investigation was of spatial variation of sum and difference frequencies as one of the input frequencies was varied. The spatial dependence of the sum frequencies is displayed in Figure 4.2. The three curves

were generated from the same crystal. Frequency limits were imposed by the transducer bandwidths and interference from reflected sidelobes of other signals. Nonetheless, one can see that the peak is stable at 7.5 mm over a bandwidth of 246 MHz, and the slopes of decay show the expected frequency dependence. In Figure 4.3, the spatial dependence of difference frequencies is shown for the same device and input transducers. The peak is stable at 11.5 mm over a bandwidth of 188 MHz, and again the slopes of decay show the expected frequency dependence. Finally, refer to Figure 4.4. The results were obtained with a crystal from a different batch. The vendor and polishing specifications were the same, but the crystal had been purchased several years earlier. Also, the transducers were different. The presence of additional dispersion causes the difference signal of 568 MHz to peak sooner than the difference signal of 615 MHz in Figure 4.3. And the sum of 1312 MHz peaks much sooner than the sum of 1279 MHz in Figure 4.2. Also, the sum shows a second peak characteristic of a traveling wave in the presence of dispersion.^{4.3-4.5}

In terms of a practical device, the placement of the output transducer is not critical, for example, if one can tolerate a 3 dB loss, then a difference signal can be obtained from a transducer located anywhere in the range of 5 to 20 mm from the input transducer for either the device of Figure 4.3 or Figure 4.4. In a production environment, this tolerance would be more than adequate.

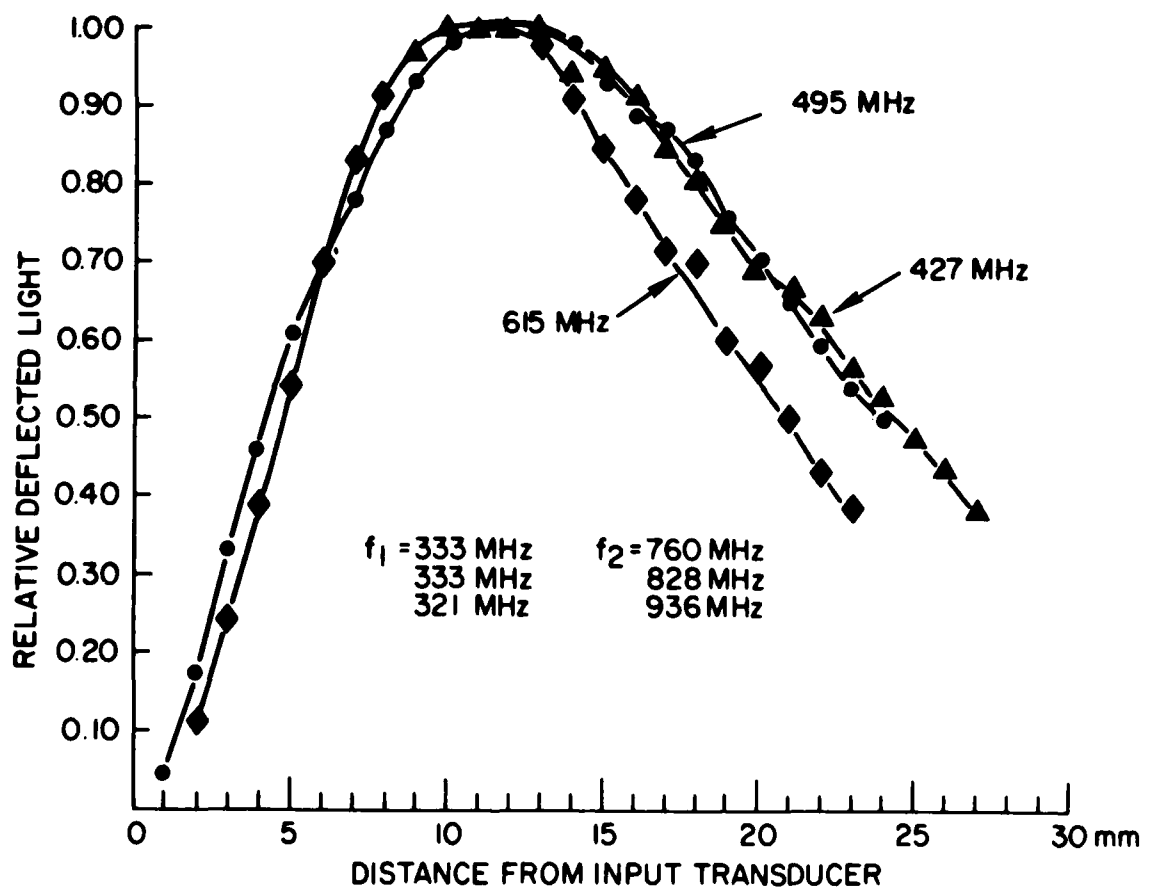


Figure 4.3 Laser probe measurements giving relative power levels versus distance for three difference frequencies on the same crystal.

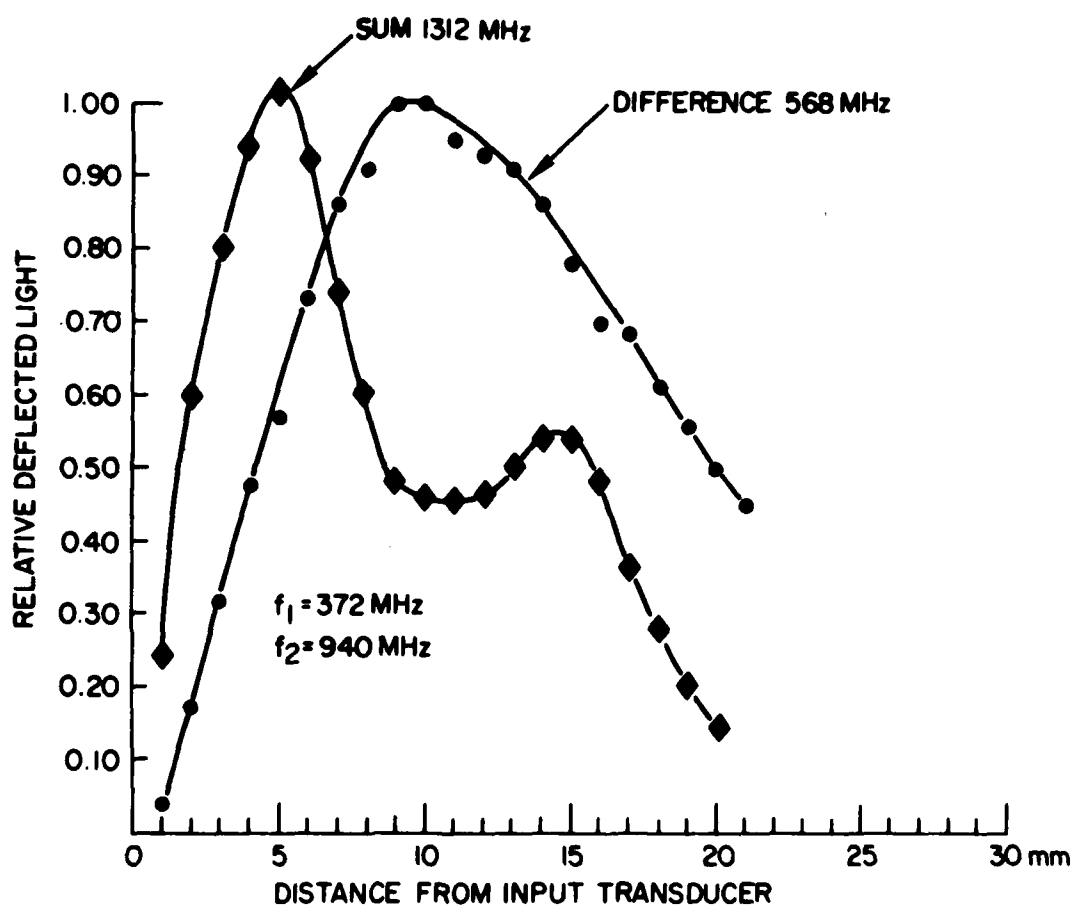


Figure 4.4 Laser probe measurements giving relative power levels versus distance for a sum frequency and a difference frequency on a crystal different from the crystal used in Figure 4.2 and 4.3.

4.3 Broadband Mixing

This section describes the use of a SAW mixer to replace a double-balanced diode mixer and filters in an existing system.^{4.6} The frequency requirements are shown in Figure 4.5. The first input band of frequencies, f_1 , covers 321 to 345 MHz, and the other input band, f_2 , covers 720 to 936 MHz. It is desired to pass the difference frequencies and reject all others by 60 dB. This is a very demanding goal since the signals f_1 and $2f_1$ are very close-in, and f_1 is much stronger (37 dB in Figure 4.8) than the desired difference signal. This means 60 dB of attenuation for unwanted acoustic signals at the output and over 97 dB suppression of direct electromagnetic feedthrough at the output.

Assuming the performance goals can be met, the benefits of such a device are reduced size and cost, and improved ruggedness. The size advantage is shown in Figure 4.6 by comparing 6 SAW mixers on one substrate to the equivalent combination of a double-balanced diode mixer and tubular bandpass filter. Actually the tubular bandpass filter needs several more sections to achieve the system requirement of 60 dB suppression for all unwanted signals. The SAW cost and ruggedness advantages result from the use of planar construction and fabrication techniques similar to those used to fabricate integrated circuits. A close-up view of the SAW mixers is given in Figure 4.7. Four of the channels are 12 mm in length; the other two are 14 mm in

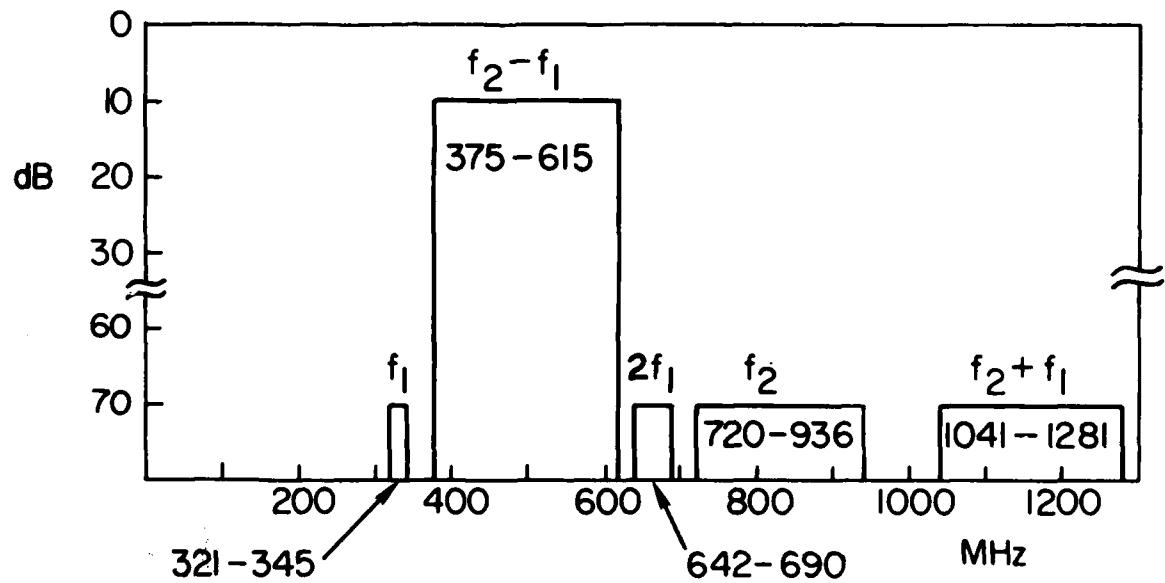


Figure 4.5 Desired frequency spectrum of the output for the mixer discussed in this section.

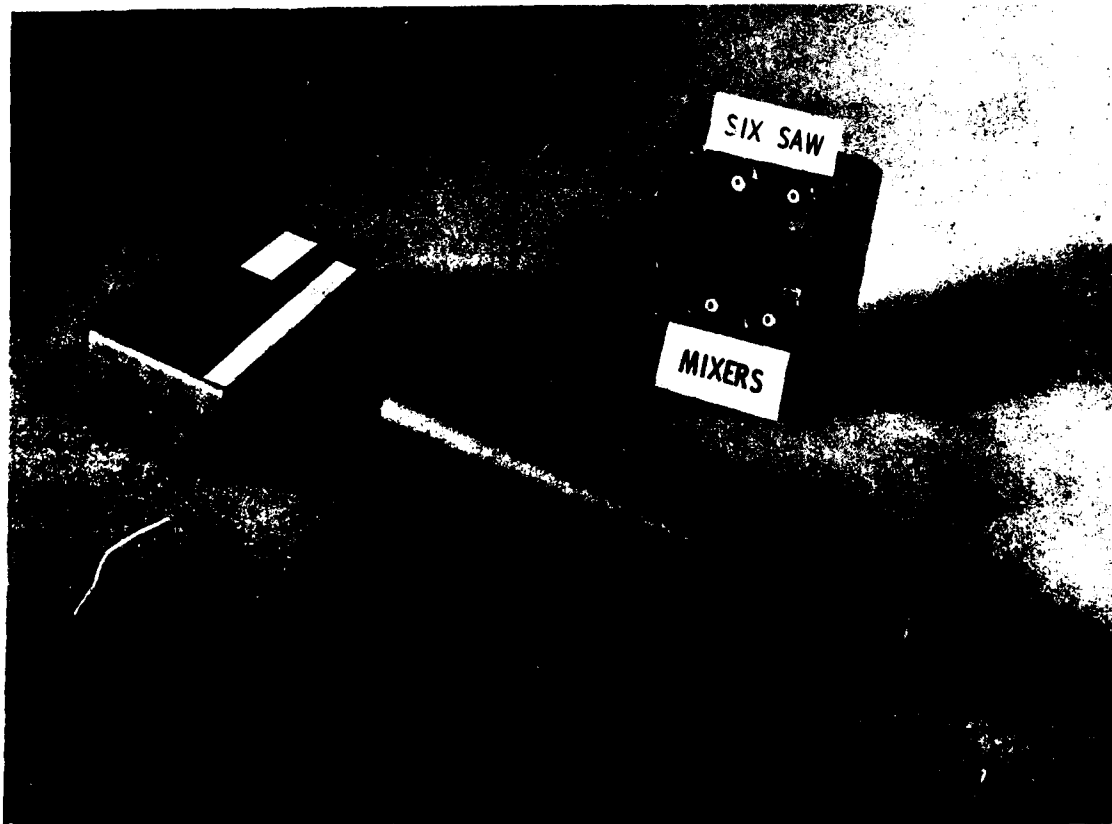


Figure 4.6 Comparison of a conventional double balanced diode mixer and tubular bandpass filter with six equivalent SAW mixers.

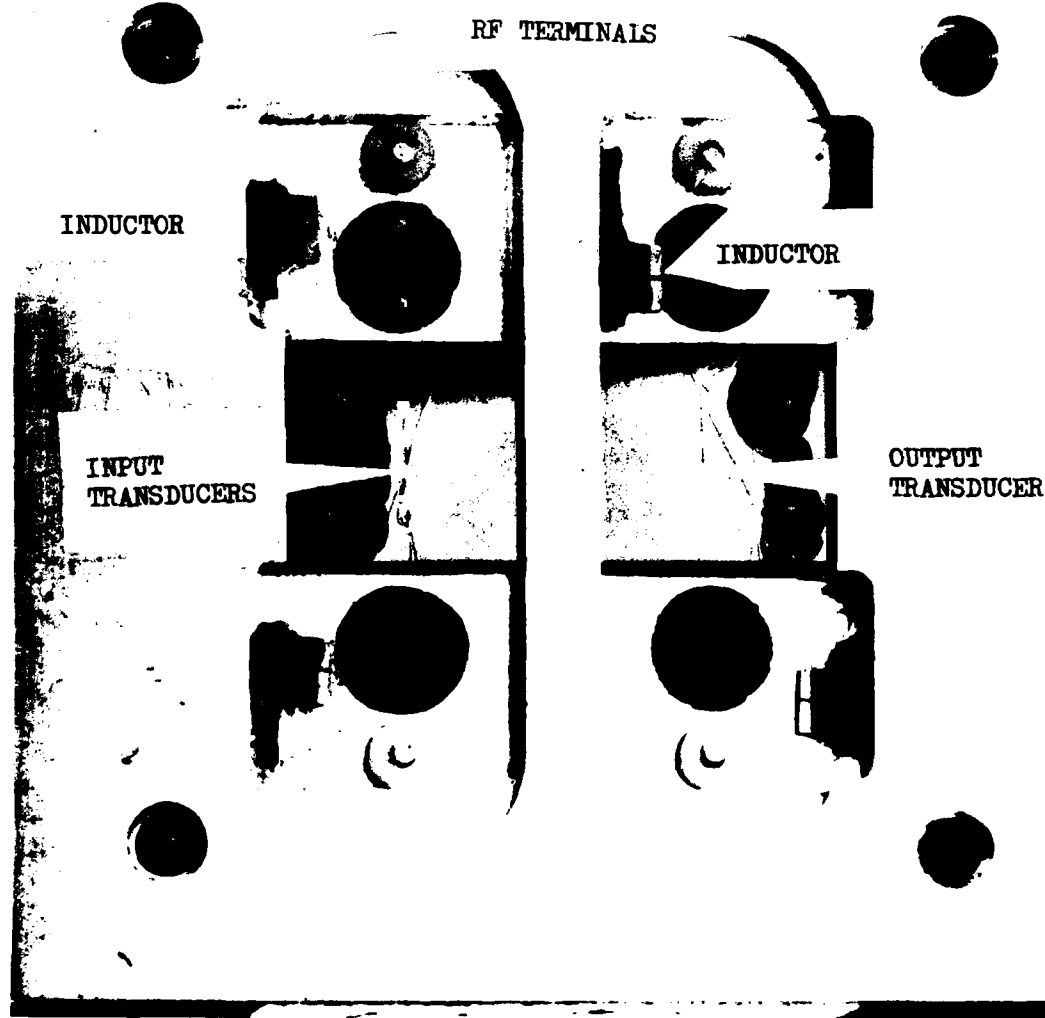


Figure 4.7 Closeup of the six SAW mixers. There are four channels of 12 mm length and two channels of 14 mm length.

length. The entire fabrication process consists of one aluminum evaporation to deposit the transducers on the bare piezoelectric substrate. Several types of inductors are in evidence; they are used to tune out the capacitance of the transducers in order to achieve a minimum insertion loss.

Figure 4.8 is a schematic representation of a single-channel mixer. Y,Z LiNbO₃ was chosen for its low insertion loss and large fraction bandwidth due to high piezoelectric coupling and for its relatively efficient mixing.^{4.1-4.5} The input frequencies were chosen, as explained above, to be compatible with an existing system. The sum frequency could have been used just as well, but it was not, only because of the system requirement. The first experiment yielded the results shown in Figure 4.9. The values are the same as shown in Figure 4.8 except f_1 is 321 MHz instead of 318 MHz and its input power is 4 mw instead of 20 mw. The null in the f_2 band results from the first upper null in the broadband output transducer.

The results shown in Figure 4.10 correspond to the schematic of Figure 4.8. The major difference between the first experiments and this experiment is the addition of a periodic grating with 160 lines in the path of the acoustic signal located just in front of the output transducer. This grating is shown schematically in Figure 4.8 as five vertical lines. The grating was originally designed to be a multistrip coupler,^{4.7,4.8} but is being used here simply as a frequency dependent mass loading to damp the higher

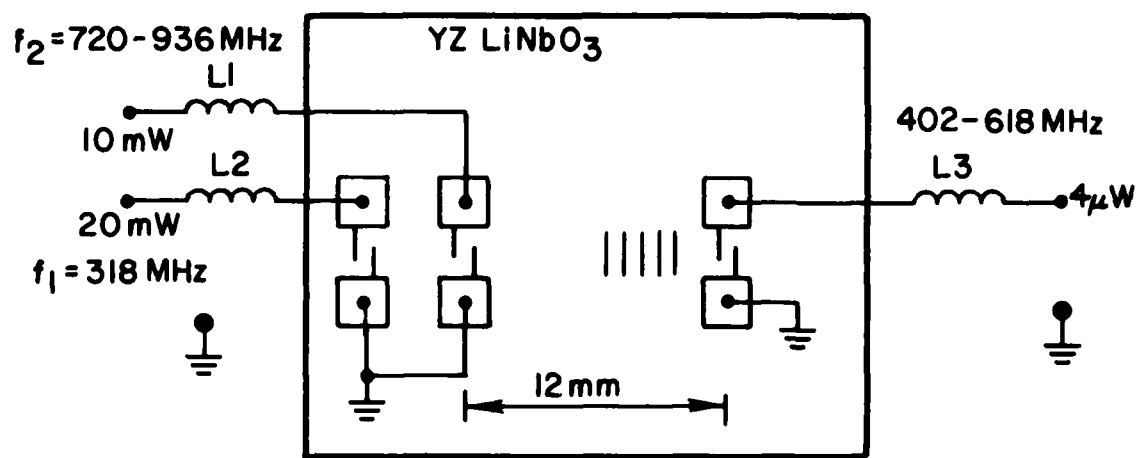


Figure 4.8 Schematic representation of the single channel mixer.

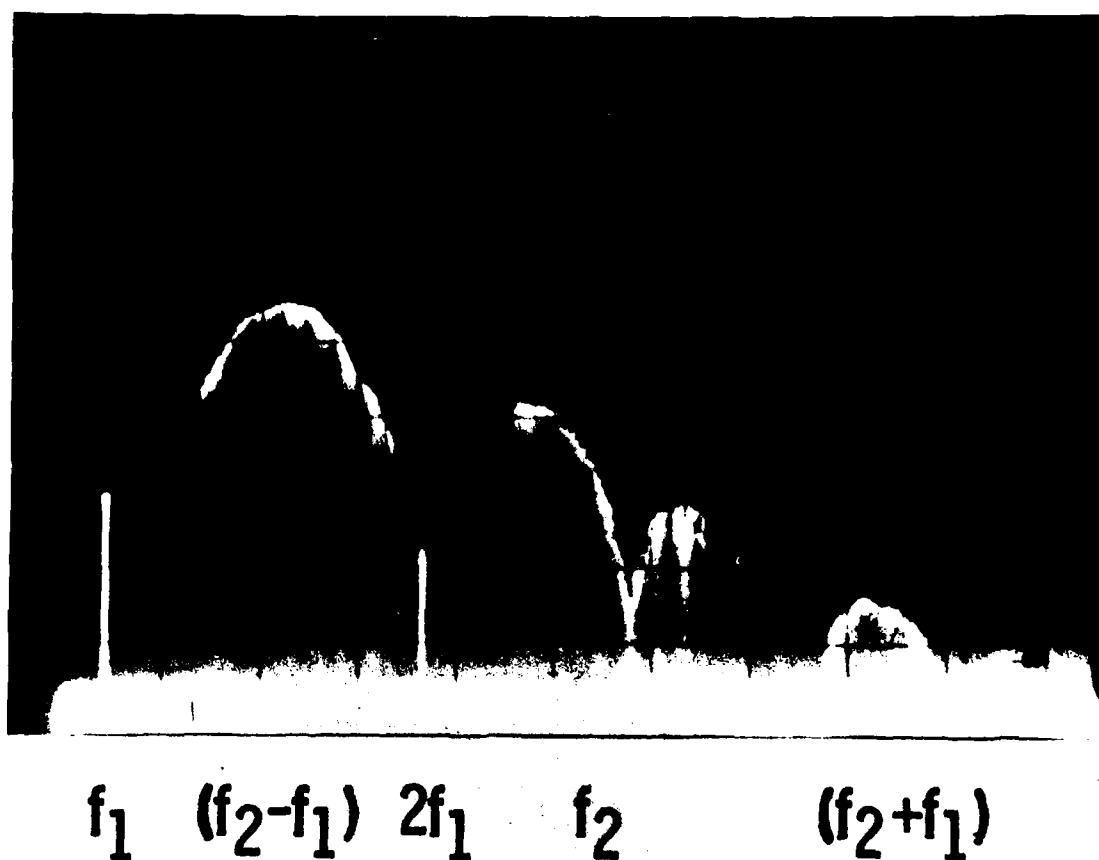


Figure 4.9 Output of single channel mixer seen by a spectrum analyzer with cross-hatched center frequency (f_0) of 700 MHz, Horiz. 100 MHz/Div. and Vert. 10 dB/div. (amplitudes are relative), f_1 is 321 MHz, f_2 is 720-936 MHz, and $(f_2 - f_1)$ is 402-618 MHz. P_1 is 4 mw, and P_2 is 10 mw.

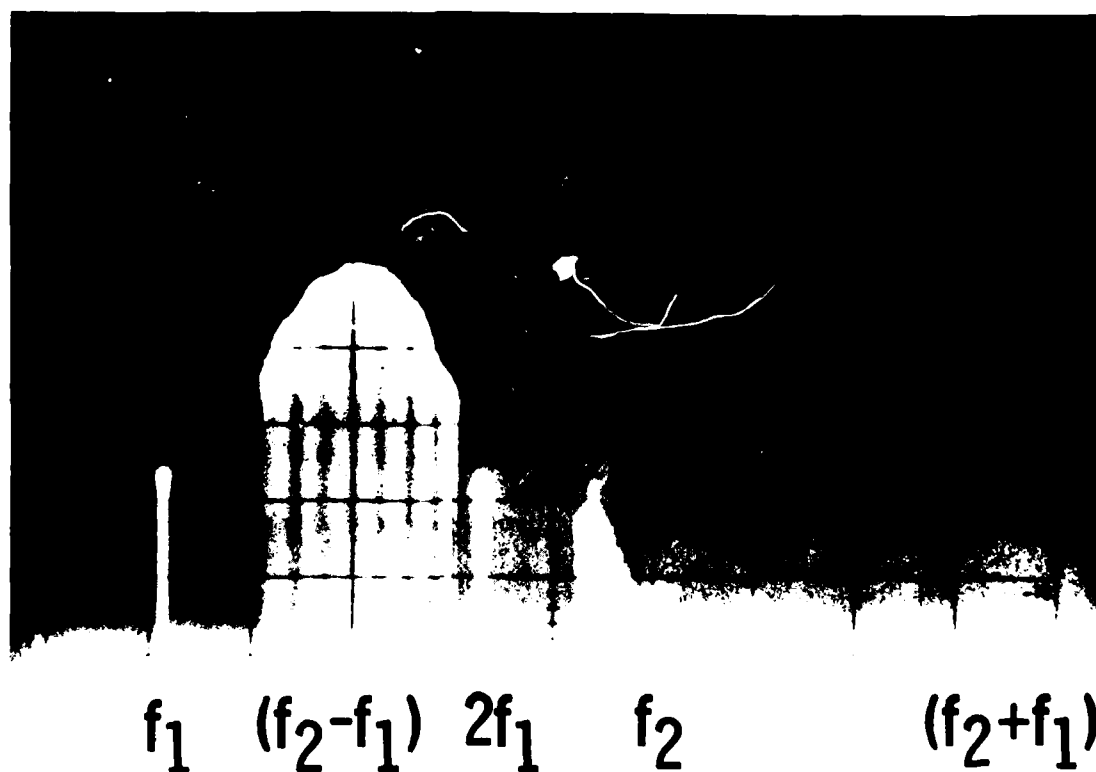


Figure 4.10 Same as Figure 4.9 except f_1 is 318 MHz and 20 mw as shown in Figure 4.8. The main difference is the addition of a grating in the SAW propagation path which has significantly reduced f_2 and $(f_2 + f_1)$.

frequencies; f_2 and (f_2+f_1) . The grating's synchronous frequency is about 770 MHz. Above this frequency it creates more loss (in addition to simple mass loading) by converting a significant amount of surface waves into bulk modes.^{4,9} These bulk modes, however, are at a high enough frequency not to interfere with the desired difference frequency. The 3 dB bandwidth for the desired difference frequency (402-618 MHz) is 20 percent. The low frequency input (f_1) is suppressed 26 dB relative to the difference frequency (f_2-f_1); f_2 is suppressed 27 to 45 dB, and the sum frequency (f_2+f_1) is suppressed more than 52 dB. A third order intermodulation product (not visible in this picture) does exist within the desired passband, but is suppressed by more than 50 dB. All unwanted frequencies are due to acoustic energy detected by the output transducer and not due to electromagnetic leakage. The added attenuation due to the grating was 2 dB in the desired passband (f_2-f_1), 4 to 8 dB for f_2 , and greater than 8 dB for the sum frequency (f_2+f_1). Location of the grating is not critical but should be near the output transducer so the input frequency (f_2) is not attenuated until mixing has been accomplished. Note that this mixer gives better suppression of f_2 and (f_2+f_1) than did the mixer of Figure 4.9.

Center-to-center spacing of the input transducers is not critical, and the 12 mm spacing of input to output transducer was determined from the laser probe results. In all cases transducer apertures were 131 μ m which is

relatively small but necessary, because high acoustic power density is needed for mixing. The limit on aperture smallness is imposed by diffraction and by increased insertion loss of the transducers. The transducer capacitive reactance can be tuned out, but the radiation resistance becomes too large to match into a 50 ohm system. The low frequency transducer was placed behind the high frequency transducer (Figure 4.8) to minimize the SAW attenuation.

Figure 4.11 gives a schematic representation of the dual channel mixer circuit. The purpose of this approach was to achieve wider bandwidth by using output transducers with staggered center frequencies. Inductor L_3 was chosen to tune out the transducer capacitance below the synchronous frequency of its transducer, and L_4 was chosen to tune out the transducer capacitance above the synchronous frequency of its transducer. This is similar in principle to stagger tuning common in radio and television IF strips. This approach is different from broadband matching of microwave circuits reported by others^{4.10-4.12} in that the transducer matching elements occur before the electrical interconnection rather than after. This gives two distinct advantages. First, the required discrete matching elements are of practical size for UHF and higher frequencies, and second, much sharper out-of-band roll-off is realized, i.e., better shape factor. However, there are several problems with this approach. The primary one is the phase difference

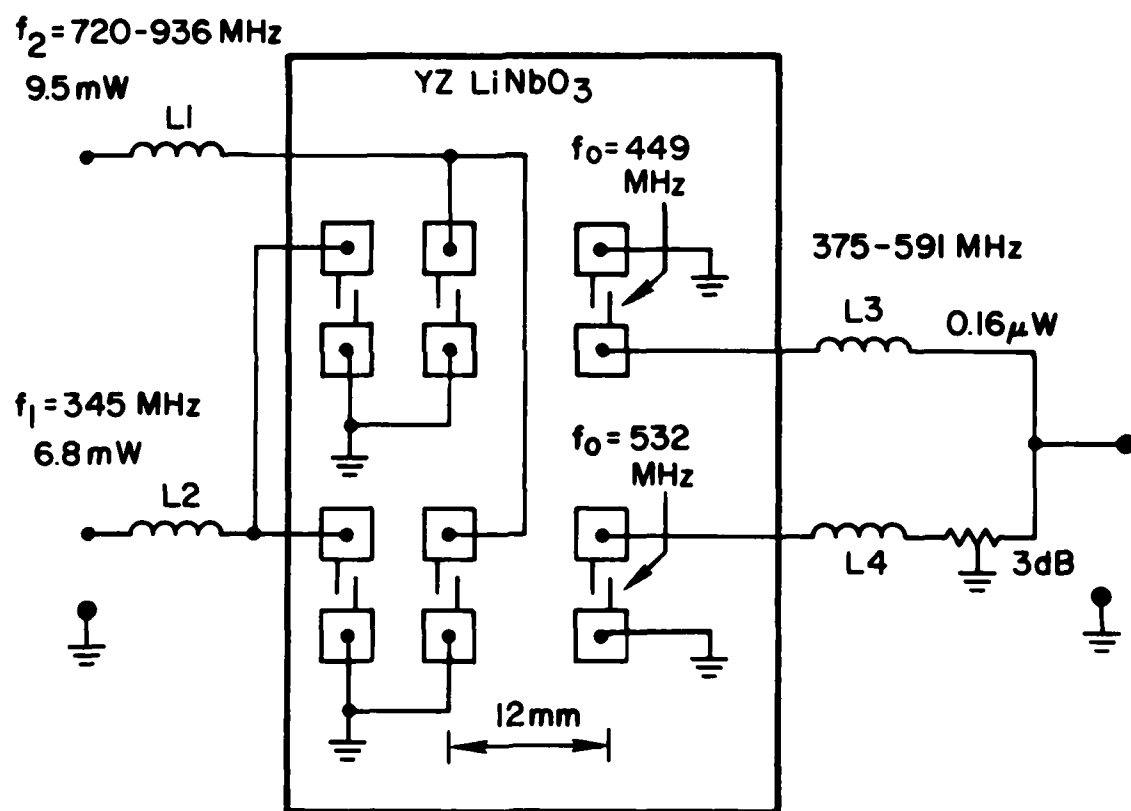


Figure 4.11 Schematic representation of the dual channel mixer.

that results from L_3 and L_4 in combination with their respective transducers having different impedance values. This filter approach is described in more detail in Appendix C. The 3 dB pad was used because one channel was stronger than the other. This is not a recommended practice since both channels are attenuated. It is better, but more time consuming, to vary values of L_3 and L_4 . This mixer contained a grating in each channel as described for the single channel mixer. The performance of the device is given in Figure 4.12. The 3 dB bandwidth is 36 percent. Isolation was 43 dB for f_2 at the f_1 port (RF-LO) and 27 dB for f_1 at the f_2 port (LO-RF).

In order to achieve additional spurious suppression, a SAW filter was added. It, too, was a dual channel design with input and output nearly identical to the output portion of the dual channel mixer shown in Figure 4.11. Again, refer to Appendix C for more details on the filter. The final composite device is shown in Figure 4.13; the performance is given in Figure 4.14. The 3 dB bandwidth is 31 percent, and all spurious signals are suppressed by at least 54 dB. By using a SAW filter, it is implied that both mixer and filter (and other SAW devices) could be fabricated on the same substrate.

The electromagnetic output power (P_-) of a mixer can be expressed as a constant times the product of the input powers (P_1, P_2):

$$P_- = F_{\text{ext}} P_1 P_2 \quad (4.1)$$

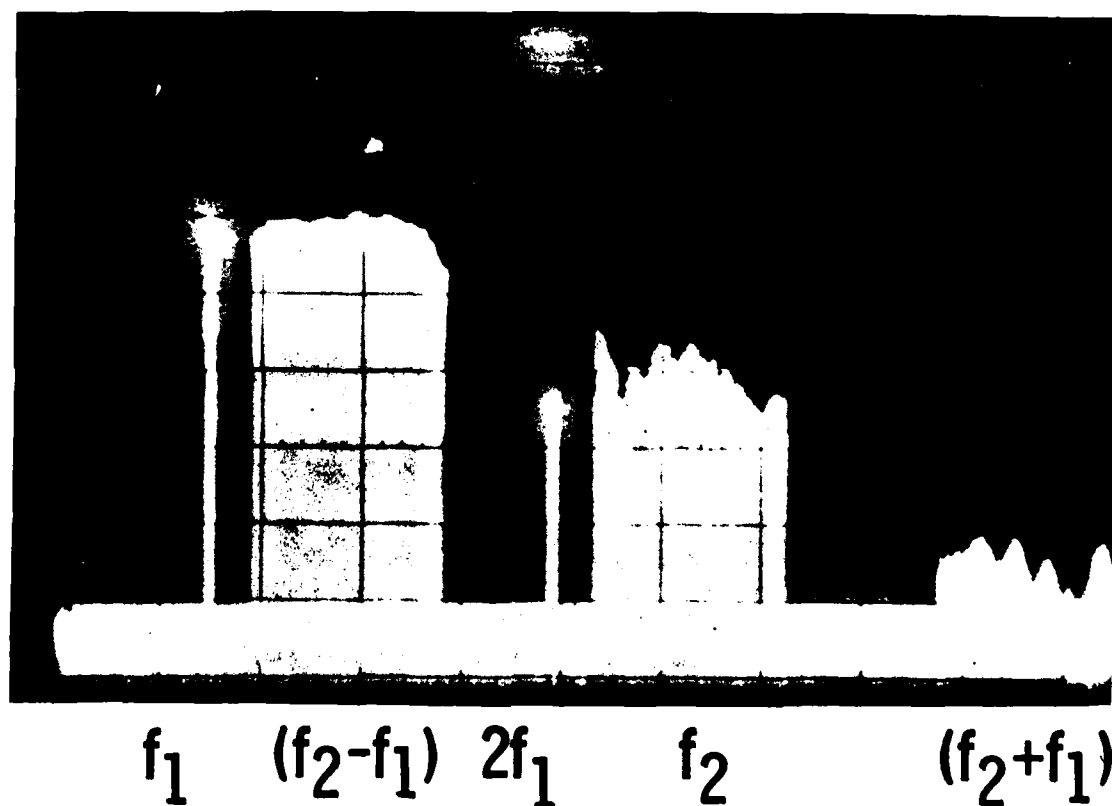


Figure 4.12 Output of dual channel mixer with cross-hatched center frequency (f_0) of 700 MHz, horizontal scale of 100 MHz/div. and vertical scale of 10 dB/div. (amplitudes are relative). f_1 is 345 MHz, f_2 is 720-936 MHz, and $(f_2 - f_1)$ is 375-591 MHz.

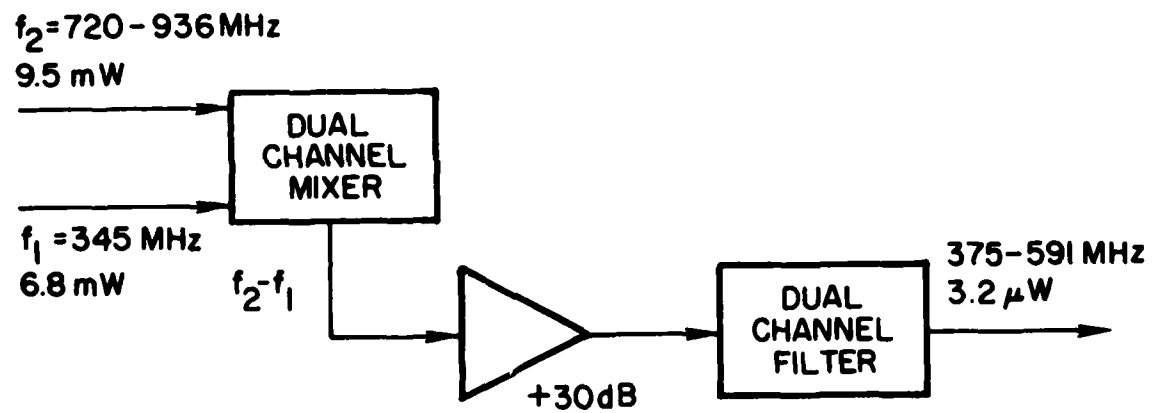


Figure 4.13 Schematic representation of the final device: dual channel mixer plus amplifier plus dual channel SAW filter.

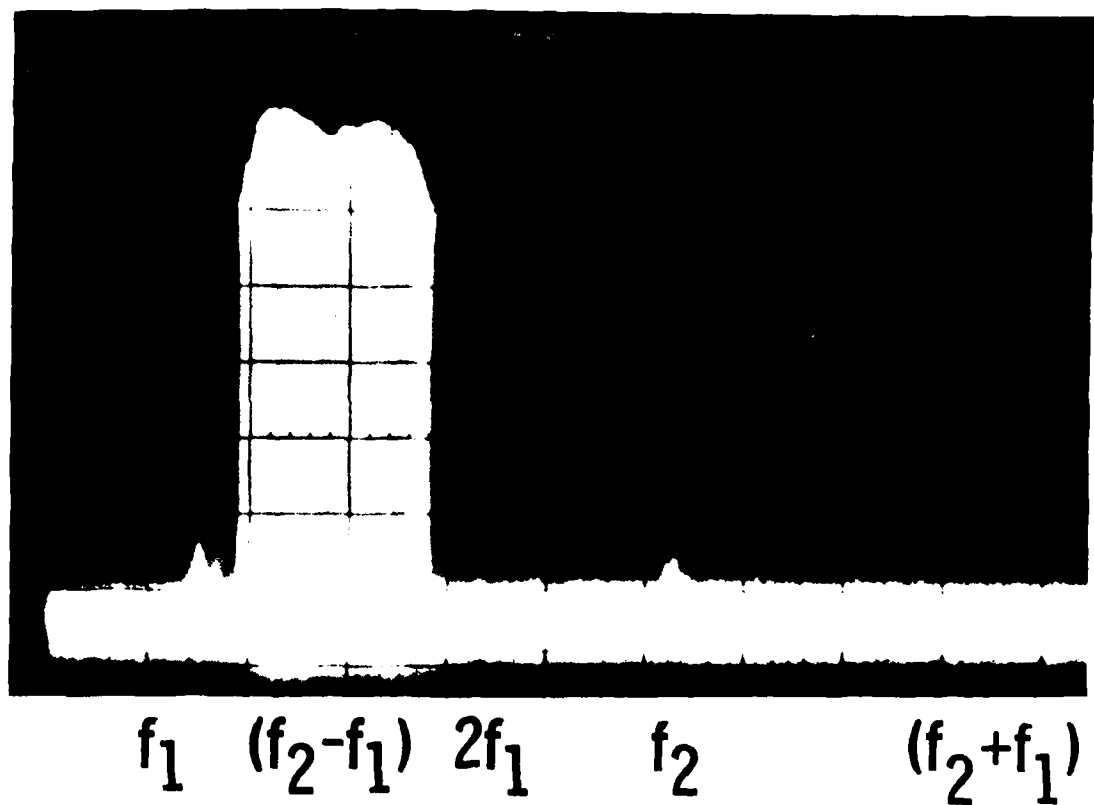


Figure 4.14 Output of final device: dual channel mixer plus amplifier plus dual channel SAW filter. Cross-hatched center frequency (f_0) is 700 MHz, horizontal scale 100 MHz/div. and vertical scale 10 dB/div. (amplitudes are relative). f_1 is 345 MHz, f_2 is 720-936 MHz, and (f_2-f_1) is 375-591 MHz.

F_{ext} is called the F factor and gives a measure of the efficiency. It is also useful to know this constant for the acoustic case, i.e., with the insertion loss (IL) of the transducers removed. This case is described as:

$$F_{int} = F_{ext} - (IL_{-} + IL_1 + IL_2) \quad (4.2)$$

(Note: This form of the equations requires the F factors to be in dBm and IL to be in dB). Insertion loss for the transducers used in the single channel mixer (Figure 4.8) and the dual channel mixer (Figure 4.11) are given in Table 4.1. F_{ext} and F_{int} and corresponding conversion losses are given in Table 4.2. According to convention, the LO is a fixed frequency (f_1), with power P_1 , and the RF is the wide band signal (f_2), with power P_2 . Then using the conventional definition, conversion loss is:

$$CONV. LOSS_{EM} (dB) = 10 \log_{10} (P_{-}/P_2). \quad (4.3)$$

This can also be calculated for the acoustic case as:

$$CONV. LOSS_{AC} (dB) = CONV. LOSS_{EM} - (IL_{-} + IL_2) \quad (4.4)$$

It is interesting to note that F_{int} for the dual channel mixer is about 3 dB less than that of the single channel mixer. This is because the efficiency is proportional to the input powers ($P_1 P_2$), which are split between the two channels. Finally we see that the double balanced diode mixer is a more efficient device. This means the acoustic mixer must have an amplifier to make up the difference and probably limits its use to cases where it can be integrated with other acoustic devices on the same substrate or where its bilinearity properties are required. (Bilinearity is

	IL_1	IL_2	IL_-	
SINGLE CHANNEL	-4.4	-5.2	-5.4	dB
DUAL CHANNEL	-3.9	-8.7	-8.8	dB

Table 4.1 Insertion losses of transducers used in SAW mixers of Section 4.3.

	ELECTROMAGNETIC		ACOUSTIC	
	F_{ext} (dBm)	CONV. LOSSEM (dB)	F_{int} (dBm)	CONV. LOSS _{AC} (dB)
SINGLE CHANNEL	-47	-34	-32	-23.4
DUAL CHANNEL	-56	-47.7	-34.7	-30.3
DOUBLE BALANCED DIODE	-14.5	-7.5		

Table 4.2 Conversion loss for SAW and diode broadband mixers.

described in the next section).

In summary, this section has described a SAW mixer used as a down-converter at UHF with 36 percent bandwidth. By adding an additional SAW filter, all spurious signals were reduced more than 54 dB, while maintaining a 31 percent bandwidth.

4.4 Narrow Band Mixing and Bilinearity

In certain signal processing schemes, such as the chirp transform, it would be advantageous to use a bilinear mixer, i.e. a device in which the output varies linearly when both input (f_1 and f_2) power levels change. Conventional double-balanced diode mixers do not have this property; however, this author discovered that the Surface Acoustic Wave (SAW) mixer is bilinear over 60 dB of dynamic range. This mixer can also be used in a UHF superheterodyne radio where two broadband inputs track together to produce a constant (narrow band) IF frequency output.

A SAW mixer was built and tested on Y,Z lithium niobate with f_1 of 510 MHz at +23 dBm and f_2 of 838 MHz at +26 dBm. The desired difference frequency ($f_2 - f_1$) had over 65 dB dynamic range with electromagnetic conversion loss of 42 dB and acoustic conversion loss of 19 dB. The strongest spurious signal was suppressed 33 dB, and all other spurious signals were at least 55 dB below the desired difference signal.

A schematic of the device is shown in Figure 4.15.

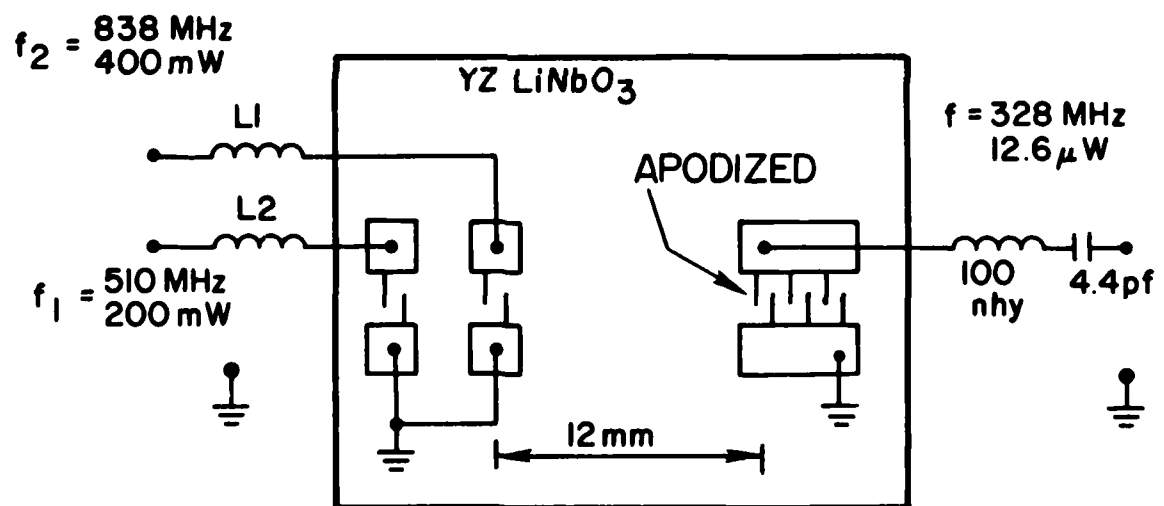


Figure 4.15 Schematic of bilinear SAW mixer. The difference frequency is passed by the apodized and narrow band matched output filter.

Collinear propagating surface acoustic waves are launched from each input transducer at frequencies f_1 and f_2 . As discussed previously, the position of the maximum for the desired sum or difference signal is determined by laser probing and is a function of frequency. The maximum for the difference signal occurred at 12 mm, but the maximum is broad enough that plus or minus 2 mm in transducer location is usually permissible for either the sum or difference signal - see Figures 4.1 and 4.3.

Figure 4.15 shows the simulation of a superheterodyne radio with two broadband inputs (RF and LO) that track together to produce a constant IF frequency of 328 MHz. The input bandwidths were only 10 percent and 13 percent, but it is quite easy to get 40 percent with this type transducer and a quarter wave impedance inverter/transformer^{4.13} on microstrip. It should also be noted that the SAW mixer can have two broadband inputs not tracking together and a broadband output as has been demonstrated in Section 4.3.

The SAW mixer was first tested (Figure 4.16) by holding the LO at a fixed level and then varying the RF. Then the RF was held at a fixed level and the LO varied. In both cases the device was linear within the experimental error. The same was done for an off-the-shelf double-balanced diode mixer. It, too, was linear and showed that the RF and LO can be interchanged while observing certain power limitations. However, when both input levels were varied (Figure 4.17) the SAW mixer was bilinear, but the

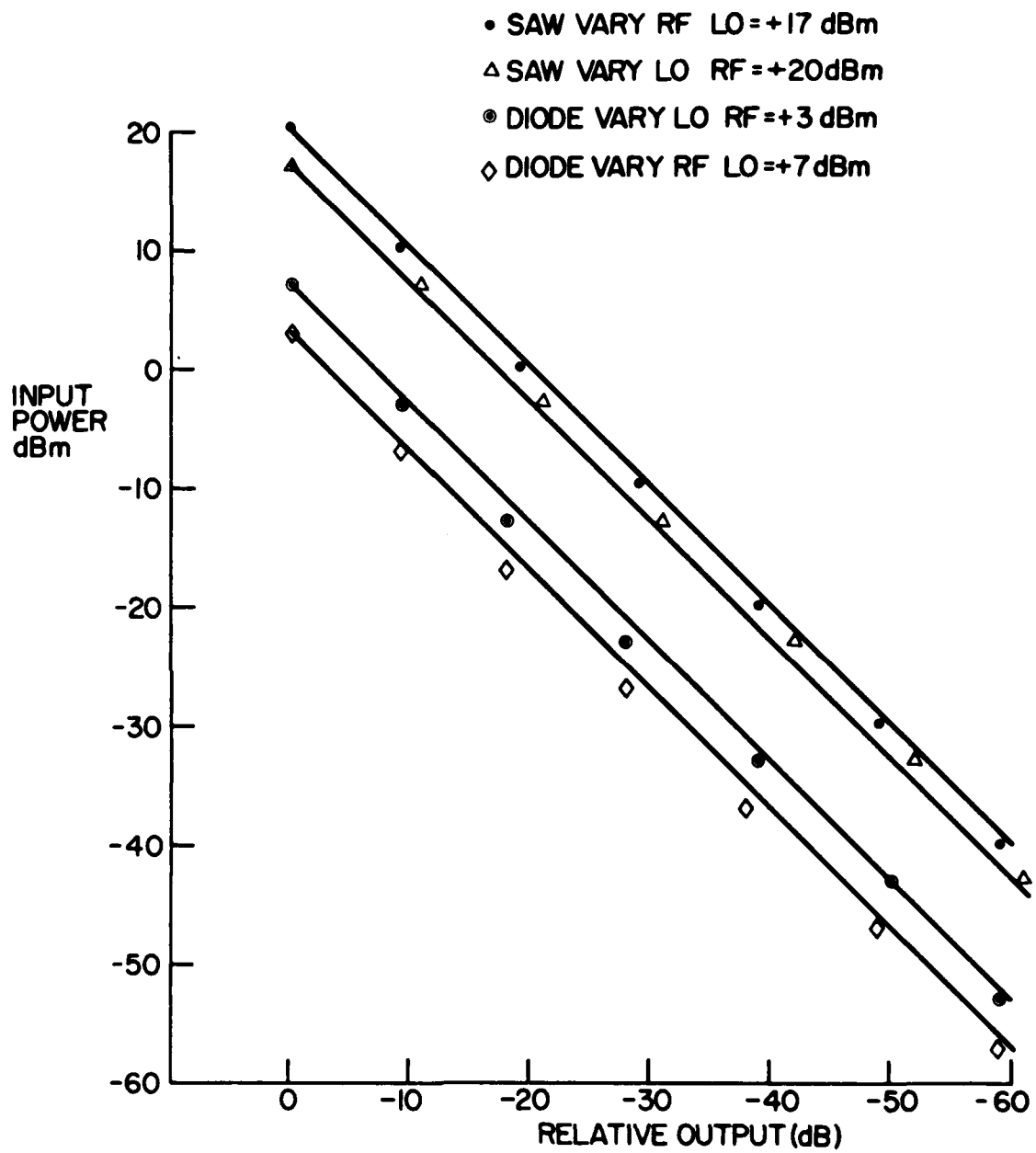


Figure 4.16 Input power versus relative output power for bilinear SAW mixer and double balanced diode mixer. First the RF is varied while the LO is held at a constant level, then the LO is varied while the RF is held at a constant level.

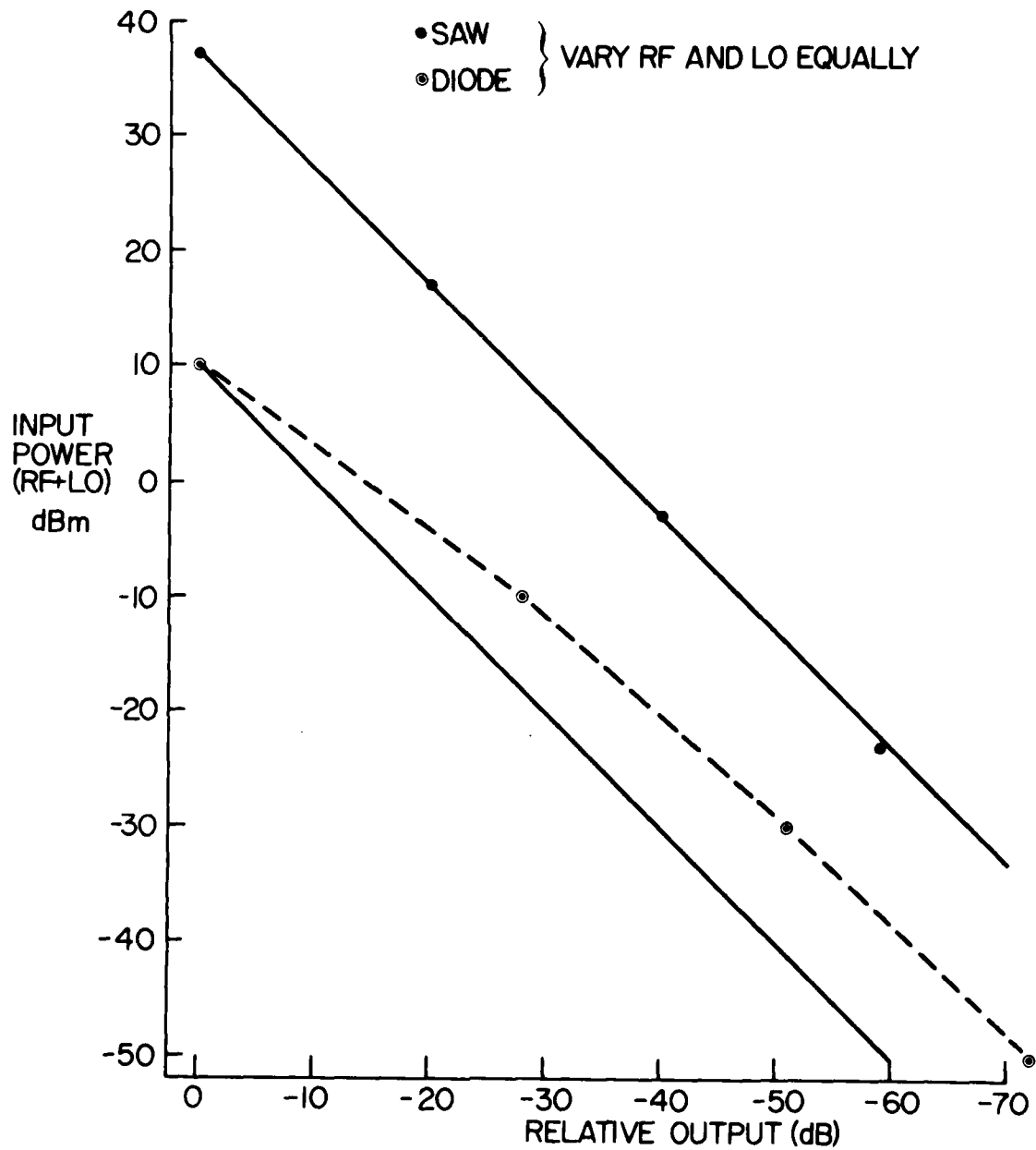


Figure 4.17 Input power versus relative output power for bilinear SAW mixer and double balanced diode mixer. Both inputs are varied equally.

diode mixer was not.

Table 4.3 gives the complete set of data for both SAW and double-balanced diode mixers. In addition to the cases depicted graphically in Figures 4.16 and 4.17, the cases of both input levels varying by different amounts is given. An example could be for the RF to decrease 10 dB and the LO to decrease 20 dB. The output should decrease by 30 dB. Again the SAW mixer was bilinear, and the diode mixer was not.

A dynamic range of 70 dB above the noise floor is shown in Figure 4.18 for the desired difference frequency ($f_2 - f_1$) of 328 MHz. This was for c.w. input signals of +23 dBm at $f_1 = 510$ MHz and +26 dBm at $f_2 = 838$ MHz. The desired difference frequency was 38 dB below the +23 dBm input, which is a 38 dB conversion loss. If the inputs had been pulses instead of c.w., the conversion loss and dynamic range would have been even better, since larger input powers are possible using pulses.

The output transducer had a center frequency of 326 MHz, 63 periods of double electrode fingers which were apodized with a Hamming function, and 1.5 percent bandwidth. It was desired to suppress the unwanted frequencies as much as possible, so the narrow band LC resonant filter shown in Figure 4.15 was added to the output. This narrow band filter gave 18 dB additional suppression at 703 MHz and 23 dB additional suppression at 978 MHz. Details concerning the output transducer and LC resonant filter can be found in Appendix D. The variable inductor was tuned to maximize the

DOUBLE BALANCED DIODE MIXER

INPUT POWERS	+3	-7	-17	-27	-37	-47	-57	dBm
+7	0	-9	-18	-28	-38	-49	-59	RF = 840 MHz
-3	-9	-28	-41	-51	-62	-72		
-13	-18	-41	-51	-62	-72			
-23	-28	-51	-62	-72				
-33	-39	-62	-72					
-43	-50	-72						
-53	-59							

dBm
LO = 512 MHz

RELATIVE OUTPUT POWER

SAW

INPUT POWERS	+20	10	0	-10	-20	-30	-40	dBm
+17	0	-9	-19	-29	-39	-49	-59	RF = 840 MHz
+7	-11	-20	-30	-40	-50	-58		
-3	-21	-30	-40	-50	-59			
-13	-31	-40	-50	-59				
-23	-42	-51	-59					
-33	-52	-59						
-43	-61							

dBm
LO = 512 MHz

RELATIVE OUTPUT POWER

Table 4.3 Data for bilinearity of double balanced diode mixer (top) and SAW mixer (bottom).

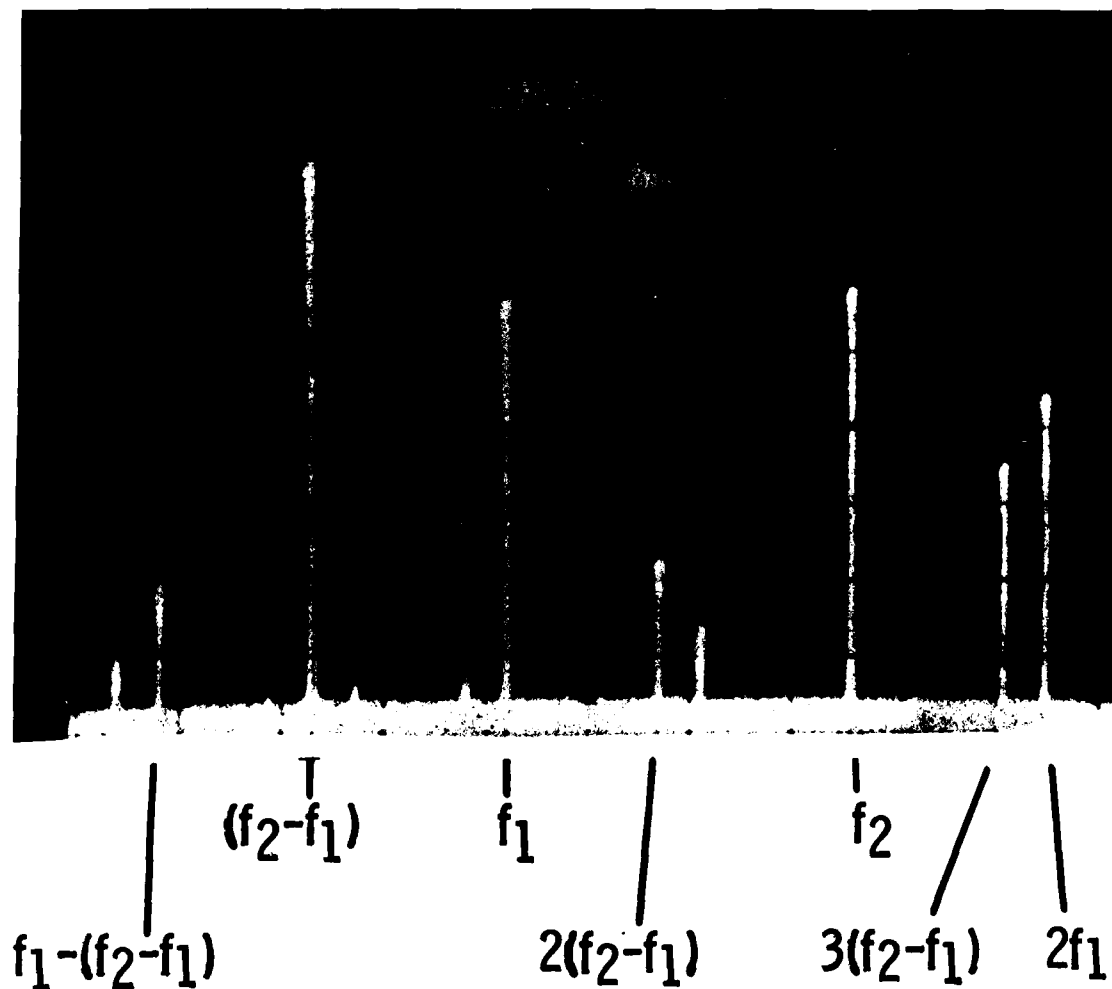


Figure 4.18 Output spectrum of bilinear SAW mixer with no output matching - 600 MHz center frequency and 100 MHz/div. Inputs at $f_1 = 510$ MHz and $f_2 = 838$ MHz, output at $(f_2 - f_1) = 328$ MHz.

spurious rejection which imposed a 4 dB penalty in insertion loss. This matching method has been used before with similar components and frequencies, 4.14, 4.15 and by minimizing insertion loss rather than maximizing spurious rejection, a 1 dB penalty in insertion loss was incurred.

Using the inductor and capacitor described above, the results of Figure 4.19 were obtained. Input power levels and frequencies were the same as in Figure 4.18. Dynamic range is greater than 65 dB above the noise floor for the desired difference frequency ($f_2 - f_1$) of 328 MHz. The strongest spurious signal (f_1) is now suppressed 33 dB below the desired frequency, and all other spurious signals are suppressed at least 55 dB.

The conversion losses (Equations 4.3 and 4.4) and F factors (Equations 4.1 and 4.2) are given in Table 4.4. For the mixer with matching (LC filter on the output), the conversion loss is 42 dB. To express this in acoustic power, one subtracts out the transducer insertion losses and obtains $\text{CONV. LOSS}_{\text{AC}} = -19$ dB. F_{ext} with matching is -68 dBm. Subtracting out all three transducer insertion losses, one obtains $F_{\text{int}} = -38$ dBm.

The SAW bilinear mixer was designed, built, and tested. It has a dynamic range greater than 65 dB, electromagnetic conversion loss of 42 dB, acoustic conversion loss of 19 dB and is useful at the same frequencies as any SAW based device. Its use as a bilinear or linear mixer is most attractive when other SAW based

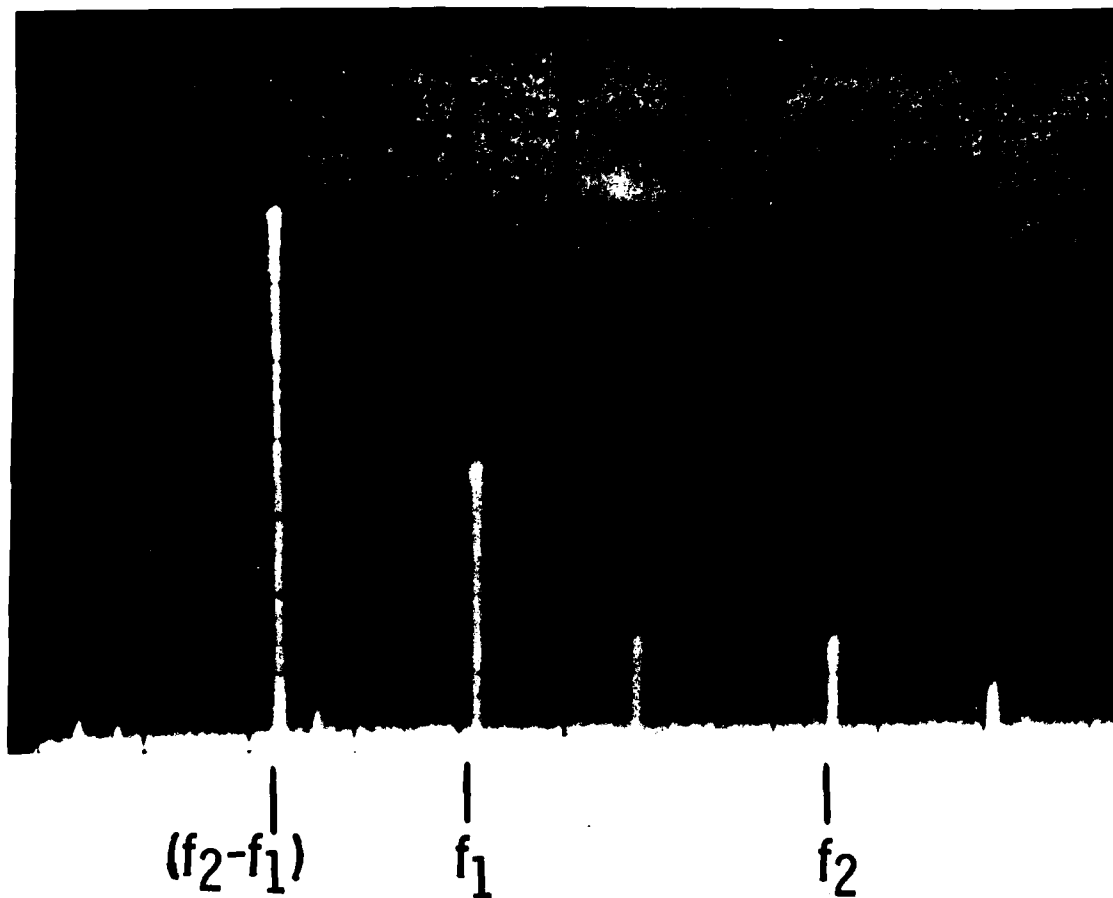


Figure 4.19 Output spectrum of bilinear SAW mixer with optimum output matching - 600 MHz center frequency and 100 MHz/div. Inputs at $f_1 = 510$ MHz and $f_2 = 838$ MHz, output at $(f_2 - f_1) = 328$ MHz.

	ELECTROMAGNETIC		ACOUSTIC	
	F_{ext} (dBm)	CONV. LOSS _{EM} (dB)	F_{int} (dBm)	CONV. LOSS _{AC} (dB)
NOT MATCHED	-64	-38	-38	-19
MATCHED	-68	-42	-38	-19

Table 4.4 Conversion loss for SAW bilinear mixers.

functions can be integrated on a single, monolithic substrate. One such application is the chirp transform module. The chirp transform module includes two chirp delay lines (the electrode spacing in the transducers varies linearly from one end of the transducer to the other end) and a mixer in the MCM (Multiplication - Convolution - Multiplication) configuration.^{4.16,4.17} It is desirable to amplitude weight (apodize) the input chirp (generated externally to the mixer) to reduce the time side lobes. This means that both input levels of the mixer must vary simultaneously. This requirement describes a bilinear mixer which has not been available heretofore. Even more exciting is the possibility of replacing one of the input transducers on the SAW mixer (Figure 4.15) with a weighted chirp transducer. This eliminates the insertion loss of two transducers and the propagation loss of the chirp generator. The output transducer on the SAW mixer can be replaced with the reversed chirp transducer - again with the same savings in insertion loss, propagation loss, and size. Also, by using a multi-strip coupler this reversed chirp transducer can also be amplitude weighted.

CHAPTER V

NON-COLLINEAR MIXING

5.1 Introduction

These investigations were undertaken with the hope of improving the performance of the collinear mixer discussed in Chapter 4. Specifically, better rejection of the input signals was needed while maintaining or improving the dynamic range of the difference frequency at the output. Attaining a bandwidth comparable to a collinear mixer was an added challenge since the beam position (azimuth) of the non-collinear mixer is so frequency sensitive. While these goals were not achieved, from an academic point of view, the non-collinear mixing investigations are considered to be the most interesting ones in this thesis because they are theoretically more complex and because more degrees of freedom exist in the design of a mixer.

Non-collinear mixing can only occur in anisotropic crystals.^{5.1} Prior investigations have been conducted on lithium niobate^{5.1} (LiNbO_3) and bismuth germanium oxide^{5.2-5.5} (BGO), both of which are highly anisotropic. One consequence is that the phase velocity and group velocity have very different angles of propagations. Also, the velocity surface of Y,Z LiNbO_3 cannot be precisely calculated because the material constants are not known

accurately enough. Further more, the velocity surface is not parabolic,^{5,6} a fact that complicates the theory. The other orientations of LiNbO_3 and most other commonly used crystals have parabolic velocity surfaces. The parabola is a well-defined, smoothly varying function that allows the theory to be greatly simplified.

The investigations in this chapter are an extension of the work presented in Davis' PhD dissertation.^{5.5} His experiments used BGO and were conducted in the 10 to 30 MHz range. The difference frequency amplitude in those experiments was very weak, and he resorted to semiconductor enhancement to increase the signals. It was reasonable to assume that the approach taken here would yield much stronger signals for the following reasons. The piezoelectric coupling of LiNbO_3 is higher, the frequency was at least 20 times higher, and the apertures were at least 10 times smaller. The last two factors mean that the acoustic power densities were at least 200 times greater (23 dB) since most of the energy is confined to a depth of one wavelength, and power density is in mw/mm rather than mw/λ .

5.2 Results for Y,Z LiNbO_3 with $\omega_1/\omega_2 = 2.60$

The first experiment was conducted with Y cut, Z propagating lithium niobate. The input frequencies were 823 MHz (f_1) and 316 MHz (f_2) with angles of 100° (θ_1) and 90° (θ_2) respectively. Thus $\omega_1/\omega_2 = 2.60$. The curve in

Figure 5.1 was generated using the following equation from Chapter 2.3.

$$\frac{\omega_1}{\omega_2} = \frac{-V(\theta_1) \sin(\theta_2 - \theta_3)}{V(\theta_2) \sin(\theta_3 - \theta_1)} \quad (5.1)$$

The velocities were obtained from Reference 5.7 and the dashed line applies to this experiment. Note that $\theta_3 = 106^\circ$. The experiment can further be visualized with the aid of Figure 5.2. The input transducers are located at $\theta = 90^\circ$ which is a pure mode axis, and at $\theta = 100^\circ$ from the +X axis - a notation corresponding to that used in Reference 5.7. As mentioned before, these are phase velocities-not group velocities. This distinction is graphically depicted in Figure 5.3. The phase velocity is at angle θ . However, due to the anisotropy of the crystal, the group velocity is different by an amount ϕ which may be either positive (defocussing) or negative (focussing). (All ϕ were negative in these experiments). The result is that the power flow is at angle $\alpha = \theta + \phi$. As shown in Figure 5.2, for this experiment, $\phi_2 = 0^\circ$, $\phi_1 = -3.90^\circ$ and $\phi_3 = -2.22^\circ$. Note that input transducer f_1 is tilted 10° from the pure mode axis, and is located 1 mm back and 0.176 mm up corresponding to 10° . It should have been up 0.105 mm corresponding to a group velocity of 6° . The error is insignificant since the beams still cross at the same angle.

The laser probe was used to investigate the interactions. The profiles are shown in Figure 5.4 at 6 mm

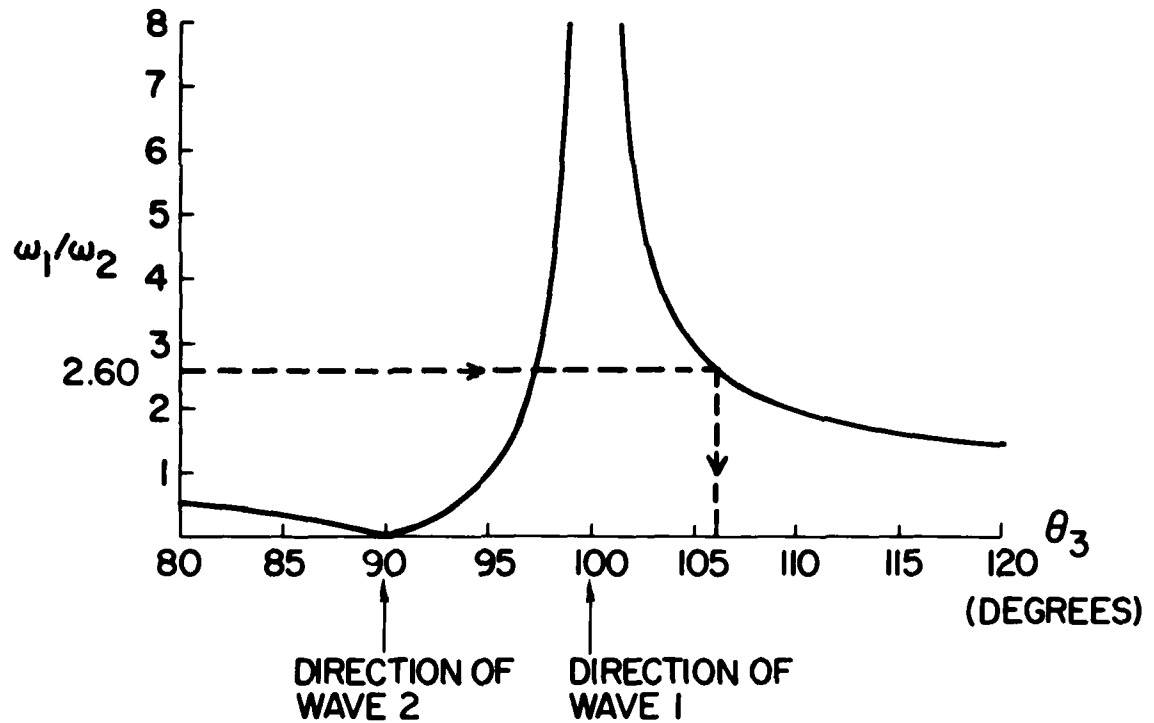


Figure 5.1 Frequency ratio required to steer mixed frequency beam in various directions on Y,Z LiNbO₃ with inputs at 90° and 100° [Eq.(5.1)]. Dashed line is experimental point.

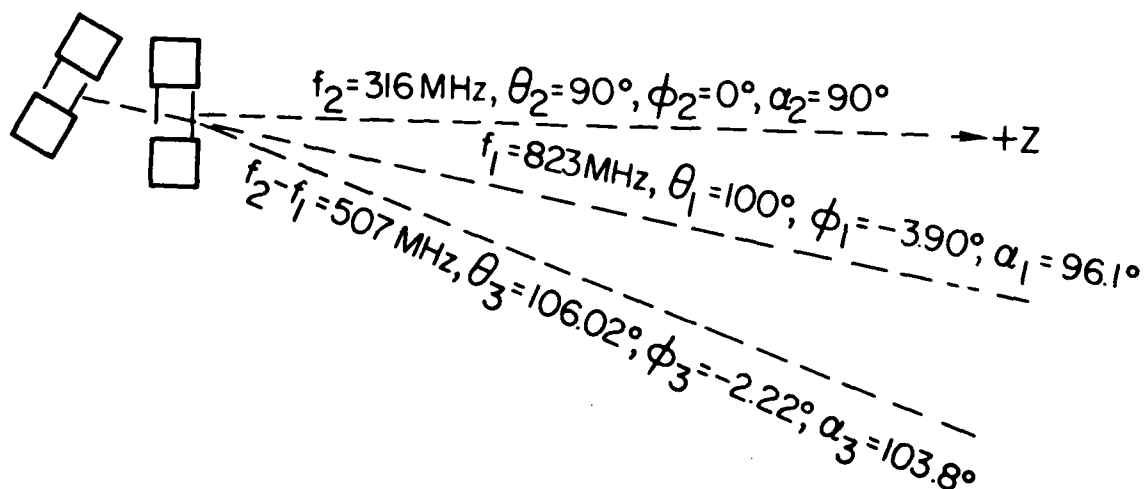


Figure 5.2 Schematic of input transducer placement for mixing experiment on Y,Z LiNbO₃ and having frequency ratio $\omega_1/\omega_2 = 2.60$. Angles are defined in Figure 5.3 ($\alpha = \theta + \phi$).

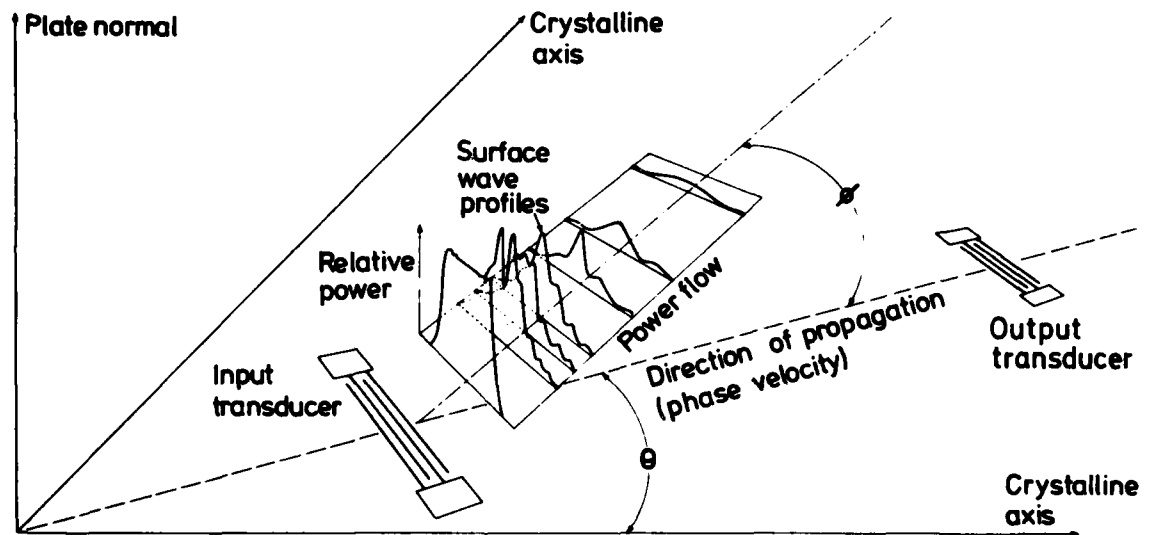


Figure 5.3 Schematic representation of angles for phase velocity, θ , and the change in group velocity due to crystalline anisotropy, ϕ . Power flows at $\alpha = \theta + \phi$.

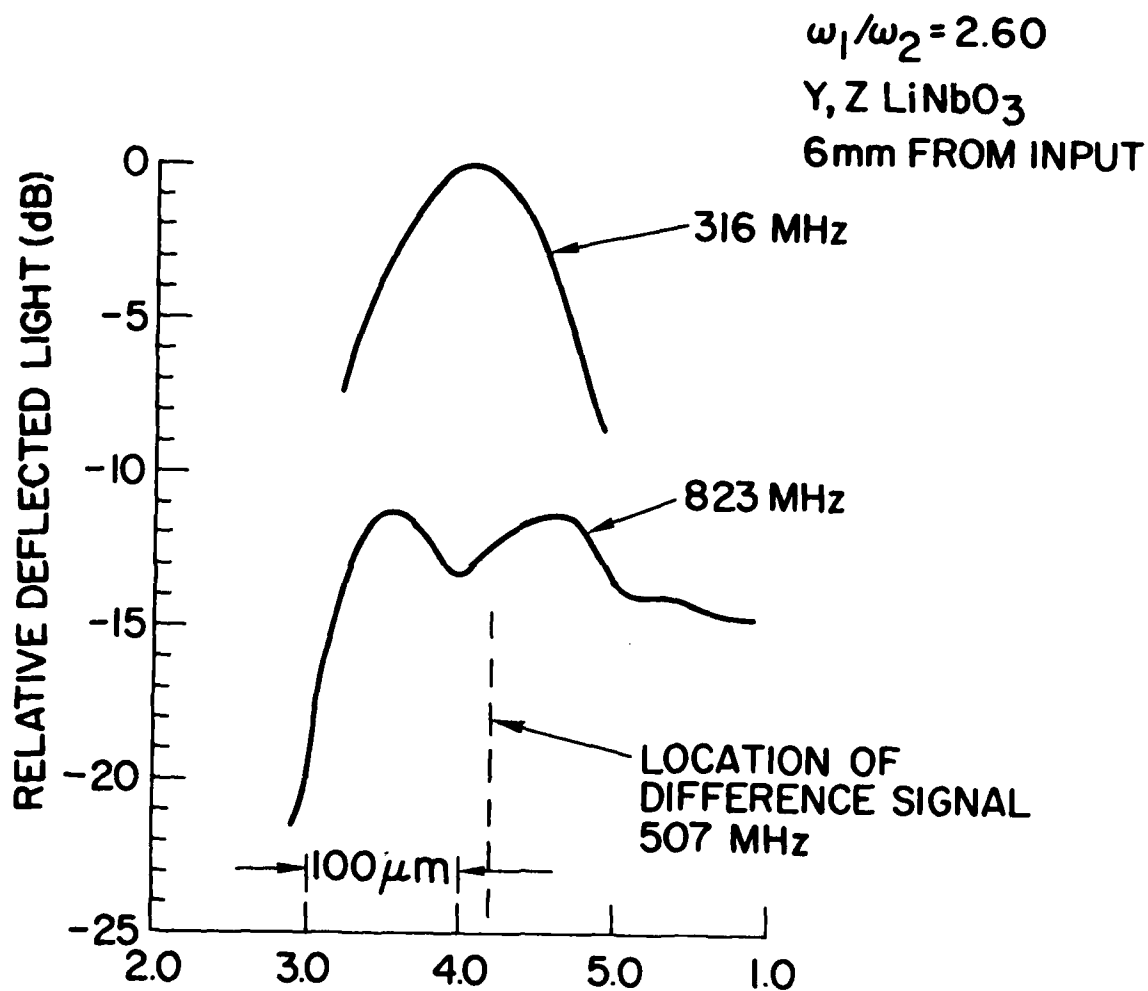


Figure 5.4 Profiles of acoustic signals on Y,Z LiNbO₃ taken 6 mm from input transducer f_2 . The abscissa increments are 100 μ m each, taken from a micrometer dial that repeats every 500 μ m.

from transducer f_2 . The figure shows that frequency f_2 at 316 MHz is well behaved as it propagates down the pure mode Z axis. Frequency f_1 at 823 MHz shows two distinct peaks and a "smearing out" of energy. These two distinct peaks also occur between the transducers and behind transducer f_1 . The peaks are not of equal amplitude at all positions down the propagation length, and in many cases the valley between is deeper than the one in Figure 5.4. The profile of signal f_1 was obtained again with transducer f_2 removed (after all other testing was completed). This verified that having transducer f_2 in the path caused negligible effect. The double peaks are probably due to the combined effect of diffraction and the large angle away from a pure mode axis in this highly anisotropic crystal. Apparently, the interaction of the acoustic wave with the crystalline lattice is a more complex process than predicted by existing theory since including a beam steering angle of -3.9° predicts that wave f_1 should be $600 \mu\text{m}$ to the right of wave f_2 after traveling 6 mm. Figure 5.4 does show that a small portion of wave f_2 has propagated to the right of centerline, but it was expected that nearly all the wave would propagate in that direction. The laser probe detected a very weak difference frequency only in the path of signal f_2 . However, the difference frequency was found at the predicted angle with the added sensitivity of an output transducer.

An output transducer (not shown in Figure 5.2) was

located 10 mm from input transducer f_2 and down 2.68 mm corresponding to 15° , and it was tilted 15° from vertical. Its output is shown in Figure 5.5 with f_2 at 316 MHz and f_1 sweeping from 700 to 920 MHz. The vertical scale is 5 dB/div., and the horizontal scale is 100 MHz/div., centered on 600 MHz. The difference signal is indeed weak, and the input signals are unacceptably large. For comparison purposes, a figure of merit is used to describe the efficiency. The figure of merit is called an F factor and

is defined as $F_{\text{external}} = \frac{P_3}{P_1 P_2}$. The subscript external

is used because the powers used here are the powers applied to and received from transducers. (The same three transducers were used for all the non-collinear experiments). The input powers P_1 and P_2 were 10 mw and 90 mw, respectively. The ratio of output power, P_3 , to input P_2 was -85 dB. This leads to

$$F_{\text{ext}} = \frac{P_3}{P_1 P_2} = \frac{-85\text{dB}}{10\text{dBm}} = -95\text{dBm} . \quad (5.2)$$

5.3 Results for 38,X LiNbO₃ With $\omega_1/\omega_2 = 0.41$

Experiments were also conducted with 38,X LiNbO₃. (The actual rotation was 37.95° which we shall henceforth call 38°). This orientation is a popular one because of its weak coupling to volume waves, its high velocity, and its high piezoelectric coupling.^{5.8} The input frequencies were

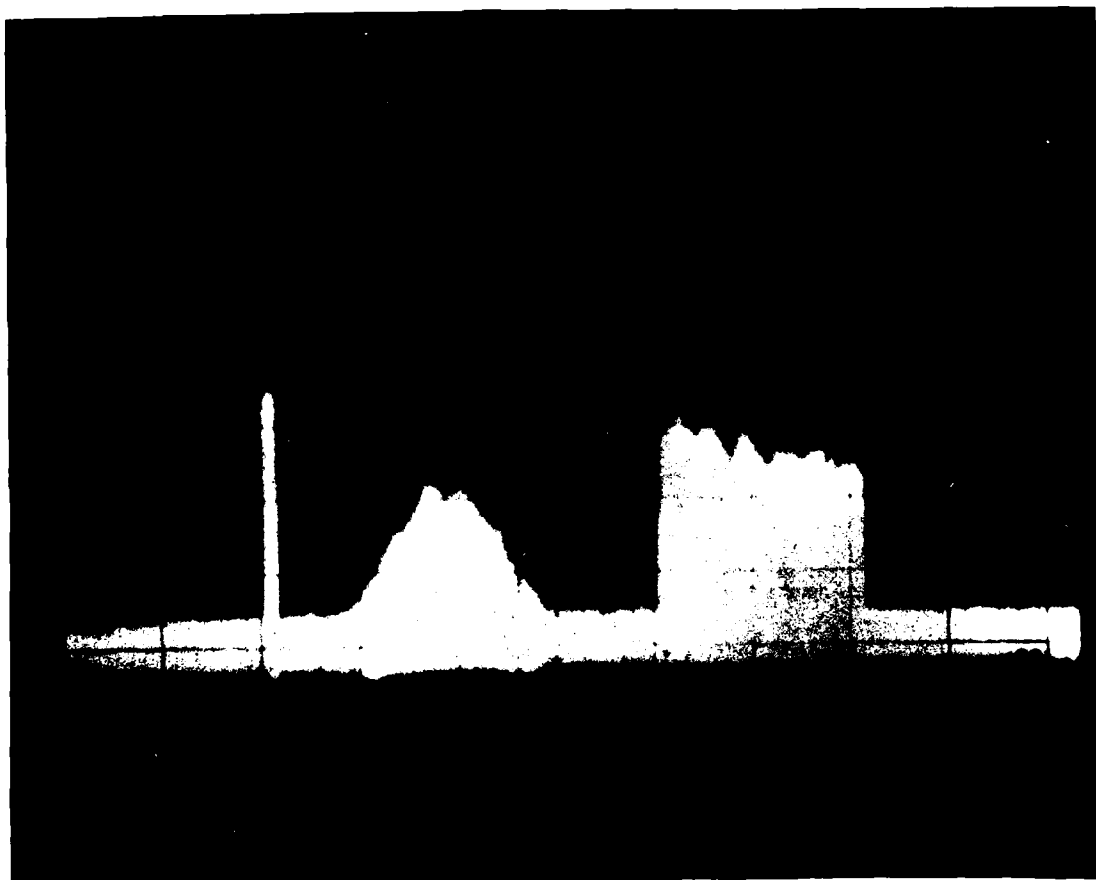


Figure 5.5 Output from the mixer shown schematically in Figure 5.2. Output transducer is 10 mm from input and at an angle of 15° . Difference signal is between f_2 at 316 MHz and f_1 sweeping 700 to 900 MHz. 5 dB/div. vert., 100 MHz/div horiz. centered on 600 MHz.

386 MHz and 940 MHz with respective angles of 10° and 0° from +X. Like Figure 5.1, the curve in Figure 5.6 was generated using Equation (5.1) and velocities from Reference 5.7. Note that there are two sets of dotted lines; the one corresponding to $\omega_1/\omega_2 = 0.41$ applies to this section and predicts $\theta_3 = -6.8^\circ$; the other one corresponds to $\omega_1/\omega_2 = 2.44$ and applies to section 5.4. Figure 5.7 serves the same purpose as Figure 5.2 in the previous section. Note that the data is based on a 37° rotation, but the actual crystal had a 38° rotation. This is because the handbook^{5.7} did not contain the 38° rotation, so the nearest available one was used. The various angles are given as before in Figure 5.2. The major difference between Figures 5.2 and 5.7 besides orientation, is that transducers f_1 and f_2 are interchanged such that ω_1/ω_2 is less than 1 in this case. As a consequence, the difference signal propagates out of the interaction region at a negative angle rather than a positive angle. Input transducer f_1 was tilted 10° from vertical and was located 1 mm back and 0.121 mm up corresponding to 6.9° - the angle of the group velocity.

Laser probe profiles at 6 mm from transducer f_2 are given in Figure 5.8. As before, f_2 propagates down a pure mode axis, +X, and is well behaved. Signal f_1 , on the other hand, is considerably spread out. Once again, this is attributed to the combination of diffraction and propagation at a large angle from the pure mode axis. Diffraction is particularly severe from transducer f_1 because its radiating

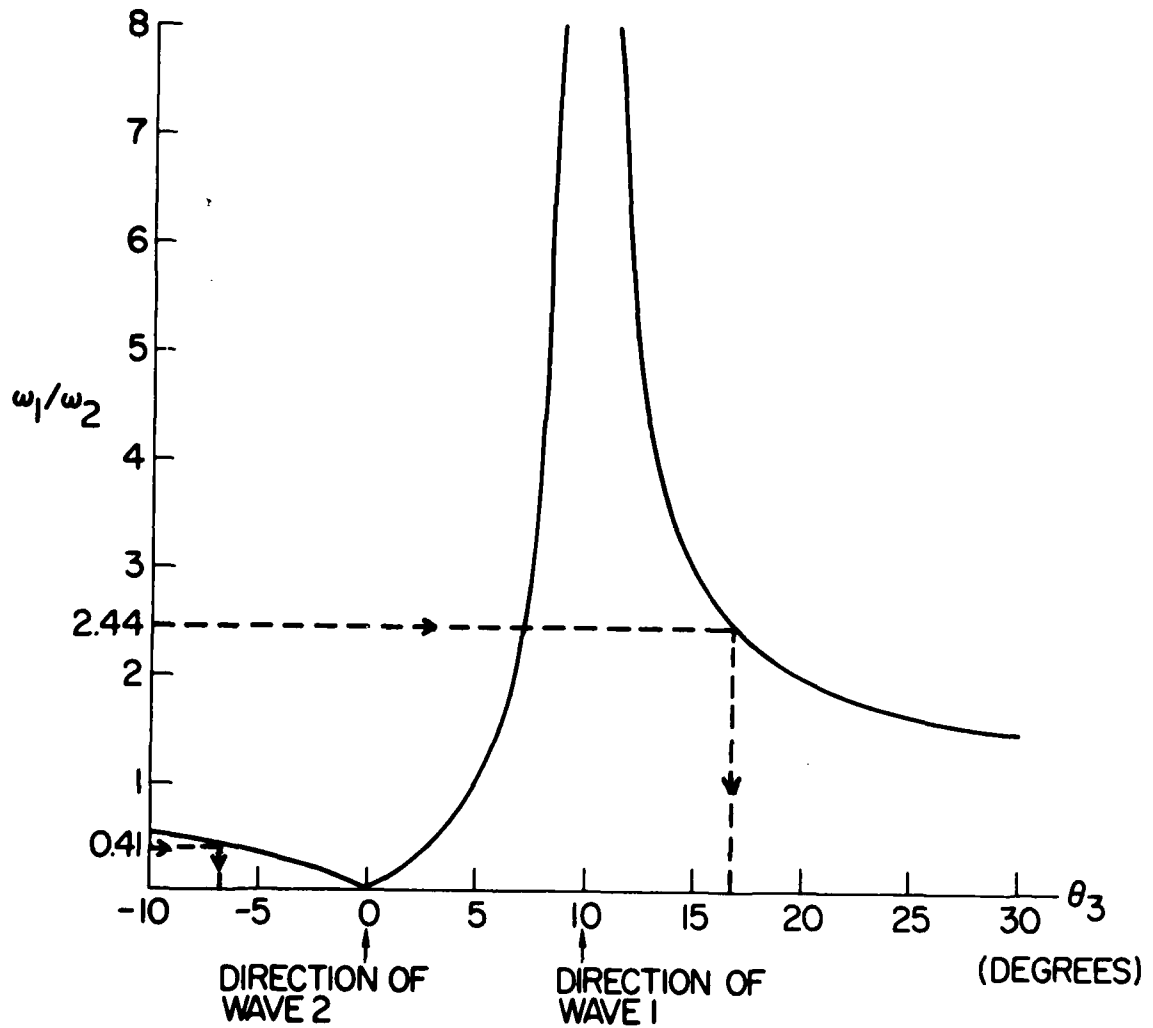


Figure 5.6 Frequency ratio required to steer mixed frequency beam in various directions on 37,X LiNbO₃ with inputs at 0° and 10° [Eq.(5.1)]. Dashed lines are experimental points.

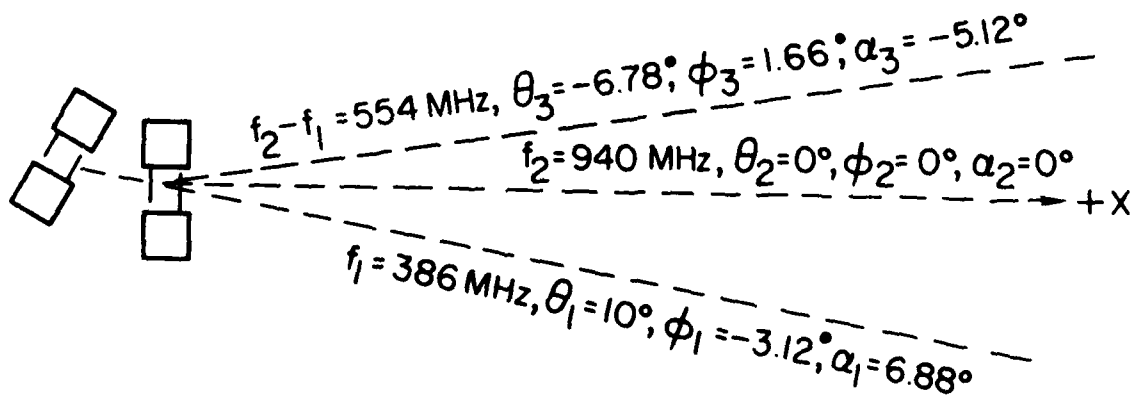


Figure 5.7 Schematic of input transducer placement for mixing experiment on $37, X \text{ LiNbO}_3$, and having frequency ratio $\omega_1/\omega_2 = 0.41$. Angles are defined in Figure 5.3.

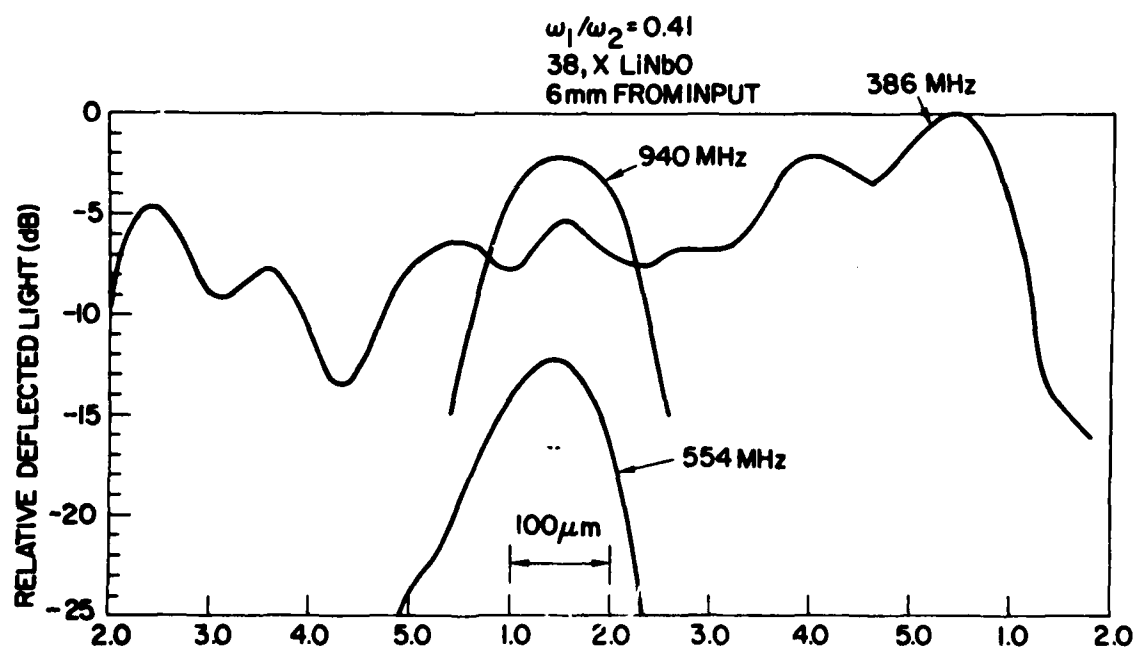


Figure 5.8 Profiles of acoustic signals on 38,X LiNbO₃ ($\omega_1/\omega_2 = 0.41$) taken 6 mm from input transducer f_2 . The abscissa increments are 100 μ m each, taken from a micrometer dial that repeats every 500 μ m.

aperture is only 12.5λ . Signal f_2 has an aperture of 31λ . This spreading was also observed by Davis^{5.5} on BGO at 10 MHz using a laser probe. Note also that the 386 MHz input has 2 dB more intensity than the 940 MHz input even though it is being driven with 10 dB more power. This gives a rough indication of how much power has been generally dispersed. The difference signal was found in the same path as signal f_2 . As in the previous experiment, the added sensitivity of a transducer was needed to detect the difference signal at the expected angle.

As before, an output transducer (not shown in Figure 5.7) was located 9 mm from input transducer f_2 and up 0.79 mm corresponding to -5° , and it was tilted 6.5° from vertical. Its output is shown in the top of Figure 5.9 with signal f_2 sweeping 730 to 1130 MHz and signal f_1 at 386 MHz. The vertical scale is 10 dB/div, and the horizontal scale is 100 MHz/div, centered on 600 MHz. The input powers P_1 and P_2 were 90 mw and 4 mw, respectively. The ratio of output power, P_3 , to input P_1 was -70dB, leading to

$$F_{\text{ext}} = \frac{P_3}{P_1 P_2} = \frac{-70\text{dB}}{6\text{dBm}} = -76\text{dBm}. \quad (5.3)$$

5.4 Results for 38,X LiNbO₃ With $\omega_1/\omega_2 = 2.44$

In this case, the dashed line in Figure 5.6 corresponding to $\omega_1/\omega_2 = 2.44$ is used and shows that θ_3 is 16.8° . Figure 5.10 shows the arrangement of the

AD-A127 570

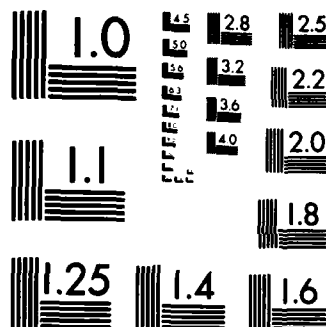
SURFACE ACOUSTIC WAVE NON-LINEAR INTERACTIONS IN
LITHIUM NIOBATE(U) ROME AIR DEVELOPMENT CENTER GRIFFISS
AFB NY R D COLVIN JAN 83 RADC-TR-83-9

3/4

UNCLASSIFIED

F/G 20/5 NL





MICROCOPY RESOLUTION TEST CHART
NATIONAL BUREAU OF STANDARDS-1963-A

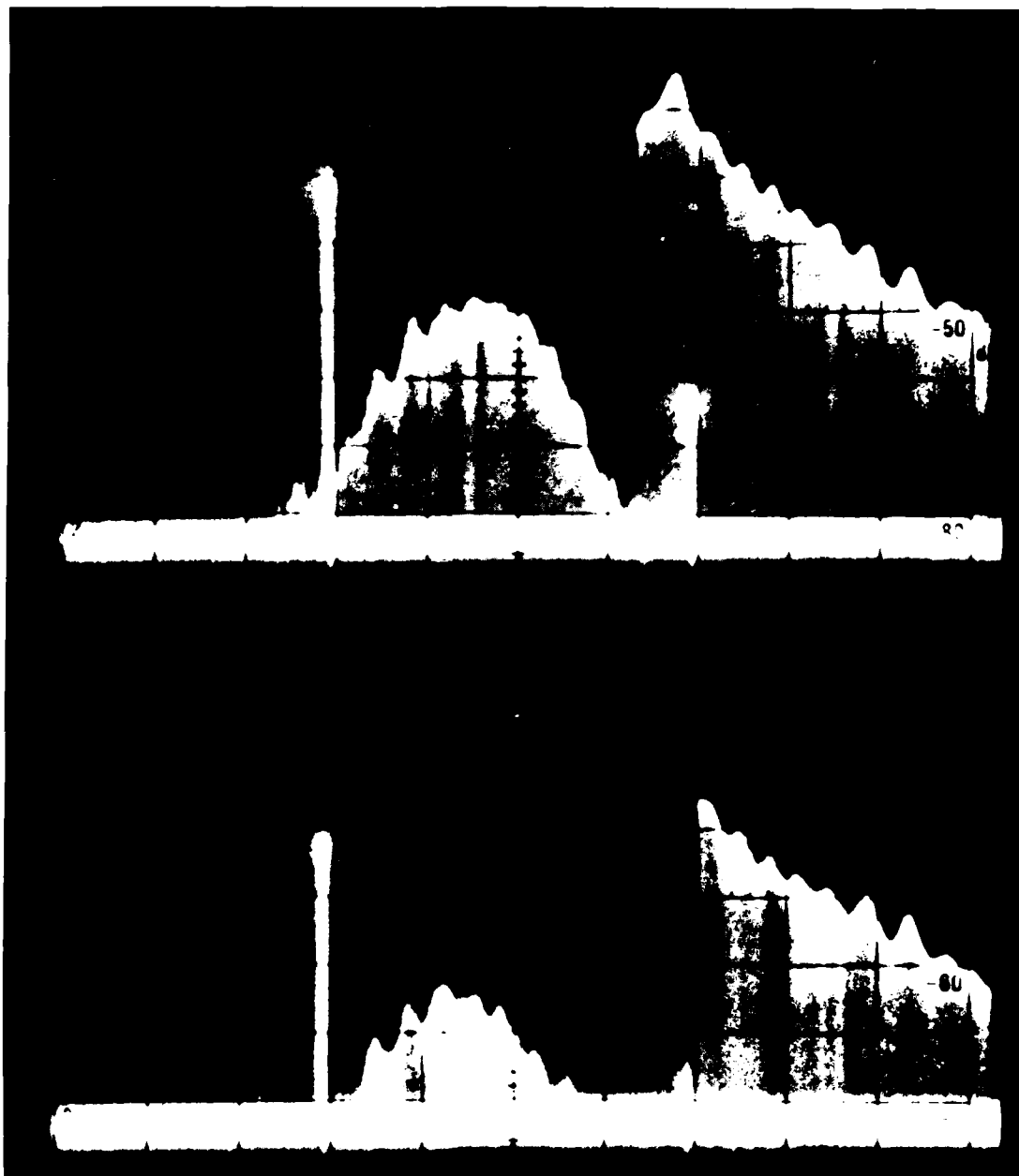


Figure 5.9 (Top) Output from the mixer shown schematically in Figure 5.7. Output transducer is 9 mm from input and at angle of -5° . Difference signal is between f_1 at 386 MHz and f_2 sweeping 730 to 1130 MHz.

(Bottom) Output from the mixer shown schematically in Figure 5.10. Output transducer is 10 mm from input and at angle 6.3° . Difference signal is between f_2 at 386 MHz and f_1 sweeping 800 to 1140 MHz. 10 dB/div. vert., 100 MHz/div. horz. centered on 600 MHz.

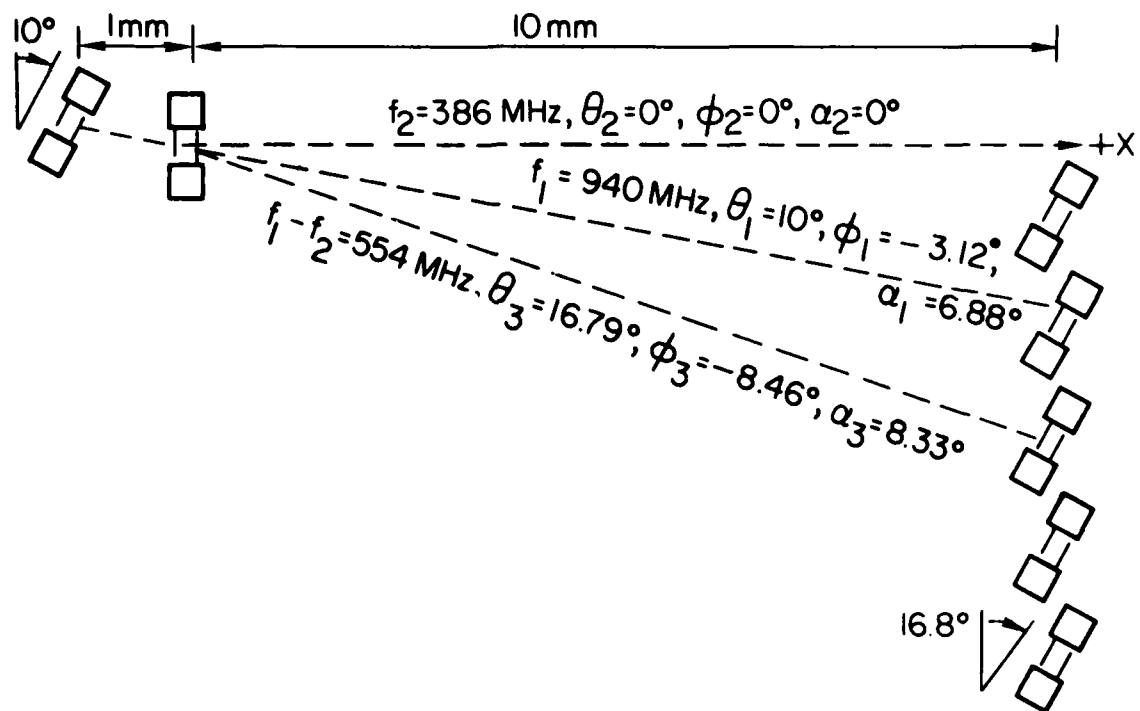


Figure 5.10 Schematic of transducer placement for mixing experiment on 37,X LiNbO₃, and having frequency ratio $\omega_1/\omega_2 = 2.44$. Angles are defined in Figure 5.3.

transducers, the various signals, and their associated angles. The only difference from Figure 5.7 is that transducers f_1 and f_2 have been interchanged. As a consequence, the difference signal propagates out of the interaction region with a phase velocity angle of 16.8° .

This device was also laser probed; the profiles at 3 mm from transducer f_2 are given in Figure 5.11. As in section 5.3, signal f_2 propagates down a pure mode axis, $+X$, and is well behaved, while signal f_1 is considerably spread out. Note that the 940 MHz input has 29 dB less intensity than the 386 MHz input. 10dB can be attributed to a smaller input drive level, but this still leaves a 19 dB discrepancy. Comparing Figure 5.11 to Figure 5.8, it can be concluded that 940 MHz is about 10 times more sensitive (11 dB) to the spreading of energy than the 386 MHz signal. Again the difference signal was found in the same path as signal f_2 , and the added sensitivity of a transducer was required to detect the difference signal at the expected angle.

Output transducers were placed as indicated in Figure 5.10. In addition, there was another column of output transducers at 11 mm from transducer f_2 . They were staggered relative to the first column such that an aperture occurred every 0.35 mm going down the crystal. Each transducer was connected in turn with everything else held constant. The transducer with strongest output, was identified, indicating the angle of the maximum group

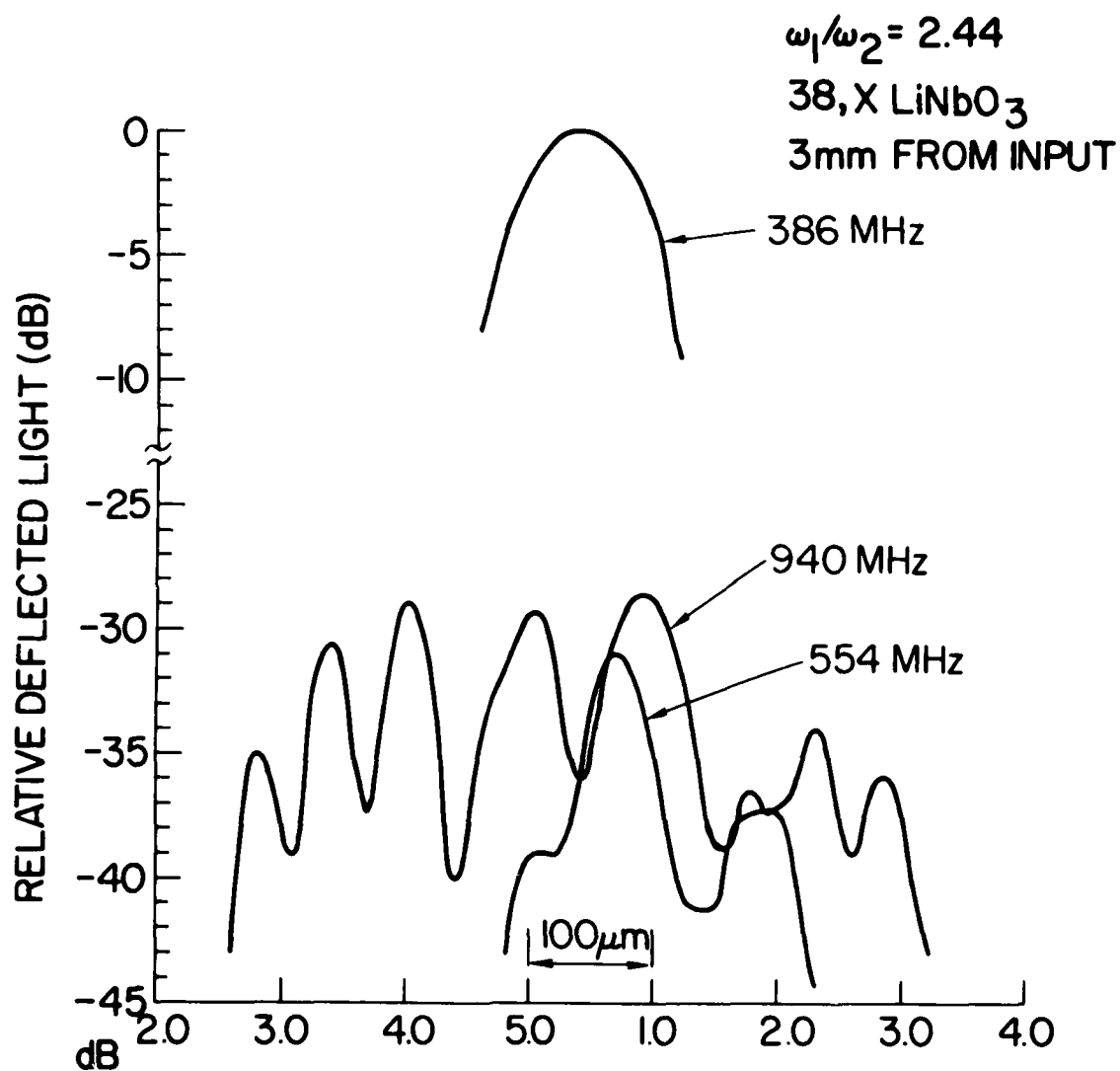


Figure 5.11 Profiles of acoustic signals on 38,X LiNbO₃ ($\omega_1/\omega_2 = 2.44$) 3 mm from input transducer f_2 . The abscissa increments are 100 μ m each, taken from a micrometer dial that repeats every 500 μ m.

velocity for the difference signal leaving the interaction region. This output is shown in the bottom of Figure 5.9. It corresponds to an angle of $6.3^\circ \pm 1^\circ$ compared to a theoretical prediction of 8.3° . Signal f_2 is at 386 MHz and signal f_1 sweeps from 800 to 1140 MHz. The vertical scale is 10 dB/div., and the horizontal scale is 100 MHz/div, centered on 600 MHz. The input powers, P_1 and P_2 , were 10 mw and 77 mw, respectively. The ratio of output power, P_3 , to input, P_2 , was -86 dB leading to

$$F_{\text{ext}} = \frac{P_3}{P_1 P_2} = \frac{-86\text{dB}}{10\text{dBm}} = -96\text{dBm}. \quad (5.4)$$

The insertion loss of all three transducers is estimated at 26 dB.

In addition to the profiles of difference signals propagating in the path of signals f_2 , their growth and decay were observed with the laser probe. The results are shown in Figure 5.12. It is reasonable to assume that the difference signals propagating at angle α_3 will have similar growth and decay rates.

5.5 Conclusion

The fast build up and decay of the difference signal on 38,X LiNbO₃ with $\omega_1/\omega_2 = 2.44$ is probably due to the large amount of energy spreading in the 940 MHz signal (see Figure 5.11). All three rates of decay are similar as one would expect since they are all for roughly the same

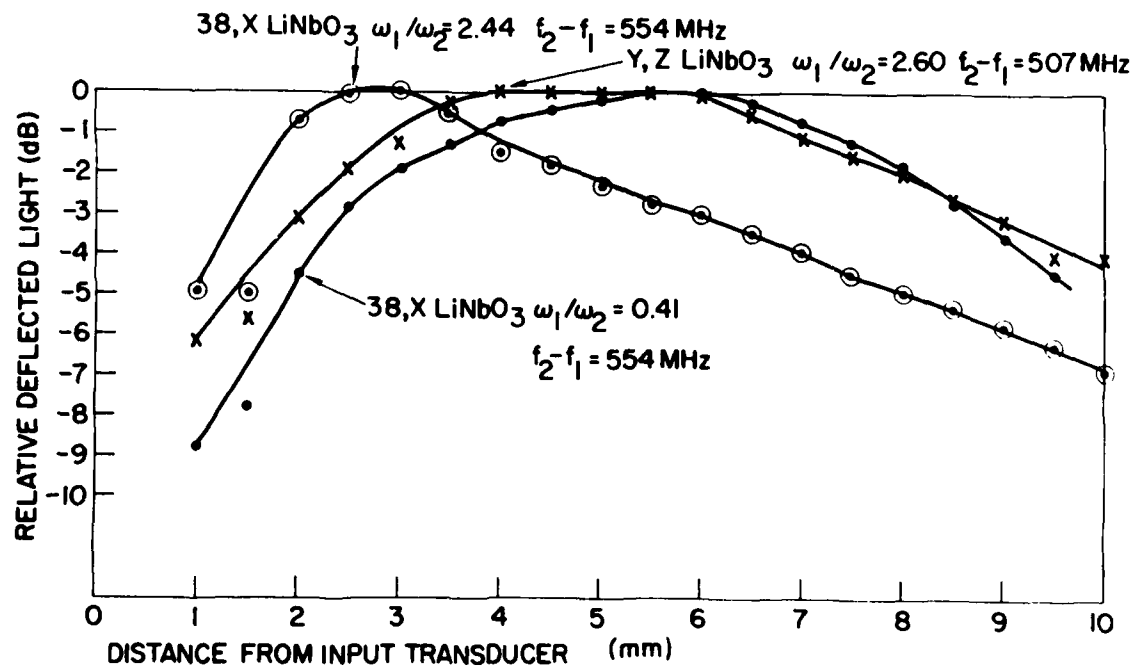


Figure 5.12 Growth and decay of difference signals along same path as signal f_2 .

frequency. The shape of the curves is characteristic of simple attenuation starting to dominate the build-up of a traveling wave non-linear product.

In all cases, the output transducer was placed too far away for optimum output power. As stated earlier, this was deliberately done to obtain greater spatial separation from the undesired input frequencies. The device on 38,X LiNbO₃ with $\omega_1/\omega_2 = 0.41$ had the strongest output and best efficiency. This is partly explained by slower growth and decay rates and by the output transducer being 9 mm instead of 10 mm from the input transducer. It does not, however, totally explain the 20 dB difference. Thus, comparing the two 38,X experiments, one would conclude that $\omega_1/\omega_2 = 0.41$ is more efficient because it is less susceptible to the input energy spreading. In comparing it to the Y,Z device with $\omega_1/\omega_2 = 2.60$, one would conclude that the 38,X is a more efficient orientation for this non-linear interaction. Errors in output transducer location were probably 1° to 2° in each case. (A 3° error in the tilt of the transducer adds 6.5 dB of loss.^{5.5,5.9} Also, there is a 6 dB loss if the transducer is properly tilted but the acoustic wave misses one half the transducer.^{5.9})

For the 38,X device with $\omega_1/\omega_2 = 2.44$ (Section 5.4), there was an error in output transducer location of approximately 2°. This may be partly due to using data for 37° rotation rather than the 38° rotation. Also, this case had a correction for ϕ (-8.5°) which was four times

larger than that for either of the other cases. In view of these facts, agreement between theory and experiment is considered to be reasonably good.

CHAPTER VI

SUMMARY AND CONCLUSIONS

This thesis presents investigations of three types of non-linear surface acoustic wave (SAW) interactions in lithium niobate (LiNbO_3). In all cases there are two waves interacting. In the first case, convolution, the waves are collinear and counter-propagating. In the second case, collinear mixing, the waves are collinear and co-propagating. In the third case, non-collinear mixing, the waves are non-collinear and co-propagating. These interactions can be visualized with the aid of Figures 2.1, 2.2, and 2.5.

Chapter 1 provides a survey and historical background for each of these three subjects areas. Chapter 2 gives a general piezoelectric theory followed by the applicable theory for each of the three non-linear interactions. Chapter 3 contains experiments on high frequency convolvers with an emphasis on understanding the various losses and improving the efficiency for high frequency (≈ 800 MHz) operation. Investigations include propagation loss, diffraction, beam steering, attenuation, multimoding, output plate resistivity, and output matching. An upper practical limit seems to be 800 MHz input frequency. This provides the potential for 300 MHz instantaneous bandwidth.

Autoconvolution and double transit convolution are the worst spurious signals. However, the higher attenuation at these frequencies has the benefit of reducing these spurious signals which are the result of reflections. To date, Y,Z lithium niobate is the optimum material and orientation when all factors are considered. The aluminum integrating electrode suppresses harmonics and allows a linear dynamic range up to 1 watt of input power. Beamwidth compressors are not needed at high frequencies because transducers can be both broadband and have a small aperture. Multimoding effects were not evident in the convolved output. However, longer interaction times and successful achievement of low time sidelobes for coded signals may preclude working at these frequencies depending on the level of mode suppression required. The convolvers were only 2.5 microsec. long, but using the data presented here, they can be successfully designed and fabricated for longer lengths. Dynamic range is adequate for many applications, and methods are available for reducing the undesired spurious signals even further.

A logical extension of the convolver work would be to match the input and output of the 800 MHz convolver so that 300 MHz bandwidth could be demonstrated. (A 40 percent bandwidth has been demonstrated at 500 MHz input frequency.^{3,4}) Also, the length should be extended from 2.5 to 10 microsec. Convolution was performed with long, cw RF pulses. These pulses should be replaced with phase-shift keyed (PSK) modulated RF pulses because the final measure of

performance is how the time sidelobes of a correlated code are degraded due to spurious reflections and multimoding effects.

Chapter 4 presents the experimental investigations of collinear mixing. Emphasis is on improving efficiency, making the interaction broadband, and suppressing unwanted frequencies. Investigations include profiles of fundamental modes and mixing products obtained with a laser probe, broadband and narrowband transducers for the output (depending on application), and a measure of the bilinearity of the mixer. The SAW bilinear mixer has a dynamic range greater than 65 dB, electromagnetic conversion loss of 42 dB, acoustic conversion loss of 19 dB, and is useful at the same frequencies as any other SAW device. Its use as a bilinear mixer or linear mixer is most attractive when other SAW based functions can be integrated on a single, monolithic substrate. One such application is the chirp transform module^{4.16,4.17} which includes two chirp (linear FM) delay lines and a mixer. In that case one of the broadband input transducers of the SAW mixer could be replaced by a chirp transducer. It would also be desirable to amplitude weight (apodize) the input chirp transducer to reduce the time sidelobes. This has not been done in the past because it means both inputs would be varying in amplitude requiring a bilinear mixer. Not only is a bilinear mixer now available, but the apodized chirp transducer and bilinear mixer can be combined on the same

substrate with this technology.

To extend the collinear mixing work, it would be interesting to see how much bandwidth could be achieved. This would require better input matching (more than a single inductor) and perhaps three parallel paths and transducers for the output. In the area of integration, it would be interesting to let one of the inputs serve as a frequency doubler prior to mixing with the other input. For the chirp transform module application, it is recommended that one of the input transducers be replaced with a chirped (linear FM) transducer. Then in the next chirp transform device, this chirped transducer should be apodized to demonstrate the reduction in time sidelobes at the output and the bilinear capability of the mixer.

Chapter 5 details experiments of non-collinear mixing on three different devices. The goal was to gain additional suppression of unwanted frequencies over that obtained in the previous chapter using collinear mixing. On all three devices, the output transducer was placed too far down the propagation path to obtain optimum output power. This was intentionally done to obtain greater spatial separation from the undesired input frequencies. The 38,X LiNbO₃ device with $\omega_1/\omega_2 = 0.41$ was the most efficient because the angled input acoustic wave was less susceptible to spreading (diffraction). Comparing the 38,X device with $\omega_1/\omega_2 = 0.41$ to the Y,Z device with $\omega_1/\omega_2 = 2.60$, one concludes that the 38,X is a more efficient orientation for this type non-

linear interaction. Comparing the best of these non-collinear interactions to the collinear case, one sees that the non-collinear interaction is at least 8.5 dB weaker. Also, the suppression of the unwanted frequencies would not be any better even if the desired signal was 8.5 dB stronger, and anything done to improve the spatial filtering would only decrease the mixing efficiency. Therefore, this approach is not recommended for mixing, but it could perhaps be useful when exploiting some of its other possible applications. 5.4, 5.5

To extend the non-collinear work, two sets of experiments are recommended. To determine what is happening with the mixed frequency after it has left the interaction region, a series of transducers should be placed along the propagation path. By examining each in turn, a plot of build up and decay would be obtained. It would also be advisable to add a row of transducers on each side to obtain an estimate of how rapidly the energy varies in azimuth. A second set of experiments should be designed to evaluate the effects of longer and shorter interaction regions, thus determining the optimum angle of intersection for the two input acoustic waves.

REFERENCES

CHAPTER I

- 1.1 G.S. Kino "Acoustoelectric Interactions in Acoustic-Surface-Wave Devices," Proc IEEE, 64, pp 724-748, 1976
- 1.2 S.A. Reible, J.H. Cafarella, R.W. Ralston, and E. Stern, "Convolvers for DPSK Demodulation of Spread Spectrum Signals," IEEE Ultrason Symp Proc, pp 451-455, 1976.
- 1.3 J.H. Goll and N.J. Tolar, "Improved Efficiency of High BT Product SAW Convolvers," IEEE Ultrason Symp Proc, pp 469-471, 1977.
- 1.4 L.P. Solie, "A New Mode of Operation for the Surface-Wave Convolver," Proc IEEE, 64, pp 760-763, 1976.
- 1.5 K.A. Ingebrigtsen, "The Schottky Diode Acoustoelectric Memory and Correlator - A Novel Programmable Signal Processor," Proc IEEE, 64, pp 764-769, 1976.
- 1.6 D.H. Hurlburt, R.W. Ralston, R.P. Baker and E. Stern, "An Acoustoelectric Schottky-Diode Memory - Correlator Subsystem," IEEE Ultrason Symp Proc, pp 33-37, 1978.
- 1.7 R.W. Ralston and E. Stern, "Four-Wave Interactions in Acoustoelectric Integrating Correlators," IEEE Ultrason Symp Proc, pp 761-766, 1979.
- 1.8 D.L. Smythe, R.W. Ralston, and E. Stern, "A CCD-Programmable SAW Matched Filter," IEEE Ultrason Symp Proc, pp 767-770, 1979.
- 1.9 R.W. Ralston, D.L. Smythe, and E. Stern, "A SAW Accumulating Correlator with COD Readout," IEEE Ultrason Symp Proc, pp 771-775, 1979.
- 1.10 K.L. Davis, "Mixing Between Non-Collinear Surface Elastic Waves," Ph.D. Thesis, Purdue School of Electrical Engineering, 1973. Also Purdue University Technical Report, No. TR-EE-73-38, 1973 (Unpublished).
- 1.11 C.W. Lee and R.L. Gunshor, "Enhancement of Non-linearity in Surface - Acoustic - Wave Propagation from Coupling to Charge Carriers," Appl Phys Lett, 21 pp 11-13, 1972.

- 1.12 R.W. Myers, R.L. Gunshor, and C.L. Chen, "Second Harmonic SAW Generation In Devices Involving Semiconductor Coupling," Wave Electronics, 3, pp 285-309, 1979.
- 1.13 W.C. Wang, "A Novel Ultrasonic Oscillator and Convolution Integrator," presented at the Joint Services Technical Advisory Committee Meeting, Polytechnic Institute of Brooklyn, Brooklyn, NY, 1966; also W.C. Wang and P. Das, "Surface Wave Convolver Via Space Charge Nonlinearity, IEEE Ultrason Symp Proc, pp 316-321, 1972.
- 1.14 C.F. Quate and R.B. Thompson, "Convolution and Correlation in Real Time with Nonlinear Acoustics," Appl Phys Lett, 16, pp 494-496, 1970.
- 1.15 L.O. Svaasand, "Interaction Between Elastic Surface Waves in Piezoelectric Materials," Appl Phys Lett, 15, pp 300-302, 1969.
- 1.16 M.V. Luukkala and G.S. Kino, "Convolution and Time Inversion Using Parametric Interactions of Acoustic Surface Waves," Appl Phys Lett, 18, pp 393-394, 1971.
- 1.17 G.S. Kino, S. Ludvik, H.J. Shaw, W.R. Shreve, J.M. White, and D.K. Winslow, "Signal Processing by Parametric Interactions in Delay-Line Devices," IEEE Trans Microwave Theory and Tech, MTT-21, pp 244-255, 1973.
- 1.18 P. Defranould and C. Maerfeld, "A SAW Planar Piezoelectric Convolver," Proc IEEE, 64, pp 748-751, 1976.
- 1.19 C. Maerfeld, K. Gordon, and G.W. Farnell, "Resistive Losses in Acoustic Surface Wave Multistrip Couplers," IEEE Trans Sonics and Ultrason, SU-22, pp 358-368, 1975.
- 1.20 C. Maerfeld, "Multistrip Couplers," Wave Electronics, 2, pp 82-110, 1976.
- 1.21 T.M. Reeder, W.R. Shreve, and P.L. Adams, "A New Broadband Coupling Network for Interdigital Surface Wave Transducers," IEEE Trans Sonics and Ultrason, SU-19, pp 466-470, 1972.
- 1.22 P.H. Carr, "Second Harmonic Generation of Microwave Phonons in Quartz and Sapphire," Physical Review, 169, pp 718-729, 1968.
- 1.23 E.L. Adler, E. Bridoux, G. Coussot, and E. Dieulesaint, "Harmonic Generation of Acoustic Surface Waves in $\text{Bi}_{12}\text{GeO}_{20}$ and LiNbO_3 , IEEE Trans Sonics and Ultrason, SU-20, pp 13-16, 1973.

- 1.24 E.G.H. Lean, C.C. Tseng, and C.G. Powell, "Optical Probing of Acoustic Surface-Wave Harmonic Generation," Appl Phys Lett, 16, pp 32-35, 1970.
- 1.25 E.G.H. Lean, C.G. Powell, and L. Kuhn, "Acoustic Surface Wave Mixing on α -Quartz," Appl Phys Lett, 15, pp 10-12, 1969
- 1.26 R. Torquet, C. Carles, E. Bridoux and M. Moriametz, "Diffraction of Light By Finite Amplitude Acoustic Waves in Nonlinear Crystals," IEEE Ultrason Symp Proc, pp 147-150, 1972.
- 1.27 P.O. Lopen, "Second-Harmonic Generation of an Elastic Surface Wave in α -Quartz," J Appl Phys, 39, pp 5400-5404, 1968.
- 1.28 H.F. Tiersten and J.C. Bauhauer, "Second Harmonic Generation and Parametric Excitation of Surface Waves in Elastic and Piezoelectric Solids," J Appl Phys, 45, pp 4272-4287, 1974.
- 1.29 P.J. Vella, T.C. Padmore, and G.I. Stegeman, "Non-linear Surface Wave Interactions: Parametric Mixing and Harmonic Generation," J Appl Physics, 45, pp 1993-2006, 1974.
- 1.30 A.J. Slobodnik, Jr., "Non-linear Effects in Microwave Acoustic LiNbO_3 Surface-Wave Delay Lines," J Acoust Soc Am, 48, pp 203-210, 1970.
- 1.31 E.G. Lean and C.C. Tseng, "Nonlinear Effects in Surface Acoustic Waves," J Appl Phys, 41, pp 3912-3917, 1970.
- 1.32 E.G. Lean and C.G. Powell, "Nondestructive Testing of Thin Films by Harmonic Generation of Dispersive Rayleigh Waves," Appl Phys Lett, 19, pp 356-359, 1971.
- 1.33 J.W. Gibson, P.H.E. Meijer, "Nonlinearly Generated Harmonics and Attenuation of Rayleigh Waves on Crystalline Quartz," J Appl Phys, 45, pp 3288-3295, 1974.
- 1.34 E.L. Adler and A.A. Nassar, "Effect of Dispersion on Harmonic Generation of Acoustic Surface Waves," IEEE Ultrason Symp Proc, pp 268-270, 1973.
- 1.35 A.K. Ganguly and K.L. Davis, "Theory of Degenerate SAW Elastic Convolver," IEEE Ultrason Symp Proc, pp 715-720, 1979.

- 1.36 P.H. Carr, "Mixing of Noncollinear Elastic Surface Waves on LiNbO_3 ," J Appl Phys, 42, pp 5330-5332, 1971.
- 1.37 W.J. Tanski and W.G. Mayer, "Detection of Surface Wave Three-Phonon Interaction," Appl Phys Lett, 19, pp 148-150, 1971.
- 1.38 W.J. Tanski and W.G. Mayer, "Further Investigation of Non-Collinear Surface Wave Interaction," J Appl Phys, 44, pp 506-507, 1973.
- 1.39 M. Feldmann and J. Henaff, "Nonlinear Interactions Using Leaky Surface Waves," IEEE Ultrason Symp Proc, pp 310-313, 1972.
- 1.40 K.L. Davis and V.L. Newhouse, "Steering Acoustic Surface Waves by Nonlinear Mixing," Appl Phys Lett, 21, pp 323-325, 1972.
- 1.41 K.L. Davis and V.L. Newhouse, C.W. Lee, and R.L. Gunshor, "Active Surface Wave Directional Coupler," Elect Lett, 9, pp 199-201, 1973.
- 1.42 K.L. Davis and V.L. Newhouse, "Mixing Between Non-collinear Surface Elastic Waves," IEEE Trans Sonics and Ultrason, SU-22, pp 33-38, 1975.

CHAPTER II

- 2.1 A.J. Slobodnik, Jr., "Microwave Rectification Using Quartz," Air Force Cambridge Research Laboratories Tech Report No AFCRL-67-0143, pp 4-9, 1967 (unpublished).
- 2.2 H. Jeffreys, Cartesian Tensors, Cambridge University Press, New York, 1952.
- 2.3 W.P. Mason, Piezoelectric Crystals and Their Application to Ultrasonics, Van Nostrand, New York, pp 34, 463, 1950.
- 2.4 H.F. Tiersten, "Thickness Vibrations of Piezoelectric Plates," J Acous Soc Am, 35, pp 53-58, 1963.
- 2.5 A.K. Ganguly and K.L. Davis, "Theory of Degenerate SAW Elastic Convolver," IEEE Ultrason Symp Proc, pp 715-720, 1979.
- 2.6 L.E. Malvern, Introduction to the Mechanics of a Continuous Medium, Prentice-Hall, Englewood Cliffs, NJ, p 161, 1969.
- 2.7 D.F. Nelson, "Theory of Nonlinear Electroacoustics of Dielectric, Piezoelectric, and Pyroelectric Crystals," J Acoust Soc Am, 63, pp 1738-1748, 1978.
- 2.8 J.J. Campbell and W.R. Jones, "A Method for Estimating Optimal Crystal Cuts and Propagation Directions for Excitation of Piezoelectric Surface Waves," IEEE Trans Sonics and Ultrason, SU-15, pp 209-217, 1968.
- 2.9 P. Defranould and C. Maerfeld, "A SAW Planar Piezoelectric Convolver, Proc IEEE, 64, pp 748-751, 1976.
- 2.10 T.C. Lim, E.A. Kraut, and R.B. Thomson, "Nonlinear Materials for Acoustic Surface Wave Convolver," Appl Phys Lett, 20, pp 127-129, 1972.
- 2.11 G.S. Kino, S. Ludvik, H.J. Shaw, W.R. Shreve, J.M. White, and D.K. Winslow, "Signal Processing by Parametric Interactions in Delay-Line Devices," IEEE Trans Microwave Theory and Tech, MTT-21, pp 244-255, 1973.

- 2.12 R.A. Becker, S.A. Reible, and R.W. Ralston, "Comparison of Acoustic-Electric and Acoustic-Optic Signal Processing Devices," Proc of the Soc of Photo-Optical Instr Engr (SPIE) - Optical Signal Processing for C3I, 209, pp 126-133, 1979.
- 2.13 E.L. Adler, E. Bridoux, G. Coussot, and E. Dieulesaint, "Harmonic Generation of Acoustic Surface Waves in $\text{Bi}_{12}\text{GeO}_{20}$ and LiNbO_3 ," IEEE Trans Sonics and Ultrason, SU-20, pp 13-16, 1973.
- 2.14 E.G.H. Lean, C.C. Tseng, and C.G. Powell, "Optical Probing of Acoustic Surface-Wave Harmonic Generation," Appl Phys Lett, 16, pp 32-35, 1970.
- 2.15 P.O. Lopen, "Second-Harmonic Generation of an Elastic Surface Wave in α -Quartz," J Appl Phys, 39, pp 5400-5404, 1968.
- 2.16 A.J. Slobodnik, Jr., "Nonlinear Effects in Microwave Acoustic LiNbO_3 Surface-Wave Delay Lines," J Acoust Soc Am, 48, pp 203-210, 1970.
- 2.17 E.G. Lean and C.C. Tseng, "Nonlinear Effects in Surface Acoustic Waves," J Appl Phys, 41, pp 3912-3917, 1970.
- 2.18 E.G. Lean and C.G. Powell, "Nondestructive Testing of Thin Films by Harmonic Generation of Dispersive Rayleigh Waves," Appl Phys Lett, 19, pp 356-359, 1971.
- 2.19 E.G.H. Lean, C.G. Powell, and L. Kuhn, "Acoustic Surface Wave Mixing on α -Quartz," Appl Phys Lett, 15, pp 10-12, 1969.
- 2.20 E.L. Adler and A.A. Nassar, "Effect of Dispersion on Harmonic Generation of Acoustic Surface Waves," IEEE Ultrason Symp Proc, pp 268-270, 1973.
- 2.21 A.J. Slobodnik, Jr., "Surface Acoustic Waves and SAW Materials," Proc IEEE, 64, pp 581-595, 1976.
- 2.22 K.L. Davis, "Mixing Between Non-Collinear Surface Elastic Waves," Ph.D. Thesis, Purdue School of Electrical Engineering, 1973. Also Purdue University Technical Report, No. TR-EE-73-38, 1973 (unpublished).
- 2.23 A.J. Slobodnik, Jr., R.T. Delmonico, and E.D. Conway, "Microwave Acoustics Handbook-Volume 2. Surface Wave Velocities-Numerical Data," Air Force Cambridge Research Laboratories Tech Report No AFCRL-TR-74-0536, pp 109-112, 129-132, 1974 (unpublished).

CHAPTER III

- 3.1 G.S. Kino, S. Ludvik, H.J. Shaw, W.R. Shreve, J.M. White and D.K. Winslow, "Signal Processing by Parametric Interactions in Delay Line Devices," IEEE Trans Microwave Theory and Tech, MTT-21, pp 244-255, 1973.
- 3.2 D. Brodtkort and J.E. Laynor, "Fast Synchronization in a Spread Spectrum System Based on Acoustoelectric Convolvers," IEEE Ultrason Symp Proc, pp 561-566, 1978.
- 3.3 T.M. Reeder, W.R. Shreve and P.L. Adams, "A New Broadband Coupling Network for Interdigital Surface Wave Transducers," IEEE Trans Sonics and Ultrason, SU-19, pp 466-470, 1972.
- 3.4 I. Yao and S.A. Reible, "Wide Bandwidth Acoustoelectric Convolvers," IEEE Ultrason Symp Proc, pp 701-705, 1979.
- 3.5 A.J. Slobodnik, Jr., "Surface Acoustic Waves and SAW Materials," Proc IEEE, 64, pp 581-595, 1976.
- 3.6 A.J. Slobodnik, Jr., "Non-Linear Effects in Microwave Acoustic LiNbO₃ Surface Wave Delay Lines," J Acoust Soc Am, 48, pp 203-210, 1970.
- 3.7 R.A. Waldron, "Power Transfer Factors for Non-Uniformly Irradiated Interdigital Piezoelectric Transducers," IEEE Trans Sonics and Ultrason, SU-19, pp 448-453, 1972.
- 3.8 A.J. Slobodnik, Jr., and T.L. Szabo, "Design of Optimum Acoustic Surface Wave Delay Lines at Microwave Frequencies," IEEE Trans Microwave Theory and Tech, MTT-22, pp 458-462, 1974.
- 3.9 R.D. Colvin, P.H. Carr, G.A. Roberts, and E.J. Charlson, "1 GHz Surface-Acoustic-Wave Plate Convolvers," IEEE Ultrason Symp Proc, pp 711-714, 1979.

- 3.10 K.L. Davis and J.F. Weller, "SAW Attenuation in Metal Film - Coated Delay Lines, IEEE Ultrason Symp Proc, pp 659-662, 1979.
- 3.11 R.V. Schmidt and L.A. Coldren, "Thin Film Acoustic Surface Waveguides on Anisotropic Media," IEEE Trans Sonics and Ultrason, SU-22, pp 115-122, 1975.
- 3.12 P. Defranould and C. Maerfeld, "A SAW Planar Piezo-electric Convolver," Proc IEEE, 64, pp 748-751, 1976.
- 3.13 S.A. Reible, K.L. Wang and V.S. Dolat, "Transverse Modes in Acoustoelectric Convolvers," IEEE Ultrason Symp Proc, pp 48-53, 1978.
- 3.14 R.A. Waldron, Theory of Guided Electromagnetic Waves, Van Nostrand Reinhold, London, pp 448-483, 1970.
- 3.15 D. Marcuse, "Mode Conversion Caused by Surface Imperfections of a Dielectric Slab Waveguide," Bell System Tech Jour, pp 3187-3215, 1969.
- 3.16 The 5λ waveguide used for this paper was designed and fabricated by Anderson Laboratories, Inc, Bloomfield, CT, under contract to Rome Air Development Center, Hanscom AFB, MA. The aluminum integrating electrode originally had eleven interconnects to a long bus bar to alleviate the resistivity problem. These were completely removed for the laser probing experiments.
- 3.17 C. Maerfeld, "Multistrip Couplers," Wave Electronics 2, pp 82-110, 1976.
- 3.18 D.P. Morgan, "Effect of Dispersion in Surface-Acoustic-Wave Convolvers," IEEE Trans Sonics and Ultrason, SU-22, pp 274-277, 1975.
- 3.19 O.R. Baiocchi and I.M. Mason, "The Influence of Diffraction and Dispersion on the Fidelity of Degenerate Convolution," IEEE Trans Sonics and Ultrason, SU-22, pp 347-354, 1975.
- 3.20 A.K. Ganguly and K.L. Davis, "Theory of Degenerate SAW Elastic Convolver," IEEE Ultrason Symp Proc, pp 715-720, 1979.
- 3.21 V.V. Sktykov, I.M. Mason and M.D. Motz, "On the Anisotropy of Guided Acoustic Surface Wave Degenerate Convolution," IEEE Trans Sonics and Ultrason, SU-22, pp 131-136, 1975.

- 3.22 R.A. Becker and I. Yao, MIT Lincoln Laboratory, Feb 1980, Private communication.
- 3.23 W.R. Smith, Hughes Aircraft Co, Feb 1980, private communication.
- 3.24 J.H. Cafarella, MIT Lincoln Laboratory, Feb 1980, private communication.
- 3.25 The device labeled T-CSF in Table 3.2 was a convolver made by Thomson-CSF, Cagnes-sur-Mer, France and was on loan from MIT Lincoln Laboratory. It is described in Reference 3.12.
- 3.26 J. Temmyo and S. Yoshikawa, "Aluminum Evaporation Conditions for SAW Interdigital Transducers," IEEE Trans Sonics and Ultrason, SU-27, pp 219-221, 1980.
- 3.27 J.H. Goll and R.C. Bennett, "Reactive Output Tuning of High BT Product SAW Convolver," IEEE Ultrason Symp Proc, pp 44-47, 1978.
- 3.28 J.H. Cafarella, W.M. Brown, Jr., E. Stern, and J.A. Alusow, "Acoustoelectric Convolver for Programmable Matched Filtering in Spread Spectrum Systems," Proc IEEE, 64, pp 756-759, 1976.
- 3.29 E.G. Lean and C.G. Powell, "Nondestructive Testing of Thin Films by Harmonic Generation of Dispersive Rayleigh Waves," Appl Phys Lett, 19, pp 356-359, 1971.
- 3.30 H.F. Tiersten and B.K. Sinha, "A Perturbation Analysis of the Attenuation and Dispersion of Surface Waves," J Appl Phys, 49, pp 87-95, Jan 1978.
- 3.31 R.A. Becker and D.H. Hurlburt, "Wideband LiNbO_3 Elastic Convolver With Parabolic Horns," IEEE Ultrason Symp Proc, pp 729-731, 1979.
- 3.32 W.R. Smith, Jr., "Minimizing Multiple Transit Echoes in Surface Wave Devices," IEEE Ultrason Symp Proc, pp 410-413, 1973.
- 3.33 C.S. Hartmann, W.S. Jones and H. Vollers, "Wideband Uni-directional Interdigital Surface Wave Transducers," IEEE Trans Sonics and Ultrason, SU-19, pp 378-381, 1972.
- 3.34 J. Otomo, S. Nichiyama, Y. Kanno, and K. Shibayama, "UHF Range SAW Filters Using Group - Type Uni-Directional Interdigital Transducers," 31st Freq Control Symp, pp 275-280, 1977.

- 3.35 C. Maerfeld, K. Gordon, and G.W. Farnell, "Resistive Losses in Acoustic Surface Wave Multistrip Couplers," IEEE Trans Sonics and Ultrason, SU-22, pp 358-368, 1975.
- 3.36 C.W. Chapman and T.W. Bristol, "The Analysis and Design of Broadband Fractional Efficiency Multistrip Couplers," IEEE Trans Sonics and Ultrason, SU-23, pp 174-184, 1976.
- 3.37 I. Yao, "High Performance Elastic Convolver with Parabolic Horns," IEEE Ultrason Symp Proc, Session F, 1980.

CHAPTER IV

- 4.1 E.G.H. Lean, C.G. Powell, and L. Kuhn, "Acoustic Surface Wave Mixing on α -Quartz," Appl Phys Lett, 15, pp 10-12, 1969.
- 4.2 A.J. Slobodnik, Jr., "Nonlinear Effects In Microwave Acoustic LiNbO₃ Surface-Wave Delay Lines," J Acous Soc Am, 48, pp 203-210, 1970.
- 4.3 E.G. Lean and C.C. Tseng, "Nonlinear Effects in Surface Acoustic Waves," J Appl Phys, 41, pp 3912-3917, 1970.
- 4.4 E.L. Adler and A.A. Nassar, "Effect of Dispersion on Harmonic Generation of Acoustic Surface Waves," IEEE Ultrason Symp Proc, pp 268-270, 1973.
- 4.5 E.G. Lean and C.G. Powell, "Nondestructive Testing of Thin Films by Harmonic Generation of Dispersive Rayleigh Waves," Appl Phys Lett, 19, pp 356-359, 1971.
- 4.6 A.J. Budreau and P.H. Carr, "Direct SAW Frequency Synthesizer," IEEE Ultrason Symp Proc, pp 511-513, 1977.
- 4.7 C. Maerfeld, K. Gordon, and G.W. Farnell, "Resistive Losses in Acoustic Surface Wave Multistrip Couplers," IEEE Trans Sonics and Ultrason, SU-22, pp 358-368, 1975.
- 4.8 F.G. Marshall, C.O. Newton, and E.G.S. Paige, "Surface Acoustic Wave Multistrip Components and Their Applications," IEEE Trans Microwave Theory and Tech, MTT-21, pp 216-225, 1973.
- 4.9 T.L. Szabo, "Surface Acoustic Wave Losses of Thin-Film Gratings," Appl Phys Lett, 22, pp 484-486, 1973.
- 4.10 W.R. Smith, H.M. Gerard, J.H. Collins, T.M. Reeder and H.J. Shaw, "Design of Surface Wave Delay Lines with Interdigital Transducers," IEEE Trans Microwave Theory and Tech, MTT-17, pp 865-873, 1969.

- 4.11 T.M. Reeder and W.R. Sperry, "Broad Band Coupling to High-Q Resonant Loads," IEEE Trans Microwave Theory and Tech, MTT-20, pp 453-458, 1972.
- 4.12 R. LaRosa and S.J. Kerbel, "Synthesis of Transfer Functions by Parallel-Channel SAW Filter Banks," IEEE Ultrason Symp Proc, pp 322-327, 1976.
- 4.13 T.M. Reeder, W.R. Shreve and P.L. Adams, "A New Broadband Coupling Network for Interdigital Surface Wave Transducers," IEEE Trans Sonics and Ultrason, SU-19, pp 466-470, 1972.
- 4.14 A. Slobodnik, Jr., G. Roberts, J. Silva, J. Sethares and T. Szabo, "UHF Switchable SAW Filterbanks," IEEE Ultrason Symp Proc, pp 486-489, 1978.
- 4.15 A. Slobodnik, Jr., G. Roberts, J. Silva, W. Kearns, J. Sethares, T. Szabo, "Switchable SAW Filterbanks at UHF," IEEE Trans Sonics and Ultrason, SU-26, pp 120-126, 1979.
- 4.16 H.M. Gerard, P.S. Yao and O.W. Otto, "Performance of a Programmable Radar Pulse Compression Filter Based on a Chirp Transformation with RAC Filters," IEEE Ultrason Symp Proc, pp 947-951, 1977.
- 4.17 C. Lardat, "Improved SAW Chirp Spectrum Analyzer with 80 dB Dynamic Range," IEEE Ultrason Symp Proc, pp 518-521, 1978.

CHAPTER V

- 5.1 P.H. Carr, "Mixing of Noncollinear Elastic Surface Waves on LiNbO_3 ", J Appl Phys, 42, pp 5330-5332, 1971.
- 5.2 V.L. Newhouse, C.L. Chen, and K.L. Davis, "Possibility of Switching and Steering Surface Waves by Nonlinear Mixing in Anisotropic Media", J Appl Phys 43, pp 2603-2608, 1972.
- 5.3 K.L. Davis and V.L. Newhouse, "Steering Acoustic Surface Waves by Nonlinear Mixing," Appl Phys Lett, 21, pp 323-325, 1972.
- 5.4 K.L. Davis and V.L. Newhouse, "Mixing Between Non-collinear Surface Elastic Waves," IEEE Trans Sonics and Ultrason, SU-22, pp 33-38, 1975.
- 5.5 K.L. Davis, "Mixing Between Non-Collinear Surface Elastic Waves", PhD Thesis, Purdue School of Electrical Engineering, 1973. Also, Purdue University Technical Report, No TR-EE 73-38, 1973 (unpublished).
- 5.6 D. Murray and E.A. Ash, "Precision Measurement of SAW Velocities," IEEE Ultrason Symp Proc, pp 823-826, 1977.
- 5.7 A.J. Slobodnik, Jr., R.T. Delmonico, and E.D. Conway, "Microwave Acoustics Handbook Volume 2. Surface Wave Velocities-Numerical Data," Air Force Cambridge Research Laboratories Tech Report No AFCRL-TR-74-0536, pp 109-112, 129-132, 1974 (unpublished).
- 5.8 K. Shibayama, K. Yamanouchi, H. Sato, and T. Maguro, "Optimum Cut for Rotated Y-Cut LiNbO_3 Crystal Used as the Substrate of Acoustic Surface Wave Filters," Proc IEEE, 64, pp 595-597, 1976.
- 5.9 R.A. Waldron, "Power Transfer Factors for Nonuniformly Irradiated Interdigital Piezoelectric Transducers," IEEE Trans Sonics and Ultrason, SU-19, pp 448-453, 1972.

APPENDIX A

- A.1 A.J. Slobodnik, Jr., "Microwave Frequency Acoustic Surface Wave Propagation Losses in LiNbO_3 ", Appl Phys Lett, 14, pp 94-96, 1969.
- A.2 A.J. Slobodnik, Jr., "Nonlinear Effects in Microwave Acoustic LiNbO_3 Surface-Wave Delay Lines", J Acoust Soc Am, 48, pp 203-210, 1970.
- A.3 A.A. Oliner, Editor, Topics in Applied Physics: Acoustic Surface Waves, 24, Springer-Verlag, New York, pp 225-303, 1978.
- A.4 A.J. Slobodnik, Jr., "Microwave Acoustic Surface Wave Investigations Using Laser Light Deflection", Proc IEEE, 58, pp 488-490, 1970.
- A.5 B.A. Richardson and G.S. Kino, "Probing of Elastic Surface Waves in Piezoelectric Media", Appl Phys Lett, 16, pp 82-84, 1970.
- A.6 E. Salzmann, T. Plieninger and K. Dransfeld, "Attenuation of Elastic Surface Waves in Quartz at Frequencies of 316 MHz and 1047 MHz", Appl Phys Lett, 13, pp 14-15, 1968.
- A.7 A.J. Slobodnik, Jr., and E.D. Conway, "The Effects of Beam Steering on the Design of Microwave Acoustic Surface Wave Devices", IEEE Int'l Microwave Symp Digest, pp 314-318, 1970.
- A.8 T.L. Szabo and A.J. Slobodnik, Jr., "The Effect of Diffraction on the Design of Acoustic Surface Wave Devices", IEEE Trans Sonics and Ultrason, SU-20, pp 240-251, 1973.
- A.9 P. Beckmann and A. Spizzichino, The Scattering of Electromagnetic Waves from Rough Surfaces, Macmillan, New York, pp 34-48, 1963.
- A.10 J.D. DeLorenzo and E.S. Cassedy, "A Study of the Mechanism of Sea Surface Scattering", IEEE Trans Ant and Prop, AP-14, pp 611-620, 1966.
- A.11 E. Salzmann and D. Weismann, "Optical Detection of Rayleigh Waves", J Appl Phys, 40, pp 3408-3409, 1969.

- A.12 H. Engan, "Phase Sensitive Laser Probe for High Frequency Surface Acoustic Wave Measurements", IEEE Trans Sonics and Ultrason, SU-25, pp 372-377, 1978.
- A.13 B. Rossi, Optics, 2nd edition, Addison-Wesley, Reading, Mass., p 210 and pp 372-375, 1959.
- A.14 Data sheet from Crystal Technology, Inc., Mountain View, CA, on properties of acoustic single crystals.
- A.15 M. Born and E. Wolf, Principles of Optics, 4th edition, Pergamon, New York, p 631, 680, 1970.

APPENDIX C

- C.1 A.J. Slobodnik, Jr., T.L. Szabo, and K.R. Laker, "Miniature Surface - Acoustic - Wave Filters," Proc IEEE, 67, pp 129-146, 1979.
- C.2 J.S. Schoenwald, "Ultra Low Shape Factor SAW Filters Using Assymmetrically Truncated Transducers," IEEE Ultrason Symp Proc, pp 478-481, 1978.
- C.3 T.M. Reeder, W.R. Shreve and P.L. Adams, "A New Broad-band Coupling Network for Interdigital Surface Wave Transducers," IEEE Trans Sonics and Ultrason, SU-19, pp 466-470, 1972.
- C.4 R. LaRosa and S.J. Kerbel, "Synthesis of Transfer Functions by Parallel - Channel SAW Filter Banks," IEEE Ultrason Symp Proc, pp 322-327, 1976.
- C.5 R.D. Colvin, P.H. Carr, and E.J. Charlson, "Monolithic SAW Mixer with Single Sideband Output," IEEE Ultrason Symp Proc, pp 724-727, 1978.
- C.6 T.L. Szabo, "Interdigital Transducer Models: Design Options," IEEE Ultrason Symp Proc, pp 701-704, 1978; also see T.L. Szabo, K.R. Laker, and E. Cohen, "Interdigital Transducer Models: Their Impact on Filter Synthesis," IEEE Trans Sonics and Ultrason, SU-26, pp 321-333, 1979.

APPENDIX A

A LASER PROBE FOR MICROWAVE ACOUSTIC SURFACE WAVE INVESTIGATIONS

A.1 Spot size much larger than acoustic wavelength

The subject of this appendix is the detailed description of a laser probe developed for studying microwave acoustic surface wave phenomena.A.1-A.5 This probe is essential for obtaining design data for all surface wave devices operating in the VHF through microwave frequencies where small wavelengths make the use of mechanical probes quite difficult.A.5

The basic operation of this device is illustrated schematically in Figure A.1. Coherent light from a low-power laser is directed onto a surface-wave delay line. Due to the presence of the surface wave on the crystal acting as a diffraction grating, light is deflected into side lobes in addition to the specular direction. The intensities of these side lobes, which are directly related to the intensity of the surface wave, can then be monitored by a photomultiplier tube. This provides a convenient method of probing the behavior of the surface wave. For example, by scanning the laser along the acoustic beam one can measure the acoustic propagation loss.A.1,A.6 At microwave frequencies this is, of course, an important quantity as it

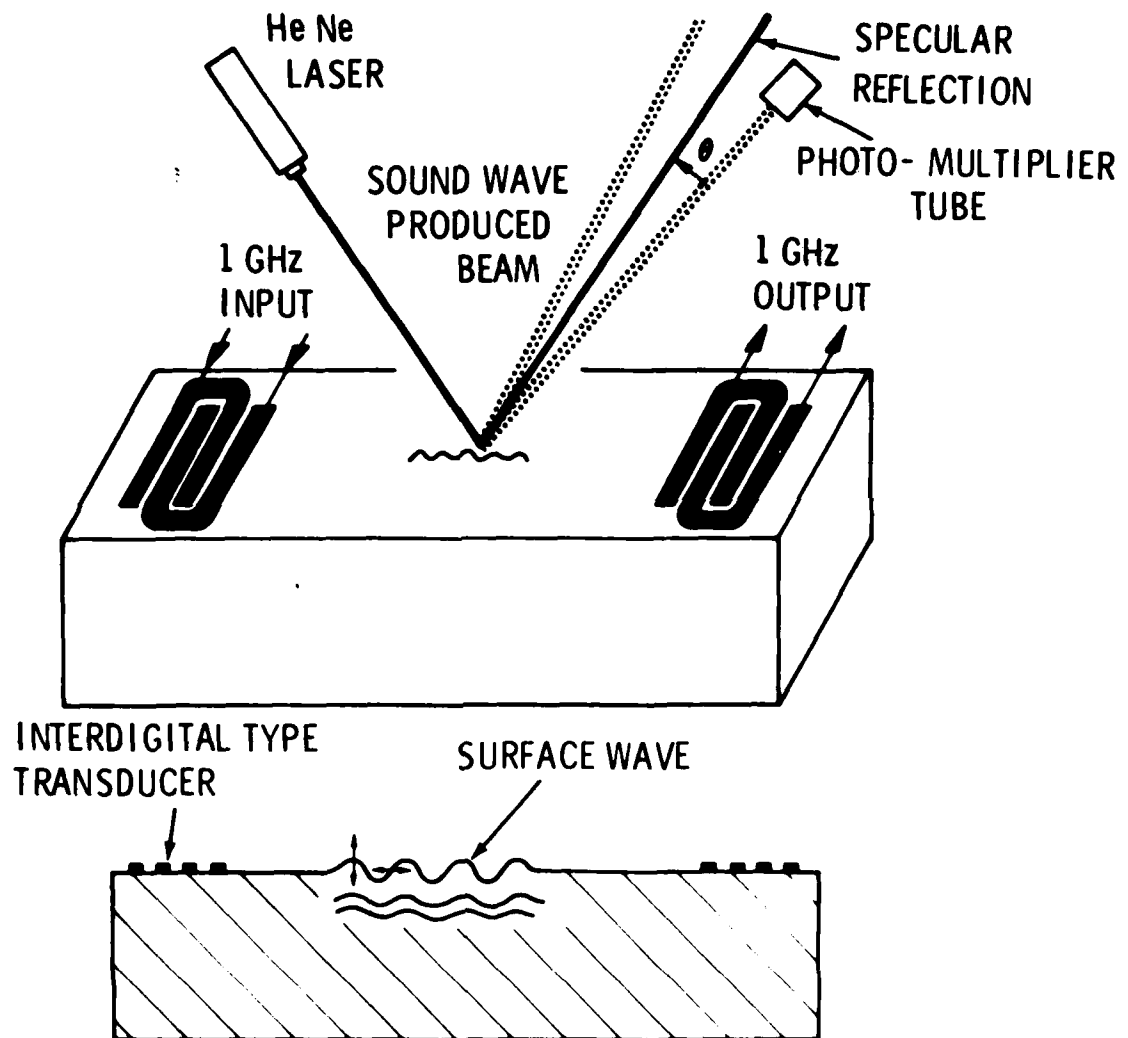


Figure A.1 Schematic diagram of a surface wave and the laser probe used for investigating surface wave devices.

is a significant portion of the overall insertion loss of any device. By investigating various materials with the laser probe, one can choose the material having the lowest loss for a given device application. In addition, by scanning the laser across the acoustic beam, the surface-wave profile or shape of the beam can be determined.^{A.7,A.8} This information also provides valuable design data as will be seen in section A.3. The remainder of this section provides a detailed description of the laser deflection technique.

It is well known in electromagnetic theory that a periodically modulated surface causes plane waves of electromagnetic energy to be deflected into sidelobes in addition to the specular direction.^{A.9,A.10} The angular directions of these sidelobes are given by the grating equation

$$\sin \theta_m = \sin \theta_o + \frac{m\lambda}{\Lambda}, \quad m = 0, \pm 1, \pm 2, \dots \quad (\text{A.1})$$

where λ is the wavelength of the incident energy, Λ is the surface wavelength, θ_o is the angle of incidence (from vertical), and θ_m is the scattering angle (from vertical). $m=0$ is the specular direction. $m = \pm 1$ is always used for acoustic work since these sidelobes have the largest amplitude.^{A.9} This scattering process is shown schematically in Figure A.2.

The next question is, "What is the amplitude of each

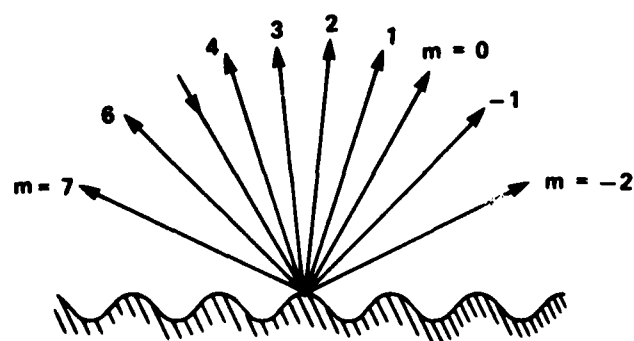


Figure A.2 The directions in which various modes, m , are scattered by a periodic surface, or directions of the side lobes of the scattering diagram.

sidelobe relative to the specular reflection?" This is expressed by a scattering coefficient

$$\rho = \frac{E_2}{E_{20}} \quad (\text{A.2})$$

where E_{20} is the field reflected in the direction of the specular reflection and E_2 is the field reflected into one of the sidelobes. L is a half surface that the E wave is incident upon - Figure A.3.

For $L \gg \lambda$, a smooth perfectly conducting surface will concentrate practically all of the reflected energy into the specular direction, $m = 0$. However, for a rough surface, one has^{A.9}

$$\rho(\theta_0, \theta_m) = \sec \theta_0 \cdot \frac{1 + \cos(\theta_0 + \theta_m)}{\cos \theta_0 + \cos \theta_m} \cdot \frac{1}{\Lambda} \int_0^\Lambda e^{i\vec{v} \cdot \vec{r}} dx + \frac{c(n_1)}{2L}, \quad (\text{A.3})$$

where $\frac{c(n_1)}{2L}$ is a correction term or "edge effect". This correction term is negligible when either $n_1 = 0$, i.e. when L/Λ is integral, or when $L \gg \Lambda$. In our case, L is the laserbeam diameter, and Λ is the acoustic surface wavelength.

The scattering angles θ_m are determined by the grating equation (A.1). To each integer m there corresponds a scattered mode of laser light propagated in a direction

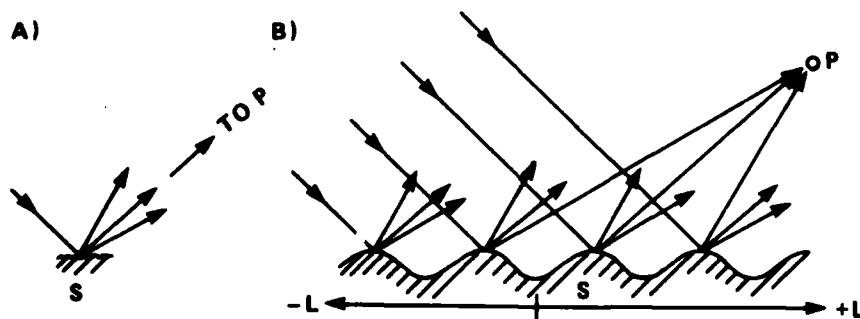


Figure A.3 The field at the point of observation consists (a) of a single mode in the Fraunhofer zone, (b) of the sum of many scattering modes in the Fresnel zone.

θ_m . The total number of possible modes is limited by the condition A.9

$$|\sin \theta_m| \leq 1. \quad (\text{A.4})$$

The mode with $m = 0$ is seen to be the specular mode. The modes $m = \pm 1$ lie to either side of the specular direction as shown in Figure A.2. The modes continue thus to either side of the specular mode until the last modes that will satisfy Equation (A.4) are reached; they are propagated at angles near $\pm \pi/2$. If λ/Λ is small, m will run through a large number of integral values before Equation (A.4) is violated. If the wavelength of the incident radiation is small compared to the wavelength of the surface, the incident wave will be broken up into many scattering waves. On the other hand, for $\lambda/\Lambda \gg 1$ there will be only the mode $m=0$, so that for $\lambda \gg \Lambda$ any periodic surface will reflect specularly regardless of its roughness.

The directions of the maxima of the lobes are given by Equation (A.1) and their amplitude by Equation (A.3); the only other interesting quantity is the half-width of the lobes, $\Delta\theta_m$. This is given as A.9

$$\Delta\theta_m = \frac{\lambda}{2L} \sec \theta_m \quad (\text{A.5})$$

with the following conditions: (a) $\lambda \ll 2L$, and (b) θ_m not too near $\pi/2$ because as $\theta_m \rightarrow \pi/2$, $\Delta\theta_m \rightarrow 0$. Thus for a fixed θ_m and λ , the half width $\Delta\theta_m$ increases as L

decreases. Figure A.3b may help to visualize this. As the laser spot grows smaller (L decreases), there will be less coherent contributions at point P . As there are less contributions at P the radiation pattern (sidelobes) will broaden. This figure also helps visualize the growth of the error term, or "edge effect", in Equation (A.3).

The final step is to relate relative deflected light intensity measurements to the amplitudes of the surface wave disturbances. By assuming the surface to be purely sinusoidal, the integral in Equation (A.3) can be evaluated. All terms are squared to convert amplitude to intensity, hence $I(\theta_0, \theta_m)$ instead of $\rho(\theta_0, \theta_m)$. The error term $\frac{C(n_1)}{2L}$ is still there and subject to the same conditions as in Equation (A.3).

The ratio of the intensity of light deflected into sidelobes to that specularly reflected from a smooth surface of the same material is given by A.3, A.9

$$I(\theta_0, \theta_m) = \sec^2 \theta_0 \left[\frac{1 + \cos(\theta_0 + \theta_m)}{\cos \theta_0 + \cos \theta_m} \right]^2$$

$$J_m^2 \left[\frac{2\pi h}{\lambda} (\cos \theta_0 + \cos \theta_m) \right], \quad (A.6)$$

where h is the amplitude of the sinusoidal surface disturbance. Since only the first diffraction order ($m = -1$) of extremely small amplitude surface waves will be considered, the Bessel function may be approximated to

within a high degree of accuracy by one-half its argument.

This means

$$I(\theta_0, \theta_{-1}) = \sec^2 \theta_0 \left[1 + \cos(\theta_0 + \theta_{-1}) \right]^2 \left[\frac{\pi h}{\lambda} \right]^2 \quad (\text{A.7})$$

The actual surface acoustic wave disturbance is not purely sinusoidal, but the error due to this is quite small.^{A.3} One final comment on the use of the Bechmann-Spizzichino theory - this theory assumes that the deflected light is caused by an actual surface disturbance and not by any modulation of the index of refraction which might be caused by the surface wave. The former effect is indeed predominant for the conditions of the present experiments, as demonstrated by the results of Salzmann and Weismann.^{A.11}

A detailed block diagram of the experimental laser probe system is shown in Figure A.4. By square-wave modulating the electromagnetic input to the interdigital transducer, the light deflected by the surface wave is also square wave modulated. This allows phase-locked detection to be used, and results in an improved signal-to-noise ratio. Using this system, measurements have been easily made of acoustic surface wave power density as low as 0.08 mw/mm at frequencies as high as 4 GHz.^{A.3} A more detailed diagram of the optical detection circuit is given in Figure A.5. The beam expander is used only for applications requiring a laser spot small with respect to the acoustic beam. Recall that the diameter of a focussed diffraction-

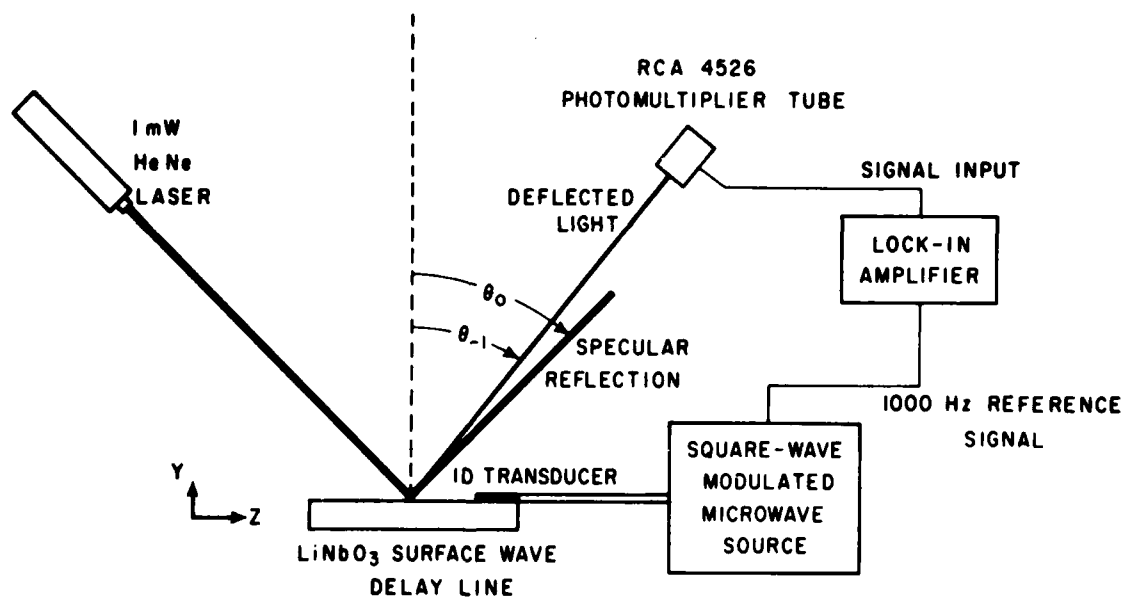


Figure A.4 Detailed block diagram of the laser probe system used for investigating microwave-acoustic surface waves. The angles shown in this figure are defined in Equation (A.1).

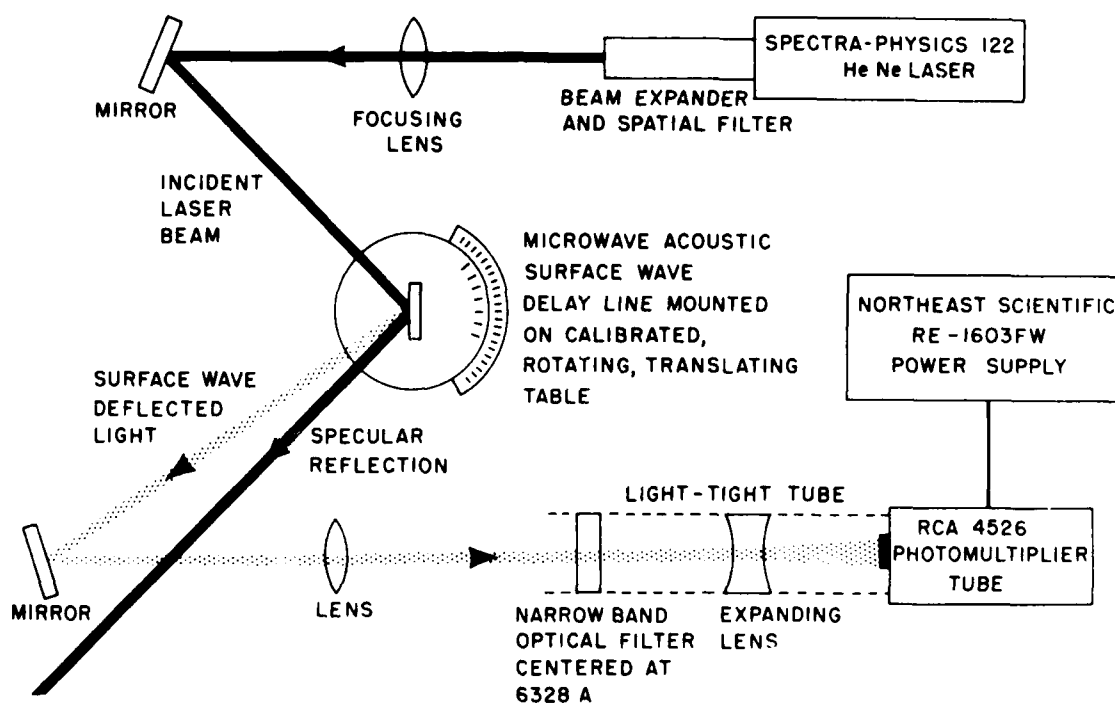


Figure A.5 Detailed schematic diagram of the optical circuit used with the laser probe.

limited spot is inversely proportional to the input beam diameter. The optical filter is used to reject stray light, and the expanding lens fills the entire aperture of the photomultiplier tube and therefore eliminates effects of an inhomogeneous light sensitive surface. The rotating table is, of course, used to obtain the precise angles required by Equation (A.1) as well as to translate the delay line in the two perpendicular directions. A photograph of the overall system is shown in Figure A.6, and a closeup of the rotating table is given in Figure A.7.

The validity of Equation (A.1) was experimentally confirmed by measuring the angle of deflection of the first sidelobe for light incident at various angles on surface waves propagating along the Z-axis of Y-cut LiNbO_3 .^{A.3} Experimental results for two frequencies (635 MHz and 1950 MHz) are compared with the theory in Figure A.8. Agreement is excellent.

One final comment on the laser deflection technique should be made. All quantitative deflected-light measurements were taken directly from the output meter on the lock-in amplifier. This was done only after extensive calibration with precision optical attenuators showed the entire photomultiplier, lock-in system to be linear.

A.2 Spot Size Much Smaller Than Acoustic Wavelength

The laser probe described in Section A.1 above gives amplitude informatin only. However, if the spot size can be

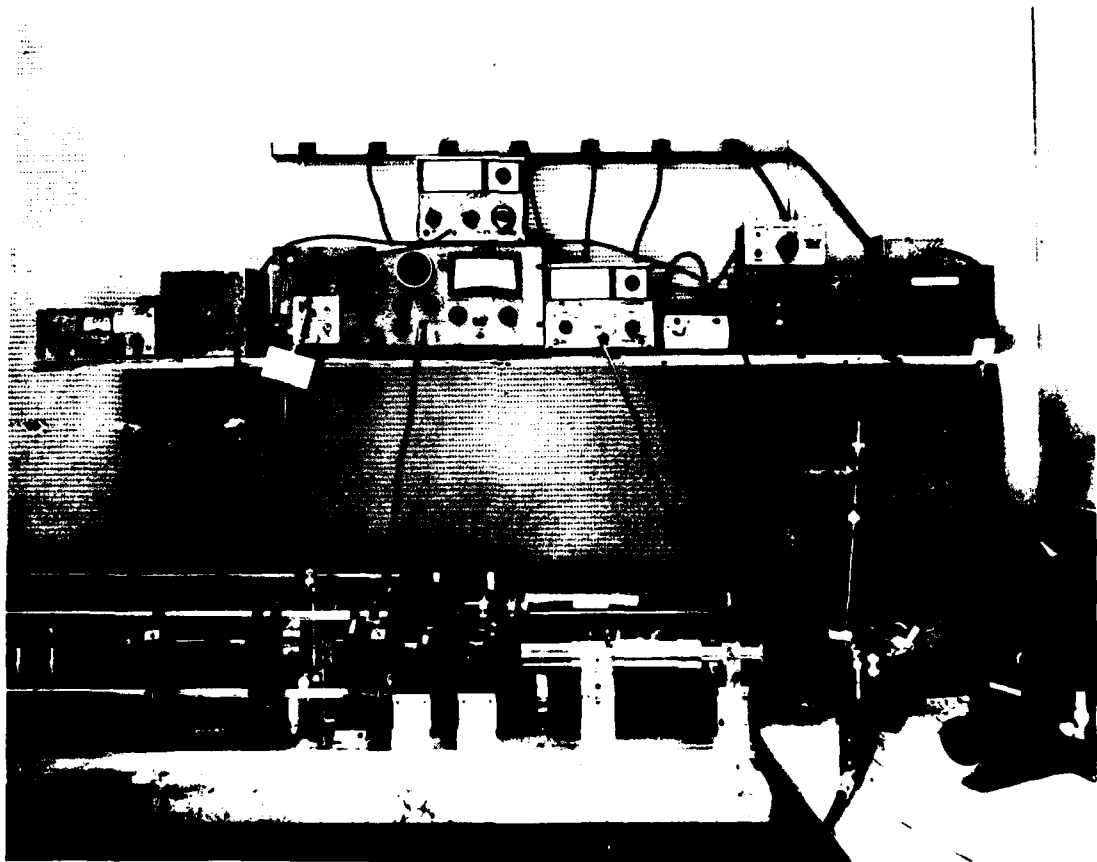


Figure A.6 Photograph of the overall microwave and optical circuits used for laser light deflection experiments.

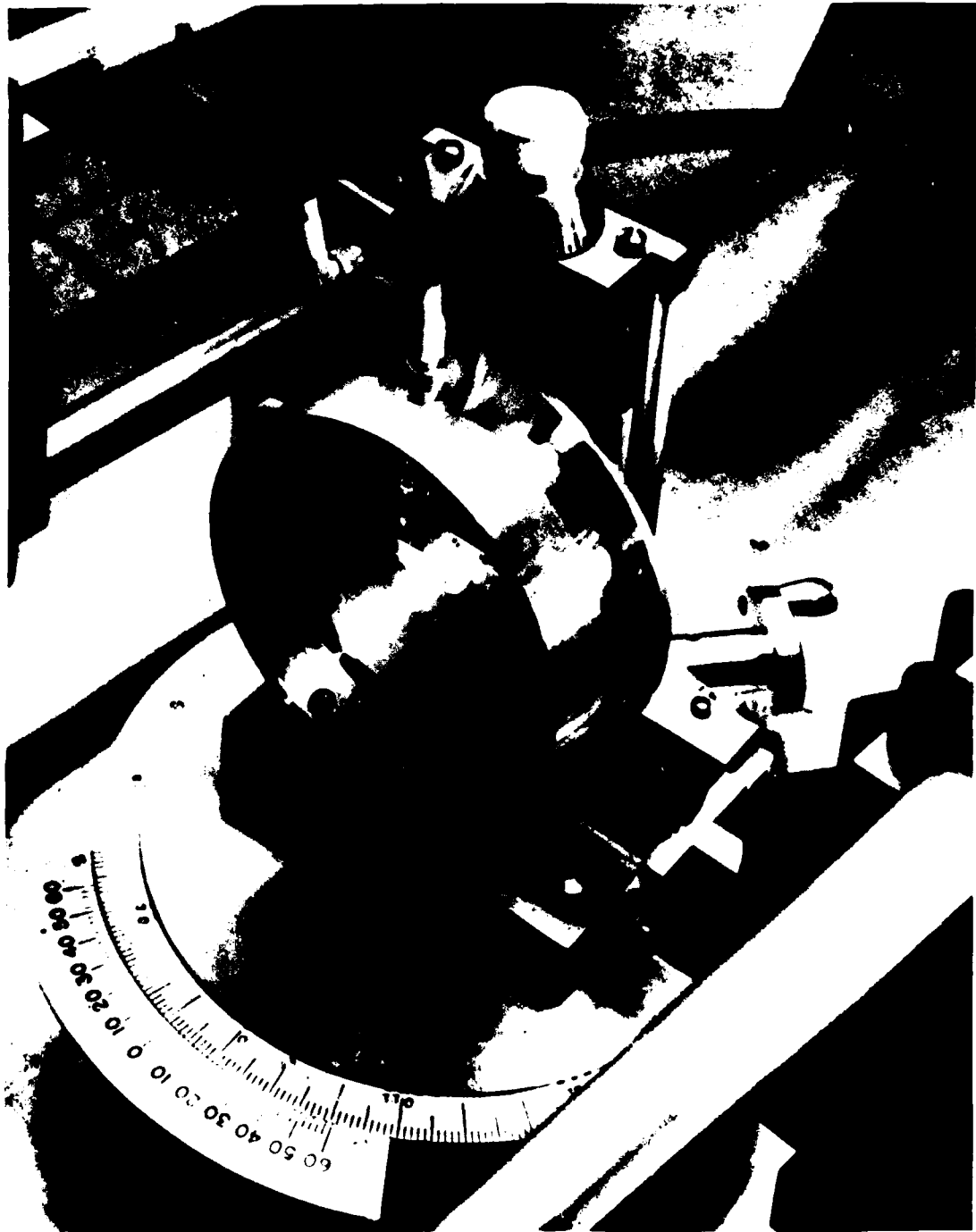


Figure A.7 Photograph of the rotating, translating table used in the optical circuit. Also shown is a surface-wave delay line protected from contamination by a hermetically sealed can. Laser measurements are made through the AR-coated optical window.

made small with respect to the acoustic wavelength, it is possible to get both phase and amplitude information. Helge Engan has given a good survey of the half dozen or so variations possible in the setup of hardware to implement this method. In the same paper, he has published his setup which in the opinion of this author is the best yet.^{A.12} The variations all have in common the splitting of the beam prior to SAW interaction to establish a reference, and they all use the specular reflection $m=0$. Most of these methods use a physical "knife edge" which partially blocks the transmission of the specularly reflected laser beam. The SAW then modulates the deflection of the laser beam causing a periodic tilting of the light beam and hence a continuously varying amplitude at the detector. Engan's method does not use a "knife edge". Details can be found in Reference A.12. There are numerous advantages in this method; the most important are improved sensitivity and high frequency operation. Engan's method also differs in that it still works if the laser spot is larger than an acoustic wavelength, thus, it should be capable of detecting 3 GHz. In the published version, the 450 MHz limit was due to an optical modulator.

A.3 Applications

The most important applications for the laser probe are the measurement of beam steering, diffraction, and attenuation. Each is illustrated schematically in Figure

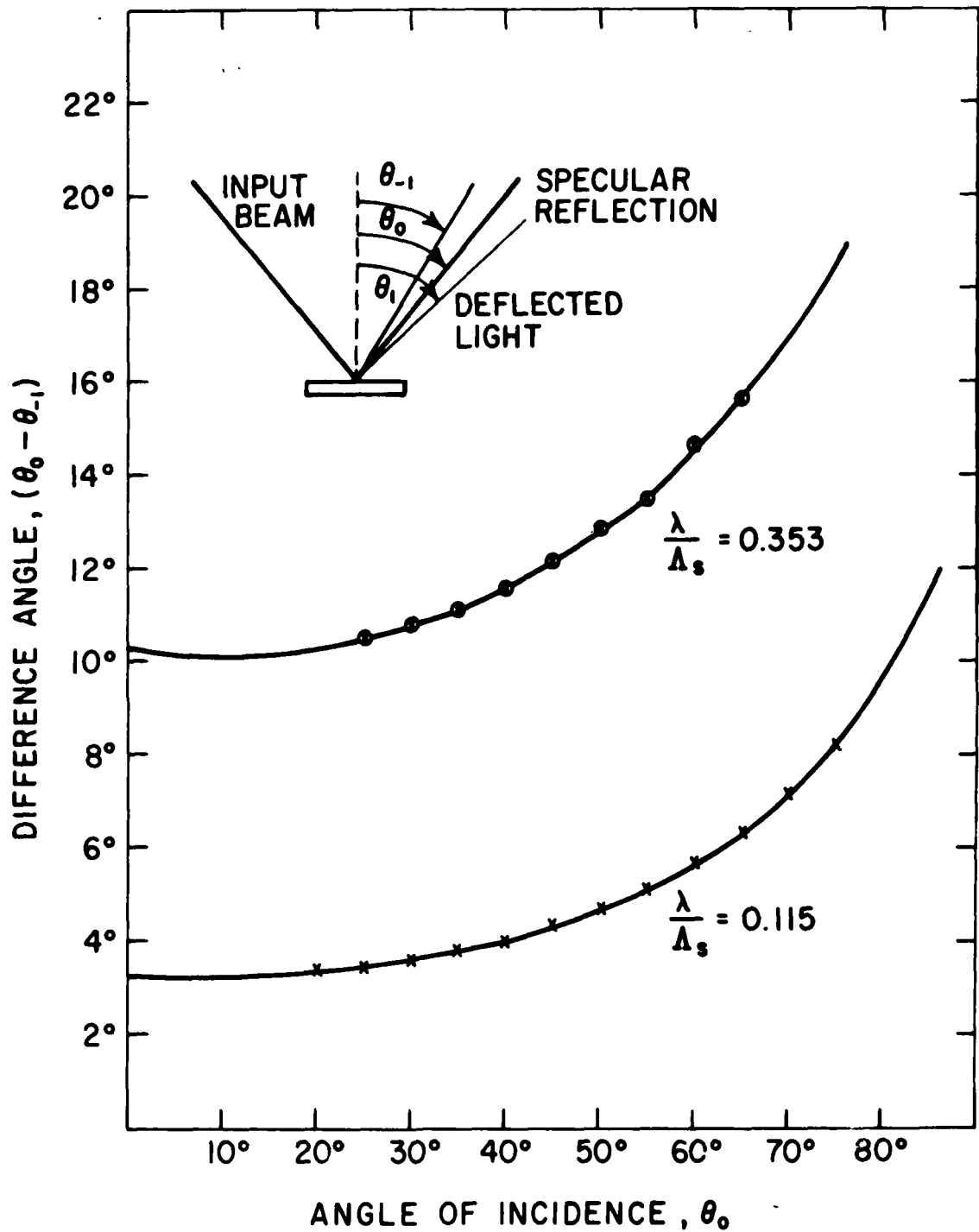


Figure A.8 Confirmation of the grating equation using deflected light from microwave-acoustic surface waves at 635 and 1950 MHz. Experimental data points are shown together with theoretical curves derived from Equation (A.1).

A.9 which depicts the launching and subsequent propagation of an acoustic surface wave on an anisotropic crystalline substrate. To measure attenuation (or propagation) losses, one uses a laser beam wider than the acoustic beam (for averaging purposes) and then scans the light along the acoustic path.A.1,A.3,A.6 To avoid non-linear effects, low input powers must be used. Illustrations of low-power attenuation curves as well as high-power nonlinear effects are shown in References A.2 and A.3.

Beam steering arises from the misalignment of transducers from the desired pure mode crystalline axes, causing the group and phase-velocity vectors of the surface wave to lie in different directions. The acoustic beam can then miss part or all of the output transducer. Beam steering can be studied by focusing the laser to a spot small with respect to the acoustic beamwidth, and scanning the laser across the acoustic beam. The angle θ defines the direction of propagation (phase velocity direction) with respect to a reference crystalline axis, while the angle ϕ defines the power flow (group velocity) from the phase velocity direction (Figure A.9). Although practical devices are generally designed for surface wave propagation along pure-mode axes (specific directions for which $\phi = 0$), some unintentional misalignment always results thus causing beam steering.A.7 The slope of the power flow angle $\partial\phi / \partial\theta$ can be used to provide a direct measure of the seriousness of a given misalignment in the

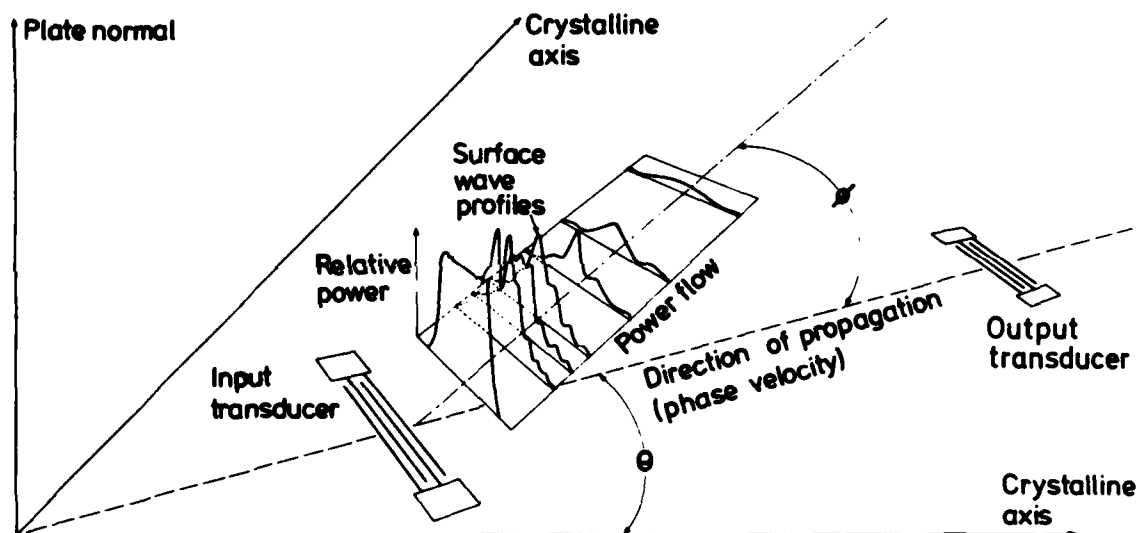


Figure A.9 Schematic representation of the launching and subsequent propagation of an acoustic surface wave on a crystalline substrate. Angle θ defines the direction of propagation with respect to the reference crystalline axis, and angle ϕ defines the deviation of power flow from the phase velocity direction. A pure-mode axis is one for which $\phi = 0$.

amount of beam steering it causes. High values of $\partial\phi/\partial\theta$ obviously result in large amounts of beam steering.

Diffraction^{A.8} is also illustrated in Figure A.9 by the changing acoustic beam profile and eventual beam spreading. Depending on the value of $\partial\phi/\partial\theta$, diffraction may be quite drastically increased or significantly retarded in contrast to the analogous case of light diffraction in an isotropic medium.

A.4 Determining Spot Size

This section discusses measurement of laser spot size. The diffraction limited spot size is^{A.13}

$$D = \frac{2.44 \lambda f}{a}, \quad (\text{A.8})$$

where D is the spot diameter (to first dark ring), λ is the laser wavelength, f is focal length of the lens, and a is the lens diameter. Assume the image is located at the focal length of the lens. In our case the diffraction limited spot size

$$D = 51 \mu\text{m} = \frac{(2.44) (0.6328 \mu\text{m}) (393 \text{ mm})}{12 \text{ mm}}. \quad (\text{A.9})$$

The laser was scanned across the aluminum film of the device in Figure 3.5 onto the bare crystal. The result is the curve labeled "metal film" in Figure A.10; it has been normalized to go from 100 to 0. The specular reflection was

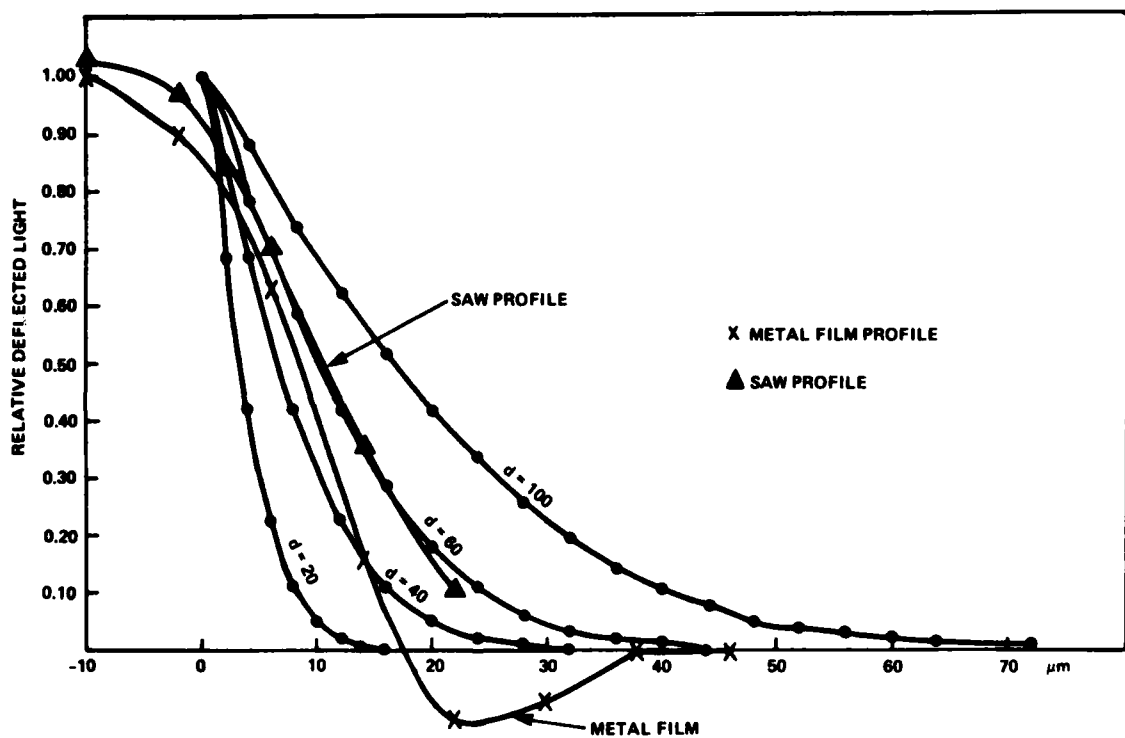


Figure A.10 Determination of laser spot size. "SAW Profile" is data taken near a launching transducer. "Metal film" is data taken as laser probe scans across Al film onto a bare crystal (using specular reflection and optical chopper). The curves $d = 20$ through $d = 100$ are theoretical curves for the various laser spot diameters.

used ($m=0$), and an optical chopper was used for modulation for the lock-in amplifier. A second scan was taken near the launching transducer where there was no aluminum film. The result is the curve labeled "SAW profile". Comparing the two curves, one can conclude the SAW profile had a nearly vertical edge.

The family of theoretical curves were generated by convolving a gaussian function with a step function. Indeed, the laser beam intensity distribution is gaussian (measured at e^{-2} points), the Al film is a step function, and the SAW profile is almost a step function. A computer program is available which uses the actual SAW profile. However, it could not be used in this case since γ , slope of the power flow angle, for Y,Z LiNbO₃ is not known exactly. Even a good approximation for γ is not adequate since γ fits a parabolic curve, and the velocity surface of Y,Z LiNbO₃ is not parabolic.

Thus the theory used here is the convolution of a gaussian function with a step function. The gaussian laser intensity is given by

$$I(r) = \frac{2P_0}{\pi a^2} \exp \left[\frac{-2y^2}{a^2} \right], \quad (A.10)$$

where P_0 is the total output power, $d=2a$ is the beam diameter at e^{-2} points, and y is the variable distance. The step function is realized as a one dimensional integration.

Hence, the convolution is given by

$$C(r) = \int_{y=0}^{y=r} \frac{2P_0}{\pi a^2} \exp \left[\frac{-2y^2}{a^2} \right] dy, \text{ and}$$

by change of variable, let $t^2 = \frac{2y^2}{a^2}$. Then

$$c(r) = \frac{P_0 a}{a^2 \sqrt{2\pi}} \frac{2}{\sqrt{\pi}} \int_{t=0}^{t = \frac{\sqrt{2}}{a} r} \exp(-t^2) dt,$$

and by changing limits of integration,

$$c(r) = \frac{P_0}{a\sqrt{2\pi}} \frac{2}{\sqrt{\pi}} \int_{t=\frac{\sqrt{2}}{a} r}^{t=\infty} \exp(-t^2) dt.$$

$$c(r) = \frac{P_0}{a\sqrt{2\pi}} \operatorname{erfc} \left[\frac{\sqrt{2}}{a} r \right], \text{ or}$$

$$c(r) = \frac{P_0}{a\sqrt{2\pi}} \left(1 - \operatorname{erf} \left[\frac{\sqrt{2}}{a} r \right] \right). \quad (\text{A.11})$$

The theoretical curves in Figure A.10 were generated using Equation (A.11). For each value $d=2a$ of laser diameter, r varied from 0 to 70 μm . From the curve fit and the knowledge that the SAW profile is not quite a step function at its edge, one can conclude that the spot size is near the diffraction limit of 50 μm .

A.5 Reflectivity of Lithium Niobate

The difference in reflections from aluminum and the

bare crystal was measured to be 5.55 dB, a linear factor of 3.6. This leads one to ask, "What does theory predict?" Knowing that the laser beam E field is vertically polarized, which results in E being perpendicular to the plane of incidence and using Reference A.13, one finds the ratio of light reflected from bare lithium niobate, A'', to that reflected from aluminum, A, is

$$\frac{A''}{A} = \frac{-\sin(\theta - \theta_1)}{\sin(\theta + \theta_1)}, \quad (\text{A.12})$$

where θ is the incident angle (from vertical) and θ_1 is the refracted angle. In the case considered here, $\theta = 55$ degrees, and θ_1 is found from Snell's Law: A.13

$$\sin \theta_1 = \sin \theta \frac{\sqrt{\epsilon_r}}{\sqrt{\epsilon_{r1}}}, \quad (\text{A.13})$$

where ϵ_r is optical rather than electromagnetic. Since lithium niobate is anisotropic; ϵ_r is also anisotropic, and $\eta_0 = \sqrt{\epsilon_{r1}}$ where the subscript "o" means ordinary and applies when the E vector is perpendicular to the optical axis. Since the optical axis for lithium niobate is the Z axis, and the acoustic wave is propagating in the Z direction, $\eta_0 = \sqrt{\epsilon_{r1}} = 2.3$. Also, $\eta_e = \sqrt{\epsilon_{r1}} = 2.2$ where the subscript "e" mean extraordinary and applies when the E vector is parallel to the optical axis. A.14, A.15 Thus in the case considered here,

$$\sin \theta_1 = \frac{\sin(55)}{2.3} ;$$

$$\theta_1 = 20.86 \text{ degrees, and}$$

$$\frac{A''}{A} = \frac{-\sin(55-20.86)}{\sin(55+20.86)} = 0.579 .$$

Converting this amplitude to intensity gives

$$\frac{|A''|^2}{|A|^2} = -4.75 \text{ dB} \quad (\text{A.14})$$

If, on the other hand, E was in the plane of incidence, one would use $n_e = 2.2$; $\theta = 55$ degrees; and $\theta_1 = 21.86$ degrees. In this case

$$\frac{A''}{A} = \frac{-\tan(\theta - \theta_1)}{\tan(\theta + \theta_1)} , \text{ and}$$

$$\frac{|A''|^2}{|A|^2} = -16.3 \text{ dB} . \quad (\text{A.15})$$

The next question was, "How nearly vertical was the laser polarization, and how sensitive was the reflectivity to small errors in polarization?" To answer these questions the beam expander (Figure A.5) was removed and replaced with a polarization rotator. The results of this experiment are given in Figure A.11. The null, corresponding to vertical polarization, gives a ratio of -4.8 dB in excellent agreement with Equation (A.14). One can further conclude

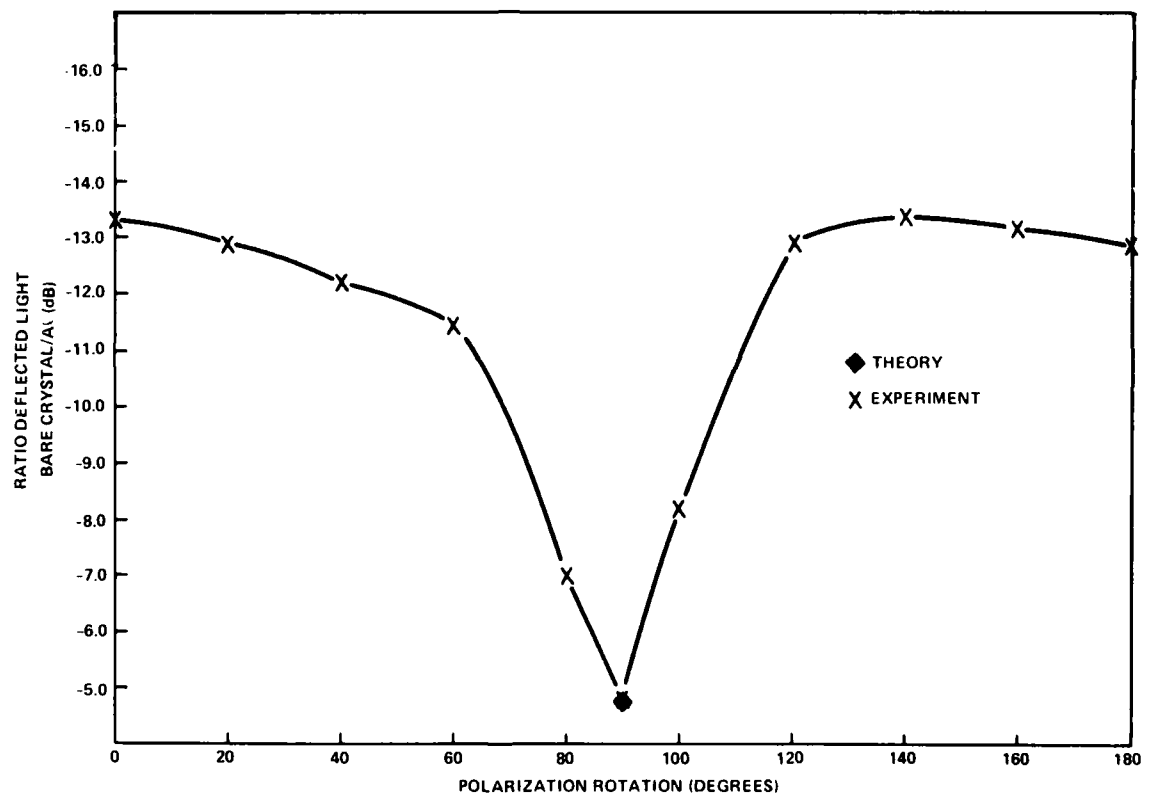


Figure A.11 A plot of LiNbO_3 reflectivity versus laser beam polarization. 90 degrees is vertical.

that the discrepancy between Equation (A.14) and the measured value of 5.55 dB mentioned earlier is probably due to a 4 degree error in the vertical polarization of the laser. Also, if the polarization rotates during warm up, this would explain why the ratio varies somewhat during the warmup period. Absolute intensity also varies during the warmup but should not effect the ratio. As a final note, all devices were laser probed with an incident angle of 45 degrees except the one in Figure 3.5 which was probed with an incident angle 55 degrees. This angle was necessary to get adequate sidelobe separation at 120 MHz.

APPENDIX B

COMPUTER PROGRAMS FOR SAW TRANSDUCER ANALYSIS

B.1 Analysis of Single Channel SAW Filters

Analysis of single channel SAW filters was performed by a series of computer programs written in Fortran IV for a CDC 6600 computer. The series of programs are collectively called the "Raytheon Program" because they were written by Frank Sandy of the Raytheon Company, Waltham, Mass, under a series of three contracts with the Air Force Cambridge Research Laboratory (AFCRL) during the period 1972 to 1979. A block diagram of these programs is given in Figure B.1, and the symbols are explained in Figure B.2.

The analysis of a surface acoustic wave device is broken into several distinct steps. A main program has been written for each step. These main programs can be executed separately or together as part of the same job, depending, for example, on whether the operator is analyzing a device for the first time or is merely examining the changes caused by a new matching network. The output from one main program is stored on a mass storage device for use by other main programs. The function of each of the main programs is described below.

CONVERT - 1267 Fortran statements - This program converts from the user oriented RADC/ET format to the

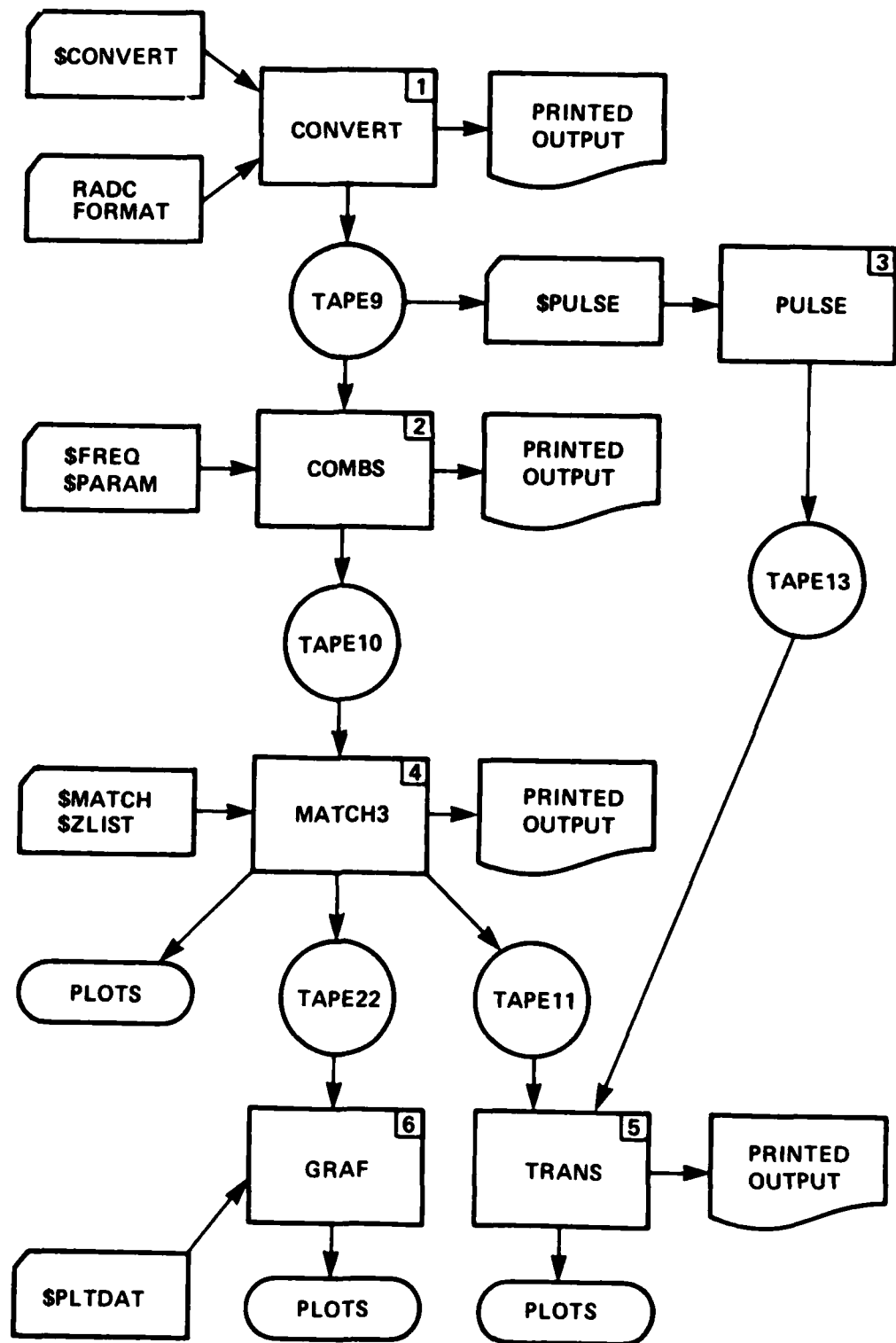
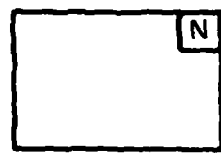


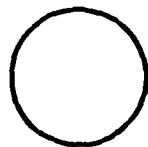
Figure B.1 Block diagram for the "Raytheon Program" used to analyze SAW delay lines.



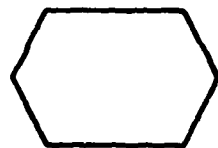
THE RUNNING OF A PROGRAM. THE
N'th PROGRAM TO RUN



PRINTED OUTPUT



DISK FILE ACTING LIKE
MAGNETIC TAPE



PHYSICAL MAGNETIC TAPE



PUNCHED CARD INPUT



PLOTS



FLOW CHART CONNECTOR

Figure B.2 Explanation of symbols used in Figure B.1.

Raytheon format. It was written by a company named ASCI under a separate contract after the first Raytheon contract was completed. The Raytheon format is that required by COMBS and consists of giving every corner of every finger an X,Y coordinate position. Thus each finger has 4 X,Y coordinates (or 8 if it is apodized and the remaining space filled with a dummy finger). Since it is not uncommon for a narrowband transducer to have 1200 fingers (using double electrodes) and including a factor of 2 to account for the output transducer, this could mean typing in 21,600 coordinate pairs. The RADC/ET format instead consists of only one data card per finger.

COMBS - 1641 Fortran statements - This program computes and stores electrical admittance matrices as a function of frequency for a surface acoustic wave device that is appropriately described to it. The device may consist of up to six interdigital transducers or reflective gratings. The most important feature of this program is that it takes into account many second-order effects such as triple transit echo, regenerated waves, and acoustic mismatch under metal electrodes. In addition to computing the admittance matrix, this program also prints out the insertion loss and time delay with a 50 ohm generator and load on two specified electrical ports. It also prints the input and output admittance and impedance for these two ports at all frequencies computed. Optionally it can store additional acoustic matrices from which acoustic wave fronts can be

calculated.

MATCH3 - 845 Fortran Statements - This program accepts the electrical admittance matrices that were produced by COMBS, adds electrical matching networks appropriately described to it, and prints the insertion loss, time delay, phase, and input and output impedance of the complete device at some or all frequencies. Optionally it displays some or all of these functions on the system CRT or XY plotter. The admittance matrices produced by COMBS which are used as inputs to this program are not changed in this computation and thus remain available for re-examination with other matching networks. This program optionally stores the complex transmission coefficient of the matched device as a function of frequency on a mass storage device for further analysis.

TRANS - 1284 Fortran Statement - This program gives the time domain response of one or more cascaded devices. It accepts as inputs from mass storage the complex transmission coefficients as a function of frequency produced by MATCH3, for up to four separate matched surface acoustic wave devices. The product of these matrices is obtained which represents the transfer function for the cascaded devices taken as a unit. The product can be stored on a mass storage device, or its inverse Fourier transform can be evaluated. The transform is either printed or plotted on a CRT or XY plotter.

PULSE - 19 Fortran statements - Program TRANS can accept any type of input. This short program simulates an impulse to be used as the input to TRANS, thus giving the device impulse response.

GRAF - 420 Fortran statements - This program was written by ASCI and plots insertion loss versus frequency from the data on TAPE22 produced by MATCH3. It is possible to get these plots from MATCH3; however, GRAF provides for multiple plots in multiple formats including extra labeling and marker dots.

The above programs represent 5476 Fortran statements. Typically they are compiled once and stored on permanent files. The "Raytheon Program" is then run by using control cards which attach the already compiled permanent files and by using data describing the SAW transducers in RADC/ET format. This "run deck" is 70 cards plus data of one card per transducer electrode. It is not uncommon for this program to take 1 hour (3600 sec) or more of CPU time (central processing unit) depending on the complexity of the transducers. This excludes compile time and input/output time.

B.2 Analysis of SAW Filters With Two or More Channels

The "Raytheon Program" can only analyze one channel. This channel may have two to six transducers (or gratings), but they must all be acoustically in series. To do the analysis of acoustically parallel channels, e.g. the stagger

tuning described in Appendix C, it was necessary to use a different combination of programs. The series of programs collectively known as "RC#2M" are shown in block diagram form in Figures B.3 and B.4. The blocks in Figure 3 were part of an already existing program and compute S_{11} for the combined SAW transducers with individual matching networks. RIND and GILPM in Figure B.4 were written especially for this analysis. They compute insertion loss versus frequency for the combined SAW transducers with individual matching networks using S_{11} only. The output is assumed to be the mirror image of the input so the insertion loss is doubled to get the overall insertion loss.

The input to the RC#2M program is TAPE11 and TAPE12 although in general it can use up to eight input files: TAPE 11, 12, 13, 14, 15, 16, 17 and 18. Each file must be created by a separate COMBS run. Presumably each COMBS run has been for a different transducer pair. The data transferred from these files includes frequency and corresponding input impedance, although more data is available.

SEE IT - 28 Fortran statements - This program takes data from TAPE11 or any file having that format and prints it out. Since the data is in binary format, SEE IT must also convert it to the normal floating point format.

MERGE G, ICAMG and DECODG - 487 Fortran statements - MERGE G, ICAMG, and DECODG are part of the "FENSTERMACHER Program" so named because it was written by an RADC employee

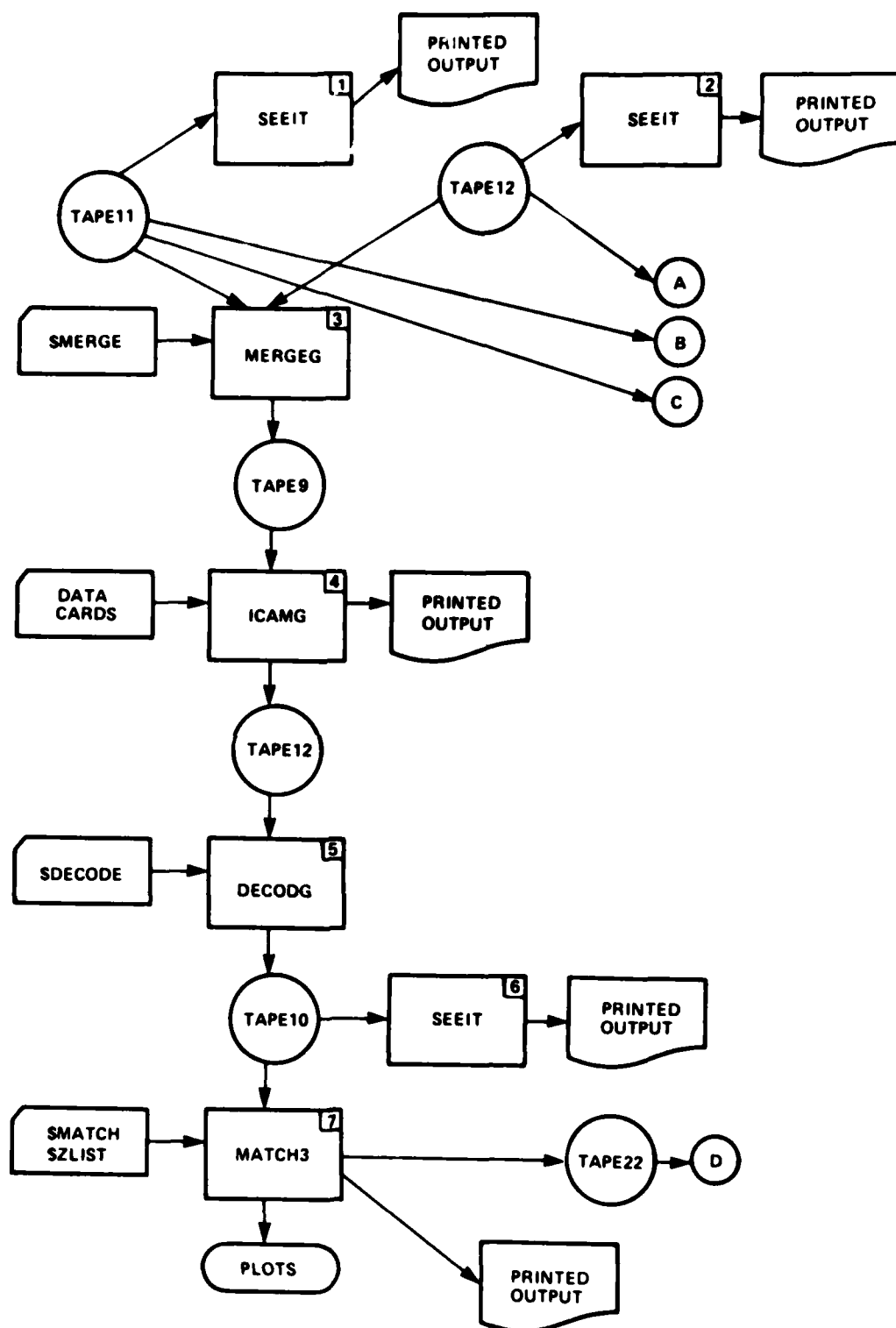


Figure B.3 Block diagram for the "RC#2M" program used to analyze two or more SAW delay lines acoustically in parallel.

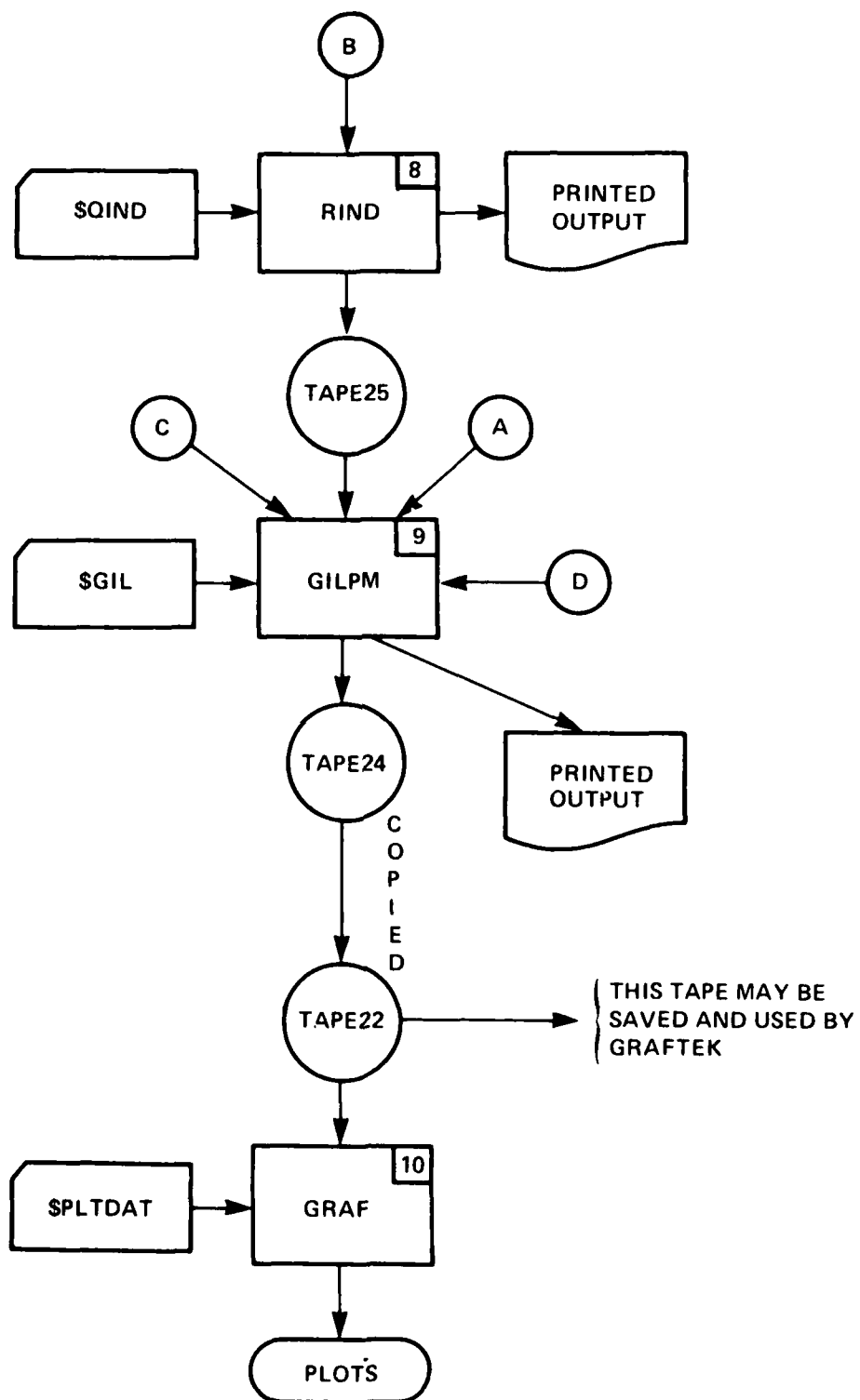


Figure B.4 Continuation of Figure B.3.

with that name. The program was designed to analyze a SAW filterbank - many transducers acoustically in parallel having one common electrical input and many individual outputs. It was useful in RC#2M for obtaining input impedance, S_{11} , but not insertion loss because each output except the one being analyzed was individually terminated in 50 ohms. The first step in the operation of the FENSTERMACHER program is to merge the files using MERGEG. MERGEG takes the Y matrices produced by COMBS which are stored on TAPE11-18, and merges them into a single file on TAPE9, which may be used directly or cataloged. The interconnection progra, ICAM, takes the Y matrices at each frequency, converts them to A,B,C,D matrices, and applies matching networks and interconnections. It then converts them back to Y matrices, and writes them on TAPE12. DECODG then selects one filter, extracts the Y matrices, and writes them on TAPE10 to be used by MATCH3. As many filters as desired can be extracted one at a time by DECODG, and processed by MATCH3.

MATCH3 - 845 Fortran statements - This program is used to give Smith Chart plots of S_{11} for the interconnected filters and matching networks. Further explanation is contained in B.1 of this appendix.

INSERTION LOSS ANALYSIS - This portion of RC#2M is done by the programs shown in block diagram form in Figure B.4. As stated before, a maximum of eight channels may be interconnected. However, for the investigation in Chapter 4

and Appendix C only two channel were used. These are depicted in Figure B.5 and B.6 and will be used here as an example to aid the explanation of the computer program. Figure B.5 is the schematic diagram which is redrawn in Figure B.6 to aid circuit analysis.

RIND - 60 Fortran statements - The boxes labeled L1 and L2 in Figure B.6 may be any complex impedance. These impedances are then used by GILPM as two of the elements in the network. RIND is designed as a module that can be easily changed. In the present example it was used to compute the impedance of a Real INDUCTOR. The model of a Real INDUCTOR is reduced to a single complex number for each frequency and passed to GILPM in the form $Q_n + SQ_{n+1}$, where $S=j\omega$. When the distributed model of a real inductor was adopted at a later date, this subprogram was no longer used.

GILPM - 647 Fortran statements - GILPM is described in more detail than the other programs because it was written specifically for the investigation in Chapter 4 and Appendix C and because it was not adapted from an exiting program. GILPM is an acronym for General Insertion Loss Plots (Modified version). The original version has since been phased out, but the letter M at the end remains.

Program COMBS is designed to do a mathematical analysis of two to six combs acoustically in series having one comb as an input port and one comb as an output port. Program GILPM is capable of analyzing the insertion loss as a function of frequency of two to eight pairs of combs.

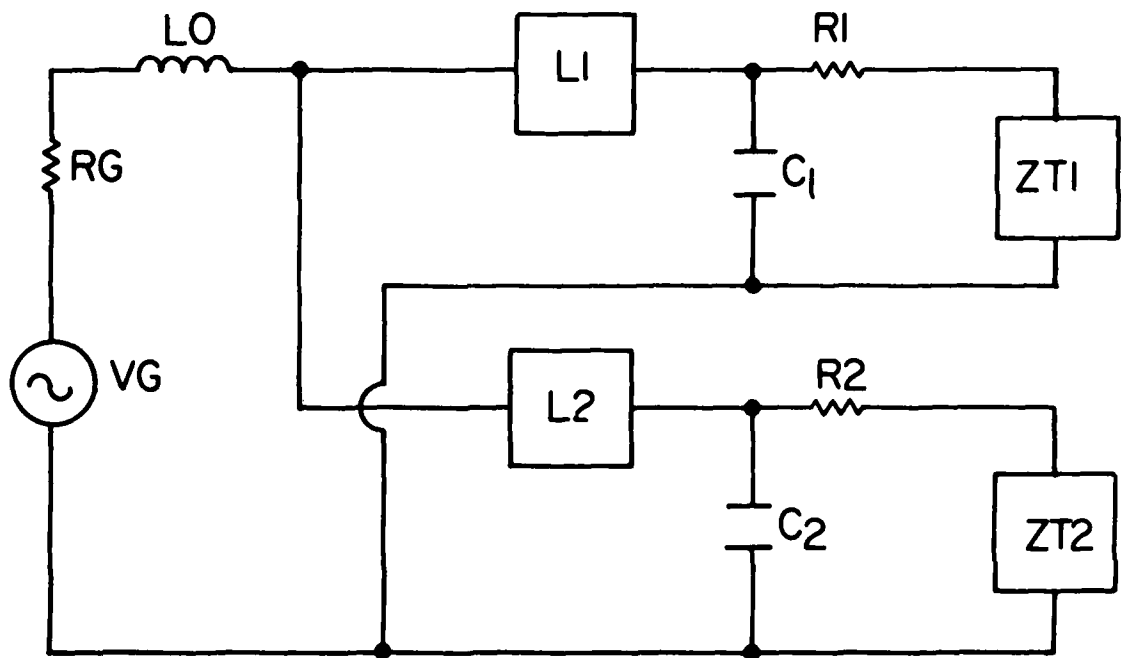


Figure B.5 Circuit schematic for input portion of two SAW delay lines connected in parallel.

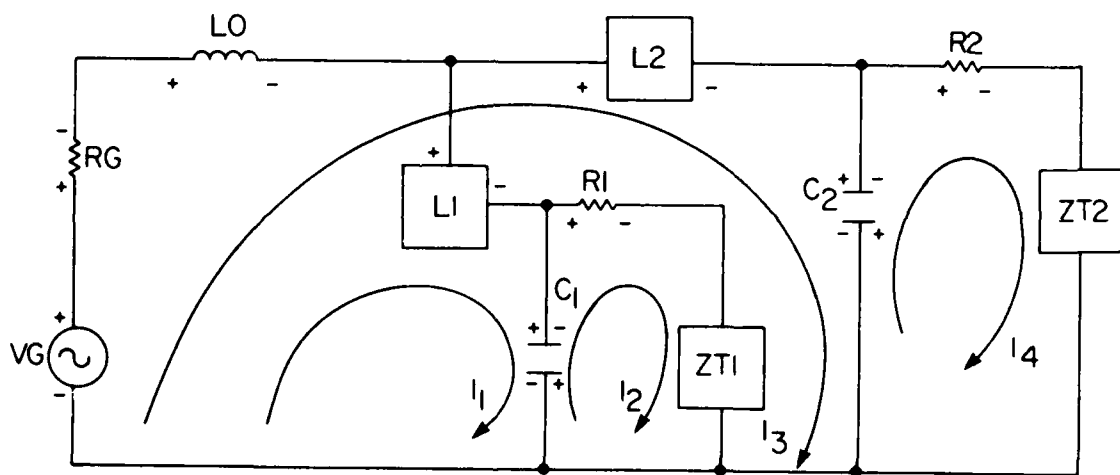


Figure B.6 Circuit schematic corresponding to Figure B.5 redrawn to aid analysis.

The analysis is performed acoustically in parallel and electrically in series, parallel, or any combination thereof having one input port and one output port. The output connection is assumed to be identical to the input connection. The user has total generality in describing the matching network of the device. Program GILPM accepts input from program COMBS and optionally from programs MATCH and RIND. Besides printed output, program GILPM produces TAPE24 which can be used (indirectly) by program GRAF and GRAFTEK to produce insertion loss plots.

Program RIND provides additional versatility to program GILPM by providing variable inputs.

Program GETMATD allows the input specifications to program GILPM to be checked for syntax errors before actually trying to run GILPM which is a large and time-consuming program.

Input to Program GILPM - For each comb on the device there must be a tape describing the input impedances as a function of frequency. The range of frequencies for which the input impedances are calculated is variable, however, it must be consistent for all combs in a particular device. The input impedance tapes are created by program COMBS. Usually each impedance tape is created with a separate COMBS run. Thus, the analysis of a four comb device using program GILPM would require five separate runs (four COMBS runs and a GILPM run). As output, each run of COMBS produces TAPE10 which must be saved as a permanent file. The actual names

of the tapes used by the program GILPM, however, are TAPE11, TAPE12, TAPE13...TAPE18. Therefore, each version of TAPE10 must be given a different name and then attached as TAPE11, TAPE12...TAPE18.

Program COMBS, as used here, analyzes two transducers acoustically in series with no matching network. TAPE10 contains the input impedance values of the first transducer at each frequency and the output impedance values of the second transducer at each frequency. Program GILPM uses only the input impedances.

TAPE22 - TAPE22 does not have to exist in order for program GILPM to run. Often program MATCH3 is run before program GILPM in which case TAPE22 will already exist. Program GILPM produces TAPE24 as output and has the same format as TAPE22 which means it can be used by program GRAF or GRAFTEK (however, the name must be changed from TAPE24 to TAPE22 before program GRAF or program GRAFTEK can run it). If TAPE22 exists then program GILPM takes the plot identification off TAPE22 and copies it on TAPE24. If TAPE22 does not exist, then TAPE24 will have the following default plot identification - "ROGER COLVIN".

TAPE25 - TAPE25 is created by program RIND and contains values of Q1, Q2, Q3, Q4, Q5, Q6, Q7, and Q8 at each frequency. TAPE25 does not have to exist as long as the input data to program GILPM does not reference any Q value. If TAPE25 does not exist and a Q value is referenced, then the program will abort.

The \$GIL Namelist Variables and Their Functions -

NUMZINS: The number of combs to be analyzed. There are NUMZINS tapes created by program COMBS.

NUMMATS: The number of matrices to be created and have their determinents calculated. NUMMATS almost always equals NUMZINS + 1.

LO: Series tuning inductor

RG: Generator characteristic impedance

VG: Generator voltage

L(n): Tuning inductor associated with the n'th comb

C(n): Parasitic shunt capacitance associated with the n'th comb

R(n): Parasitic series resistance associated with the n'th comb

PRNT: If PRNT = .True., the values of each matrix at the first frequency are printed out.

Creating the Matrices - At each frequency there are NUMMATS complex matrices created and solved. Each matrix mathematically represents an electronic circuit consisting of transducers, capacitors, resistors and inductor. The size and general format of "NUMMATS" matrices are defined once by the user. The specific entry values are recalculated at each new frequency. The "NUMMATS" matrices may vary in size from 2 x 2 matrix (four entries) to a 16 x 16 matrix (256 entries). The general description of each entry consists of from zero to sixteen descriptors. An entry described by zero descriptors represents a matrix value of zero. Each non-zero descriptor is described by exactly five characters. There are two possible formats for

these five character descriptors. They are as follows:

$$\begin{bmatrix} + \\ - \end{bmatrix}$$

$$\begin{bmatrix} \text{SN} \\ \text{SM} \\ \text{SI} \end{bmatrix}$$

$$\begin{bmatrix} \text{VG} \\ \text{LO} \\ \text{RG} \end{bmatrix}$$

or

$$\begin{bmatrix} + \\ - \end{bmatrix}$$

$$\begin{bmatrix} \text{SN} \\ \text{SM} \\ \text{SI} \end{bmatrix}$$

$$\begin{bmatrix} \text{C} \\ \text{R} \\ \text{L} \\ \text{Q} \\ \text{A} \\ \text{B} \end{bmatrix}$$

$$\begin{bmatrix} 1 \\ 2 \\ 3 \\ 4 \\ 5 \\ 6 \\ 7 \\ 8 \end{bmatrix}$$

The following formats, however, are illegal even though they are syntactically described by the second format above.

$$\begin{bmatrix} + \\ - \end{bmatrix}$$

$$\begin{bmatrix} \text{SI} \end{bmatrix}$$

$$\begin{bmatrix} \text{Q} \end{bmatrix}$$

$$\begin{bmatrix} 1 \\ 2 \\ 3 \\ 4 \\ 5 \\ 6 \\ 7 \\ 8 \end{bmatrix}$$

and

$$\begin{bmatrix} + \\ - \end{bmatrix}$$

$$\begin{bmatrix} \text{SI} \\ \text{SM} \end{bmatrix}$$

$$\begin{bmatrix} \text{A} \\ \text{B} \end{bmatrix}$$

$$\begin{bmatrix} 1 \\ 2 \\ 3 \\ 4 \\ 5 \\ 6 \\ 7 \\ 8 \end{bmatrix}$$

To form a valid descriptor using the first format (containing three brackets) take any symbol in the first

bracket, followed by any two letter set in the second bracket, followed by any two letter set in the third bracket.

To form a valid descriptor using the second format (containing four brackets) take any symbol in the first bracket, followed by any two letter set in the second bracket, followed by any letter in the third bracket, followed by any number in the fourth bracket.

To find out which of these descriptors are not legal check to see if they are syntactically described by the two "illegal" formats. In other words, a descriptor is legal if it is described by either the first or second formats and not described by either the third or fourth formats.

Thus, there are a total of
 $(2 \times 3 \times 3) + (2 \times 3 \times 6 \times 8) - (2 \times 1 \times 1 \times 8) - (2 \times 2 \times 2 \times 8) = 18 + 288$
 $- 16 - 64 = 226$ legal descriptors.

Each of the following are examples of legal descriptors:

+SNVG

-SML3

+SIQ2

+SNRG

Each of the following are examples of illegal descriptors:

+SNV3

-SMC9

+SQA3

-SMVG

+SIQ4

-SIA3

+SMB4

If the program finds even one illegal descriptor, execution is aborted. (For this reason the input should first be checked by program GETMATD, which will be described in following sections).

Definitions of Descriptor Components - The following components are defined by the \$GIL Namelist and are constants (i.e. not frequency dependent).

- VG: Generator voltage (usually normalized to 1)
- RG: Generator characteristics impedance (usually 50 ohms)
- LO: Series tuning inductor
- Cn: Parasitic shunt capacitance associated with the n'th comb
- Rn: Parasitic series resistance associated with the n'th comb
- Ln: Tuning inductor associated with the n'th comb, where $n = 1, 2, 3, \dots 8$

The following components are defined by the input tapes from program COMBS. They are frequency dependent.

- An: The real part of the input impedance associated with the n'th comb
- Bn: The imaginary part of the input impedance associated with the n'th comb, where $n = 1, 2, 3, \dots 8$.

(Note: $ZT_n = A_n + iB_n$)

The following component is defined by the input tape (TAPE25) from program RIND. It may or may not be dependent on frequency depending on the version of RIND used (program RIND is described in following sections).

Qn: In general Qn is an arbitrary number representing any electrical device the user may wish to add. The values of Qn come from TAPE25 which is created by program RIND. Program RIND was not designed to be a fixed program. The user may alter program RIND to simulate any electrical component he desires that cannot be simulated from existing components.

The following three components determine whether the descriptor represents a real or imaginary number and whether or not the descriptors are inverted.

SN: SN stands for "Not Multiplied by S". The value of SN is always equal to one (SN=1).

SM: SM means that the following component of the descriptor is multiplied by S. S is a frequency dependent imaginary number. The value of S is $i2\pi f$.

SI: SI means that the following component of the descriptor is multiplied by S and then inverted.

Examples:

<u>Descriptor Notation</u>	<u>Mathematical Notation</u>
+SNR ₃	R_3
+SMR ₃	$i2\pi f R_3$
+SIR ₃	$\frac{1}{i2\pi f R_3}$

A typical example, Figure B.5, shows two transducers

in parallel, together with matching inductors and parasitic elements. The output is assumed identical to the input and is not shown.

Figure B.6 shows the same electrical device redrawn in a form which is more convenient for circuit analysis.

The following is the mathematical analysis of these circuits.

$$V_g - R_g I_1 - S L_o I_1 - S L_1 I_1 - \left(\frac{1}{S C_1} \right) I_1 + \left(\frac{1}{S C_1} \right) I_2 - R_g I_3 - S L_o I_3 + O I_4 = 0$$

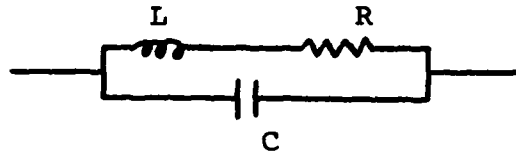
$$0 + \left(\frac{1}{S C_1} \right) I_1 - \left(\frac{1}{S C_1} \right) I_2 - R_1 I_2 - Z_{T1} I_2 + O I_3 + O I_4 = 0$$

$$V_g - R_g I_1 - S L_o I_1 + O I_2 - R_g I_3 - S L_o I_3 - S L_2 I_3 - \left(\frac{1}{S C_2} \right) I_3 + \left(\frac{1}{S C_2} \right) I_4 = 0$$

$$0 + O I_1 + O I_2 + \left(\frac{1}{S C_2} \right) I_3 - \left(\frac{1}{S C_2} \right) I_4 - R_2 I_4 - Z_{T2} I_4 = 0$$

$$\begin{bmatrix} \left(R_g + S L_o + S L_1 + \frac{1}{S C_1} \right) & \left(-\frac{1}{S C_1} \right) & \left(R_g + S L_o \right) & 0 \\ \left(-\frac{1}{S C_1} \right) & \left(\frac{1}{S C_1} + R_1 + Z_{T1} \right) & 0 & 0 \\ \left(R_g + S L_o \right) & 0 & \left(R_g + S L_o + S L_2 + \frac{1}{S C_2} \right) & \left(-\frac{1}{S C_2} \right) \\ 0 & 0 & \left(-\frac{1}{S C_2} \right) & \left(\frac{1}{S C_2} + R_2 + Z_{T2} \right) \end{bmatrix} \begin{bmatrix} I_1 \\ I_2 \\ I_3 \\ I_4 \end{bmatrix} = \begin{bmatrix} V_g \\ 0 \\ V_g \\ 0 \end{bmatrix}$$

The above equations have assumed ideal inductors. However, it was desired to use the real model for inductors L_1 and L_2 . A possible circuit model for a real inductor (to replace the ideal inductor) is



$$\text{where } C = \frac{1}{L[(2\pi \text{SRF})^2 + (R/L)^2]}$$

$$R = \frac{2\pi fL}{Q}$$

Q = finite Q of the real inductor, and SRF = self resonant frequency of the real inductor.

The impedance (Z_L) of a real inductor corresponding to the above model is given by

$$Z_L = \frac{1}{C} \frac{i\omega + (R/L)}{i\omega(R/L) + (\frac{1}{LC} - \omega^2)}$$

$$Z_L = \frac{1}{C} \frac{R/(L^2C)}{\omega^2(\frac{R}{L})^2 + (\frac{1}{LC} - \omega^2)^2} + \frac{i\omega}{C} \frac{\frac{1}{LC} - \omega^2 - (\frac{R}{L})^2}{(\frac{\omega R}{L})^2 + (\frac{1}{LC} - \omega^2)^2}$$

$$Z_L = Q_1 + i\omega Q_2, \text{ where } S=i\omega = i2\pi f$$

Thus in the matrix equations which follow SL_1 is replaced by $Q_1 + SQ_2$. Q_1 and Q_2 are computed and passed from RIND to GILPM. (These Q_n are different from the finite Q values of the real inductors found in namelist \$QIND). Q_1 is the real part of the impedance of the real inductor and Q_2 is the imaginary part of the impedance of the real inductor. Note that Q_2 as passed from RIND has not yet been multiplied by S . It then follows that SL_2 is replaced by $Q_3 + SQ_4$. (Q_3 and Q_4 are also passed from RIND).

Note that RIND is not a set unchangeable program. Program RIND may be changed by the user so that the values of $Q_1, Q_2, Q_3 \dots Q_8$ represent any mathematical equations desired by the user. In this particular example program RIND had to be specifically programmed so that the values $Q_1 + SQ_2$ and $Q_3 + SQ_4$ represented real inductors. The values Q_1, Q_2, Q_3 and Q_4 are frequency dependent.

In the matrix equations below Z_{T1} is replaced by $A_1 + iB_1$ and Z_{T2} is replaced by $A_2 + iB_2$. Z_{Tn} is a complex number representing the impedance of the n 'th transducer. When Z_{Tn} is replaced by $A_n + iB_n$, the A_n represents the real part of the impedance, and the B_n represents the imaginary part of the impedance. Now

$$\begin{bmatrix}
 (R_g + SL_o + Q_1 + SQ_2 + \frac{1}{SC_1}) & (-\frac{1}{SC_1}) & (R_g + SL_o) & 0 \\
 (-\frac{1}{SC_1}) & (\frac{1}{SC_1} + R_1 + A_1 + B_1) & 0 & 0 \\
 (R_g + SL_o) & 0 & (R_g + SL_o + Q_3 + SQ_4 + \frac{1}{SC_2}) & (-\frac{1}{SC_2}) \\
 0 & 0 & (-\frac{1}{SC_2}) & (\frac{1}{SC_2} + R_2 + A_2 + B_2)
 \end{bmatrix}
 \begin{bmatrix}
 I_1 \\
 I_2 \\
 I_3 \\
 I_4
 \end{bmatrix}
 =
 \begin{bmatrix}
 V_g \\
 0 \\
 V_g \\
 0
 \end{bmatrix}$$

This matrix equation is of the form $[A] \vec{X} = \vec{B}$, where

$$[A] = \begin{bmatrix}
 a_{11} & a_{12} & a_{13} & a_{14} \\
 a_{21} & a_{22} & a_{23} & a_{24} \\
 a_{31} & a_{32} & a_{33} & a_{34} \\
 a_{41} & a_{42} & a_{43} & a_{44}
 \end{bmatrix}$$

If $D = \text{DET } [A]$, then

$$N_1 = \text{DET} \begin{bmatrix}
 a_{11} & V_g & a_{13} & a_{14} \\
 a_{21} & 0 & a_{23} & a_{24} \\
 a_{31} & V_g & a_{33} & a_{34} \\
 a_{41} & 0 & a_{43} & a_{44}
 \end{bmatrix} \quad \text{and ,}$$

$$N_2 = \text{DET} \begin{bmatrix} a_{11} & a_{12} & a_{13} & V_g \\ a_{21} & a_{22} & a_{23} & 0 \\ a_{31} & a_{32} & a_{33} & V_g \\ a_{41} & a_{42} & a_{43} & 0 \end{bmatrix}$$

$$\text{Then } |I_2|^2 = \frac{|N_1|^2}{|D|^2} = \text{ICAP (1), and}$$

$$|I_4|^2 = \frac{|N_2|^2}{|D|^2} = \text{ICAP (2).}$$

Note: N_1 , N_2 and D are complex numbers; ICAP (N) is defined below. Finally,

$$\text{Transducer efficiency} = \frac{2R_g}{V_g} [|I_2|^2 \text{Re}Z_{T1} + |I_4|^2 \text{Re}Z_{T2}], \text{ and}$$

Insertion Loss (in dB) = $-10 \log_{10} (\text{Transducer efficiency})^2$.

SUBROUTINE ILCALC - The actual routine that computes the insertion loss, subroutine ILCALC, is not a fixed part of program GILPM, but rather a changeable subroutine that is usually part of the run deck. Inputs to subroutine ILCALC are arrays ICAP(8) and REZT(8), where

ICAP(N) = $\frac{\text{The magnitude of the determinate of the } n\text{'th matrix, and}}{\text{The magnitude of the determinate of the NUMAT'th matrix}}$

REZT(N) = A_N (from TAPE11, TAPE12, ... TAPE18).

ICAP(N) and REZT(N) are automatically passed from GILPM. Output of program ILCALC, returned to GILPM, is the

variable "IL" containing the insertion loss. The cards of subroutine ILCALC may be changed by the user to correspond with the particular device one is analyzing.

The above example yielded a 4 x 4 matrix. However, when the distributed model of a real inductor was later developed, RIND was no longer used and the resulting matrix was 6 x 6. The extension to a 6 x 6 matrix was very straightforward and is not duplicated here.

GRAF - 420 Fortran statements - Used to give a plot of insertion loss versus frequency. Further explanation can be found in B.1 of this appendix.

GRAFTEK - 368 Fortran statements - Program GRAFTEK is similar to program GRAF. The difference is that with program GRAF the insertion loss plots are plotted on a Cal-Comp plotter while in program GRAFTEK the insertion loss plots are shown on the cathode ray tube of a Tektronix machine - model 4052. By pushing a button on the Taktronix machine the user may obtain a hard copy of the plot shown on the screen from the hard copy unit-model 4631. The advantage of using the Tektronix machine is that the turnaround time is immediate. When using program GRAF the user must wait to receive the plot. Alternatively, the user may obtain a plot on the Tektronix machine by using program GRAFTEK immediately after program MATCH or program GILPM has been run.

The Run Deck - The normal mode of operation is to compile each of the programs and store them on permanent

files. When running RC#2M, the only cards needed are control cards to attach the permanent files and data cards to describe the matching networks and matrices. For a 6 x 6 matrix, 228 cards are needed. The total program consists of 2855 Fortran statements excluding the run deck and excluding CONVERT and COMBS which were needed to produce TAPE11, TAPE12,...TAPE18. A typical run takes 100 seconds of CPU time - excluding compile time, input/output time, and the generation of the tapes from CONVERT and COMBS.

APPENDIX C

STAGGER TUNING OF SAW FILTERS FOR BROAD BANDWIDTH AND GOOD SHAPE FACTOR

C.1 Introduction

The subject of this appendix is the description of SAW filters used in Chapter IV. The frequencies associated with the mixer of Chapter IV are given in Figure C.1; f_1 and f_2 are the bands of input frequencies, and it is desired to pass $(f_2 - f_1)$ and reject all other frequencies. Figure C.1 defines a design goal for the SAW filter of passing the band 375 to 615 MHz while rejecting frequencies below 345 MHz and above 642 MHz. This requires a 48 percent bandwidth, shape factor of 1.24, and center frequency of 495 MHz.

The stagger tuning technique used to achieve this goal can best be described by referring to Figure C.2. One pair of broadband SAW transducers (one input and one output) is offset in frequency from a second pair of broadband SAW transducers, and each transducer is tuned with a single series inductor. The low frequency pair of transducers is tuned for maximum response below their synchronous frequency, and the high frequency pair of transducers is tuned for maximum response above their synchronous frequency. After comparing this technique to several other

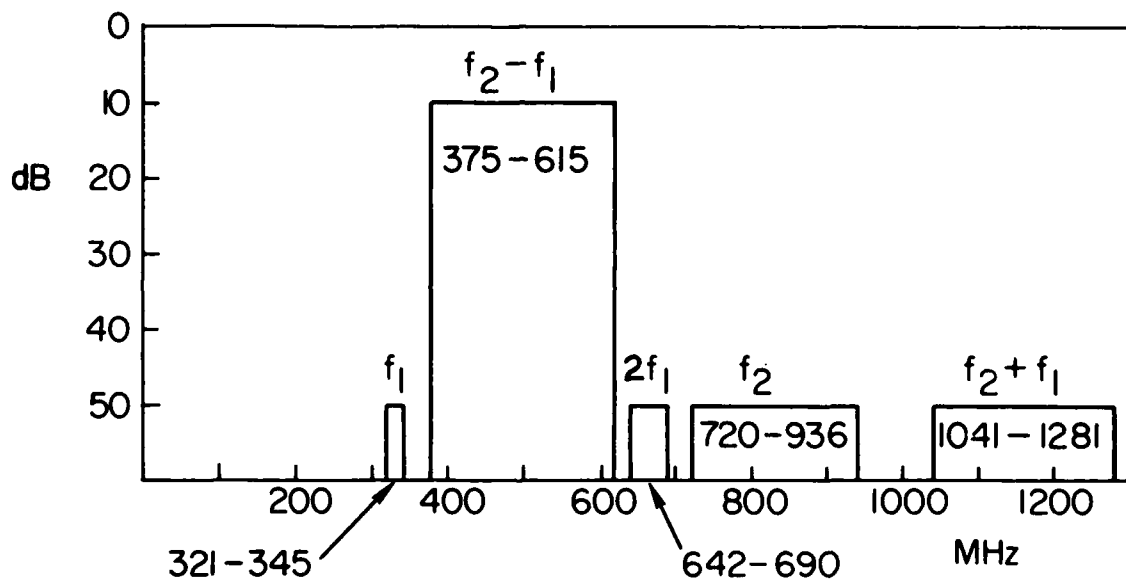


Figure C.1 Frequency spectrum requirements for the SAW filters in this appendix. It is desired to pass the difference frequency of a mixer having inputs f_1 and f_2 and reject all other frequencies.

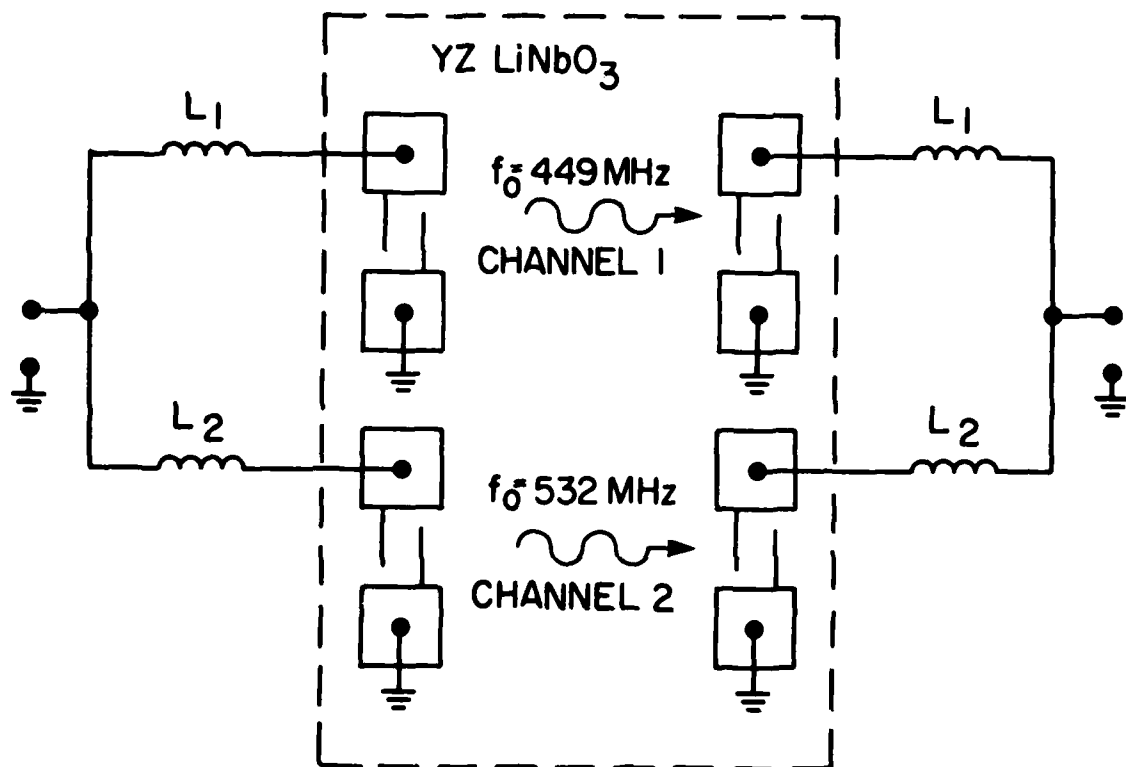


Figure C.2 Schematic diagram of stagger tuned SAW transducers. Channel 1 is tuned for maximum response below its transducer synchronous frequency, and channel 2 is tuned for maximum response above its transducer synchronous frequency.

SAW filtering approaches (explained in the next section), it was evident that this method had the highest potential for simultaneously achieving bandwidth greater than 35 percent, shape factor less than 1.6 and sidelobes less than 40 dB. Other SAW filter approaches give better performance, but none can simultaneously achieve all three parameters. Compared to the other approaches, the stagger tuning approach has the added advantages of lower insertion loss and another degree of freedom in the placement of both nulls to create frequency traps. Conversely, with a single channel you can precisely place only one of the nulls.

C.2 Other Approaches

The common techniques of obtaining good shape factor, defined as $\left(\frac{40 \text{ dB bandwidth}}{3\text{dB bandwidth}}\right)$, are generally useful for less than 10 percent bandwidth, e.g. apodization due to a weighting function^{C.1} or the three transducer approach.^{C.2} Instead, the approach taken here was to look at the shape factors obtainable from known broadband techniques. The first technique looked at was the Reeder type matching network^{C.3} for a broadband unapodized transducer. This technique uses a quarter wave inverter (or lumped element equivalent) in addition to the standard series inductor.

The theoretical filter response of the transducer is shown first without the Reeder network in Figure C.3. The top left of Figure C.3 shows the unmatched filter; the top

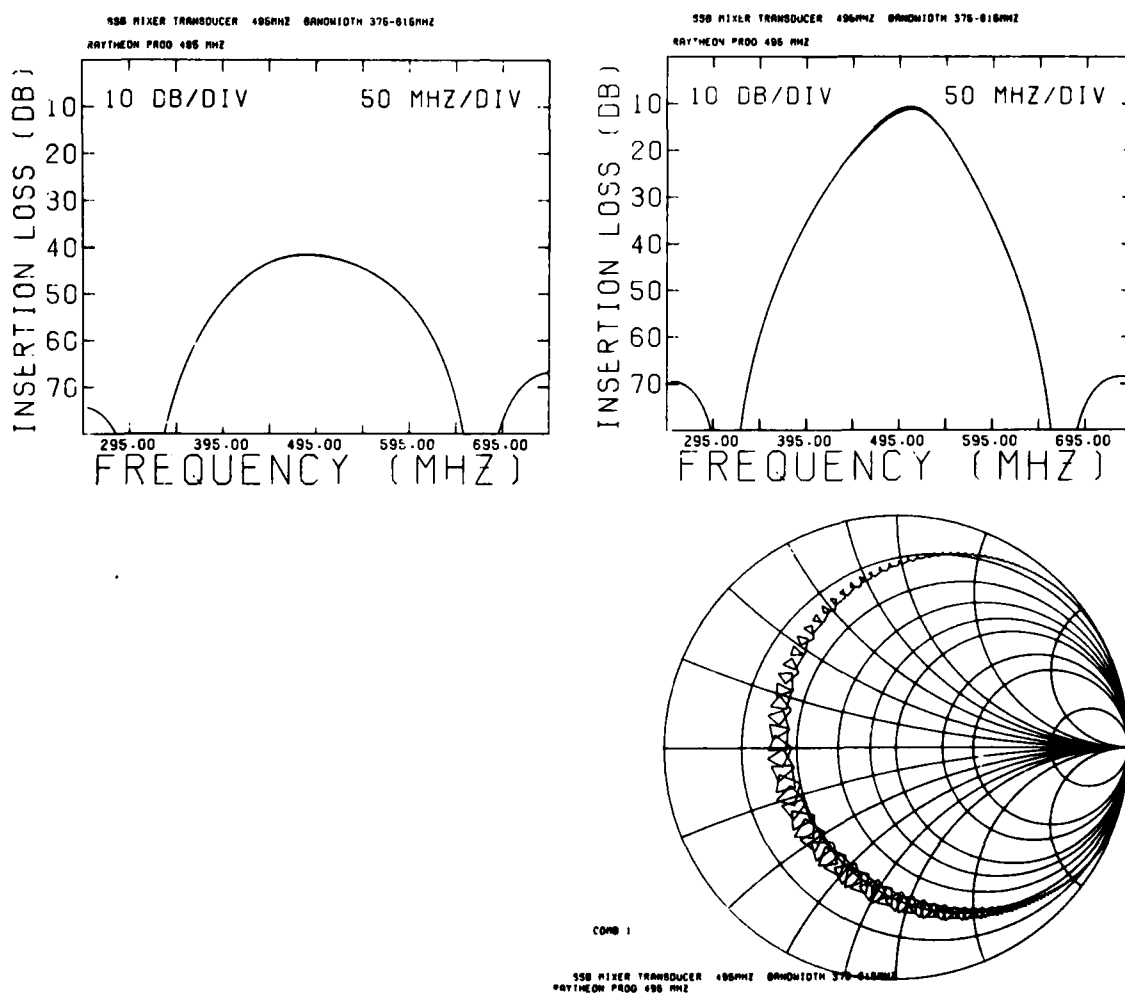


Figure C.3 (Top left) Broad band unapodized filter (single channel) used for Reeder matching. (Top right) Same filter as top left except a single series inductor is used for matching. (Bottom right) Input impedance, S_{11} , for the filter above.

right gives the insertion loss (IL) versus frequency with a single series inductor used for tuning the input and output, and the bottom right gives the corresponding input matching, S_{11} , versus frequency. Where the input matching curve crosses the zero axis corresponds to the peak in the IL curve above. By using the Reeder type network (a quarter wave impedance inverter with impedance Z_I), a family of curves was generated and is shown in Figure C.4. The impedance, Z_I , was varied from 50 to 300 ohms, and the transducer had 7 single electrode fingers giving $N = 3$ periods. The effective number of periods, N_e , computed from the pole locations is 3.2, and R_p/Z_0 is approximately 2. As Z_I increases, the bandwidth, insertion loss, and sidelobes all increase. Unfortunately, the bandwidth and shape factor never even approached the design goals. Finally, the input impedances corresponding to Figure C.4 are given in Figures C.5 and C.6.

The addition of a 4:1 impedance transformer (2:1 turns ratio) prior to the quarter wave transmission line resulted in vast improvements as shown in Figure C.7. Again a family of curves was generated with Z_I varying from 12.5 ohms to 200 ohms, and the corresponding input impedances are given in Figures C.8 and C.9. One should also note how triple transit is reduced as Z_I is increased. This can be seen as the curves get smoother in Figures C.7 - C.9 and is the result of the transformer reducing the effective source

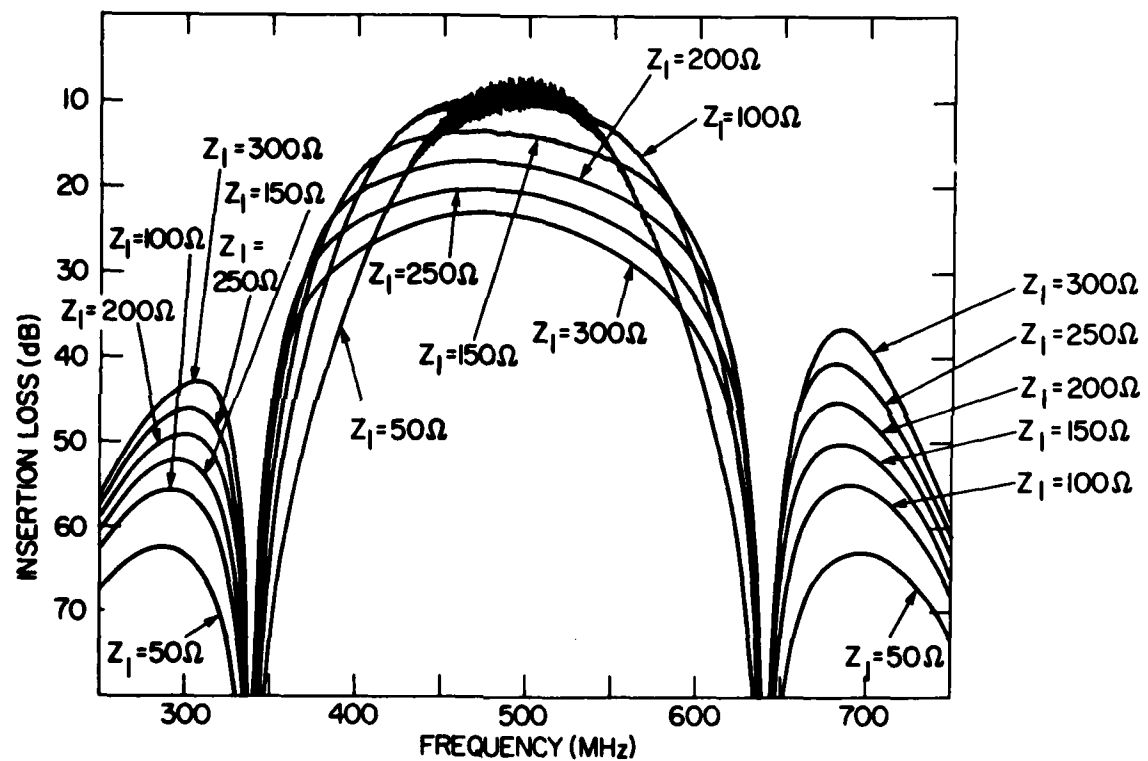


Figure C.4 The filter of Figure C.3 top right has had a $\lambda/4$ inverter added; this constitutes a ReederC.3 type matching network. The inverter impedance, Z_1 , varies from 50 to 300 ohms. Note: 90 ohms is a practical maximum.

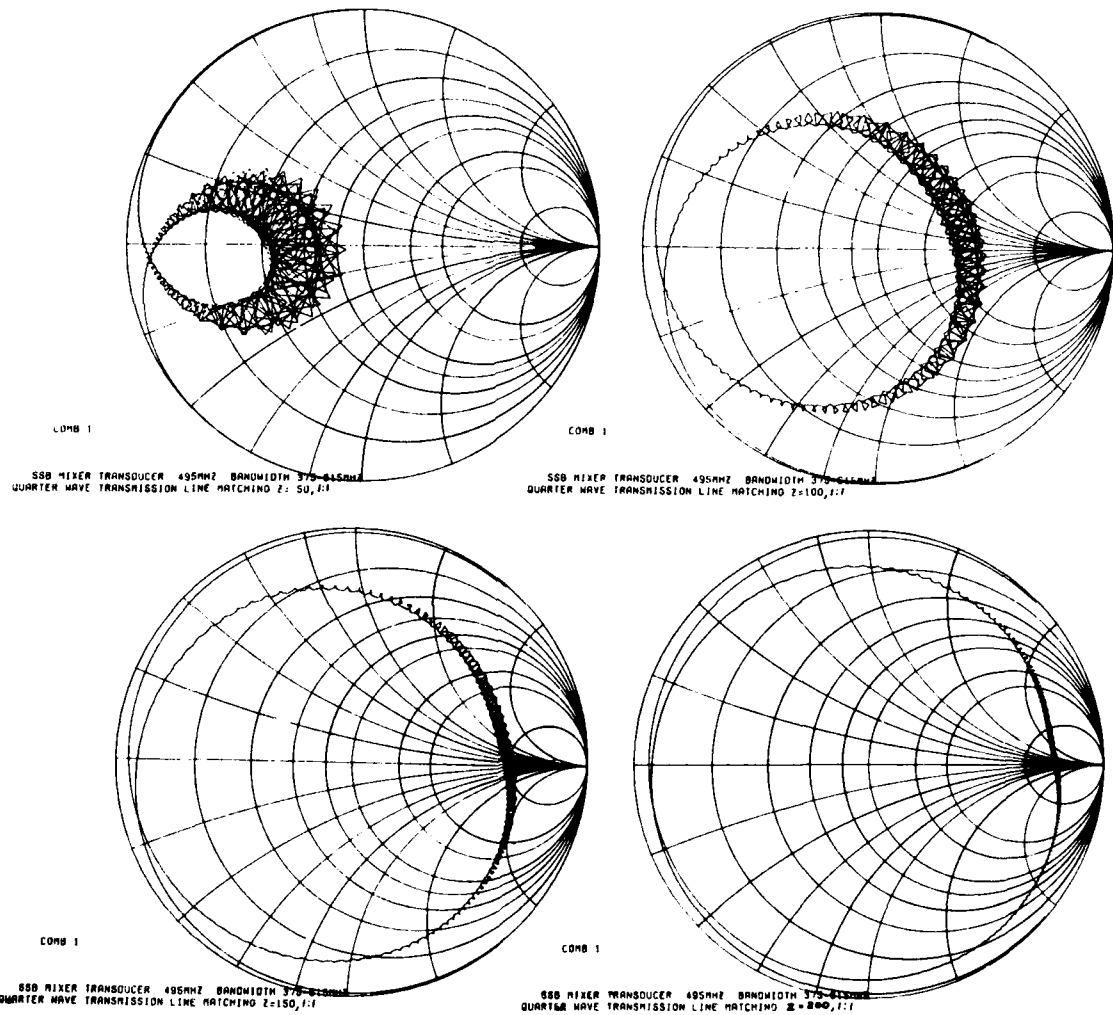


Figure C.5 Input impedances for the filters of Figure C.4.
 (Top left) $Z_1 = 50$ ohms (Top right) $Z_1 = 100$ ohms.
 (Bottom left) $Z_1 = 150$ ohm. (Bottom right) $Z_1 = 200$ ohm.

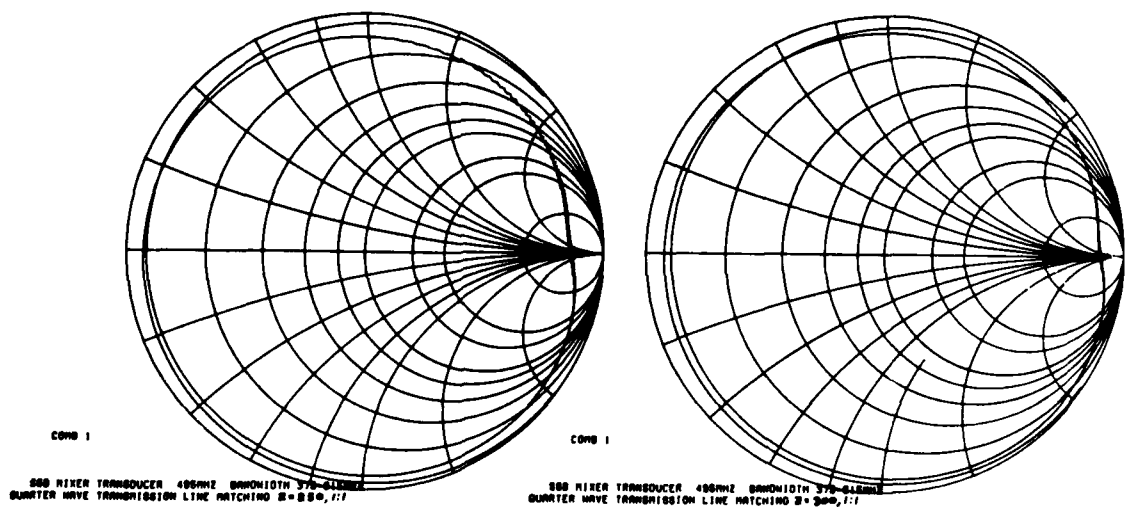


Figure C.6 Input impedances for the filters of Figure C.4.
 (Left) $Z_1 = 250$ ohm. (Right) $Z_1 = 300$ ohm.

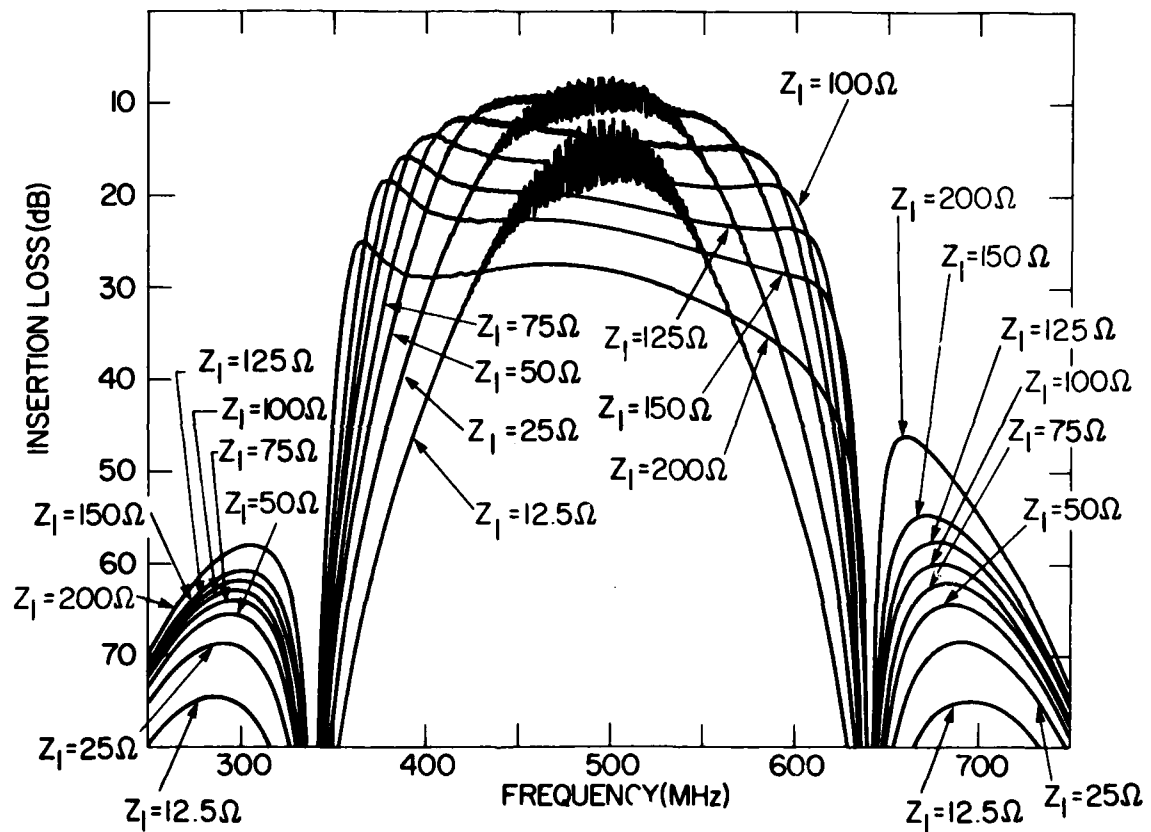


Figure C.7 Reeder type matching^{C.3} - The curves of Figure C.4 have had a 4:1 impedance transformer (2:1 turns ratio) added. This reduces the effective source, Z'_0 , to 12.5 ohms. The inverter impedance, Z_1 , varies from 12.5 to 200 ohms. Note: 90 ohms is a practical maximum.

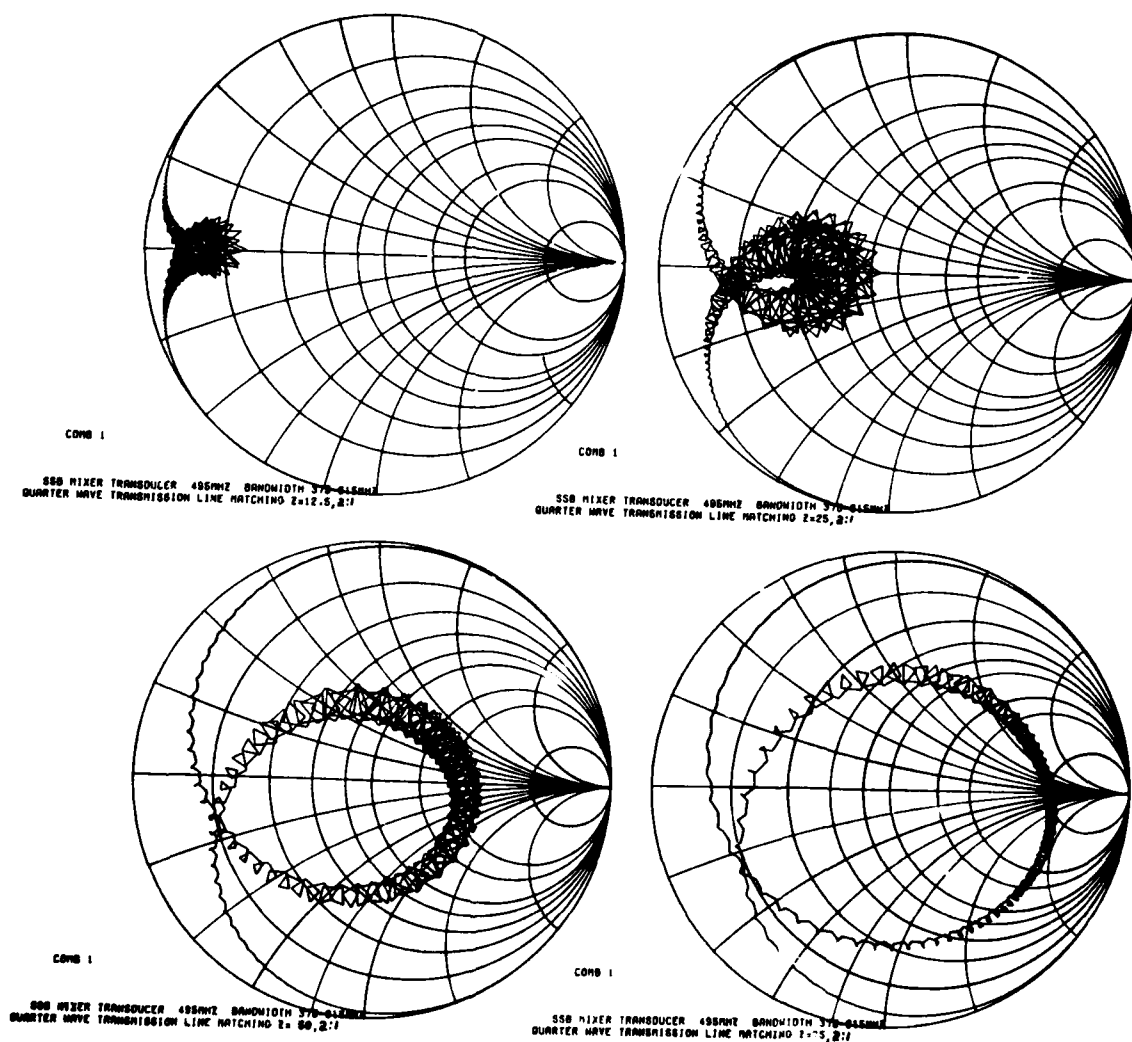


Figure C.8 Input impedances for the filters of Figure C.7. (Top left) $Z_1 = 12.5$ ohms. (Top right) $Z_1 = 25$ ohms. (Bottom left) $Z_1 = 50$ ohm. (Bottom right) $Z_1 = 75$ ohm.

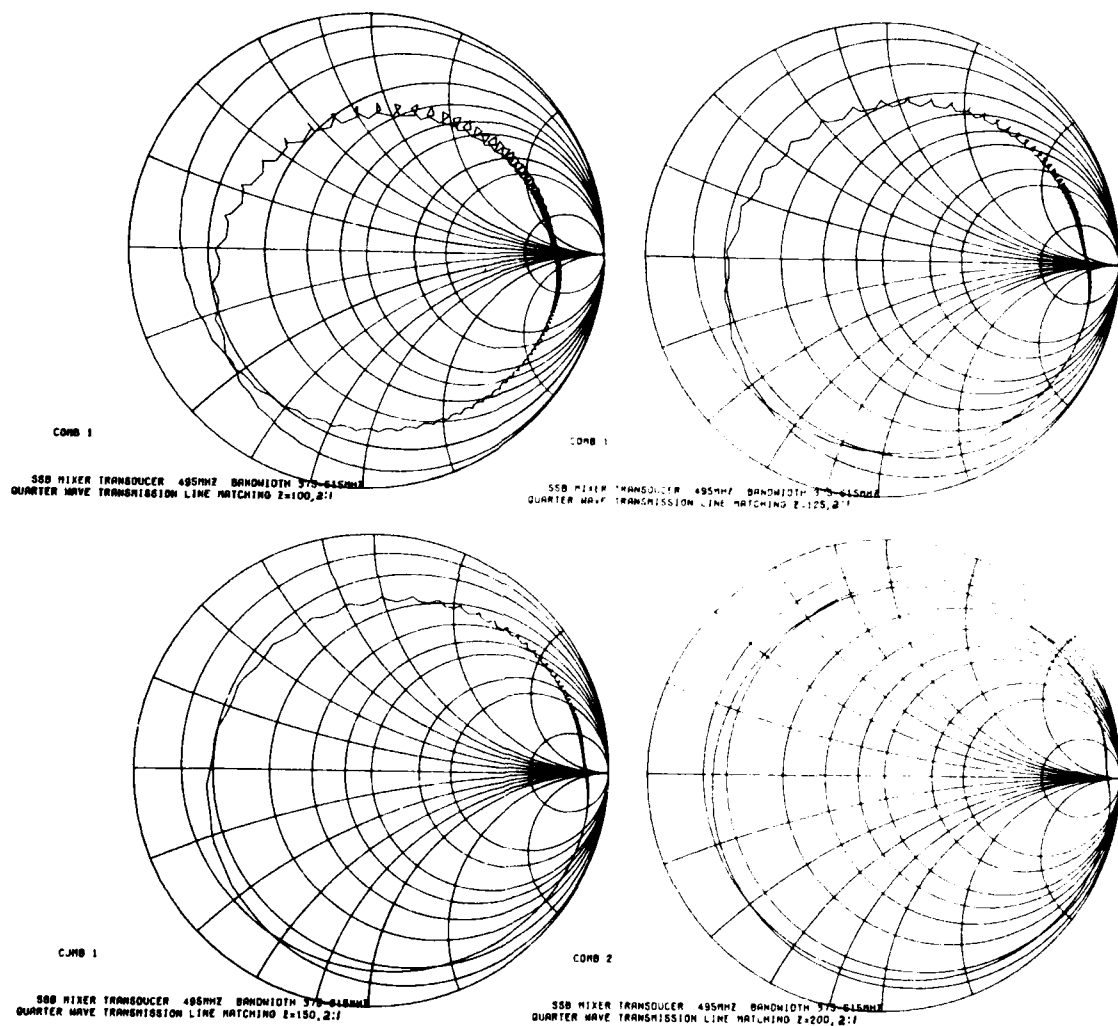


Figure C.9 Input impedances for the filters of Figure C.7.
 (Top left) $Z_1 = 100$ ohm. (Top right) $Z_1 = 125$ ohm.
 (Bottom left) $Z_1 = 150$ ohm. (Bottom right) $Z_1 = 200$ ohm.

impedance, Z_0' , seen by the matching network. Not only are insertion loss and sidelobes improved, but also the potential bandwidth is increased because 90 ohms is a practical limit in microstrip, and bandwidth increases as Z_I/Z_0 increases. Even with this improvement, however, the design goals of bandwidth and shape factor could not be simultaneously met for any value of Z_I/Z_0 .

Continuing with the Reeder type matching, Figures C.10 and C.11 give some interesting comparisons. In Figure C.10 at the top left, the reference case of a single series tuning inductor is presented. In the top right, a 50 ohm $\lambda/4$ inverter is added. The impedance is rotated 180 degrees as expected, and the IL, in the top right of Figure C.11, is unchanged. In the remaining cases, however, the ratio, Z_I/Z_0' , is the same, yet the results are markedly different. But the design goals were still not met.

Next two linear chirps were compared - one with 200 single electrode fingers in each transducer and the other with 400 single electrodes fingers each transducer. The results of this comparison are shown in the top of Figure C.12, and the input impedance of the 200 electrode transducer is given in the bottom of Figure C.12. Mass loading is causing a droop on the high frequency end of the 400 electrode transducer, however, it has a better shape factor than the 200 electrode transducer as expected. The ripple can be reduced with apodization, but the shape factor

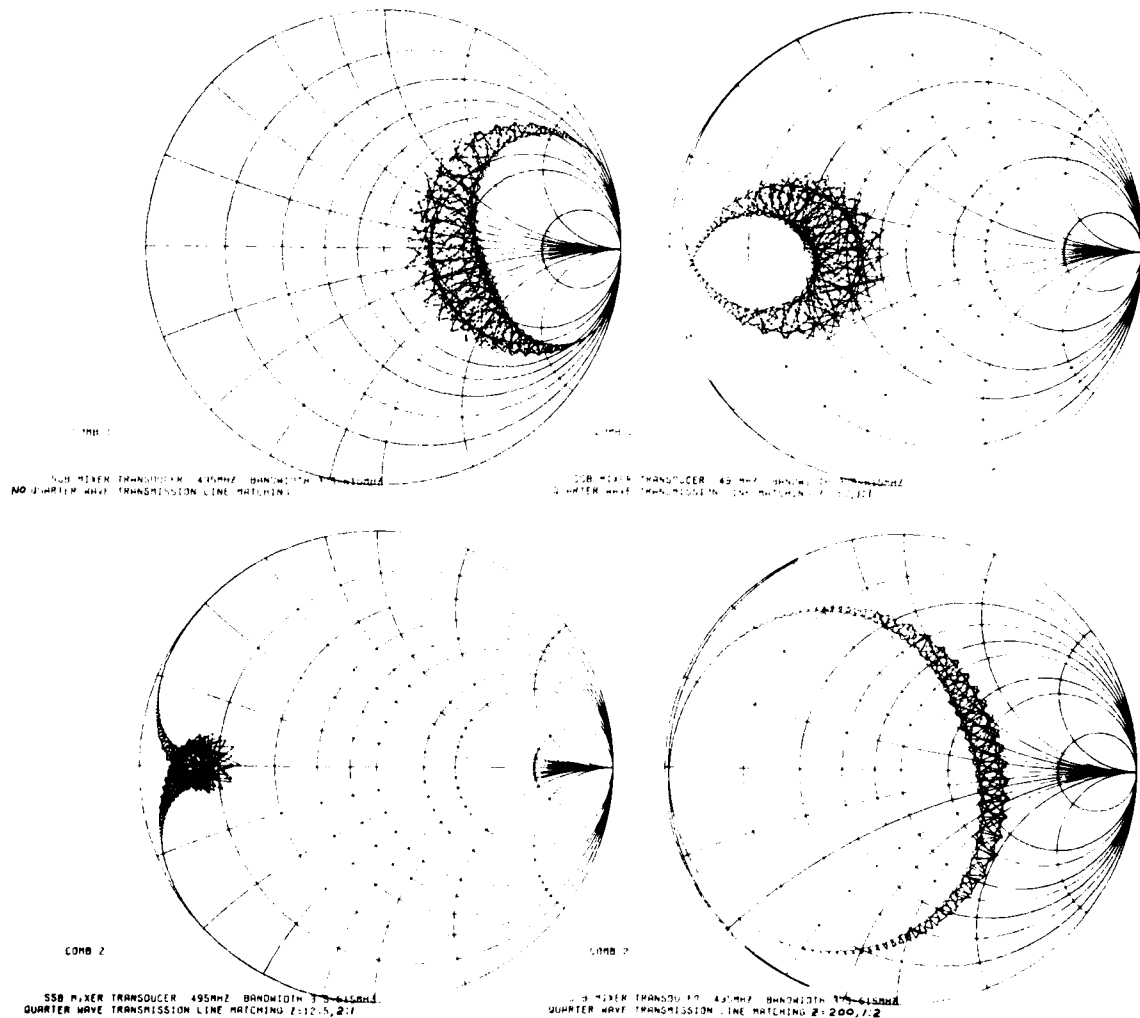


Figure C.10 Input impedances for the filters of Figure C.11-Reeder type matching. (Top left) Reference, no inverter, no transformer. (Top right) $Z_1 = 50$ ohm and no transformer. (Bottom left) $Z_1 = 12.5$ ohms and 4:1 transformer (2:1 turns ratio). (Bottom right) $Z_1 = 200$ ohms and 1:4 transformer (1:2 turns ratio). Note: the ratio Z_1/Z_0 is the same for each case.

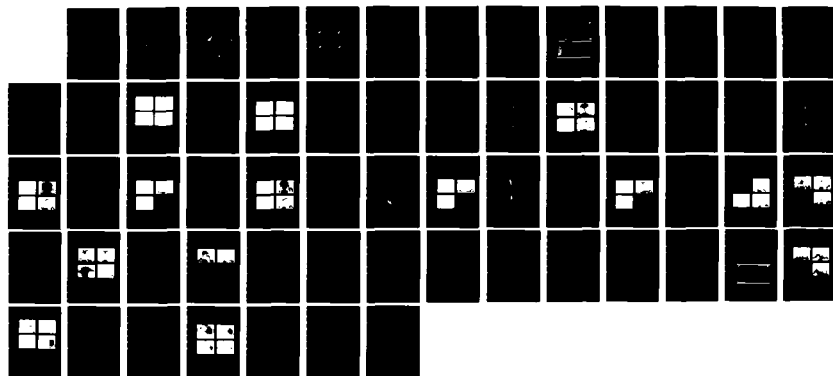
AD-A127 570

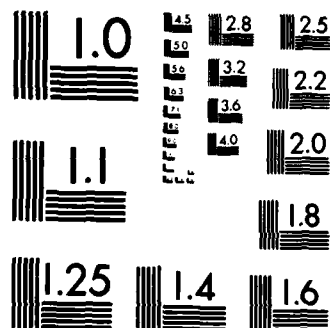
SURFACE ACOUSTIC WAVE NON-LINEAR INTERACTIONS IN
LITHIUM NIOBATE(U) ROME AIR DEVELOPMENT CENTER GRIFFISS
AFB NY R D COLVIN JAN 83 RADC-TR-83-9

4/4

UNCLASSIFIED

F/G 28/5 NL





MICROCOPY RESOLUTION TEST CHART
NATIONAL BUREAU OF STANDARDS-1963-A

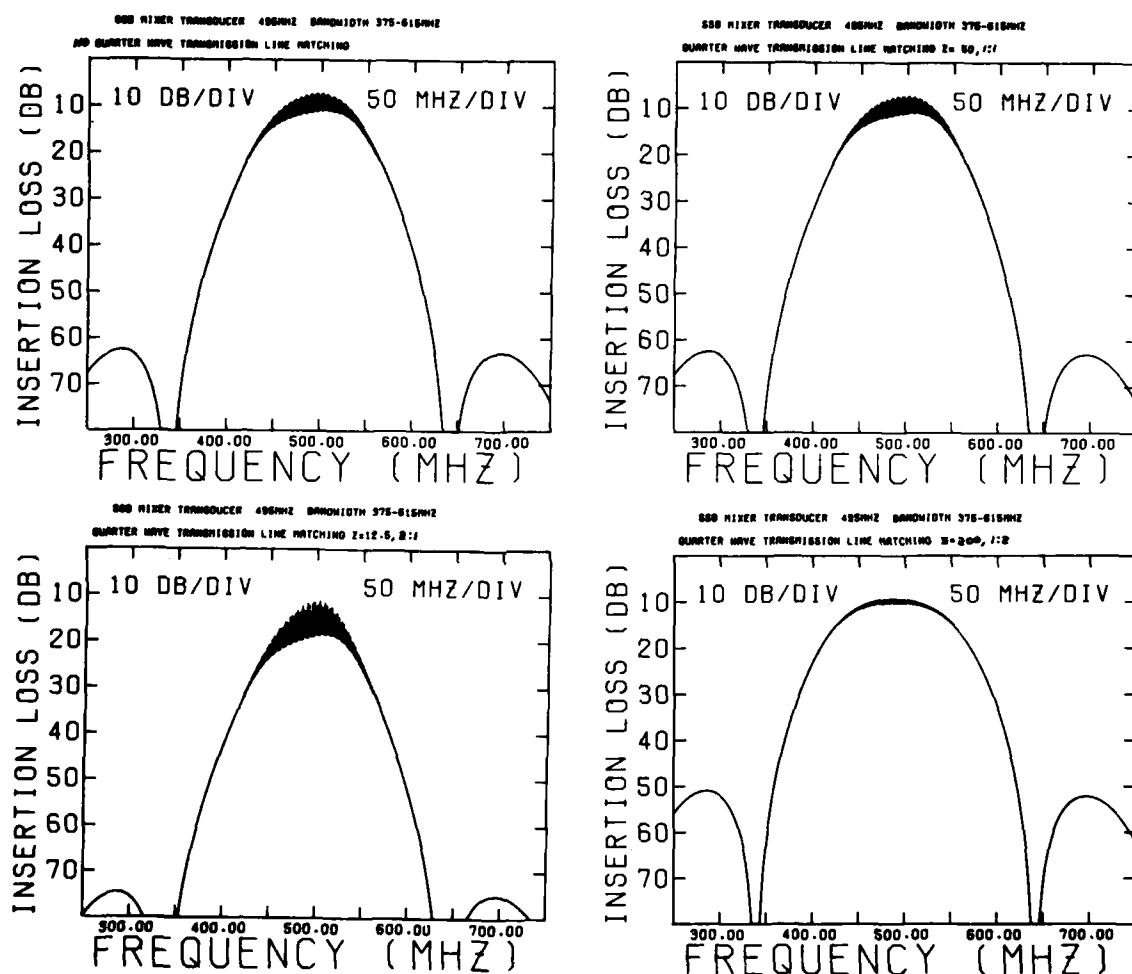


Figure C.11 Reeder type matching. (Top left) Reference, no inverter, no transformer. (Top right) $Z_1 = 50$ ohm and no transformer. (Bottom left) $Z_1 = 12.5$ ohms and 4:1 transformer (2:1 turns ratio). (Bottom right) $Z_1 = 200$ ohms and 1:4 transformer (1:2 turns ratio). Note: the ratio Z_1/Z_0' is the same for each case.

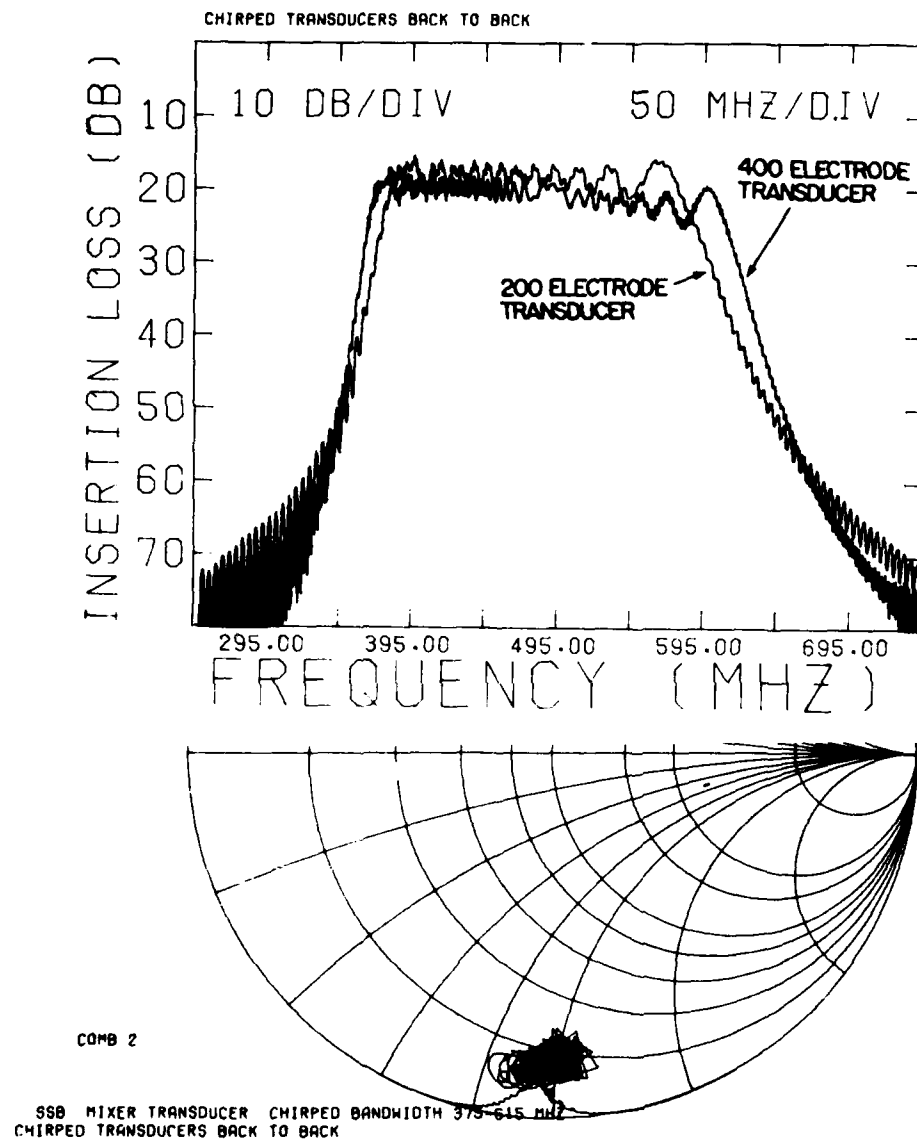


Figure C.12 (Top) Frequency response of two linear chirps - The narrow pass band obtains from a chirp of 200 fingers per transducer, and the other obtains from a chirp of 400 fingers per transducer. (Bottom) Input impedance, S_{11} , for the 400 finger linear chirp. The 200 finger transducer is very similar.

is not adequate in either transducer - especially on the high frequency side.

The linear chirp can be expressed as the superposition of a continuum of $\sin X/X$ responses. In an effort to improve the shape factor on the high frequency side, additional fingers were added to the 200 finger linear chirp. The 200 finger linear chirp is reproduced for convenience in the top left of Figure C.13. In the top right we see the result of adding 25 fingers, (25,200)(25,200), each having the same periodicity, and the periodicity is different (smaller) from any of those in the linear chirp. In the bottom left, 50 fingers have been added, (50,200)(50,200). In an effort to remove the null on the low frequency side of the 50 electrode response, the 50 electrodes were divided into two 25 electrode segments with slightly different periodicities and the result is shown in the bottom right of Figure C.13. While this exercise was interesting, it was neither adequate nor practical.

A Phase Reversal Transducer (PRT) was considered. However in this design as the bandwidth increases, the sidelobes also increase. In a typical example, the bandwidth was increased to 37 percent giving a shape factor of 1.57 and sidelobes of 12 dB as shown in Figure C.14. Increasing the bandwidth further improves shape factor but degrades sidelobes further. Therefore, this approach was not pursued.

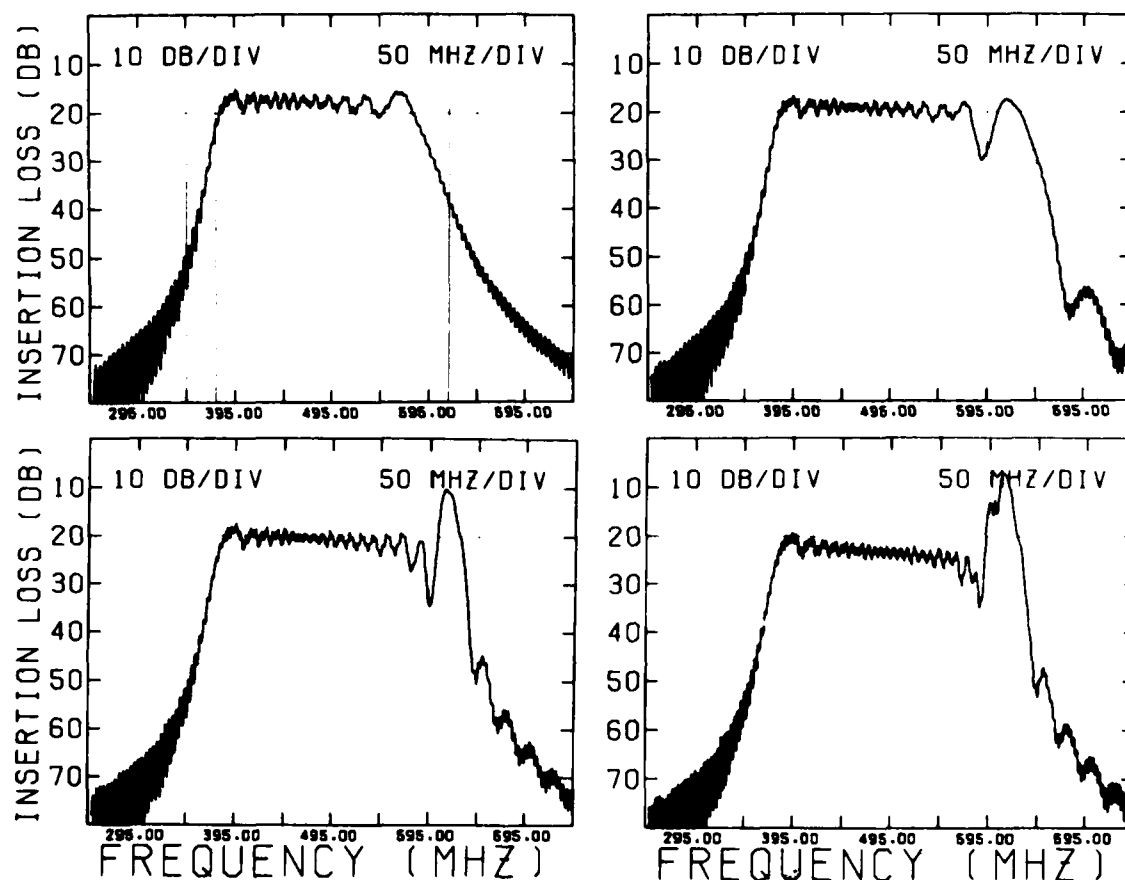


Figure C.13 Frequency response of four linear chirp filters. (Top left) 200 fingers each transducer. (Top right) Same as top left except 25 fingers have been added with periodicity less than the smallest chirp periodicity. (Bottom left) Same as top left except 50 fingers have been added with periodicity less than the smallest chirp periodicity. (Bottom right) Same as top left except 50 fingers have been added with one periodicity, and 50 fingers have been added with another periodicity, both less than the smallest periodicity of the chirp.

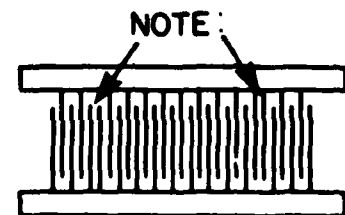
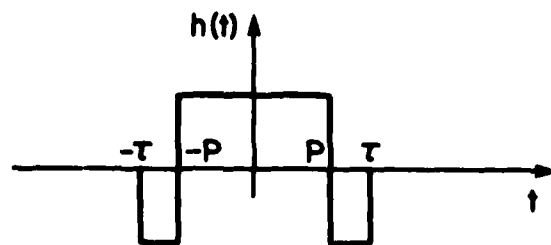
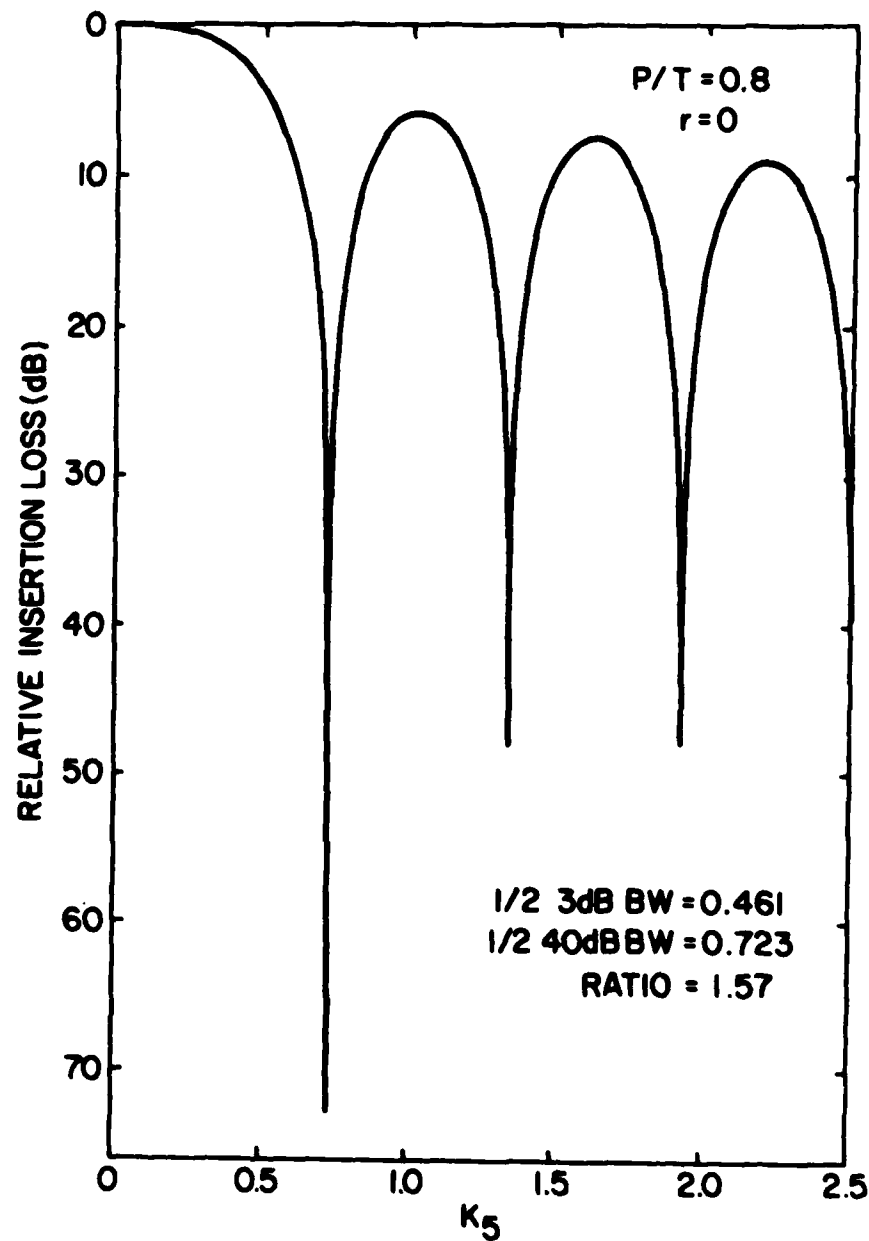


Figure C.14 (Top) Normalized frequency response of a phase reversal transducer (PRT). (Bottom left) Weighting function associated with the PRT. (Bottom right) Schematic drawing of PRT. Note phase reversals on left and right sides.

As stated above, a single apodized transducer will not meet the design goals for bandwidth and shape factor simultaneously. The next attempt then was to try stagger tuning of two different broadband apodized transducers connected in parallel, e.g. Figure C.2. The individual broadband apodized transducers were analyzed first; one of these is shown in the top left of Figure C.15. This response is for an apodized transducer on the input, and an even broader band unapodized transducer on the output. First, one should note the asymmetry of the passband. The skewing is due to second order effects of reflections and regeneration. This can be eliminated with double electrode fingers. The sidelobes of 62 dB on the low frequency side and 55 dB on the high frequency side are due to the combination of both input and output transducers, and after subtracting the contribution of the output transducer, the sidelobes due to the input transducer are 45 and 39 dB respectively. The theory for Hamming weighting as used here predicts 45 dB, so there are problems with the high frequency side even before starting. The top right of Figure C.15 shows the untuned parallel combination of two staggered, apodized transducers, and the input impedance, S_{11} , was used to compute the IL as explained in Appendix B.2. With the addition of stagger tuning (explained in the next section) the results at the bottom left were obtained, but neither the bandwidth nor the shape factor are adequate. Figure C.16 gives computer

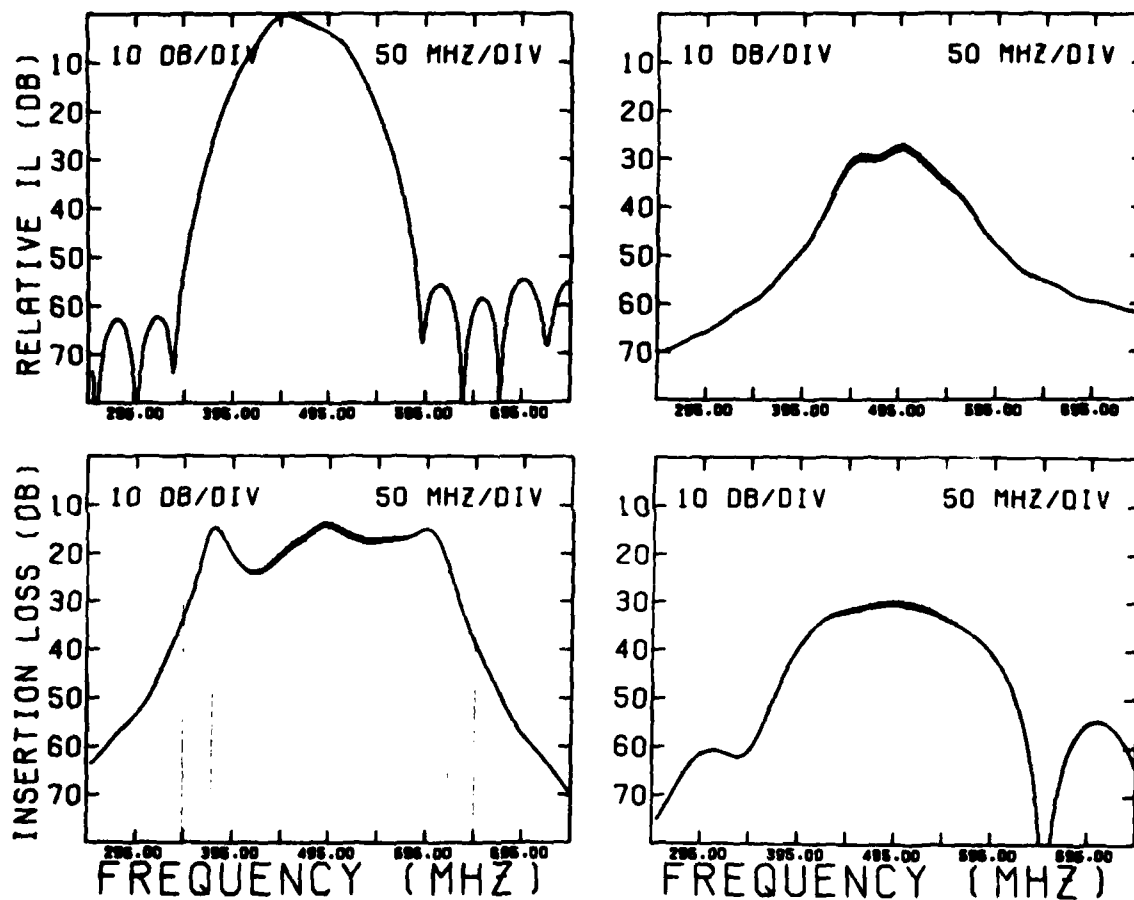


Figure C.15 (Top left) Frequency response of a Hamming weighted apodized transducer and a broad band unapodized transducer. The left and right side lobes are 45 and 39 dB due to the apodized transducer only. (Top right) Two broad band apodized transducers in parallel. (Bottom left) Same as top right except stagger tuning has been added. (Bottom right) Two broad band unapodized transducers in parallel.

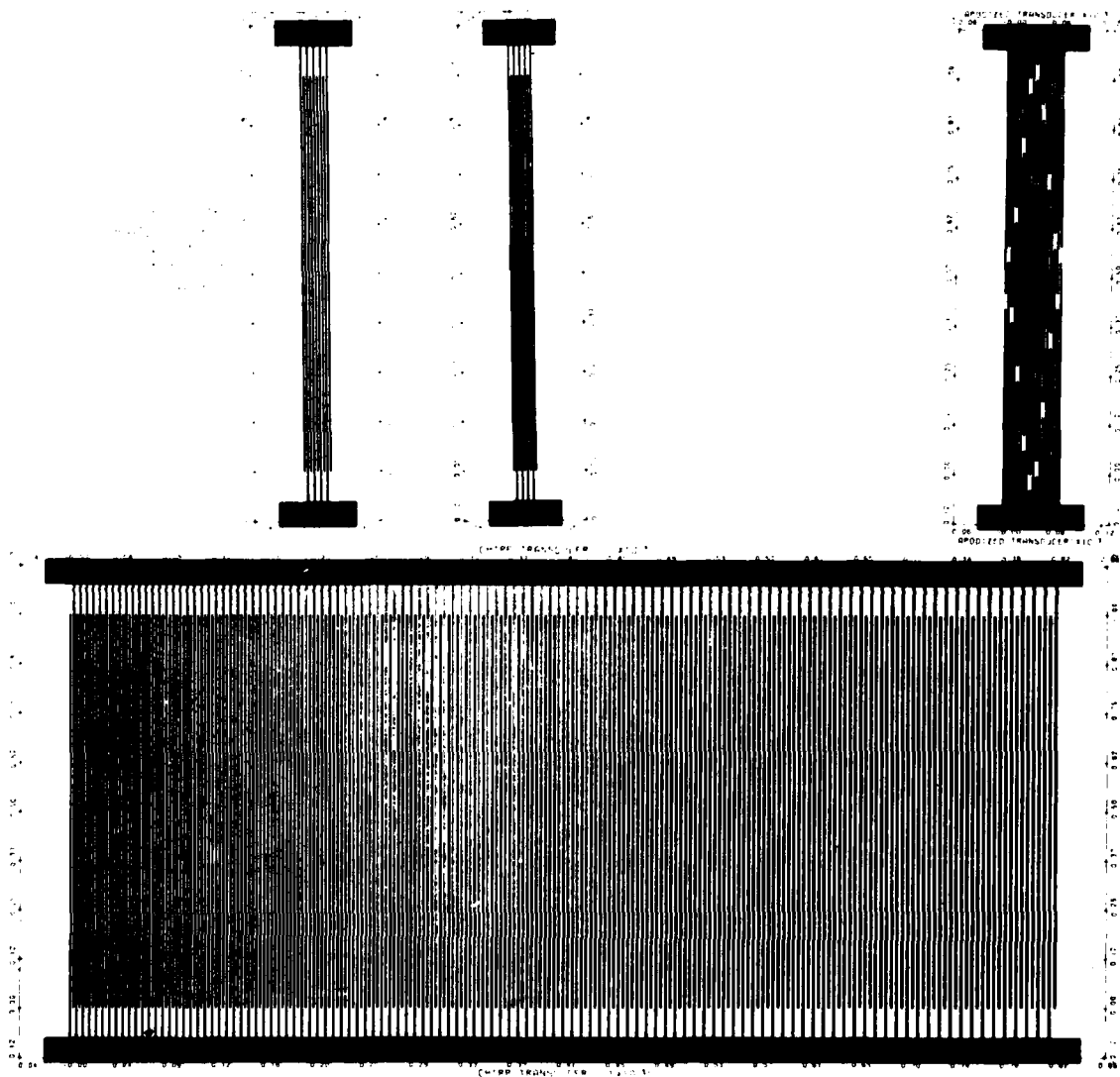


Figure C.16 (Top left) Two broad band unapodized transducers.
 (Top right) Broad band apodized transducer.
 (Bottom) 200 finger linear chirp transducer.

generated drawings of several of the above mentioned transducers; at the top right is a broadband apodized transducer, and at the bottom is a linear chirp of 200 fingers.

The final attempt at meeting the design goals, utilized stagger tuning of two different broadband unapodized transducers connected in parallel, e.g. see Figure C.2. According to the computer modeling described in the next section, this approach would meet the design goals. The frequency response of these parallel connected and untuned transducers is given in the bottom right of Figure C.15, and the computer generated drawings of the transducers appear in the top left of Figure C.16.

Staggering of the synchronous frequencies of parallel connected SAW transducers has been reported before.^{C.4} However, in that case a single series inductor was used after the transducers had been connected in parallel. In this work a series inductor was used to tune each transducer off its synchronous frequency before being connected electrically in parallel. This approach gives inherently better shape factor. It also presents a potential problem in that the combined output signals are not in phase with each other.

C.3 Stagger Tuning

The schematic of Figure C.2 was redrawn as the

network given in Figure C.17. The resulting equations (see Appendix B.2) were solved on a computer. Z_T is the radiation resistance and capacitive reactance of the transducer; R_1 and R_2 represent the finite resistivity of the aluminum electrodes in the interdigital transducers, and C_1 and C_2 are equivalent shunt capacitances due to the bond wires going from the series matching inductors to the transducer bonding pads. L_1 , R_3 and C_3 comprise the equivalent circuit of a real inductor as do L_2 , R_4 and C_4 for a different inductor.

At this point it was necessary to make some reasonable assumptions. Z_{T1} , Z_{T2} , R_1 , and R_2 were taken from a second order effects transducer analysis computer program (see Appendix B.1). R_1 and R_2 were 13.4 and 15.8 ohms respectively. The equivalent shunt capacitances, C_1 and C_2 , were assumed to be 0.1 pf. The L_1 , R_3 and C_3 model of a real inductor was assumed, although later it was shown that a different model gave better agreement with experiment. The manufacturer's specifications for Q and self resonant frequency of the inductors were used, however, measurements of these parameters later showed them to be significantly different from the manufacturer's published values. L_1 was assumed to be 390 nhy with a Q of 18 and self resonant frequency (SRF) of 6.6 GHz, and L_2 was assumed to be 110 nhy with a Q of 72 and SRF of 1 GHz. R_3 and R_4 were computed from $R = \omega L/Q$. C_3 and C_4 were computed by

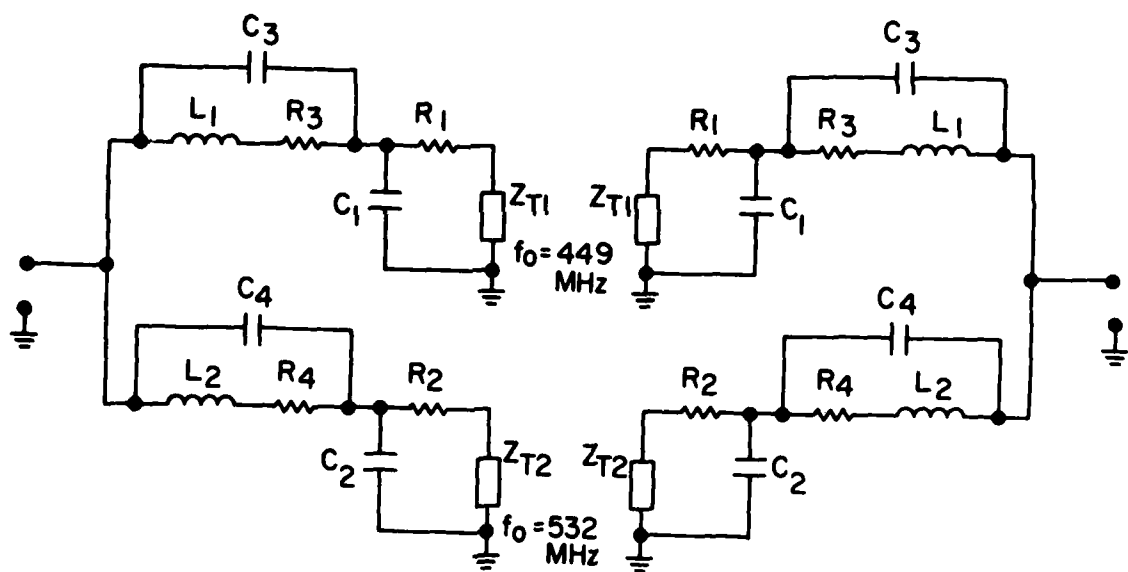


Figure C.17 Circuit model used for analysis of stagger tuned SAW filter in bottom of Figure C.18.

setting the imaginary part of the real inductor impedance equal to zero and solving for C:

$$C = L^{-1} [(2 \pi \text{SRF})^2 + (R/L)^2]^{-1} \quad (\text{C.1})$$

Transducers in Channels 1 and 2 had apertures of 17λ and 20λ respectively and 9 single electrode fingers each - see top of Figure C.18 and the top left of Figure C.16. These small, non-optimum apertures were chosen because it was desired to generate non-linear acoustic waves, and the small aperture gives a larger acoustic power density.^{C.5} The resulting performance as a filter is to increase the transducer radiation resistance and capacitance. This required a larger inductor and presented the problem of finding a large enough inductor with a high enough self resonant frequency. The results in this thesis then should be viewed as a worst case upper limit; most filter applications would require smaller inductors where it is easier to get a high self resonant frequency. The self resonant frequency reduces the effective inductance of an inductor according to the equation

$$L_T = L \left[1 - \left(\frac{f_o}{\text{SRF}} \right)^2 \right].$$

Using these values and assumptions, the result shown in the bottom of Figure C.18 was obtained. The bandwidth is 51 percent, insertion loss 14.5 dB, shape factor 1.22, and

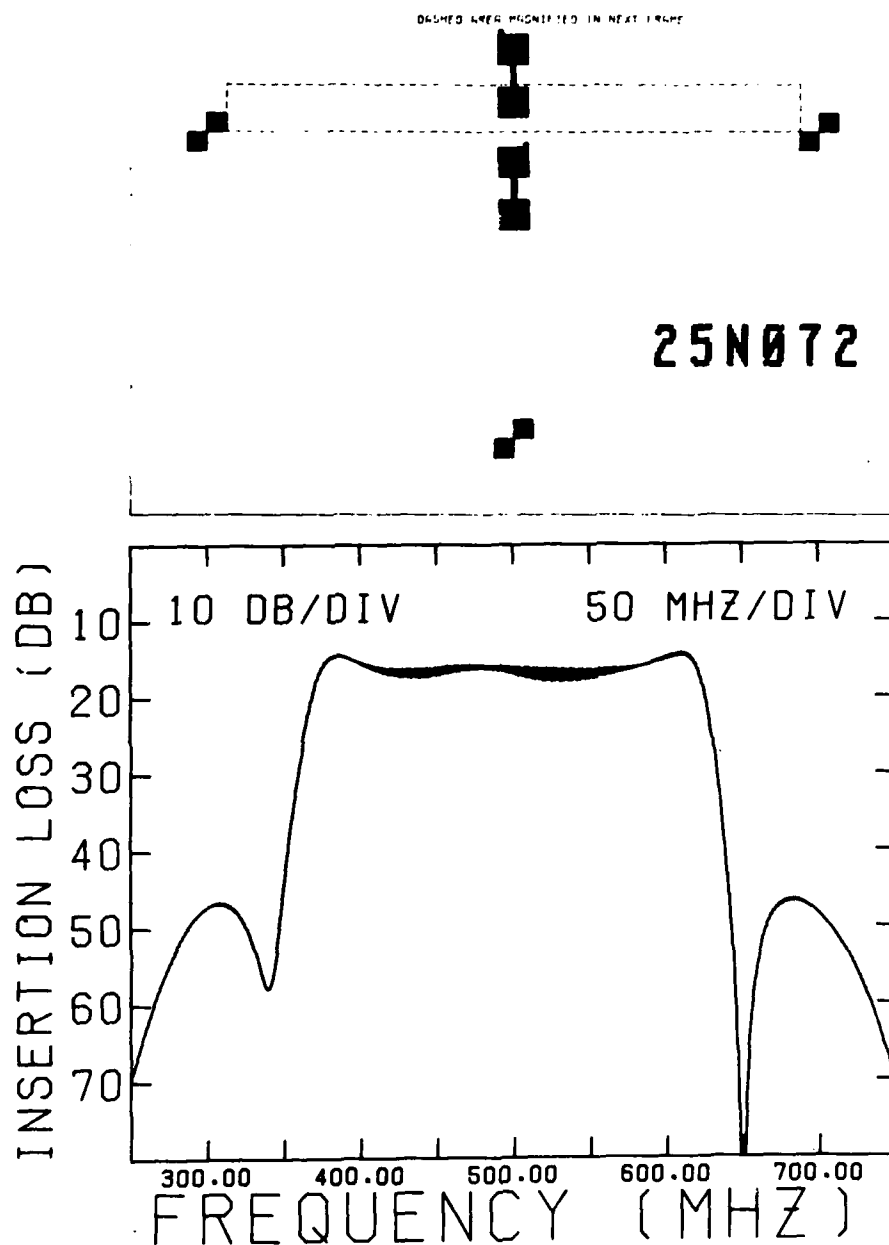


Figure C.18 (Top) Computer generated drawing of photolithographic mask with two broad band unapodized transducers used for stagger tuning. (Bottom) Stagger tuned SAW filters as shown in Figure C.2 and C.17. $L_1 = 390$ nhy, $Q = 18$, and $SRF = 6.6$ GHz. $L_2 = 110$ nhy, $Q = 72$, and $SRF = 1.0$ GHz. C_1 and $C_2 = 0.1$ pf; R_1 and $R_2 = 13.4$ and 15.8 ohms.

sidelobes are down 32 dB. Thus this approach meets the design goals.

C.4 Experiment

The best experimental effort at broad bandwidth and low shape factor is shown in the top of Figure C.19. The input impedance, S_{11} , is shown in the top left of Figure C.19 as the frequency sweeps from 375 to 615 MHz, and the corresponding frequency response is shown in the top right of Figure C.19 with a scale of 50 MHz/div. centered on 500 MHz and 10 dB/div for the ordinate. The 8 dB bandwidth is 45 percent, and the overall shape factor is 1.32. Note that the low frequency skirt is very sharp and has an effective shape factor of 1.20. In order to make theory and experiment agree more closely it was necessary to measure inductors and change the model of the real inductor. L_1 was measured with a Boonton R_x meter at 80 MHz and found to have a Q of 25.3, and its self resonant frequency (SRF) was measured to be 601 MHz with an HP 8410 network analyzer. The effective (reduced by SRF) inductance was computed to be 262 nhy using equation (C.2) and the equation

$$L = \frac{50}{2\pi f \tan(\theta/2)} \quad (C.3)$$

θ is read from the network analyzer Smith Chart display.

L_2 was measured to be 130 nhy with Q of 42.4 and SRF of 1357 MHz.

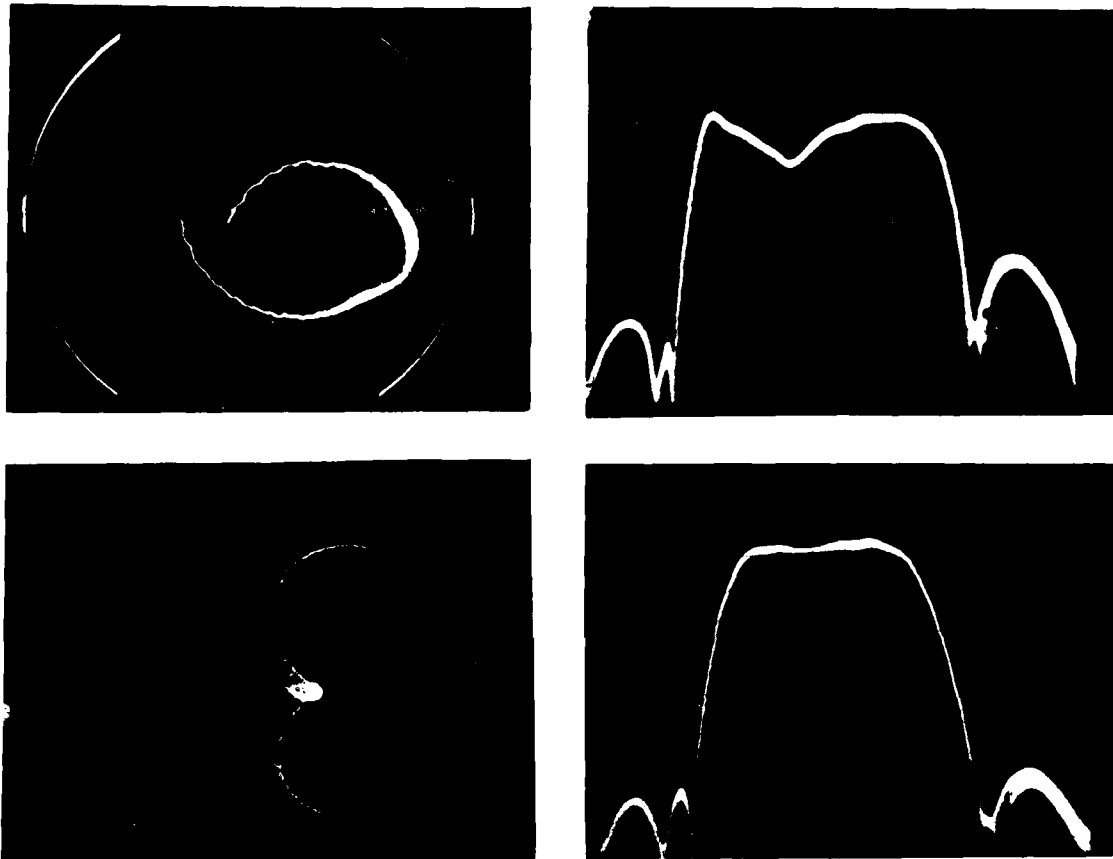


Figure C.19 (Top left) S_{11} for filter on the right as frequency sweeps 375 to 615 MHz. (Top right) Frequency response for SAW filter connected as shown in Figure C.2 except one channel has 180 degrees phase shift. L_1 is 262 nhy with Q of 25.3 and self resonant frequency (SRF) of 600 MHz. L_2 is 130 nhy with Q of 42.4 and SRF of 1357 MHz. Vert: 10 dB/div, Horiz: 50 MHz/div., $f_o = 500$ MHz. (Bottom left) S_{11} for filter on the right as frequency sweeps 375 to 615 MHz. (Bottom right) Frequency response for SAW filter connected as shown in Figure C.2 except one channel has 180 degrees phase shift. L_1 is 206 nhy with Q of 23.5 and SRF of 670 MHz. L_2 is 176 nhy with Q of 24.5 and SRF of 1940 MHz. Vert: 10 dB/div., Horiz: 50 MHz/div., $f_o = 500$ MHz.

Some examples of the above inductor measurements are given in Figure C.20. At the top left, the value of inductance was found from θ for four different frequencies. The inductor was a Piconics S500 inductor having an air core with a coat of epoxy on the outside. The values read from the Smith Chart were $\theta = 40, 30, 20,$ and 10 degrees for frequencies of 428, 537, 634, and 780 MHz respectively. The SRF was obtained when the angle θ became zero and occurred at 1446 MHz in this case. The same information can be obtained from a phase only display as shown in the top right of Figure C.20. The abscissa sweeps 500 to 1000 MHz, and the ordinate is 10 deg./div. The inductor is now a Piconics PV 101K8I. The zero crossing or SRF occurred at 634 MHz. A Piconics PV 250K8I is displayed in the bottom left as the frequency sweeps 1 to 2 GHz. By sweeping manually, the SRF was found to be 1795 MHz, and θ equaled 30 degrees at 1050 MHz. At the bottom right, the effect of adding a slug to the PV 250K8I slug tunable inductor is demonstrated. θ decreased (L increased), SRF decreased, and losses increased. The SRF is now 1330 MHz and, θ equals 13.5 degrees at 1050 MHz.

In Figure C.21 the result of measuring θ and computing L and L_T at eleven discrete frequencies is seen. In this example two inductors have been connected in series - one with 30 turns and one with 5 turns of #47 ga. wire. They are Piconics M series. The results are typical of all

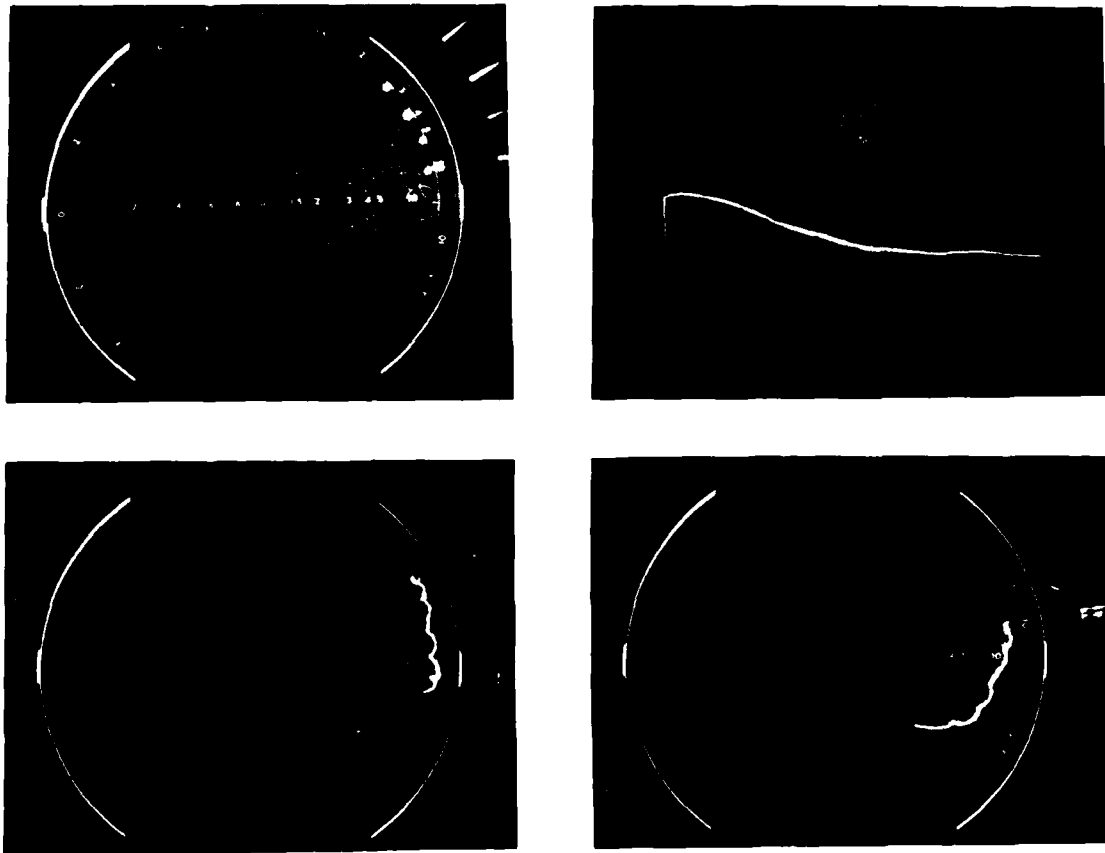


Figure C.20 (Top left) Reactance of Piconics S500 inductor at four discrete frequencies: $\theta = 40, 30, 20$, and 10 degrees for $428, 537, 634$, and 780 MHz respectively. (Top right) Phase only display of S_{11} for a Piconics PV101K81 inductor. 10 deg/div. vert., 500 to 1000 MHz Horiz. SRF occurs at 634 MHz. (Bottom left) PV 250K81 as frequency sweeps 1 to 2 GHz. (Bottom right) PV250K81 with tunable slug inserted as frequency sweeps 1 to 2 GHz.

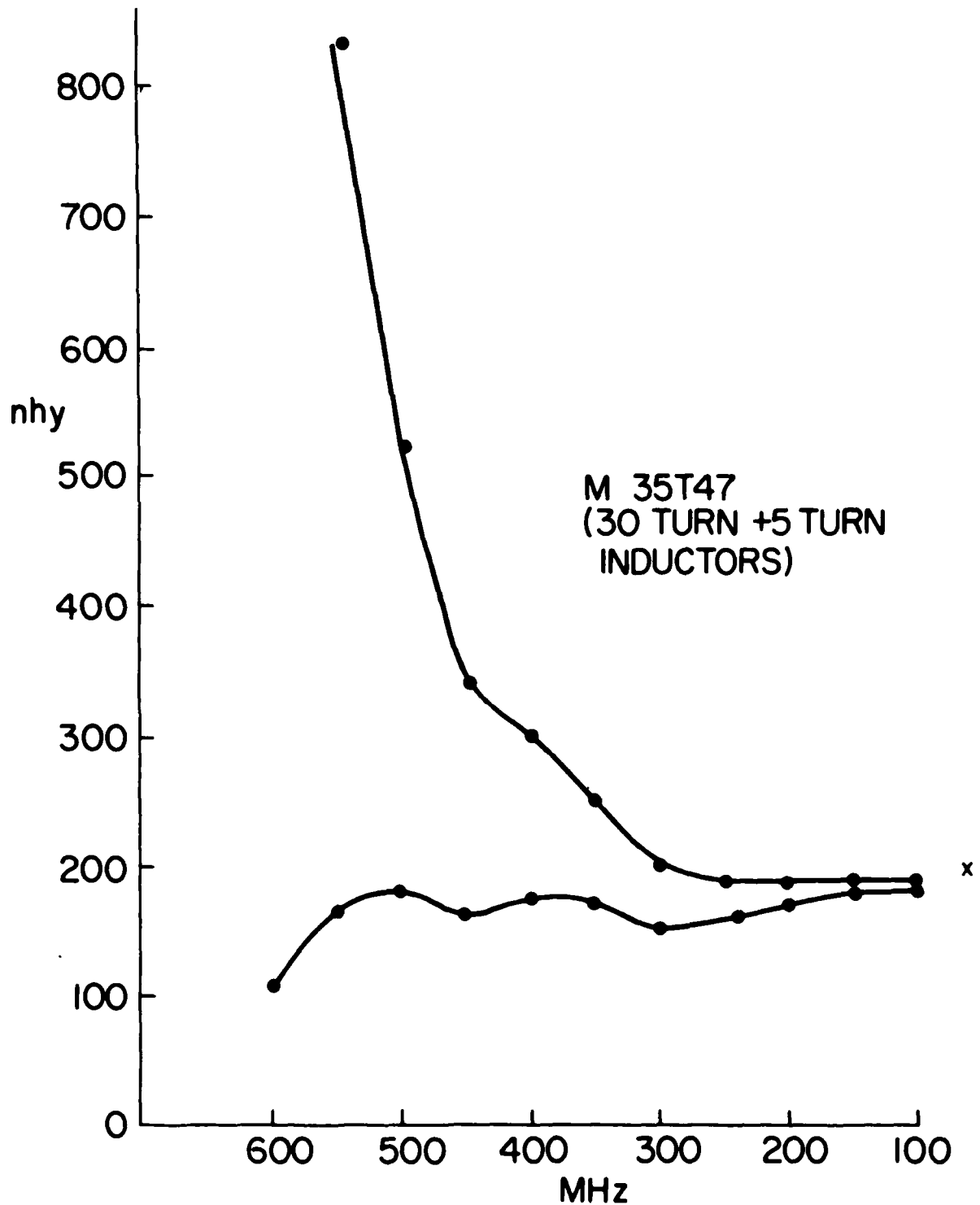


Figure C.21 Plot of inductance, L , and inductance reduced by self resonant frequency, L_T . This example is for two inductors in series (30 turn plus 5 turn) but is typical of all inductors.

inductors whether alone or in series and regardless of size or series. Neither L nor L_T are constant with frequency, and closer to the SRF they diverge more and more. The data point marked "X" was obtained from the Boonton Rx meter at 80 MHz.

With measured values of actual inductors, it was possible to resolve the differences between the theory of Figure C.17 and the bottom of Figure C.18 with the experimental observations shown in the top of Figure C.19. The first step was to get agreement between theory and experiment for each channel alone and then for the channels electrically combined. The result of this step was the adoption of the model contained within the dashed line box of Figure C.22. Best fit with data was obtained when C_3 was split and distributed which is more nearly the true situation. Also the shunt capacitance, C_1 , was changed to 0.2 pf. These changes were based on curve fitting data from 10 different sets of filters. The single channels corresponding to the top of Figure C.19 are shown in Figure C.23 (theory) and Figure C.24 (experiment); agreement is good. Careful observation revealed that when the individual channels were connected in parallel the impedances at 375 and 615 MHz changed slightly and by random amounts. This was probably due to different length bond wires resulting from new bonding configurations. L_3 , L_4 , C_5 , and C_6 were added to the model of Figure C.22 to handle this observed

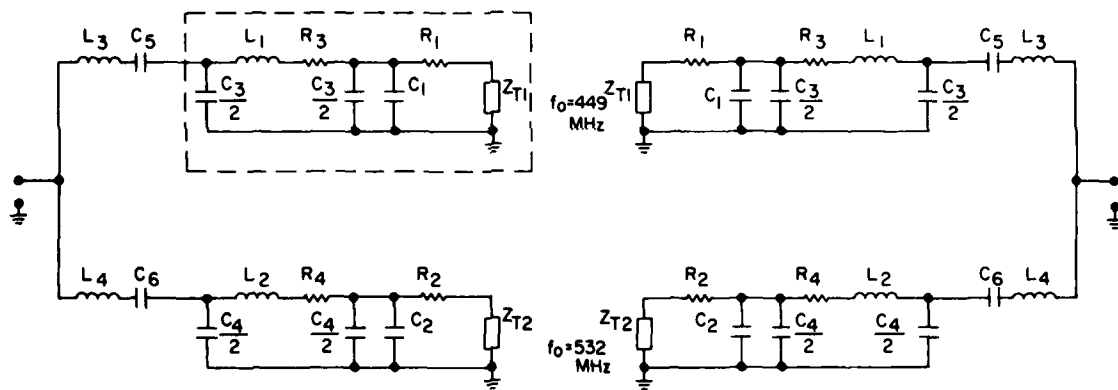


Figure C.22 Improved circuit model used for analysis of all stagger tuned SAW filters except Figure C.18. Inside the dashed box is the improved circuit model used for a single channel.

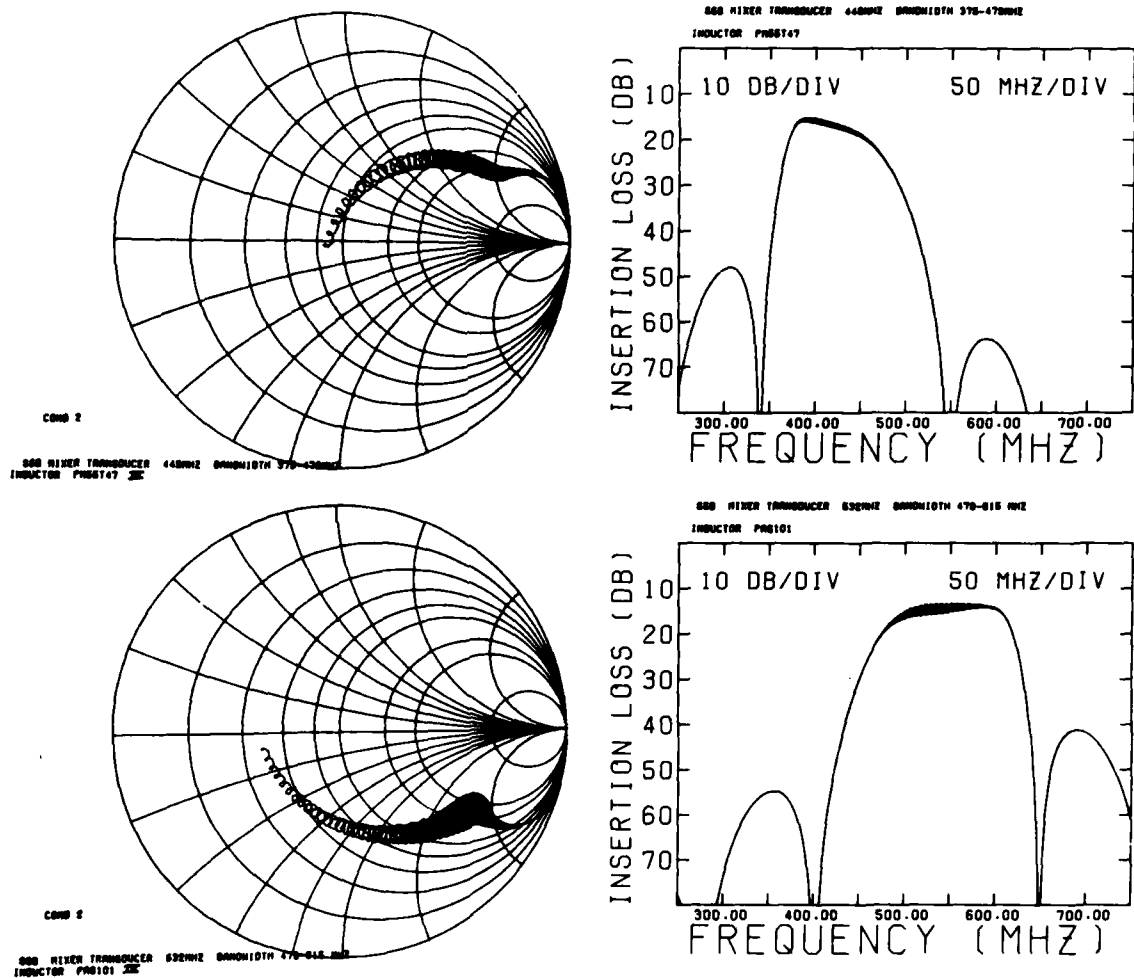


Figure C.23 Theory for individual channels of Figure C.19
(Top) S_{11} and frequency response of low frequency channel. (Bottom) S_{11} and frequency response of high frequency channel.

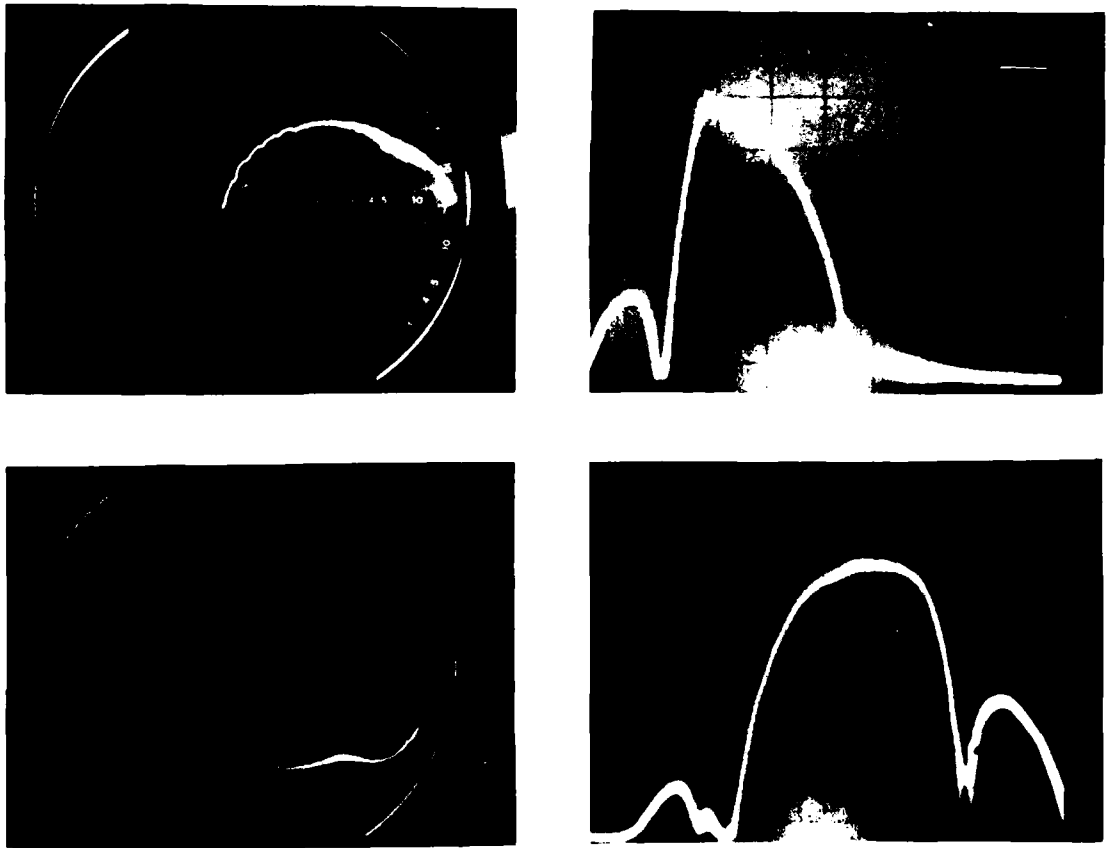


Figure C.24 Experiment corresponding to theory of Figure C.23.

variable. L_3 and L_4 (inductance of bond wires) were assumed to be 20 nhy, and C_5 and C_6 were 10.0 and 3.4 pf in this case. Rewriting the computer program for this model (see Appendix B.2), and using the new measured component values, the plots in the top of Figure C.25 were obtained. When compared with the experiment shown in the top of Figure C.19, one discrepancy is the 3 dB knee on the high frequency corner. The sharpness of this knee is sensitive to the inductor Q . However this knee will never be as sharp as the low frequency one (for the same Q) because the frequency response of a SAW transducer is not symmetric C.6. A second discrepancy is the larger dip in the middle of the frequency response of the experimental figure. This is due to phase differences in the two channels and is explained in the next section. The frequency response in the top right of Figure C.19 was obtained with the output transducers connected 180 degrees out of phase with each other to partially compensate for this effect.

Next, the inductors were changed until a 3 dB bandwidth was achieved. The new measured values for L_1 were 206 nhy, Q of 23.5, and SRF of 670 MHz, and L_2 was 176 nhy with Q of 24.5, and SRF of 1940 MHz. The SRF quoted by the manufacturer was much higher and probably correct for an inductor suspended in space. However, when it is mounted close to a ground plane the effective SRF is greatly reduced. The values cited here were obtained with the

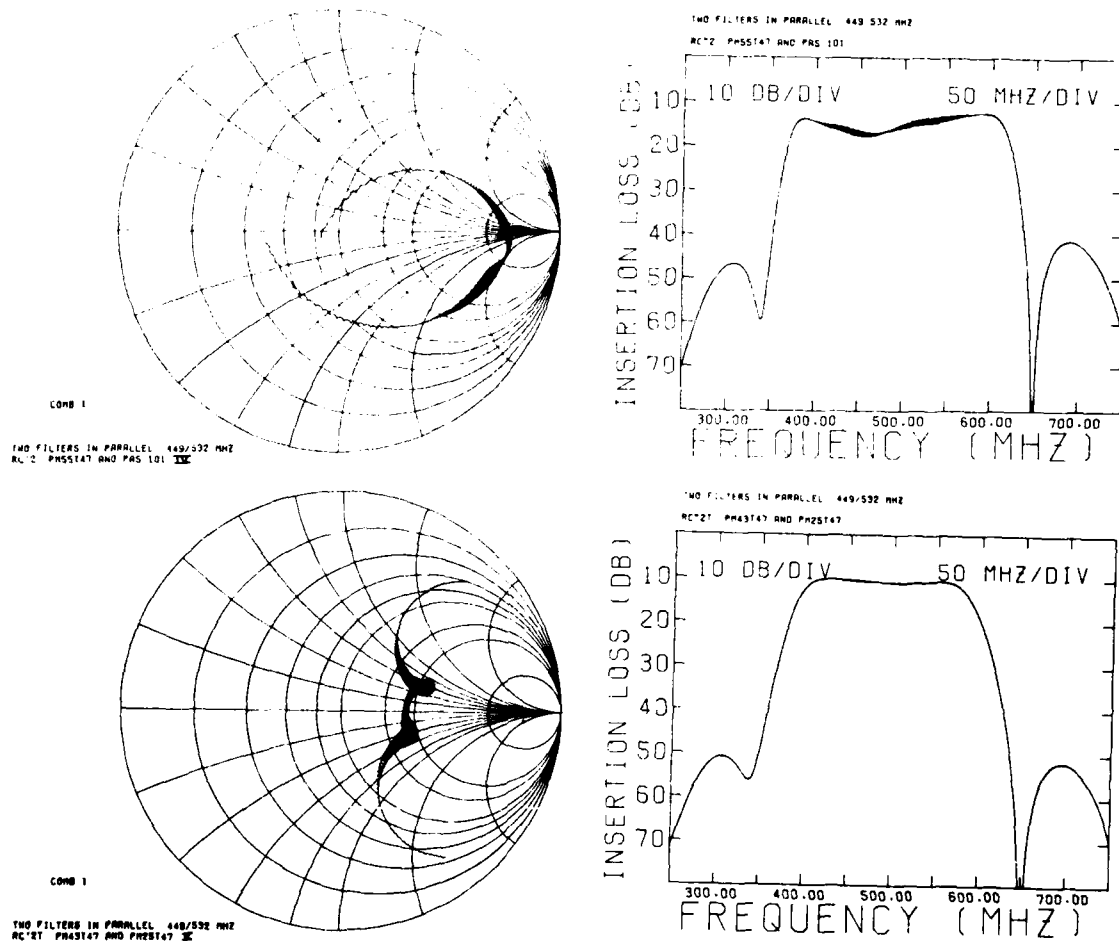


Figure C.25 Theory corresponding to experiment of Figure C.19.

inductors sitting on top of a teflon spacer block of about 0.125 inch. The associated shunt capacitance of 0.2 pf for C_1 and C_2 again gave the best fit. The response for the individual channels for this case are given in Figure C.26 (theory) and Figure C.27 (experiment); agreement is good. L_3 and L_4 were assumed to be 20 nhy; C_5 and C_6 were 11.3 and 3.3 pf. The computer generated responses for the combined channels are given in the bottom of Figure C.25 and agree very well with the experimental curves in the bottom of Figure C.19. Again the output transducers were connected 180 degrees out of phase resulting in a bandwidth of 35 percent, 1.59 shape factor, 17 dB insertion loss, and 42 dB sidelobes.

To further verify the agreement between theory and experiment, three more cases were examined. In all cases the same transducers were used, only the inductors were changed. Figure C.28 (theory) and Figure C.29 (experiment) constitute the next case. In the low frequency channel, $L_T = 258$ nhy, $Q = 25.3$, and SRF was 601 MHz, and in the high frequency channel, $L_T = 139$ nhy, $Q = 12.4$, and SRF was 1805 MHz. The combined response is shown in the top of Figure C.30 (theory) with L_3 and $L_4 = 20$ nhy, and C_5 and $C_6 = 18.6$ and 1.9 pf. The top of Figure C.31 gives the corresponding experimental response. The amplitude is lower at the cross-over frequency than predicted by theory, but this has been explained due to phase differences in the two channels that

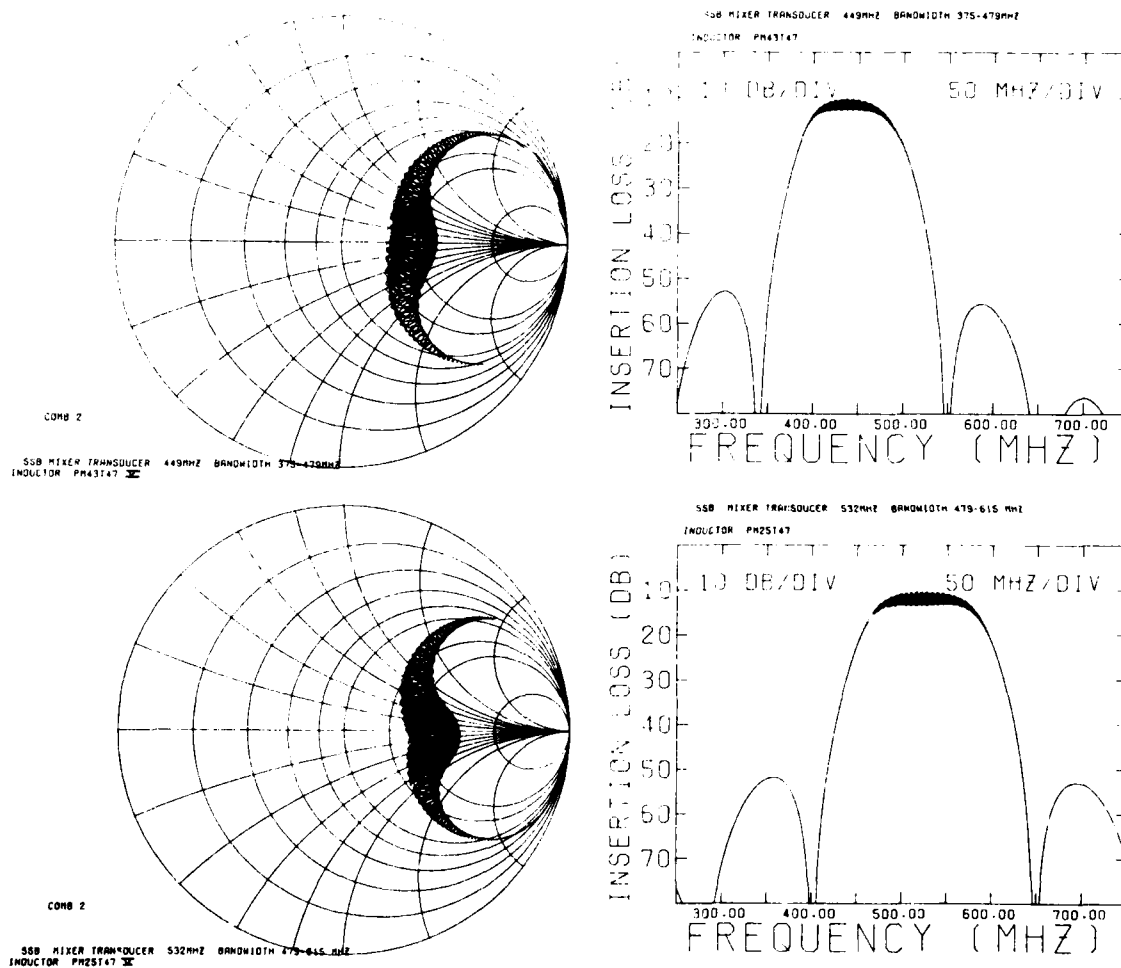


Figure C.26 Theory for individual channels of Figure C.19 bottom. (Top) S_{11} and frequency response of low frequency channel. (Bottom) S_{11} and frequency response of high frequency channel.

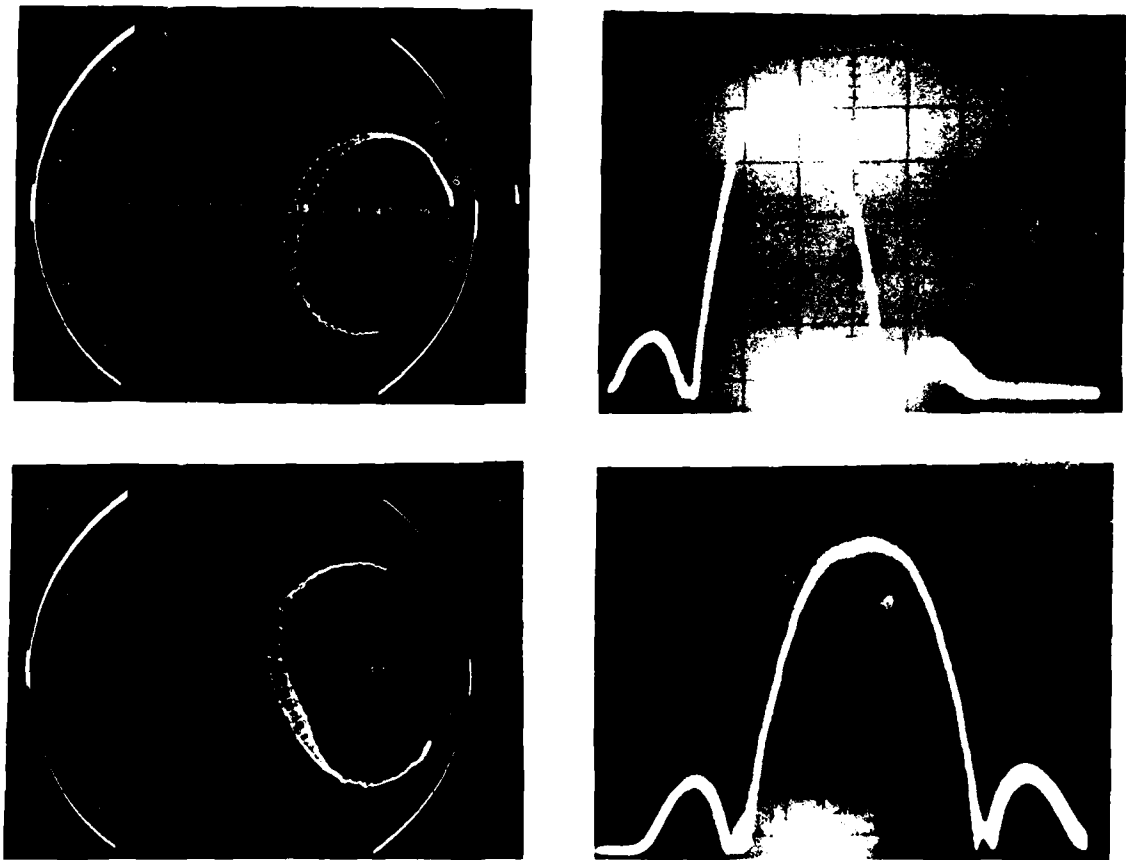


Figure C.27 Experiment corresponding to theory of Figure C.26.

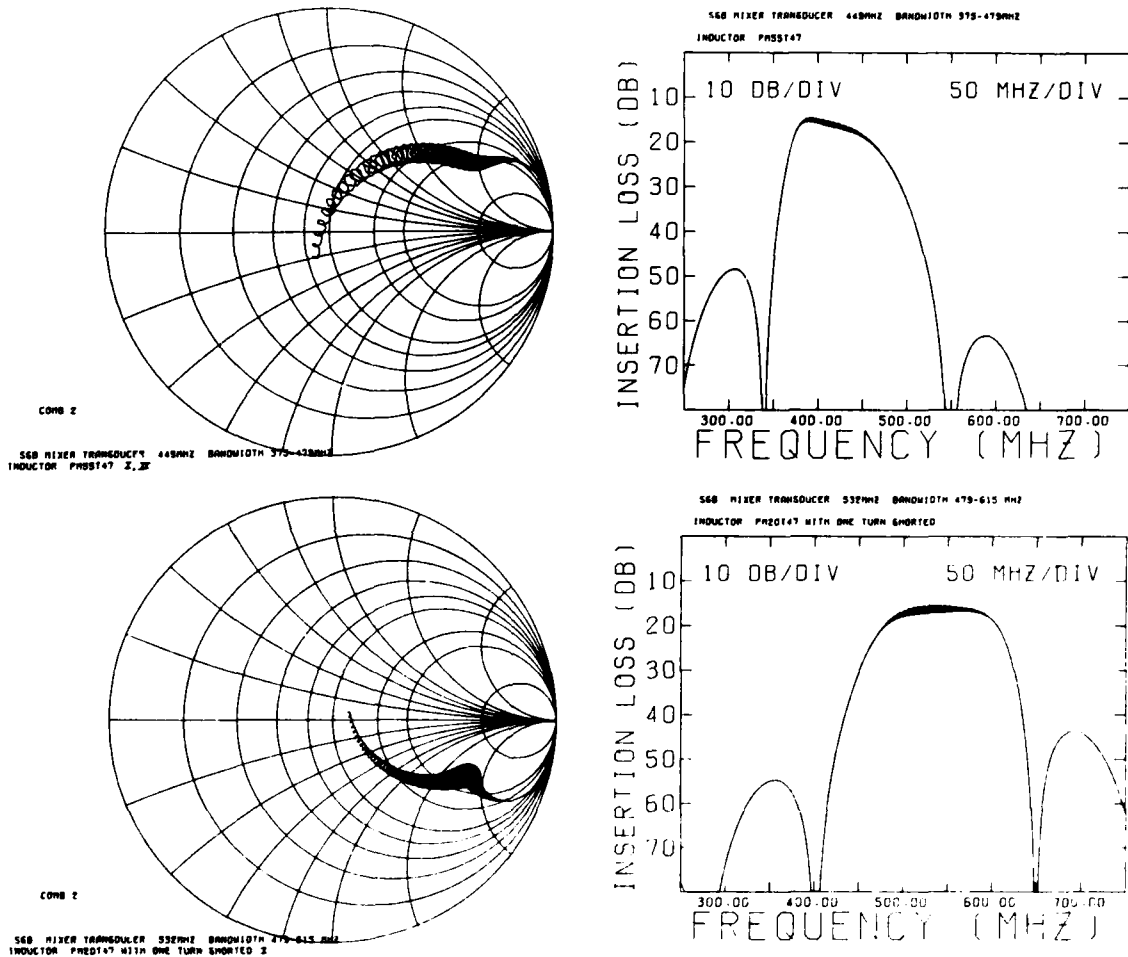


Figure C.28 Theory for individual channels corresponding to experiment of Figure C.31 top. (Top) Theory for low frequency channel, $L_1 = 258$ nhy, $Q = 25.3$, and SRF is 601 MHz. (Bottom) Theory for high frequency channel, $L_2 = 139$ nhy, $Q = 12.4$, and SRF is 1805 MHz.

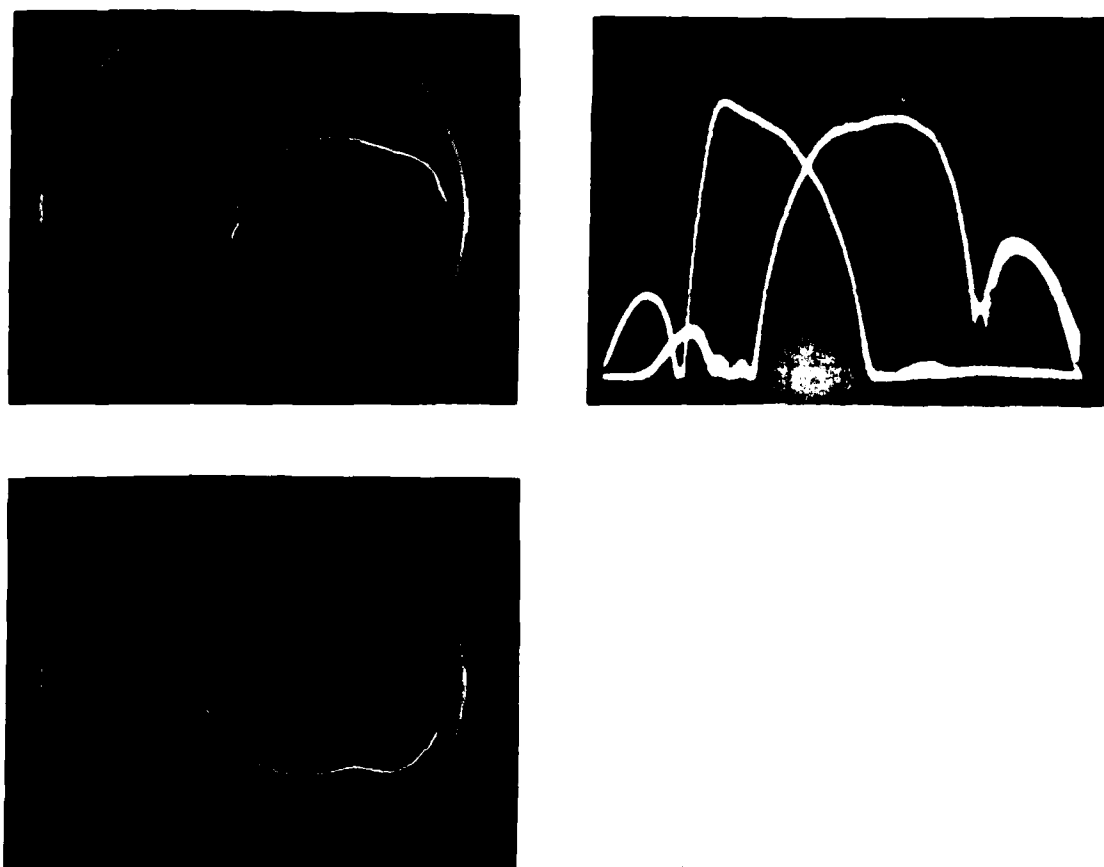


Figure C.29 Experiment corresponding to theory of Figure C.28.

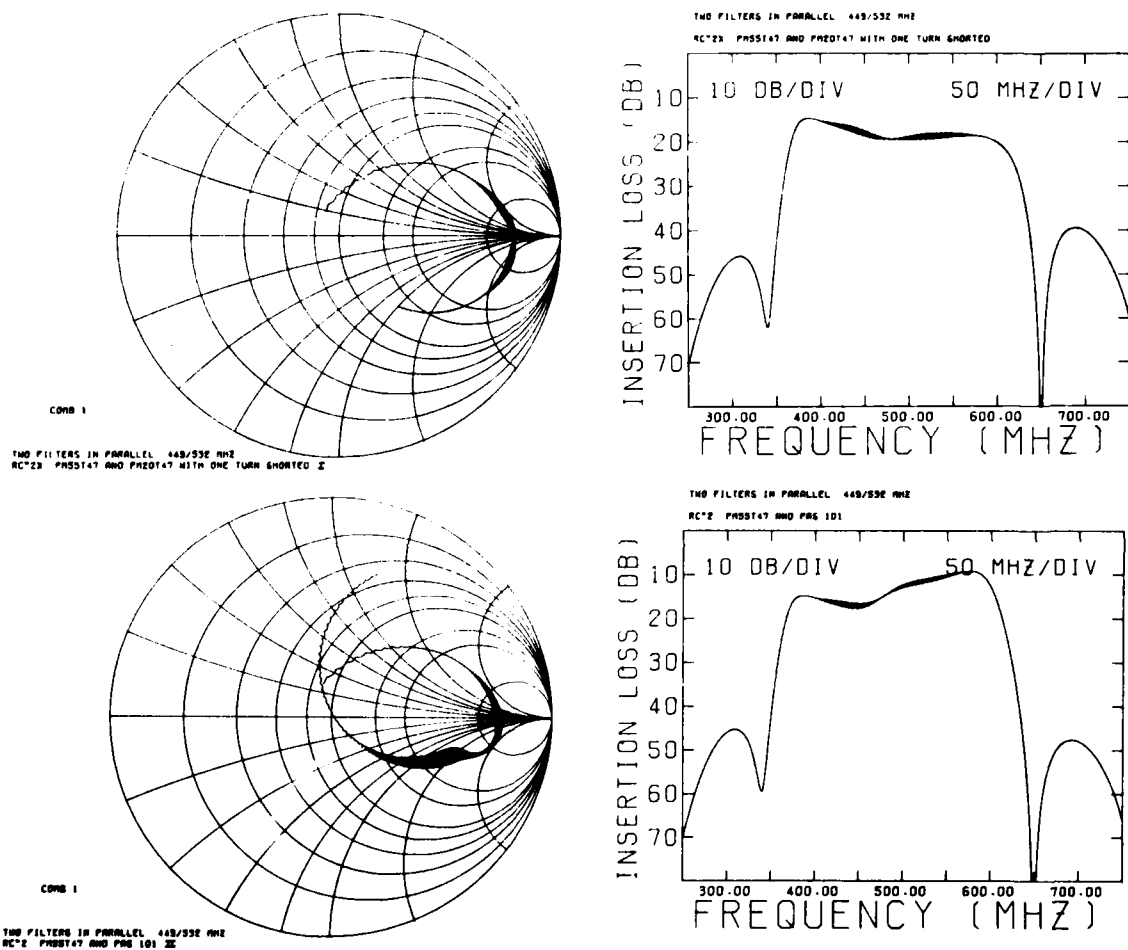


Figure C.30 Theory for combined channels corresponding to experiment of Figure C.31. (Top) Inductor values are given in caption of Figure C.28. (Bottom) L_1 is unchanged from above, $L_2 = 154$ nhy, $Q = 42.4$ and SRF is 1357 MHz.

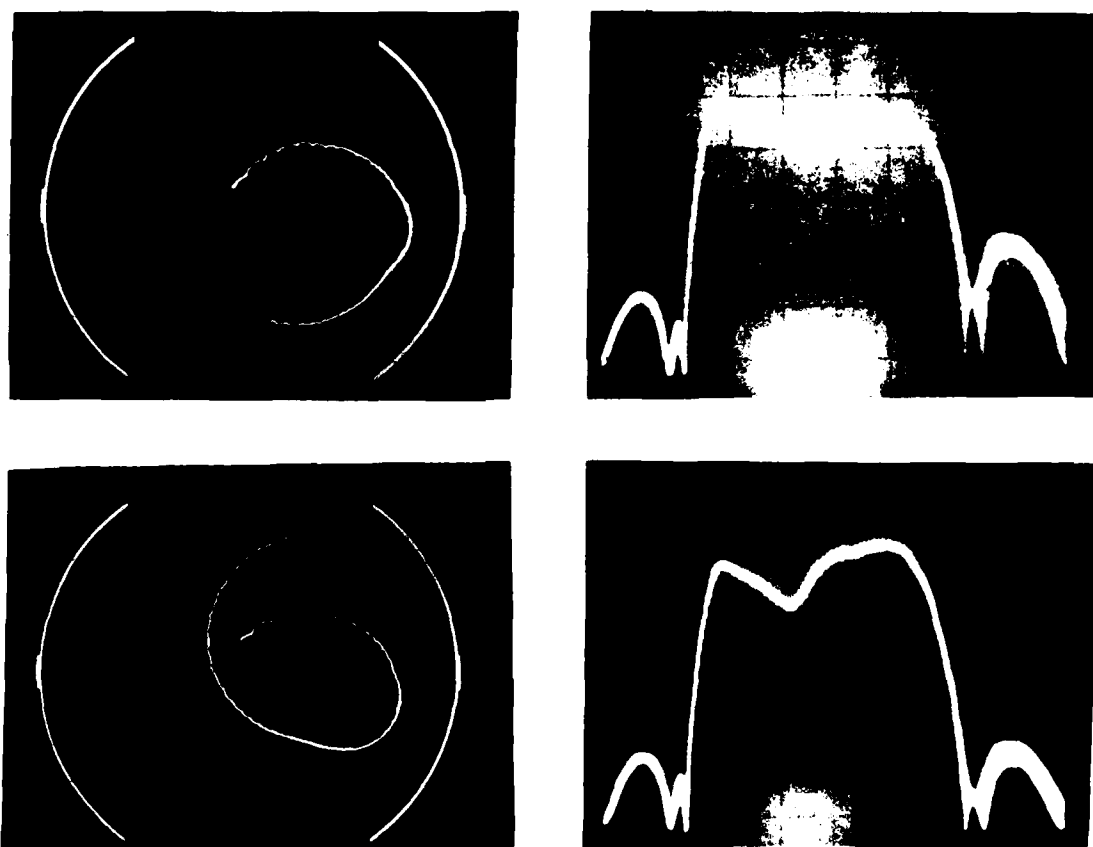


Figure C.31 Experiment corresponding to theory of Figure C.30.

are not included in the theory - see Appendix B.2. The right side is lower than the left as predicted, and the right sidelobe is very high. These effects are due to the low inductor Q and small value of inductance used for the high frequency channel (right hand side).

In the next case, only the inductor in the high frequency channel (right side) has been changed. The new values were $L_T = 154$ nhy, $Q = 42.4$, and SRF was 1357 MHz. The single channel responses are given in Figure C.32 (theory) and Figure C.33 (experiment). The combined response is shown in the bottom of Figure C.30 (theory) with L_3 and $L_4 = 20$ nhy, and C_5 and $C_6 = 23.3$ and 2.8 pf. The combined experimental response is given in the bottom of Figure C.31. Again there is a larger dip in the middle of the amplitude response than predicted by theory. Also, the right side is higher than the left side due to a higher inductor Q , and the right sidelobe is lower than the previous case because the inductor was larger, i.e. it was tuned closer to the transducer synchronous frequency.

The final case nearly duplicates the case shown in the bottom of Figures C.19 and the bottom of Figure C.25. However, different inductors were used, and although values were similar, they were not identical. In the left channel $L_T = 193$ nhy, $Q = 23.5$, and SRF was 670 MHz. In the right channel $L_T = 182$ nhy, $Q = 24.5$, and SRF was 1940 MHz. The single channel results are given in Figure C.34 (theory) and

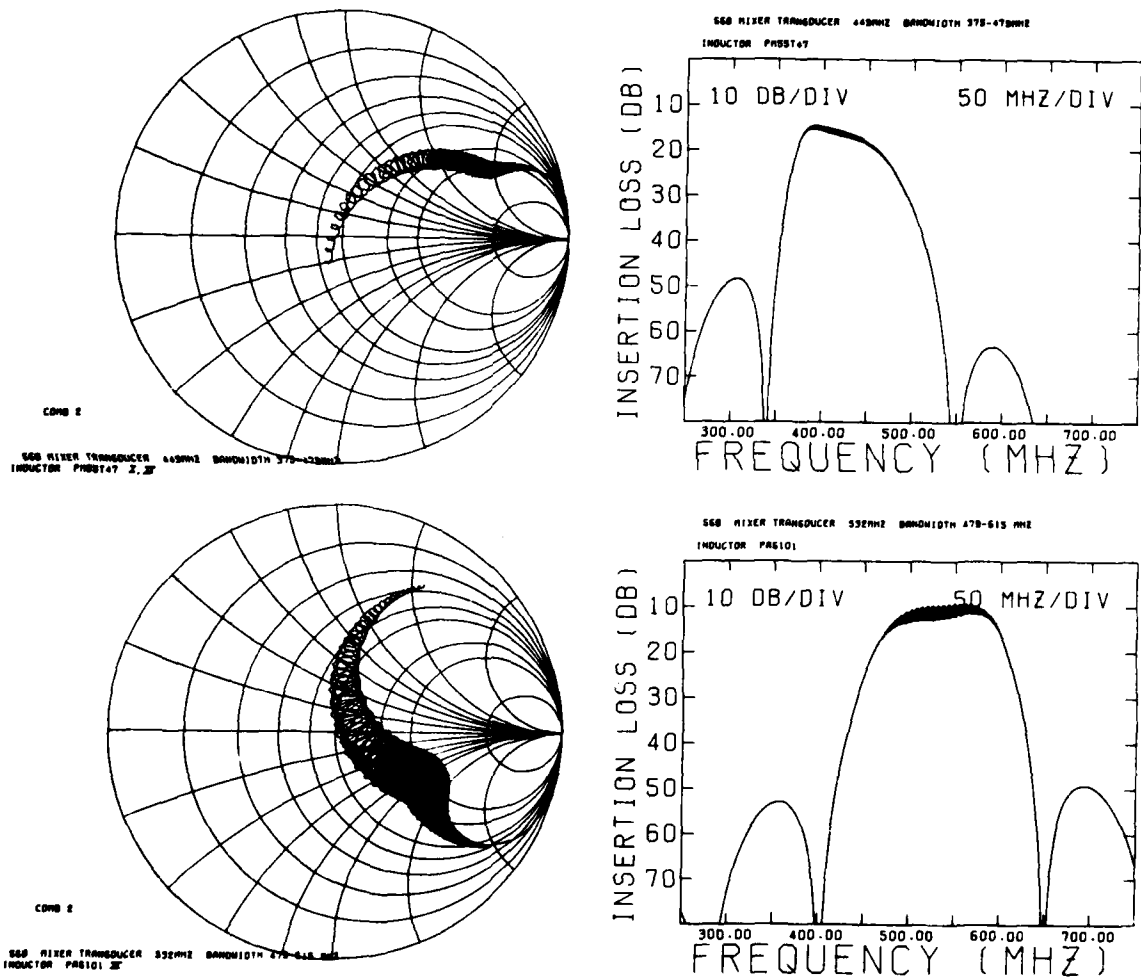


Figure C.32 Theory for individual channels corresponding to bottom of Figures C.30 and C.31.

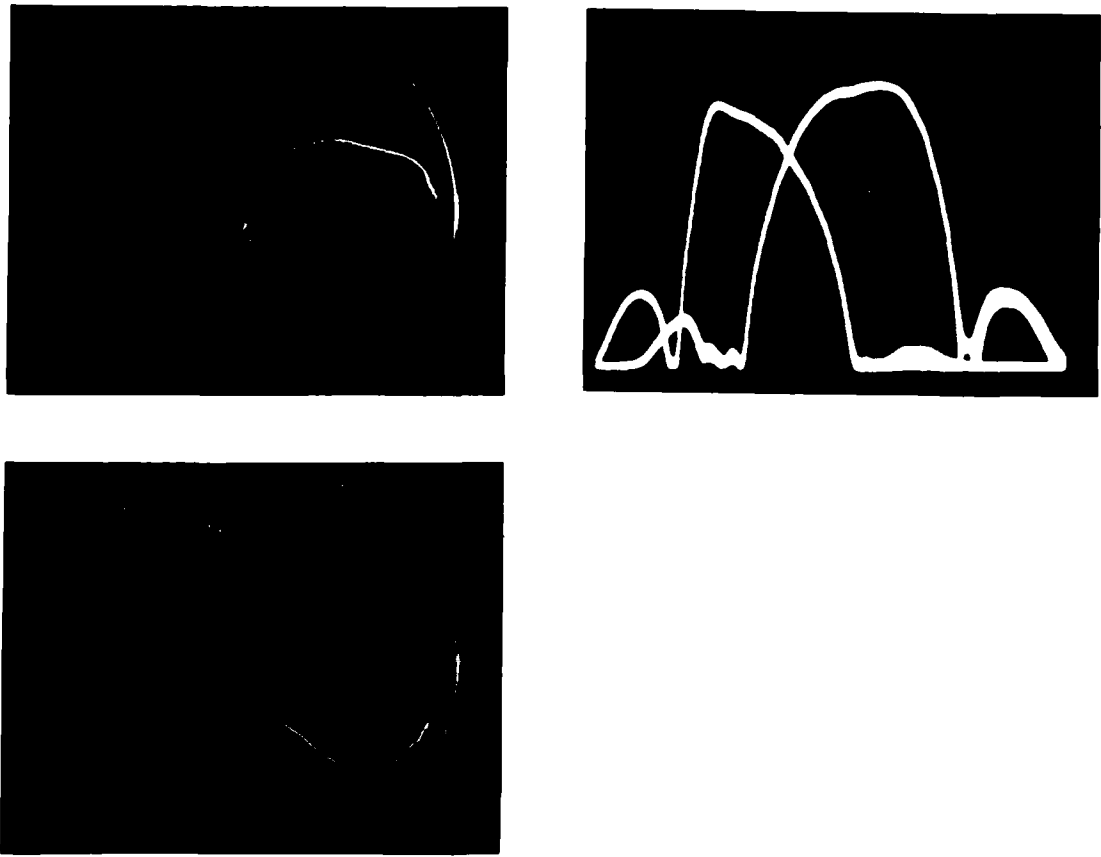


Figure C.33 Experiment corresponding to theory of Figure C.32.

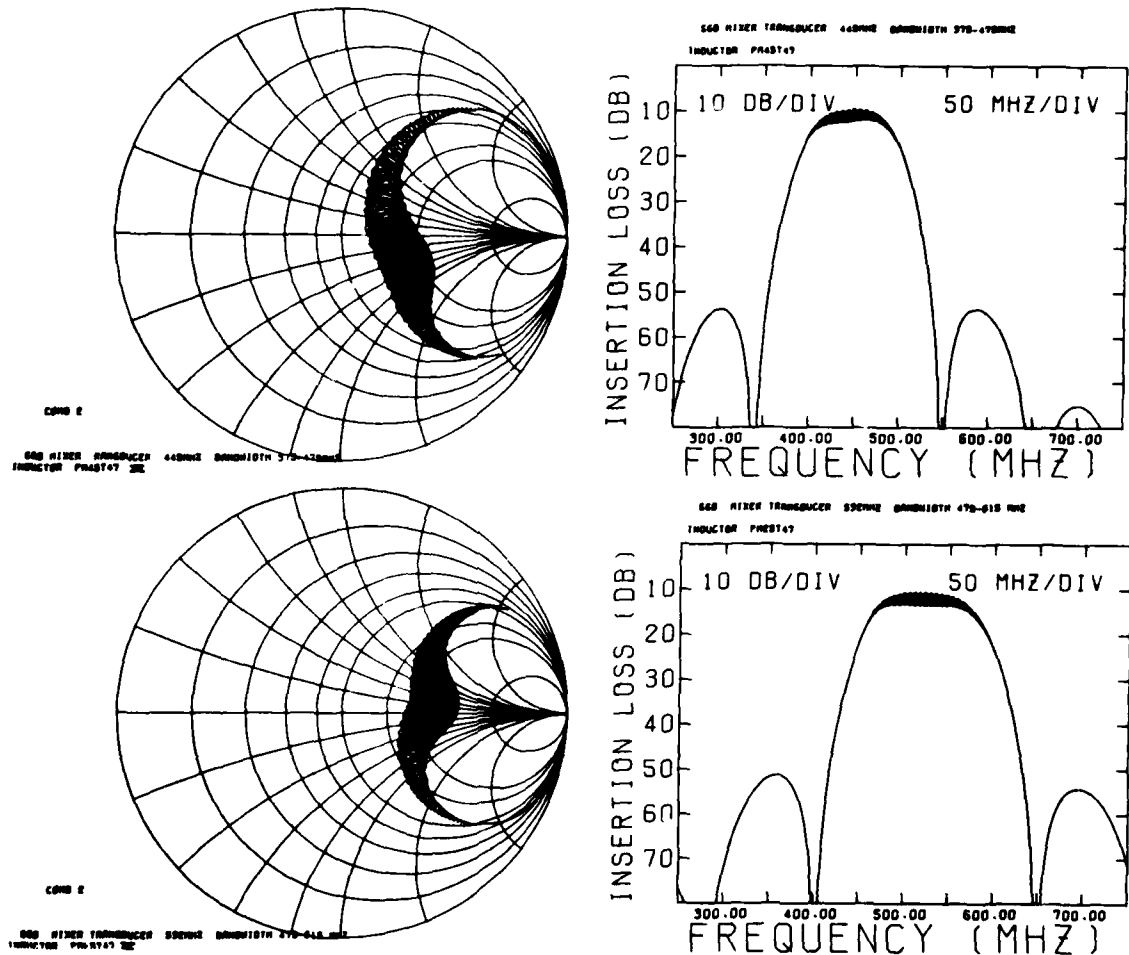


Figure C.34 Theory for individual channels corresponding to experiment of Figure C.37 (Top) Theory for low frequency channel, $L_1 = 193$ nhy, $Q = 23.5$, and SRF is 670 MHz. (Bottom) Theory for high frequency channel, $L_2 = 182$ nhy, $Q = 24.5$, and SRF is 1940 MHz.

Figure C.35 (experiment). The combined response is shown in Figure C.36 (theory) and Figure C.37 (experiment). Again the bandwidth of 35 percent, 1.59 shape factor, 17 dB insertion loss, and 42 dB sidelobes is obtained. Agreement of theory and experiment is excellent. In the top right of Figure C.37 a better perspective is provided with 100 MHz/div. abscissa centered on 500 MHz. Excepting the first sidelobes, all spurious signals are suppressed more than 50 dB. In particular, the absence of spurious bulk modes can only be appreciated if this is tried using other SAW filter approaches. In all the above cases, one of the channels was connected 180 degrees out of phase. This anomaly is explained in the next section.

C.5 Phase Differences Experiment

To establish a reference point for the discussion in this section, the two channels were connected in parallel without inductors L_1 and L_2 . Both transducer patterns were contained on the same photolithographic mask, (top of Figure C.18), ensuring precise alignment relative to each other. The individual responses are given in the top left of Figure C.38, and the parallel combination in the top right of Figure C.38. The frequency response in this case was the combination of the individual responses as expected. However, when one of the channels was connected 180 degrees out of phase, a null resulted at the cross-over frequency as

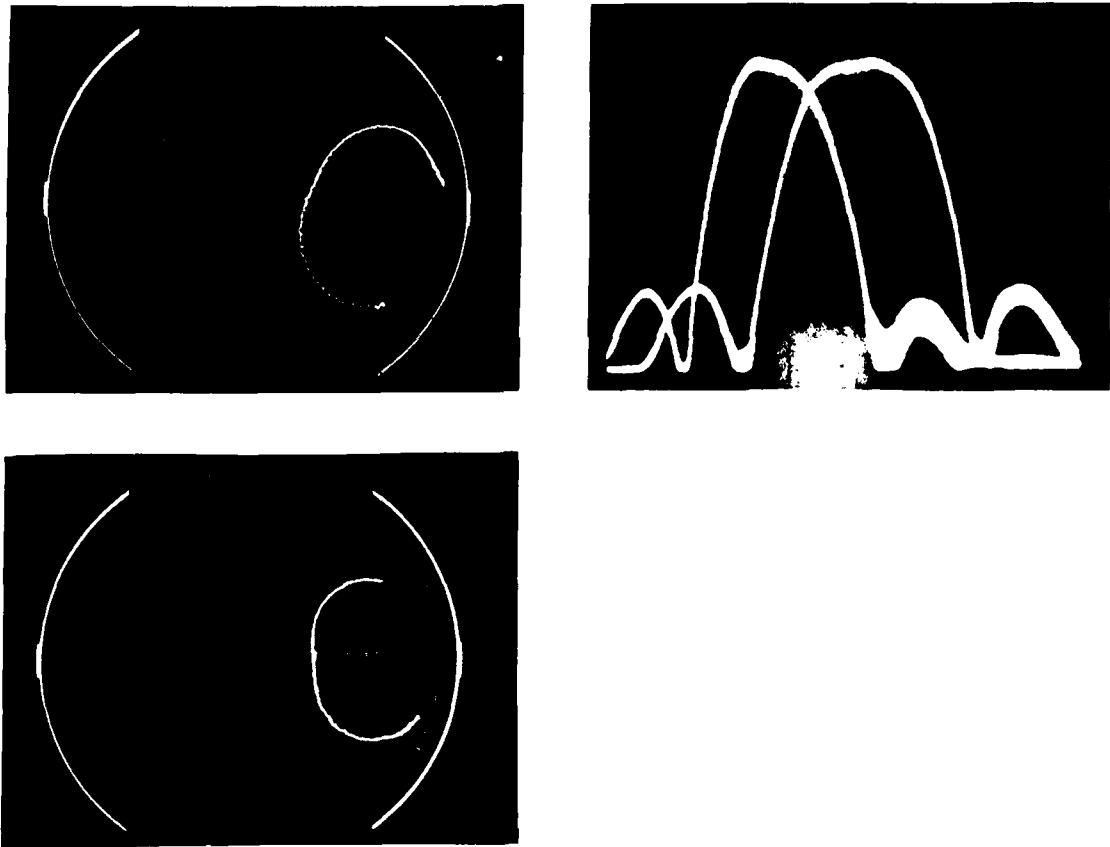


Figure C.35 Experiment corresponding to theory of Figure C.34.

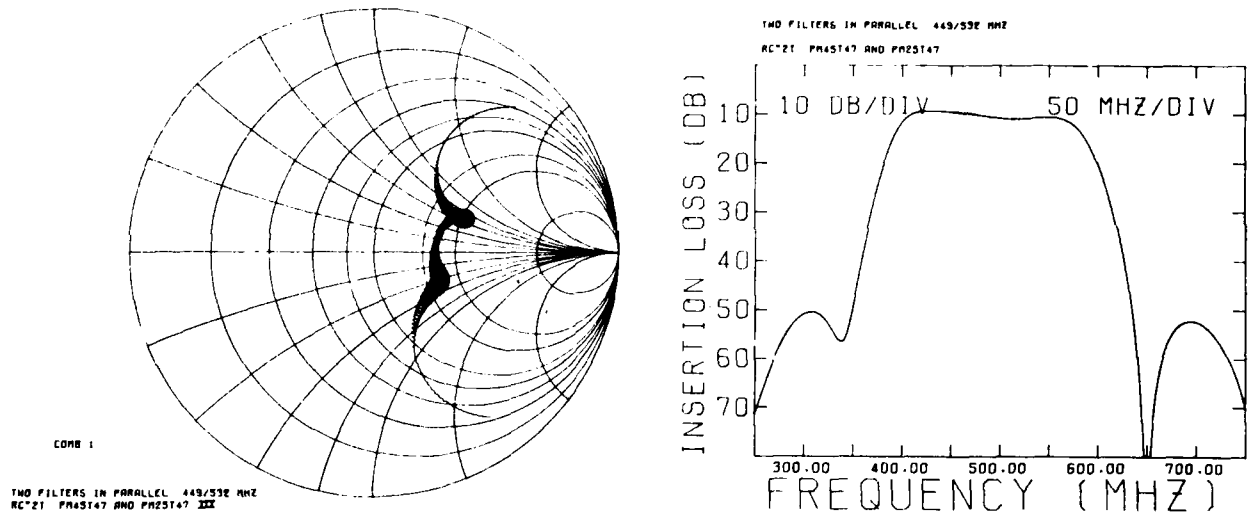


Figure C.36 Theory for combined channels corresponding to experiment of Figure C.37. Inductor values are given in caption of Figure C.34.

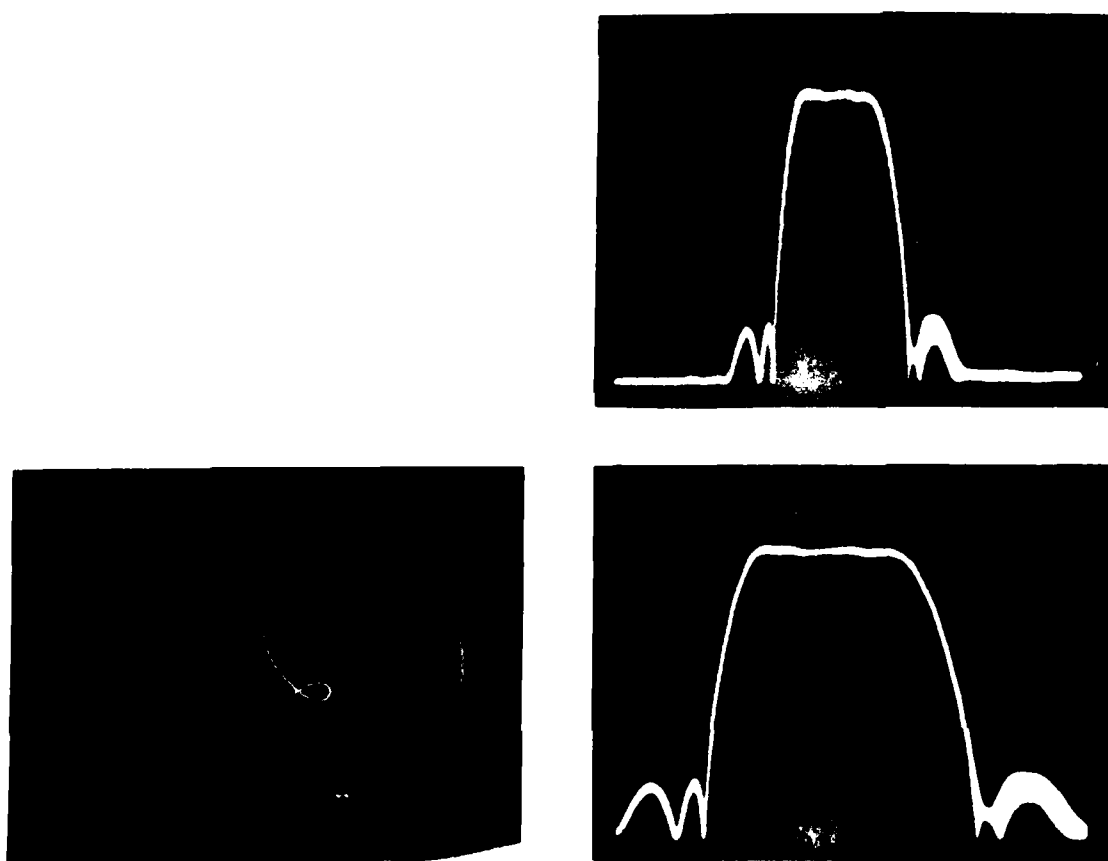


Figure C.37 Experiment corresponding to theory of Figure C.36.
Top right differs from bottom right in the Horiz.
scale: 100 MHz/div. centered on 500 MHz.

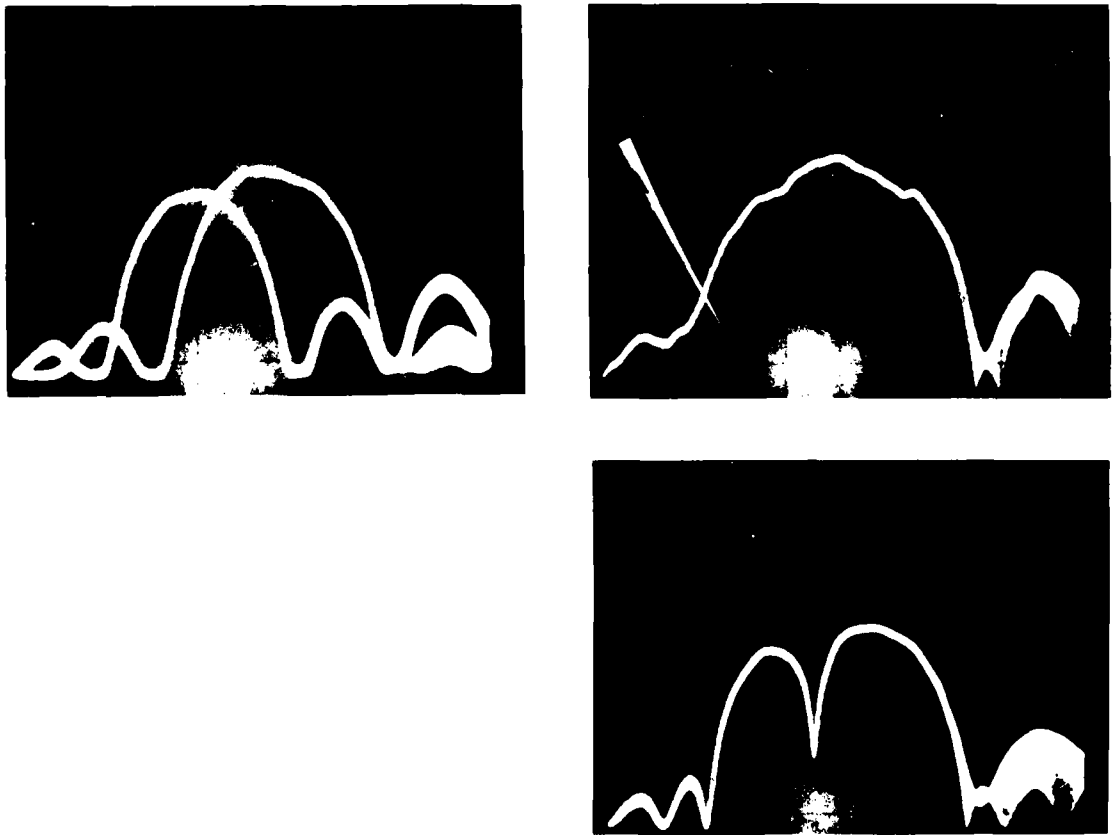


Figure C.38 (Top left) Double exposure showing frequency responses of individual unmatched SAW channels. (Top right) Unmatched SAW channels connected in parallel as shown in Figure C.2. (Bottom right) Unmatched SAW channels connected in parallel as shown in Figure C.2 except one channel is connected 180 degrees out of phase.

expected (bottom of Figure C.38).

Next, the channels were operated individually with inductors L_1 and L_2 now included. A double exposure in the top left of Figure C.39 shows the superimposed responses. When connected as shown in Figure C.2, the combined response was that of the top right in Figure C.39. The obvious conclusion is that the channels have a phase difference of nearly 180 degrees. Next, a 180 degree phase shift was introduced in one channel only by bonding one of the output transducers at the bottom pad rather than the usual top pad. The result of this new connection is shown in the bottom right of Figure C.39 - a very flat 35 percent bandwidth is now obtained. And when a variable phase shifter was added to one channel, it was possible to make the null deeper than the one in the top right of Figure C.39 and possible to make the flat response in the bottom right of Figure C.39 have a positive going bump of 2 dB at the cross-over frequency.

Finally, the phase shift was measured with a network analyzer. The desired quantity was the phase of S_{12} , however, this parameter was not practical to measure since it undergoes many thousands of phase reversals, and it is not necessary since the acoustic paths are identical. This was verified by the experiment shown in Figure C.38. Thus it was sufficient to measure the phase of S_{11} and multiply by 2 to account for S_{22} since the output of each channel was identical to the input. The bottom left of Figure C.39 is a

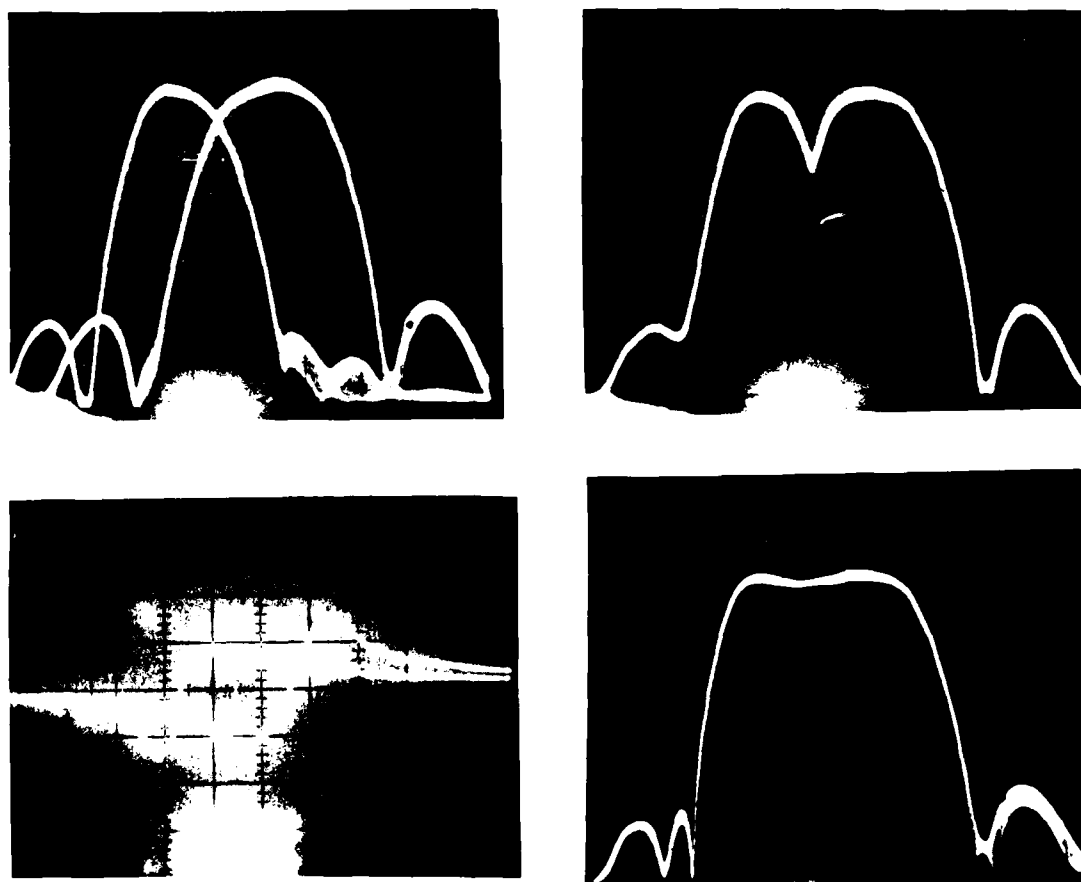


Figure C.39 (Top left) Double exposure showing frequency response of individual matched SAW channels. (Top right) Matched SAW channels connected in parallel as shown in Figure C.2. (Bottom left) Double exposure of the input impedances, S_{11} , of the matched SAW channels. Vert: 45 deg/div, Horiz: 50 MHz/div, $f_0 = 500$ MHz. (Bottom right) Matched SAW channels connected in parallel as shown in Figure C.2 except one channel is connected 180 degrees out of phase.

double exposure giving S_{11} of both channels - phase only; the scale is 45 degrees/div vertical and 50 MHz/div horizontal centered on 500 MHz. A white scratch on the abscissa denotes the cross-over frequency of 474 MHz where the signals were nearly 90 degrees out of phase. When multiplied by 2, the 180 degrees total phase shift was obtained. There were two other cross-over frequencies: 323 MHz and 348 MHz where the phase differed by about 5 degrees or 10 degrees total. This explains the two nulls in the photograph at the bottom right of Figure C.39 and their absence in the photograph at the top right of Figure C.39. An analytical theory is worked out in the next section and applied to the cross-over frequencies of 474 MHz and 348 MHz.

The results of a final experiment are given in the top of Figure C.40. The individual channels were tuned with inductors, L_1 and L_2 , in the opposite direction of that for broadening the bandwidth, i.e. the left channel was tuned for maximum response above its synchronous frequency rather than below its synchronous frequency, and the right channel vice versa. The result is shown in the top left of Figure C.40. It is obviously useless as a bandpass filter, but useful to reinforce the hypothesis concerning the phase difference problem. When the individual channels were connected as in Figure C.2, the response in top right of Figure C.40 was obtained. There are now two "cross-over"

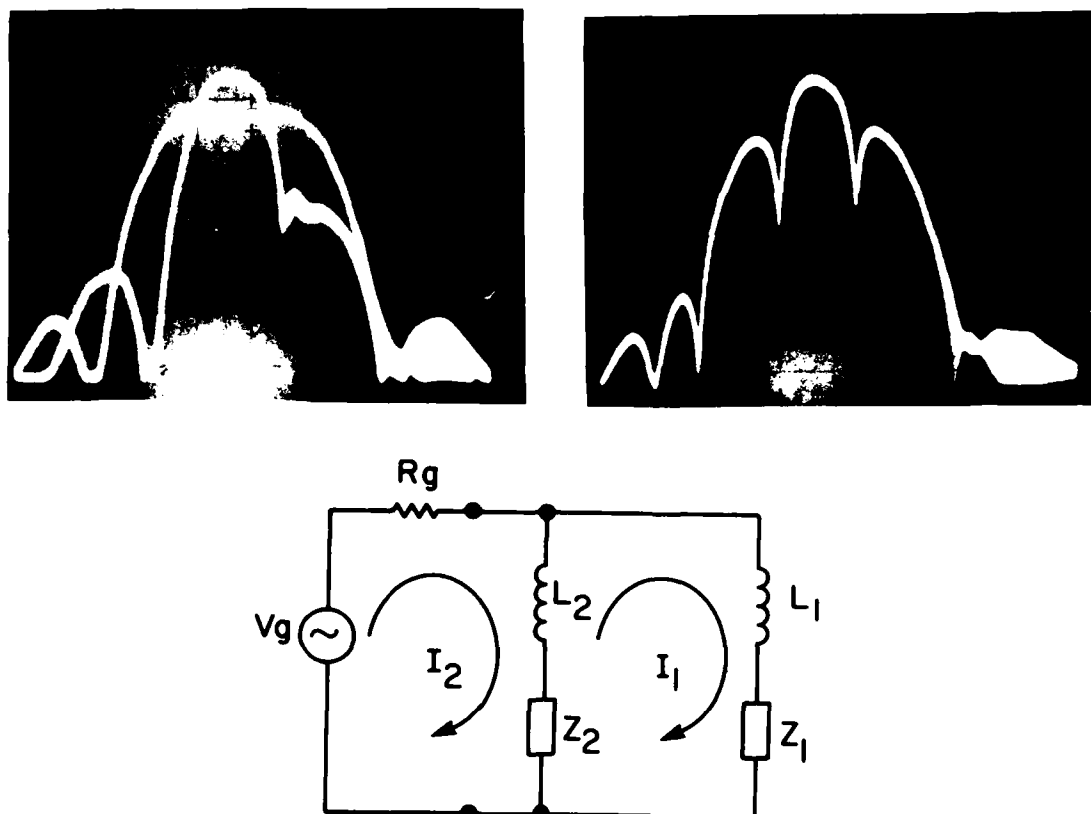


Figure C.40 (Top left) Double exposure showing frequency responses of individual SAW channels matched with a value of inductance different from that desired for broadbanding. (Top right) SAW channels at left are now connected in parallel as shown in Figure C.2. (Bottom) Simplified equivalent circuit for input portion of schematic diagram in Figure C.2.

frequencies in the intended passband, i.e. there are two frequencies where the amplitudes are nearly equal, and because of phase differences, nulls result.

C.6 Phase Differences - Theory

Two points are addressed in this section. First, why does the computer program not predict the phase shifts in the individual channels and give a null in the combined frequency response? The second point addressed is the creation of an analytic model to predict the measured phase shifts.

Referring to Figure C.17, it can be said that channel 1 has a transducer with impedance Z_{T1} and current I_1 . Likewise channel 2 has a transducer with impedance Z_{T2} and current I_2 . Insertion loss is defined as

$$IL(dB) = 20 \log_{10} \frac{2R_g}{V_g} [|I_1|^2 \text{Re}(Z_{T1}) + |I_2|^2 \text{Re}(Z_{T2})], \quad (C.4)$$

where V_g and R_g are the source voltage and internal impedance. I_1 and I_2 are complex but have had their magnitude taken before combining, therefore the phase information is lost and a null does not appear in the frequency response.

Next, an analytic model is created which will predict the phase shifts and resulting null at the cross-over frequency. The input portion of the circuit can be

simplified and redrawn as shown in the bottom of Figure C.40. Z_1 and Z_2 are the complex, frequency dependent impedances of the SAW transducers. L_1 and L_2 are the series matching inductors. V_g and R_g are the source voltage and internal impedance. Using the standard notation of $S = j\omega$ and assuming a steady state condition, the currents and radiating voltages were found to be

$$I_1 = \frac{V_g (SL_2 + Z_2)}{R_g (SL_1 + Z_1 + SL_2 + Z_2) + (SL_2 + Z_2)(SL_1 + Z_1)}, \quad (C.5)$$

$$V_1 = I_1 R_e(Z_1), \quad (C.6)$$

$$I_2 = \frac{V_g (SL_1 + Z_1)}{R_g (SL_1 + Z_1 + SL_2 + Z_2) + (SL_2 + Z_2)(SL_1 + Z_1)}, \text{ and} \quad (C.7)$$

$$V_2 = I_2 R_e(Z_2). \quad (C.8)$$

Since the denominators are identical,

$$\frac{V_1}{V_2} = \frac{V_g (SL_2 + Z_2) R_e(Z_1)}{V_g (SL_1 + Z_1) R_e(Z_2)}. \quad (C.9)$$

It is straightforward using (C.9) to show that the phases of the numerators in (C.5) and (C.7) will be equal when V_1 equals V_2 , i.e. at the cross over-frequency. It can further be shown that the numerator phases of (C.5) and (C.7) will be not only equal but of opposite sign at the cross-over

frequency if $I_m(Z_1) + SL_1$ is of opposite sign relative to $I_m(Z_2) + SL_2$. This information is a helpful check on the calculations that follow.

The first example considered was the filter of Figure C.39. The cross-over frequency was 474 MHz. The quantity $SL_1 + Z_1$ was measured with a network analyzer to be $90 + j115$. $SL_2 + Z_2$ was measured to be $55 - j70$. Using these values in (C.5) - (C.8) gives

$$I_1 = \frac{89 \angle -51.8}{20377 \angle 6.4} = 0.0044 \angle -58.2, \quad (C.10)$$

$$V_1 = I_1 \operatorname{Re}(Z_1) = 0.393 \angle -58.2, \quad (C.11)$$

$$I_2 = \frac{146 \angle 51.9}{20377 \angle 6.4} = 0.0072 \angle 45.5, \text{ and} \quad (C.12)$$

$$V_2 = I_2 \operatorname{Re}(Z_2) = 0.394 \angle 45.5. \quad (C.13)$$

From these calculations, the following conclusions can be made. The radiated voltages, V_1 and V_2 , have the same magnitude at the cross-over frequency as expected. The phases of the numerators, (C.10) and (C.12), are equal and of opposite sign. The phases of V_1 and V_2 , (C.11) and (C.13), differ by 103.8 degrees $\times 2$ or 207.6 degrees giving a partial cancellation (6.4 dB worth) and explaining why the addition of a variable phase shifter gives a deeper null. Further, the value of 103.8 degrees agrees closely with the

measured value in the bottom left of Figure C.39 at the white scratch mark (474 MHz). And finally, the phases of V_1 and V_2 , (C.11) and (C.13), are not equal and opposite which also agrees with the measured values in the bottom left of Figure C.39.

The second example considered was also the filter of Figure C.39 but now at the cross-over frequency of 348 MHz (first null from center of photo). Again $SL_1 + Z_1$ was measured with the network analyzer and equaled $30 - j200$. $SL_2 + Z_2$ was measured as $20 - j350$. In this case

$$I_1 = \frac{350.6 \angle -86.7}{78991 \angle -147.9} = 0.0044 \angle 61.2, \quad (C.14)$$

$$V_1 = I_1 R_e(Z_1) = 0.133 \angle 61.2, \quad (C.15)$$

$$I_2 = \frac{202.2 \angle -81.5}{78991 \angle -147.9} = 0.0026 \angle 66.4, \text{ and} \quad (C.16)$$

$$V_2 = I_2 R_e(Z_2) = 0.051 \angle 66.4. \quad (C.17)$$

The voltages V_1 and V_2 , (C.15) and (C.17), should have the same amplitude but do not. This discrepancy is 8 dB which is not surprising since the filter response has a steep slope at this point. Further, the discrepancy is of minor importance since it is obvious that the phase differences

are only going to be a few degrees anywhere in this region. In this case the phase difference was 5 degrees X2 or 10 degrees total. This explains the nulls or absence thereof at 348 and 323 MHz in the bottom right and the top right of Figure C.39, respectively.

C.7 Conclusions

The stagger tuning technique is very attractive for simultaneously achieving bandwidth greater than 35 percent, shape factor less than 1.6, insertion loss less than 18 dB, and sidelobes greater than 40 dB. Other SAW filter approaches give better performance, but none can simultaneously achieve all four parameters. In addition the stagger tuning approach has another degree of freedom in the placement of both nulls to create frequency traps. Finally, this approach is extendable to three or more parallel connected SAW filters. Also a theory has been developed to explain the presence of phase differences in the different channels. And the addition of a variable phase shifter may or may not be required depending on the particular design.

APPENDIX D

NARROW BAND MATCHING OF SAW FILTERS

This Appendix provides more details concerning the output transducer and narrow band matching of the SAW Bilinear Mixer discussed in Section 4.4. For convenience the mixer schematic diagram is repeated again in Figure D.1. The LiNbO_3 crystal actually contained 7 SAW channels: 2 mixers with no grating (multistrip coupler), 2 mixers with a grating in the SAW propagation path (see Section 4.3), 2 channels for the 838 MHz transducer as a simple delay line, and 1 channel for the 328 MHz apodized transducer as a simple delay line. The insertion loss of the 510 MHz transducer was not determined from this crystal.

The channel with the 328 MHz apodized transducers was measured as a delay line to establish a reference condition, and then the narrow band matching was added to one port only to determine its relative contribution. Unfortunately when two apodized transducers are operated as a delay line, the insertion loss of one is not one half of the total insertion loss. Instead, one of the transducers should be relatively broadband and unapodized to accurately determine the properties of the apodized transducer. However, this did not present a problem in this case since it was only

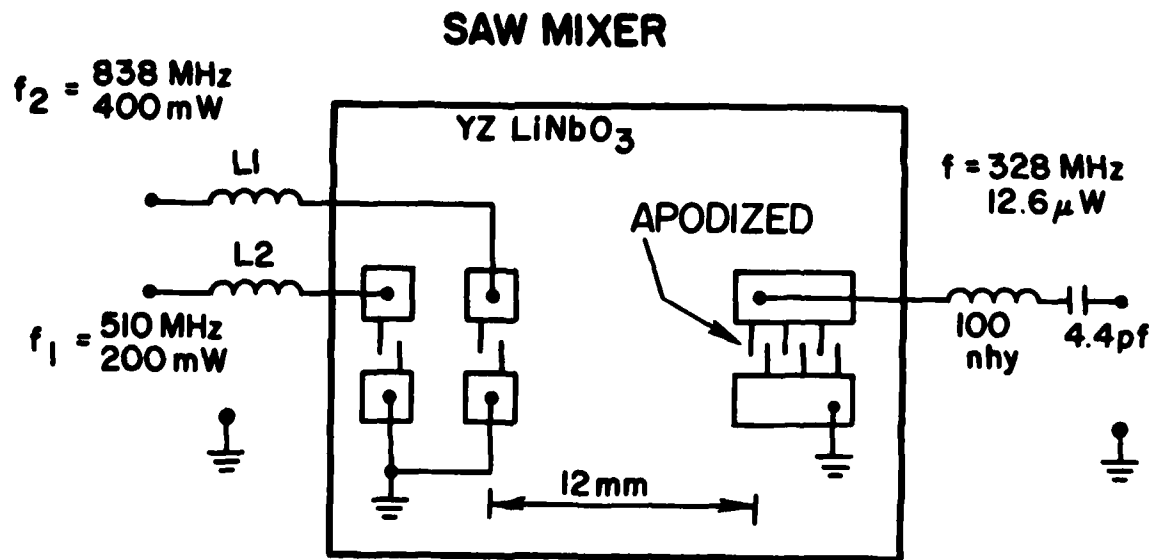


Figure D.1 Schematic of bilinear SAW mixer. The difference frequency is passed by the apodized and narrow band matched output filter.

necessary to determine the relative contribution of the narrow band matching. The transducers were Hamming weighted with $N=63$ periods of double electrode fingers, center frequency of 328 MHz, and a 1.5 percent bandwidth. The bottom of Figure D.2 shows a computer generated drawing of the transducer. The apodization is cosine squared on a pedestal with a pedestal height of 8%. This corresponds to Hamming weighting which has the lowest possible sidelobes: 43 dB for one transducer. The top of Figure D.2 shows a computer generated frequency response for one of these transducers. It is simply the Fourier transform of the weighting function for the transducer shown in the bottom of Figure D.2, however, it has no second order effects included.

The frequency response of the apodized transducers as a delay line is given in the top left of Figure D.3. In addition to the desired 328 MHz response, there is a strong bulk mode at 703 MHz and a third harmonic at 984 MHz. Fortunately the input signals, 838 MHz and 510 MHz, fall between these responses, and good rejection was still possible. The corresponding input impedance is shown in the top left of Figure D.4 as the frequency sweeps 300 to 360 MHz with an additional marker dot at 328 MHz. The small circles result from triple transit, i.e. reflections from the opposing transducer, and since the opposing transducer is identical, it reflects strongly. The lower left of Figure D.4 is identical except the apodized transducer is now in a

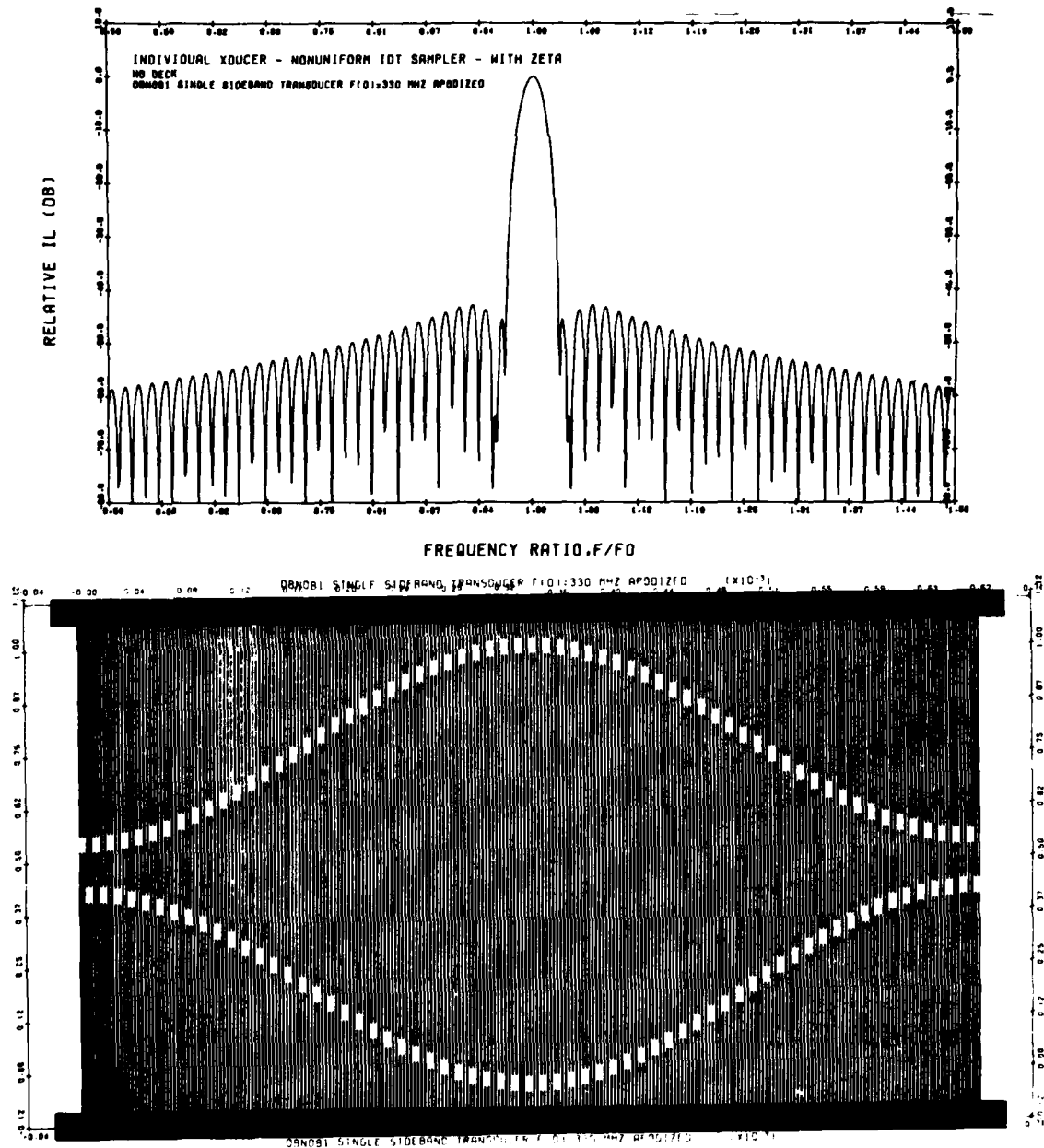


Figure D.2 (Top) Theoretical frequency response of the single apodized transducer with Hamming weighting used in this Appendix and Section 4.4. (No second order effects are included). (Bottom) Computer generated drawing of the apodized Hamming weighted transducer discussed in the Appendix and Section 4.4.

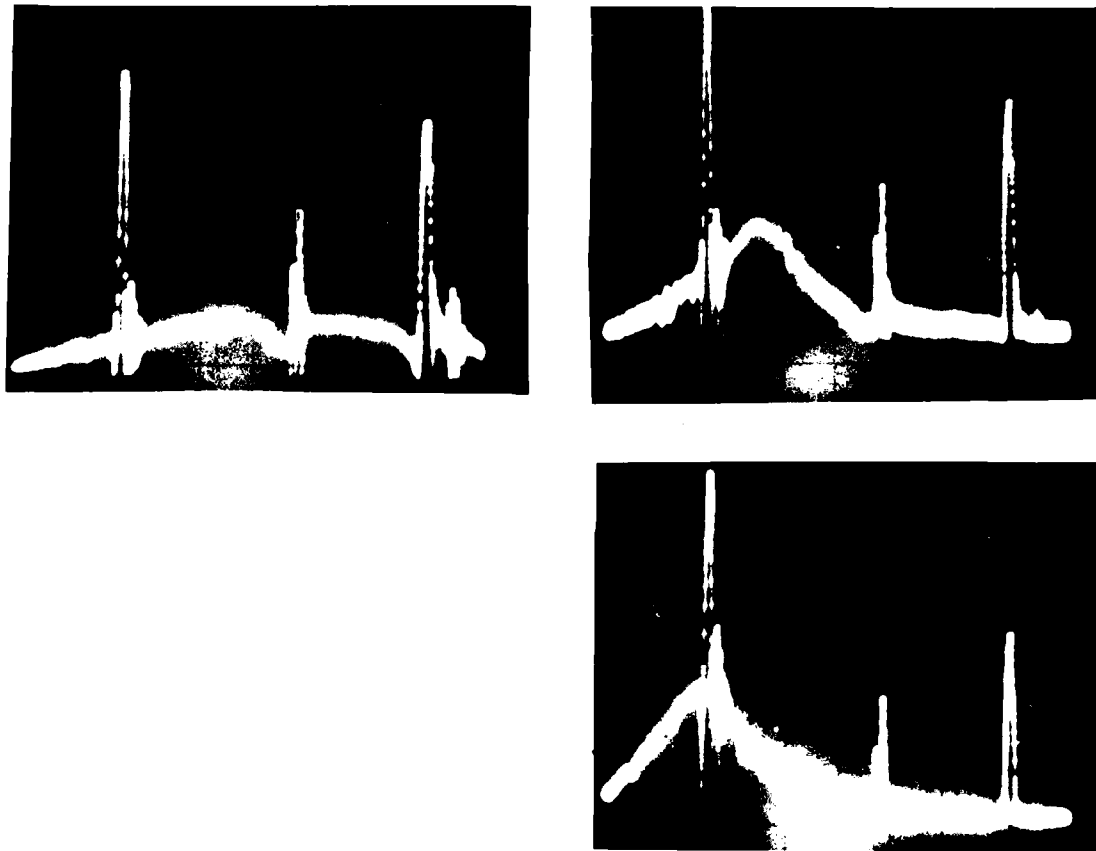


Figure D.3 (Top left) Delay line frequency response of two identical apodized transducers with no matching. The responses are 328 MHz, a bulk mode at 703 MHz, and the third harmonic at 984 MHz. Vert. is 10 dB/div., Horiz. is 100 MHz/div. and $f_0 = 600$ MHz. (Top right) The narrowband LC resonant filter has been added to the output only of the delay line on the left. L is 51 nhy, and C is 4.4 pf. (Bottom right) Same as top right except L is 100 nhy and C is 4.4 pf.

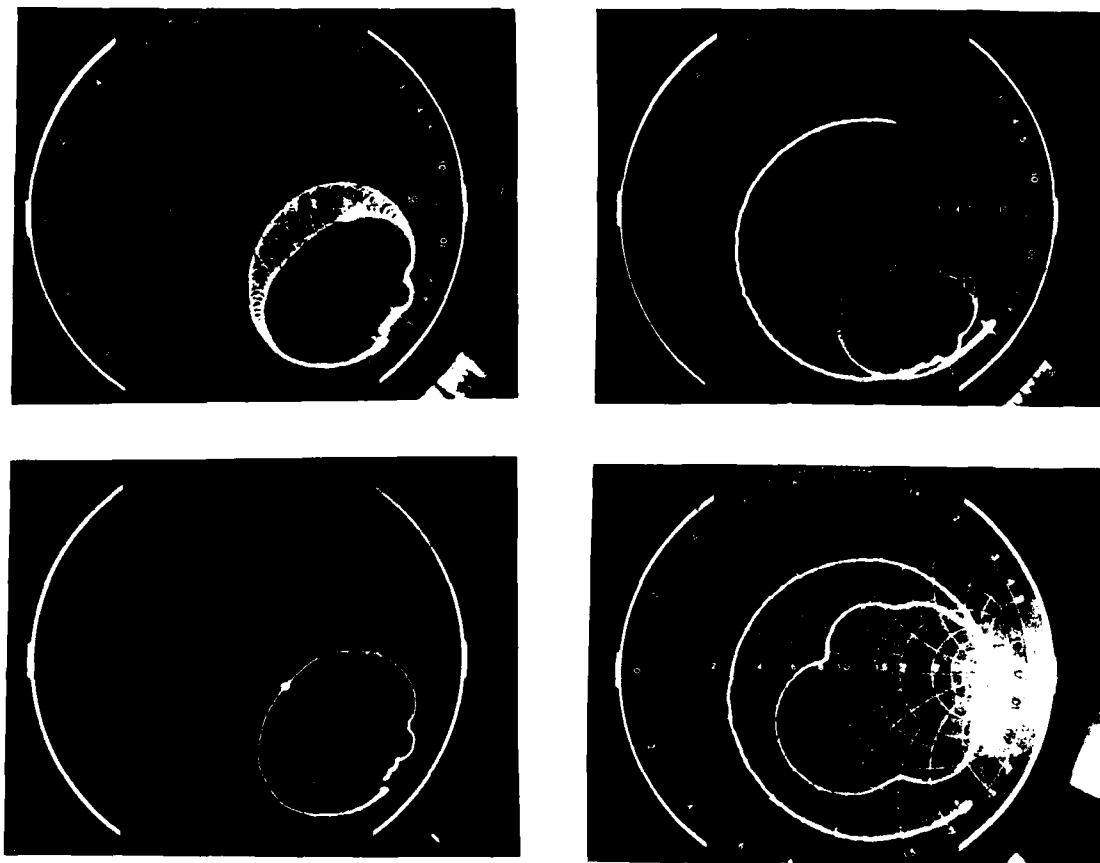


Figure D.4 Output impedances corresponding to frequency response of Figure D.3. (Top left) Output impedance of apodized transducer with no matching. Small circles within the trace are due to reflections (triple transit) from an identical input transducer. Frequency sweeps 300 MHz to 360 MHz with a marker dot at 328 MHz. (Bottom left) Same as top left except the opposing input transducers are now synchronous at 838 and 510 MHz (See mixer schematic of Figure D.1) and do not cause strong reflections. (Top right) Output impedance corresponding to top right of Figure D.3. Frequency sweeps 243 MHz to 470 MHz. (Bottom right) Output impedance corresponding to bottom right of Figure D.3. Frequency sweeps 243 MHz to 470 MHz.

mixer channel and the opposing transducers, now 838 MHz and 510 MHz, do not reflect strongly since they have different synchronous frequencies. Thus the triple transit has disappeared.

Next, the narrow band L and C (series resonance) were added to the apodized delay line to find their relative contribution. The inductor had a reactance equal and opposite to the combined capacitive reactances of the transducer plus external capacitor, C, to achieve resonance at 328 MHz. In theory, the added series LC network will have no effect on the circuit at its resonant frequency,

$$\omega = (LC)^{1/2}, \quad (D.1)$$

but it will act as a bandpass filter rejecting all other frequencies. A chip capacitor and slug tunable inductor were used for the C and L. The top right of Figure D.3 shows a peak added to the floor of the frequency response between 328 MHz and 703 MHz, and varying the tunable inductor moved the peak to the left or right as desired within the tunable range of the inductor. Using a different value inductor, the peak (resonance) was shifted to 328 MHz as shown in the bottom right of Figure D.3. The corresponding input impedances are shown in the top right and bottom right of Figure D.4, respectively.

An acceptable value and type of inductor was attained only with difficulty. A problem arose because the first several combinations of L and C had a resonance that was too

close to the self resonant frequency of the inductor. (The same problem could also arise if the self resonant frequency of the capacitor is lower than that of the inductor, but typically this is not the case). The result will be greatly increased resistance if the series resonance is less than but approaching the self resonant frequency of the inductor. This effect is dramatically demonstrated in the series of pictures in Figure D.5. The same inductor was used in each case, and the capacitor is increasingly smaller in each picture raising the series resonance closer and closer to the self resonant frequency of the inductor. The L and C are series connected with C grounded, i.e. the transducer is not included in this experiment. In each case the tunable 270 nhy inductor is set to maximum inductance, and the frequency of the input impedance sweeps 116 MHz to 275 MHz. The capacitors are 5.0 pf in the top left, 3.2 pf in the top right, 1.0 pf in the bottom left, and 0.66 pf in the bottom right. Series resonance occurs when the impedance crosses the zero reactance line, and since each trace starts at 116 MHz, it is easy to see the frequency of series resonance increases as the capacitor value decreases. It is also easy to see the resistance, which should be zero in the ideal case, increase from 6 ohms to 350 ohms rendering the device totally useless. Finally, if the intended resonance is above the inductor self resonant frequency, no resonance will be achieved.

For properly chosen values of L and C, the additional

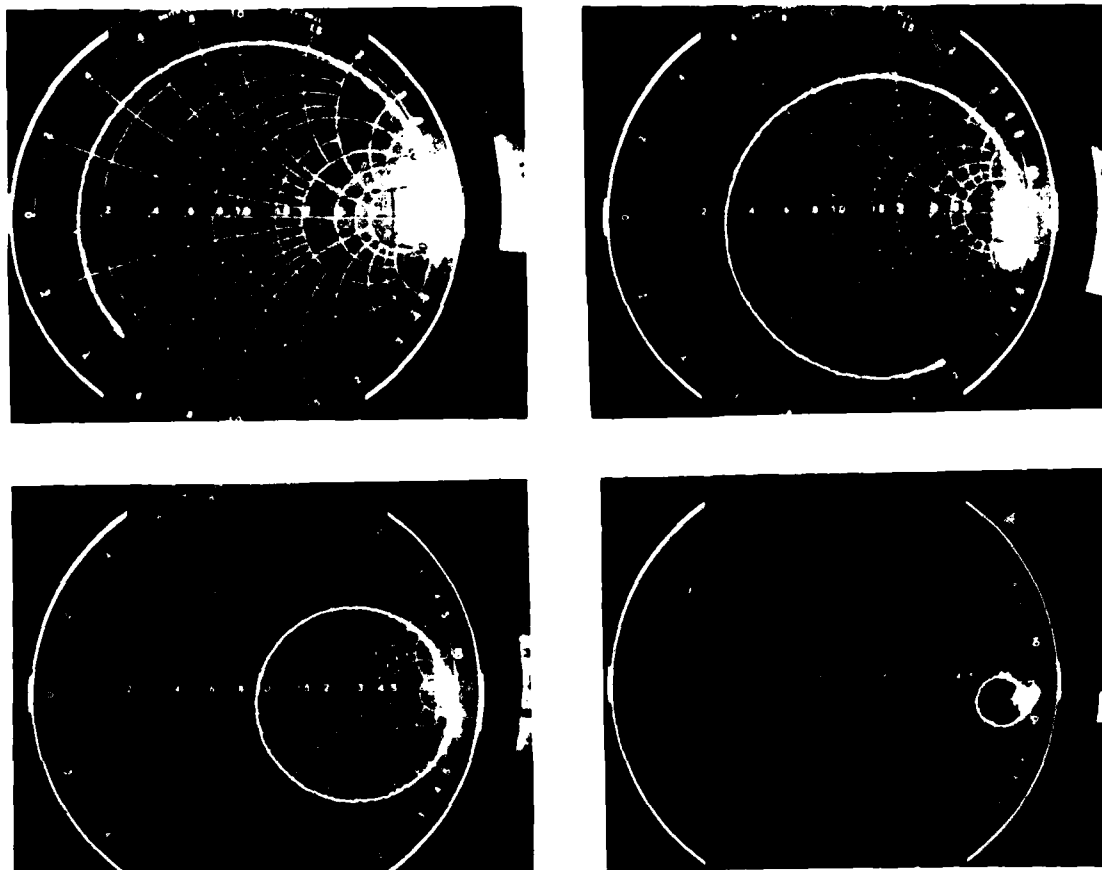


Figure D.5 Impedances of a series L and C versus frequency. (They are not connected to the transducer in this experiment). In all cases the inductor is 270 nhy, and frequency sweeps 116 MHz to 275 MHz. (Top left) C is 5.0 pf. (Top right) C is 3.2 pf. (Bottom left) C is 1.0 pf. (Bottom right) C is 0.66 pf.

resistance will be insignificant. Using this guidance, a 100 nhy slug tunable inductor and a 4.4 pf capacitor were finally used. The bulk mode at 703 MHz was suppressed an additional 18 dB, and the 984 MHz third overtone was suppressed an additional 23 dB when comparing the top left of Figure D.3 with the bottom right of Figure D.3.

VITA

Roger Dale Colvin was born near Kansas City, Missouri on February 7, 1951, son of Robert H. and E. Eileen Colvin. All twelve years of pre-college education were obtained in the rural community of Odessa, Missouri, ending with graduation in May 1969. He received a BS in Electronics Technology (cum laude) from Central Missouri State University - Warrensburg in 1974; BSEE (cum laude and honors scholar) 1975, MSEE in 1976, and completed all course work for Ph.D EE in 1977, all from University of Missouri - Columbia. His area of study was semiconductor theory and device fabrication.

He received a commission in the US Air Force through ROTC in 1975. Active duty was delayed two years for completion of graduate studies. From 1977 to present he has been with the Rome Air Development Center, Electromagnetic Sciences Division at Hanscom Air Force Base, MA. His current research interests include UHF acoustic oscillators, matched filtering and nonlinear properties of surface acoustic wave devices.

He was married to H. Frances Dochterman of Canton, Missouri on March 7, 1976.

Capt Colvin is a member of the IEEE, Society of Photo-Optical Instrumentation Engineers, Phi Eta Sigma, Eta Kappa Nu, Tau Beta Pi, Phi Kappa Phi, and Sigma Xi.



MISSION of Rome Air Development Center

RADC plans and executes research, development, test and selected acquisition programs in support of Command, Control Communications and Intelligence (C³I) activities. Technical and engineering support within areas of technical competence is provided to ESD Program Offices (POs) and other ESD elements. The principal technical mission areas are communications, electromagnetic guidance and control, surveillance of ground and aerospace objects, intelligence data collection and handling, information system technology, ionospheric propagation, solid state sciences, microwave physics and electronic reliability, maintainability and compatibility.